CR-128873
c.1

THE EFFECT OF NOSE GEOMETRY ON THE
AEROTHERMODYNAMIC ENVIRONMENT OF SHUTTLE
ENTRY CONFIGURATIONS*

by John J. Bertin
with W.R. Martindale, H. Tom Faria, Bruce W. Graumann,
M. Kathy Horn, and Gary W. Johnson

Aerospace Engineering Report 73001

(Mr. W.R. Martindale, who is a project engineer
with ARO, Inc., made significant contributions
to the preparation of this report and is, therefore,
listed as a co-author)

Department of Aerospace Engineering and
Engineering Mechanics

The University of Texas at Austin
January 1973

TABLE OF CONTENTS

INTRODUCTION

In order to determine the convective heat-transfer distribution for the
nose region of the space shuttle entry configurations, one must describe the
three-dimensional flow-field, which may include extensive regions of separated
flow. Because of the complexity of the flow field for the nose region, ex-
perimental data are needed to define the relation between the nose geometry
and the resultant flow-field. The objectives of the present program were to
study the effect of nose geometry on the transition criteria for the windward
boundary-layer, on the extent of separation, on the heat-transfer perturbation
due to the canopy, and on the surface pressure and the heat transfer in the
separated region. Although the present report will analyze the data for infor-
mation relating to each of these problems, the literature review, which forms
the principal part of the Introduction, will concentrate on separation and the
leeward flow-field.

Types of Flow Separation

A necessary condition (Ref. 1) for separation of the viscous boundary
layer from the wall is increasing pressure in the streamwise direction, i.e.,
an adverse pressure gradient along the flow path. In general, the separation
location depends upon geometric parameters, such as configuration geometry
and angle-of-attack, and upon flow parameters, such as free-stream Mach
number, Reynolds number, and the wall temperature.

Using solutions of the incompressible, laminar boundary-layer near the
symmetry plane of an inclined prolate-spheroid, Wang studied three-dimensional

1

separation patterns (Refs. 2 through 4). Whereas two-dimensional boundary-layer separation corresponds to the vanishing of skin friction, it is not necessary that the two components of skin friction vanish for three-dimensional separation. Two basic separation concepts were identified: a bubble-type separation and a free-vortex layer. Sketches of the two types of separation are presented in Fig. 1. The bubble-type separation is characterized by zero skin-friction at the separation line with subsequent reversal of the streamwise velocity direction. For the free-vortex-layer separation, Wang (Ref. 4) noted that the circumferential component of the velocity close to the body is reversed, but that the direction of the meridional velocity remains unchanged.

The boundary-layer solutions of Wang for flow over a prolate spheroid indicate that the separation pattern is essentially a bubble type for low incidence cases (alpha approximately 3°) and for extremely high incidence cases (alpha greater than 40°). For intermediate alphas, Wang (Ref. 4) states that "there are at least two stages of separation. A free vortex layer type of separation occurs first, followed by a bubble type of more conventional nature."

Surface-pressure measurements, oil-flow patterns, and pitot-pressure surveys (Refs. 5 through 7) indicate a free-vortex-layer type of separation for hypersonic flow past a blunt cone at alphas between 6° and 18°. The oil from the windward region was found to flow around the cone, turning toward the rear of the cone as it approaches the separation line. At the separation line, the oil accumulated and proceeded to travel down the separation line to the rear of the cone. The circumferential component of the flow which was initially directed toward the leeward plane of symmetry reversed direction. Two symmetrical separation lines developed downstream of the region where the circumferential component of skin friction passed through zero. The fact that

the oil near the leeward plane of symmetry continued to flow from the attached region, through the region of zero lateral skin friction, and into the vortex region indicated the longitudinal component of skin friction was always finite. This separation model, which is presented in Fig. 1, contains symmetrical, supersonic, helical vortices close to the surface with an attachment line on the most leeward ray. At angles-of-attack greater than those necessary to equalize the cone base-pressure and the leeward pressure, the leeward flow expanded to pressure levels below the base pressure and a secondary separation occured on the rear portion of the cone's leeward surface, which appeared to contain subsonic reverse flow (Ref. 8). This separation flow-field would be similar to the two stage solutions of Wang, i.e., a vortex-layer separation followed by a bubble type.

The Separated Flow Field

Using pitot-pressure measurements obtained with the axis of the probe parallel to the direction of the free-stream velocity, Stetson (Ref. 7) found no evidence of imbedded shocks in the leeward flow-field of a slender, sharp cone at an alpha of 10°. Using pitot-pressure measurements and schlieren photographs, Feldhuhn et al (Ref. 9) observed imbedded shock waves which were associated with separation and recompression in the leeward flow-field of a slender, sharp cone at an alpha of 24°. It is possible that the imbedded shock-waves observed by Feldhuhn et al are due to increased cross-flow at the higher angle-of-attack. However, it is also possible that the detection of the imbedded shock-waves is due to improved instrumentation.

The flow mechanism of greatest importance to the surface environment in

the separated region is the free-vortex layer. Reattachment of the vortical flow results in high heating-rates to the leeward surface, with local heat-transfer coefficients often exceeding the zero angle-of-attack values. The relatively high leeward-heating has been experimentally observed by Maise (Ref. 10) for circular cones, by Whitehead (Ref. 11) for delta-wings, and by Hefner and Whitehead (Refs. 12 and 13) for space-shuttle orbiter configurations.

A "featherlike" pattern having its axis in the leeward plane-of-symmetry appears in the oil-flow patterns on shuttle orbiter configurations. Hefner and Whitehead noted that the feather pattern indicates a region of high shear caused by the impingement of the vortices onto the lee surface. The thinning of the viscous shear-layer as a result of the outflow caused by these vortices produces the relatively high leeward heating rates. Whitehead et al (Ref. 14) proposed a three-zone viscous-flow model to describe the interaction of the vortex with the flow in the vicinity of the lee meridian. The three zones of the leeward flow were: (1) the apex region characterized by an inward boundary-layer flow apparently free of vortex effects, (2) a region dominated by a vortex system which draws off the boundary layer at the center line and leaves a characteristic "feather" surface-flow pattern, and (3) the downstream region where a new boundary layer which develops in the center region splitting the feather pattern into symmetrically disposed surface traces. Hefner and Whitehead (Ref. 13) found that the leeward surface-pressures were insensitive to the effects of the vortices.

The Effect of Geometry on the Separated Flow-Field

A desirable geometry is one which would minimize the effect of the

reattachment of the vortical flow, which causes the high heating-rates to the leeward surface. Rao (Ref. 15) found that the vortex-induced peak-heating on the leeside of a delta-wing could be virtually eliminated by aligning the apex region with the free-stream, i.e., "nose droop". Whitehead and Bertram (Ref. 16) found that the vortex-induced peak-heating on the leeside of a delta wing could be reduced by properly contouring the leading-edge planform.

Hefner and Whitehead (Ref. 13) found that the heat transfer to the lee surface of shuttle-like noses could be reduced by modifying the upper-surface geometry to induce vortex lift-off. The side view geometry was modified by increasing the initial slope of the lee meridian and then breaking it sharply, which reduced the heating level significantly along 50% of the leeward meridian.

Although the separated flow-field was probably modified by the presence of the model support sting in the upstream wake, thermocouple data obtained using cylindrical models showed that the cross-section had a significant effect on the heat-transfer in the separated region (Ref. 17). For the four cylindrical-models considered, the average heat-transfer rate in the separated region was a minimum for the cross-section which was approximately rectangular and was a maximum for the cross-section which was circular. The leeward heat-transfer data were correlated in terms of a single geometric parameter, i.e., the ratio of the distance which is the complement of the development length for the re-circulating flow to the width of the wake at separation.

The Effect of Test Conditions on the Separated Flow-Field

As discussed, the high heat-transfer rates measured in the separated re-gion of the shuttle configurations are due to an interaction between the vortices

and the upper-surface boundary-layer.   It is not surprising, therefore, that

the lee-surface heat-transfer measurements are dependent on the Reynolds number.

A Reynolds-number dependence is evident in the heat-transfer measurements from

the pitch plane of an MRS configuration (Ref. 18). For alphas from 20° to 50°,

the nondimensionalized heat-transfer values obtained for a unit free-stream

Reynolds number of 0.3×10^6 are significantly lower than those obtained for

unit free-stream Reynolds numbers of 1.0×10^6, 1.7×10^6, and 2.4×10^6 (for

which the heat-transfer values are approximately the same). For alphas of 55°

and 60°, the low-Reynolds-number heating values increased to the levels measured

at the other Reynolds numbers. These data suggest the existence of a "threshold"

Reynolds number (which depends on the angle-of-attack), where a marked change in

the flow field occurs.

Hefner and Whitehead (Ref. 13) discussed a "threshold" Reynolds number where

the peak heat-transfer to the lee meridian of a delta-wing orbiter at an alpha of

20° decreased abruptly. Although the heat-transfer distributions below this

Reynolds number did not exhibit a peak, the oil-flow patterns still showed the

featherlike reattachment pattern. Leeside heat-transfer data obtained over the

same Reynolds-number range, but at an alpha of 35°, showed no abrupt decrease in

peak heating. Thus, the test Reynolds numbers apparently are above the threshold

value for this higher angle-of-attack.

Hefner and Whitehead (Ref. 13) have considered the effect of the free-stream

Mach number on the leeward heat-transfer. Lee-surface heating-data were obtained

at free-stream Mach numbers of 6 and 19. The heat-transfer measurements obtained

at a Mach number of 19 for alphas of 20° and 37° showed no heating peaks and were

significantly lower than the corresponding data obtained at a Mach number of 6.

The data were considered insufficient to define Mach number effects on the lee-ward heating, since the Reynolds number influence is interrelated with Mach number.

The present investigation considered the effect of nose geometry on the aerothermodynamic environment for shuttle entry-configurations. Heat-transfer data, oil-flow patterns, and shadowgraphs were obtained in Tunnel B of AEDC for two 0.019-scale orbiter configurations. Surface-pressure data, oil-flow patterns, and schlieren photographs were obtained in the University of Texas Supersonic Wind Tunnel for 0.0047-scale models. Furthermore, because of the limited size of the test section, the University models represented only the nose region of the two orbiter configurations. The range of test conditions included free-stream Mach numbers of 5 and 8 with free-stream Reynolds numbers based on model length from 1.5×10^6 to 1.2×10^7. Data were obtained for alphas from 20° to 50°. The surface-pressure and heat-transfer measurements from the windward pitch-plane are compared with theoretical values. Boundary-layer transition parameters, which were determined using the pitch-plane heat-transfer distributions, are compared with existing criteria. Additional data are discussed in relation to the governing flow-mechanisms.

NOMENCLATURE

h	- local heat-transfer coefficient
$h_{t,R=1 \text{ ft.}}$	- calculated heat-transfer coefficient for the stagnation point of a one-foot sphere scaled to model size
L	- total model length, measured along the fuselage axis
M_e	- local Mach number at the edge of the boundary layer
M_∞	- free-stream Mach number
p	- local static pressure
p_{t2}	- stagnation pressure behind a normal shock
$Re_{x,tr}$	- Reynolds number based on local flow properties and the axial length to transition
Re/ft	- unit Reynolds number based on local flow properties
Re_θ	- Reynolds number based on local flow properties and the momentum thickness
$Re_{\infty,L}$	- free-stream Reynolds number based on model length
T_w	- wall temperature
T_t	- stagnation temperature
x	- axial coordinate, refer to Fig. 2
x_{tr}	- axial length to transition
y	- depth coordinate, refer to Fig. 2
z	- transverse coordinate, refer to Fig. 2
α	- angle of attack
ϕ	- circumferential coordinate
θ_s	- local inclination of the shock wave
θ_w	- local inclination of the wall relative to the x-axis

Subscripts

ref	- reference value
pk	- peak value

EXPERIMENTAL PROGRAM

Th⌐ experimental program was conducted to study the effect of nose geometry on the transition criteria for the windward boundary-layer, on the extent of separation, on the heat-transfer perturbation due to the canopy, and on the surface pressure and the heat transfer in the separated region. The parameters of the program included nose geometry, Reynolds number, and angle-of-attack. Heat-transfer data, oil-flow patterns, and shadowgraphs were obtained in Tunnel B of AEDC for two shuttle entry-configurations. Aft of the station where the wing-root fairing intersected the fuselage (x = 0.4L), the configurations were identical. Surface-pressure data, oil-flow patterns, and schlieren photographs were obtained in the University of Texas Supersonic Wind Tunnel (UT SWT). Because of the limited size of the test section, the University models were of smaller scale and represented only the nose region of the two orbiter configurations. Thus, surface-pressure distributions, heat-transfer distributions, and flow-visualization photographs were obtained to help define empirically the flow-field for the two configurations.

Models

The model design philosophy was to generate nose configurations whose surface geometry could be described by analytic functions. The top view plan-forms were to include both relatively blunt and relatively slender geometries. The cross-section geometries were to provide different cross-flow pressure gradients on the windward surface and different separation patterns on the leeward surface. Because of the considerable cost of a "large" scale heat-transfer

model, only two configurations could be built. To satisfy the design philos-
ophy objectives with two models, it was necessary to incorporate an acceptable
"extreme" for each of the geometric parameters in one model or in the other.
Since only the fuselage was to be instrumented, the wing geometry was the same
for both configurations.

Configuration geometry. - Since only two models were built, their profiles were
the same (except for a slight difference in the canopy), so as not to introduce
yet another geometric variable. The z-dimension of the fuselage was a maximum
in the horizontal plane containing the apex of the nose. This $(y = 0)$ plane
intersected the cross-section at $x = 0.4L$ such that the distance to the keel
was one fourth of the total vertical dimension at this station. For the pre-
sent report, that portion of the model upstream of station $x = 0.4L$ is de-
signated as the nose. The downstream portion of the model is termed the fuse-
lage. The geometry of the fuselage (and of the wings) was the same for both
configurations.

The geometry of the delta wing is illustrated in Fig. 2. The wings,
which were not instrumented, were made of 17-4 PH stainless steel. The sym-
metrical airfoil section, which had a thickness ratio of approximately 0.07,
was inclined 1.5° to the model axis. Other pertinent geometric parameters of
the wing are as follows.

Leading-edge sweep, Λ	49°02'
Trailing-edge sweep	4°59'
Wing dihedral	7°
Exposed root-chord length	1.26 ft.
Exposed semi-span	0.70 ft.
Aspect ratio	1.2

With the exception of the canopy surface and the surface fairings of the wing-root region, the nose geometries can be described by "analytical functions". The analytic functions which define the contours for the two, "clean" configurations are discussed in Appendix A. The actual configurations, which are discussed below, are illustrated in Figs. 2 through 5.

(a) UTN2. - The relatively blunt planform, the relatively flat windward surface (to reduce the cross-flow pressure gradients), and a leeward geometry which was intended to fix boundary-layer separation were incorporated into the UTN2 configuration as shown in Fig. 3. The apex of the planform in the y = 0 plane is a 5:2 ellipse. The windward surface was generated by a parallel translation of the ellipse tangent to the leading edge of the keel. Thus, taking a section in the xz-plane, the trace of the windward surface is a 5:2 ellipse (possibly modified at the downstream end by the wing-root fairing). Because of the relatively blunt character of the windward nose, the wing-root fairing requires only a slight contour modification. In the absence of the canopy, the cross sections of the leeward surface, i.e., y negative, consist of a circular arc, a linear element, and a very flat ellipse. The elements are tangent to each other to avoid sharp corners upstream of x = 0.25L. The inclination angle between the linear element and the y-axis is a linear function of x, varying from 25° at x = 0.02L to 15° at x = 0.16L and subsequently varying with x so that the inclination angle is 0° at x = 0.38L. The canopy geometry is indicated in the cross-sections of Fig. 3.

(b) UTN7. - As shown in Fig. 4, the UTN7 configuration has the more slender planform and elliptic cross-sections. The apex of the planform in the y = 0 plane is a 4:1 ellipse. The basic cross-sections (i.e., the cross-sections without the canopy and the wing-root fairing) are composed of two semi-ellipses.

The semi-axis ratios for both the windward ellipse and the leeward ellipse are uniquely defined by the maximum y- and z- coordinates for the section at a given station. The canopy geometry and the wing-root fairing modify these elliptic cross-sections, as can be seen in Fig. 4. Because both nose configurations were designed to fair into a common fuselage at station $x = 0.38L$, the wing-root fairing represented considerable modification of the basic cross-sections for the slender UTN7-configuration.

AEDC models. - The two 0.019-scale models used in Tunnel B of AEDC were built by Micro Craft, Inc. Electroformed nickel deposited on a male mandrel yielded a single surface (with no joints) for the nose-configuration:aft-fuselage surface. The composition of the resultant shell, which was roughly 0.032-in. thick, was 0.985 nickel, 0.010 cobalt, with traces of aluminum, iron, and silicon. In order to have access to the model interior, the leeward surface of the aft fuselage was made into an access panel. Thus, there was no nose: fuselage junction on the windward surface, which could promote boundary-layer transition.

Photographs of three views of each of the AEDC models are presented in Fig. 5. As can be seen in the side-view photograph, the pitch-plane radius-of-curvature of the windward keel is a smoothly varying function of x. This was done to avoid inflection points in the shock wave, which would tend to promote boundary-layer transition (Ref. 19). For $x < 0.4L$, the curves describing the windward pitch-plane geometry are an ellipse which is tangent (at $x = 0.19L$) to a straight line, inclined 3° to the x-axis.

The photographs also clearly illustrate the "jowls" which are formed when a nose region with a rounded windward surface is faired into a flat-bottomed

fuselage. The complex, concave surface which is formed by this wing-root fairing in the region from x = 0.3L to x = 0.4L had a marked effect on the windward flow-field, as will be discussed later.

Temperature histories of the thin nickel-skin were obtained using the 101 30-gage chromel-alumel thermocouples which were located as shown in Figs. 3 and 4. The local heat-transfer coefficients were computed using the temperature histories in the relation:

$$h = m \, c_p \, \frac{d \, [\ln \, (\frac{T_t - T_{wi}}{T_t - T_w})]}{dt} \qquad (1)$$

where m is the product of the model-skin density times the model-skin thickness, T_w is the wall temperature, and T_{wi} is the initial wall temperature. An experimental program was undertaken to measure the specific heat of the model skin. However, the experimental values obtained by the contractor differed significantly from the tabulated values. Thus, a subsequent exercise was undertaken by personnel from AEDC to obtain additional measurements of the specific heat of the model skin. The measured values of specific heat obtained by the AEDC personnel were in satisfactory agreement with the literature values. Therefore, the specific heat of the model skin was assumed to be:

$$c_p = 0.1467 - (2.173 \times 10^{-4}) \, T_w + (3.367 \times 10^{-7}) \, T_w^2$$
$$- (1.332 \times 10^{-10}) \, T_w^3, \, \text{Btu/lbm} \, ^\circ R \qquad (2)$$

which is a fit of the data for specific heat presented in Ref. 20.

Post-test examination of the UTN2 revealed an undulation in the vicinity of x = 0.4L. Whereas the specified slope of the model pitch-plane was to be a constant 3° in this region, careful post-test measurements of the y coordinate

indicated the slope varied from the design value of 3° to 1°, then to 6°, before returning to 3°. A comparison of the post-test measurement of the windward surface angles and the design values is presented in Fig. 6. The difference between the actual surface and the design contour was so small that it could not be illustrated on the scale of Fig. 4. Although the cause of the wrinkle is undetermined, it apparently occurred either after Group 22 or after Group 23. Since Group 24 and Group 25 are repeats of earlier test conditions, i.e., Group 20 and Group 23, respectively, these data are presented in Fig. 7 and 8. A single symbol indicates the heat transfer for that thermocouple was essentially the same for both runs. At an alpha of 20°, the heat-transfer distribution in the windward pitch plane is affected; being relatively low at the thermocouple in the "concave" region (x = 0.4L) and relatively high at downstream locations. At an alpha of 50°, the windward pitch-plane heat-transfer data were not affected by the surface change with the exception of the measurements at the wrinkle (x = 0.4L) and possibly those at x = 0.5L. The differences between the heat-transfer measurements at these two thermocouples suggest that the wrinkle occurred between the two runs. However, the distributions (with the relatively low heating at x = 0.5L) suggest that the wrinkle occurred prior to the two runs. As can be seen in Fig. 8, the surface undulation had no discernable effect on the leeward heat-transfer data at either angle of attack. This is not surprising, since the large favorable pressure gradient at the chine line would be expected to isolate any disturbance on the windward surface.

University models. - For the tests in the UT SWT, 0.0047-scale models of the nose region of the UTN2 and the UTN7 were built. Using the cross-sections of the AEDC models, a mandrel of balsa and a female mold of RTV were made prior

to casting the actual plastic pressure models. The models, which were made of polystyrene casting resin, were instrumented with pressure taps as shown in Figs. 9 and 10. The geometry of the UTN7 pressure model differed slightly from the geometry of the heat-transfer model. The difference is primarily due to the fact that the cross-sections were not exactly aligned in the original model drawings supplied to the University. The misaligned cross-sections contributed to the slight "hump" on the leeward surface, which can be seen immediately downstream of the aft-end of the canopy in Fig. 10. Although the magnitude of the hump is small (approximately 0.02 inch), the local pressure seemed significantly high. Another pressure model, whose geometry matches that of the heat-transfer model (for which the cross-sections were aligned), has been built and will be tested soon.

Test Facilities

Tunnel B of AEDC. - Tunnel B is a continuous, closed circuit, variable density wind tunnel with an axisymmetric, contoured nozzle and a 50-inch diameter test section. The tunnel can be operated at a nominal Mach number of 6 or 8 at stagnation pressures from 20 to 300 and 50 to 900 psia, respectively, with stagnation temperatures up to 1350°R. The model may be injected into the tunnel for a test run and then retracted for model cooling or for model changes which can be made without interrupting the tunnel flow.

The UT SWT. - This tunnel is of the blowdown type, capable of run times from two to four minutes. The air is accelerated to a free-stream Mach number of 5 through a two-dimensional nozzle to a 6-in. x 7-in. test section. Stagnation pressures range from 225 psia to 400 psia. Although stagnation temperatures up to 1000°R are possible (for heat-transfer tests), these pressure data were obtained with a stagnation temperature of approximately 580°R.

Test Program

The test conditions for the experimental programs conducted in Tunnel B and in the UT SWT are presented in Table 1 and in Table 2, respectively. Heat-transfer data were obtained in Tunnel B at a free-stream Mach number of 8 over a range of Reynolds numbers based on model length from 1.5×10^6 to 7.8×10^6 for alphas from 20° to 50°. The pressure data from the UT SWT were obtained at a free-stream Mach number 5 for alphas from 20° to 50°. So that the tabulated Reynolds number would be comparable, the length Reynolds number for the UT tests is based on the length which would exist if the entire configuration were simulated. The range of Reynolds number for the UT SWT tests based on this "effective" model length is 6×10^6 to 12×10^6. Additional tests in the pressure program are planned. These data will appear in the final contract documentation (scheduled for August 1973).

DISCUSSION

The objectives of the present program were to study the effect of nose geometry on the transition criteria for the windward boundary-layer, on the extent of separation, and on the surface pressure and the heat transfer in the separated region (noting the heat-transfer perturbation due to the canopy). The presentation of the data and their analysis will, therefore, be divided into three sections: the windward flow-field; the circumferential distributions, and the leeward flow-field.

The Windward Flow-Field

As indicated previously, the jowls formed by the complex, concave fairing markedly affected the windward flow-field. The windward flow-field near the plane-of-symmetry included:

(1) an interaction between the boundary layer and a shock wave generated in the corner formed by the jowls, and

(2) a thickening of the downstream boundary-layer as the jowls funnel the flow toward the plane of symmetry.

Still further downstream, the heat-transfer data indicate the effects of cross flow and of boundary-layer transition on the flow field. The strength of a particular phenomenon is dependent on the configuration and on the angle-of-attack.

The flow-visualization photographs, which are presented in Fig. 11 for the UTN7 at an alpha of 35°, graphically illustrate these phenomena. A jowl-generated shock-wave, which can be seen in the shadowgraph, crosses the nose at approximately x = 0.3L. The oil-flow pattern illustrates the effect of the shock: boundary-layer interaction and of the funneling of flow toward the pitch plane.

An accumulation of oil is evident at an x of approximately 0.3L, i.e, where the jowl-generated shock-wave crosses the body. As indicated by the oil-flow patterns, the presence of the jowls affects the flow over an extensive region of the windward surface, specifically from an x of approximately 0.25L to an x of approximately 0.5L. This should not be surprising, since an extensive fillet was required to fair from the relatively round nose-region cross-section into the flat-bottomed fuselage (refer to Fig. 5).

The effect of these flow phenomena is also evident in the heat-transfer and in the surface-pressure distributions for the pitch plane of the UTN7. These data are presented in Fig. 12 for an alpha of 30°. The surface-pressure increase, which occurs downstream of x = 0.3L, is attributed to the shock wave. Due to the shock:boundary-layer interaction, the heat transfer initially increases (from x = 0.3L to x = 0.36L). The subsequent decrease in heat transfer, which is measured at the thermocouples from x = 0.425L to x = 0.5L, is attributed to the thickened boundary-layer as the flow is funnelled toward the plane-of-symmetry. Downstream of x = 0.5L, the experimental heat-transfer coefficients increase with Reynolds number. These heat-transfer data indicate the onset of boundary-layer transition.

The oil-flow pattern for the windward surface of the UTN2 at an alpha of 35° (Fig. 13) is similar to that for the UTN7. However, because of the relatively flat windward-surface of the UTN2 nose, the fillet represents only a modest change in the cross-sections (refer to Fig. 5). Therefore, it is not surprising that the oil-flow patterns show a perturbed region of only limited extent. Nevertheless, there is a marked accumulation of oil, as was associated with the jowl-generated shock-wave for the UTN7. The surface-pressure and the heat-transfer distributions for the pitch plane of the UTN2 at an alpha of 30° (Fig. 14) do not indicate either a shock-induced increase or a subsequent decrease as the boundary layer thickens. Thus, although the oil-flow patterns

are roughly similar for the two configurations, the jowl-induced perturbations in surface pressure and in heat transfer which were observed for the UTN7 were not evident in the UTN2 data. Downstream of x = 0.4L, the heat-transfer data depend on the Reynolds number, indicating the onset of transition. Thus, transition occurs earlier on the relatively flat-bottomed configuration. Any conclusion regarding the significance of the cross-flow parameter on transition is masked, because the onset of transition is affected by cross-flow, by the shock: boundary-layer interaction and by the slight surface undulation of the UTN2.

The jowl-generated shock-waves are also evident in the pitch-plane shadow-graphs, which are presented for an alpha of 20° (Fig. 15) and for an alpha of 30° (Fig. 16). Whereas the shock-wave trace is visible on the windward side for both configurations at both alphas, a leeward trace of the jowl-generated shock-wave is evident only for the UTN7 at an alpha of 30° (Fig. 16b). No locally high heat-transfer coefficients were evident in the data from the leeward plane-of-symmetry (i.e., the leeward pitch-plane) for the UTN7 at an alpha of 30°. Thus, although a shock trace is evident on the leeside, the jowl-generated shock-wave apparently did not affect the viscous flow which governs the leeward heating.

A canopy-generated shock-wave occurs for both configurations at an alpha of 20° but not for an alpha of 30°. Although the shadowgraphs are not presented herein because they were obtained at another Reynolds number (refer to Table 1), a canopy-generated shock-wave was evident for both configurations at an alpha of 25°.

Pitch-plane correlations. - The experimentally determined heat-transfer coefficients for the windward pitch-plane are compared with the theoretical distributions for the UTN2 and for the UTN7 in Figs. 17 and 18, respectively. Theoretical

distributions are presented for a two-dimensional laminar boundary-layer, for a laminar boundary-layer with cross-flow, and for a two-dimensional turbulent boundary-layer. The flow-field techniques used to obtain the theoretical correlations are described in Appendix B. The theoretical heat-transfer distributions are independent of Reynolds number for laminar flow, but not when the boundary layer is turbulent. Thus, heat-transfer-coefficient distributions have been calculated for a turbulent boundary-layer at two different Reynolds numbers. The heat-transfer data for the UTN2 (Fig. 17) indicate that the boundary layer was laminar upstream of x = 0.3L for all angles-of-attack over the range of Reynolds numbers tested. At an alpha of 20°, the laminar heat-transfer data agree with the calculations for a two-dimensional boundary-layer, indicating that appreciable cross-flow has not yet developed. At the higher angles-of-attack, the measurements approach the calculated values which account for cross-flow.

The heat-transfer data for the UTN2 indicate the onset of boundary-layer transition occurs between x = 0.3L and x = 0.4L. When the onset of transition occurs in this interval, the location depends on the Reynolds number and on the angle-of-attack. However, the wrinkle in the model skin which occurred in the vicinity of x = 0.4L (although relatively small) apparently acted as a transition-fixing element. At the highest Reynolds number tested, i.e., $Re_{\infty,L} = 7.8 \times 10^6$, the downstream heat-transfer data indicate transition to fully turbulent boundary-layer occurs at all alphas. The length over which the experimental values agree approximately with the theoretical values for a turbulent boundary-layer increases as the angle-of-attack increases. At the lowest Reynolds-number tested, i.e., $Re_{\infty,L} = 1.6 \times 10^6$, the downstream heat-transfer

data do not even approach the theoretical values for a fully turbulent boundary-layer. Thus, at the lowest Reynolds-number tested, the boundary-layer appears to remain laminar downstream of x = 0.4L. However, the experimental coefficients in this region are considerably greater than the theoretical predictions. Possible sources of this discrepancy include: cross-flow effects (which were assumed absent for the theoretical analysis because the windward surface of the fuselage is flat in this region) and persistence of the boundary-layer perturbations induced by the jowls. The assumption of zero flow-divergence was based on the results from isolated delta-wings with larger sweep angles than the present case and with zero dihedral (whereas, the present dihedral was 7°). Therefore, some flow divergence would be expected for the present configurations. Flow divergence increases heating significantly more for a laminar boundary-layer than for a turbulent boundary-layer (Ref. 21).

As was the case for the UTN2 configuration, the experimental heat-transfer coefficients near the nose of the UTN7 (Fig. 18) agree with the theoretical values for a two-dimensional laminar boundary-layer at an alpha of 20° and agree approximately with the theoretical values for a laminar boundary-layer with cross-flow for the higher alphas. However, the theoretical heat-transfer-distribution does not predict the jowl-induced perturbations, i.e., the shock-induced increase in heating and the subsequent decrease associated with the thickening of the boundary layer. This is not surprising since the heat-transfer calculations were based on modified Newtonian pressure rather than experimental pressures (which would reflect the influence of the jowls). For a given flow condition, the onset of transition appears to be further aft on the UTN7. Nevertheless, the heat-transfer data indicate that the boundary layer becomes full turbulent

at all angles-of-attack for the highest Reynolds-number tested. Again, al-
though the low-Reynolds-number measurements for the thermocouples downstream
of x = 0.4L differ significantly from the theoretical values, the boundary
layer appears to remain laminar at all alphas.

The surface pressure distributions for the windward pitch-plane are
presented in Fig. 19. Since the pressure measurements on the windward surface
were independent of the Reynolds number (refer to Figs 12 and 14), data are
presented for only one Reynolds number. As noted previously, the jowl-generated
shock-wave increases the surface-pressure downstream of x = 0.3L for the UTN7,
but not for the UTN2. Recall that locally high values for the heat transfer
were recorded in this region for the UTN7 configuration, but not for the UTN2.
However, because these pressure data were not available at the time, the theoret-
ical heat-transfer calculations were based on the modified-Newtonian pressure-
distribution. For the present tests in the UT SWT, the experimental pressures
from the unperturbed regions of both configurations are greater than the values
calculated using modified Newtonian theory. The correlation is qualitatively
consistent with data obtained in Tunnel B at a higher Mach number, as discussed
in Appendix B. For the Tunnel B tests, the modified-Newtonian relation was
shown to approximate (albeit on the low side) the measured values.

Transition correlations for the pitch-plane. - The values of several transition-
related parameters are presented in Table 3. The onset of boundary-layer tran-
sition was chosen to be the "point" where the heating rate deviated from the
laminar distribution. The current results for the onset of boundary-layer tran-
sition are compared with the North-American Rockwell criterion (as given in
Ref. 22) in Fig. 20 and with the McDonnell-Douglas criterion (as given in Ref. 22)

in Fig. 21. The values of the transition parameters based on the present data are consistently above the level predicted using either criterion. This is somewhat surprising, since it was thought that the jowl-induced flow-field perturbations would promote transition and, hence, yield relatively low values for the transition parameters. Thus, the fact that the present transition values are slightly above the industry correlations indicates that the carefully designed windward surface (which was designed to eliminate inflection points in the bow shock-wave and the resultant transition-promoting shear layer) and the absence of surface joints in the model serve to delay transition.

The present transition results are within the range of data obtained by other investigators (which were also presented in Ref. 22 and are reproduced herein). Because boundary-layer transition is a nonlinear process dependent on numerous parameters, considerable scatter exists in the experimental transition-locations even for simple configurations. Additional scatter is introduced into the values of the transition parameters for shuttle configurations because of the uncertainty for such parameters as local Mach number, local density, etc.

The Circumferential Distributions

In this section, heat-transfer and surface-pressure data will be presented for those stations which have instrumentation distributed around the periphery of the cross-section. The location of a particular sensor is defined by the ϕ-coordinate, where $\phi = 0°$ is the windward pitch-plane and $\phi = 90°$ is the $y = 0$ plane. The location of a particular sensor relative to the geometric characteristics of the cross-section is illustrated in Figs. 3, 4, 9, and 10.

Heat-transfer data. - Heat-transfer data are presented in this section for

80 of the 98 available thermocouples for 24 of the 35 test conditions. Thus,

a majority of the heat-transfer data obtained in the present test program are

presented in these figures, should the reader also desire to analyze the data.

Note that the discussion which follows relates only to those stations which

have instrumentation distributed around the periphery.

Alpha of 20°. - The heat-transfer measurements obtained for an alpha of

20° are presented for both configurations in Fig. 22. Consider first the

measurements from the windward pitch-plane, i.e., ϕ = 0°. The fact that the

heat-transfer at the first station (i.e., x = 0.06L) is greater for the UTN7

indicates considerable cross-flow near the apex. For those stations from

x = 0.12L through x = 0.26L, the heat-transfer measurements are approximately

equal, as one would expect since the data for both configurations were found

to agree with the calculations for a two-dimensional laminar boundary-layer

without cross-flow. The jowl-induced perturbation causes the pitch-plane heat-

transfer to be higher for the UTN7 at x = 0.36L. Because of the jowl-induced

perturbations and the onset of boundary-layer transition, the heat-transfer data

at subsequent stations is a function of Reynolds number and configuration.

Consider next the other measurements from the windward surface, i.e., for

0° < ϕ < 90°. For stations from x = 0.12L through x = 0.26L, the circumferential

heat-transfer distributions are qualitatively similar to those one would expect

for a cylindrical configuration (with the same cross-section) at an alpha of

90°. (Such data are presented in Ref. 23.) Thus, the heat-transfer data sug-

gest considerable cross flow in the vicinity of the chines as the flow responds

to the large circumferential pressure gradients. The circumferential flow is

verified by the oil-flow patterns, which indicate that in the vicinity of the

chines the flow direction is roughly normal to the model axis.

Locally high heat-transfer rates which are measured for $60° < \phi < 90°$ reflect the jowl-induced flow-field perturbations. The heat-transfer data are consistent with the oil-flow patterns, inasmuch as the jowl-induced perturbation extends over a greater area for the UTN7 (for the stations $0.36L \leq x \leq 0.5L$ for the UTN7 as compared with $0.425 \leq x \leq 0.5L$ for the UTN2). Further downstream, the heat-transfer measurements for $0.5L \leq x \leq 0.7L$ indicate that these pertur-bations continue to influence the heat-transfer to the flat portions of the windward fuselage, both in and off of the pitch-plane.

It is interesting to note that, of all the leeward heat-transfer measure-ments, those and only those on the forward-facing surface of the canopy $(x = 0.2L)$ approached the windward values. For both configurations, these heat-transfer measurements are Reynolds-number dependent. At an alpha of $20°$, the heat trans-fer at the thermocouples just upstream of the canopy $(x = 0.16L)$ appeared un-affected by the presence of the canopy, which begins at $x = 0.17L$. Thus, the canopy-generated shock-wave, which is visible in the shadowgraphs at an alpha of $20°$ (Fig. 15), apparently does not perturb the upstream viscous flow.

Locally high values for the leeward heat-transfer were observed at other stations although the locations differed for the two models. For example, locally high heating occurs just downstream of the aft-end of the canopy $(x = 0.36L)$ for the UTN2 but not for the UTN7. The heat-transfer distributions for the leeward pitch-plane are discussed further in the next section.

Alpha of 30. - The circumferential heat-transfer distributions for the two configurations at an alpha of 30° are presented in Fig. 23. In the windward pitch-plane from x = 0.06L through x = 0.26L, the heat-transfer for the UTN7 is greater than the corresponding value for the UTN2. The difference is attributed to cross-flow, which is greater for the UTN7. The differences between the pitch-plane measurements for the region for x = 0.36L through x = 0.50L are attributed to the jowl-induced perturbations in the flow-field, which cause the UTN7 heating to be relatively high at first, then relatively low.

Again, the jowl-induced perturbations influence in the heat-transfer measurements for 40° < φ < 90° for x ≥ 0.36L for the UTN7 and for x ≥ 0.425L for the UTN2. The relatively high heating measured on the UTN2 at the highest Reynolds number indicates boundary-layer transition. Although the flow-visualization photographs and the heat-transfer data reflect a strong flow-field perturbation for the UTN7, the onset of transition at this high Reynolds number does not appear in the heat-transfer data upstream of x = 0.60L.

As noted for the shadowgraphs of Fig. 16, the canopy no longer generates a shock wave at an alpha of 30°. Whereas at an alpha of 20° the heat transfer appeared to be unperturbed by the canopy at the upstream thermocouples, increases in the heat-transfer data can be observed for both configurations at thermocouples upstream of the canopy at an alpha of 30°. This will be more evident when the heat-transfer data are presented in the next section as the distribution along the leeward pitch-plane. Nevertheless, of all the heat-transfer measurements from the separated region, the heat-transfer measurements on the forward-facing surface of the canopy (x = 0.20L) are the only ones approaching the windward values. However, the nondimensionalized heat-transfer measurements for the UTN7 are significantly less at an alpha of 30° than the values obtained for 20°.

Alphas of 40° and of 50°. - The circumferential heat-transfer distributions for the two configurations are presented in Fig. 24 for an alpha of 40° and in Fig. 25 for an alpha of 50°. The general comments which were used to describe the flow at an alpha of 30° hold for these higher angles-of-attack.

Surface-pressure data. Circumferential pressure-distributions for the UTN2 are presented in Fig. 26 for an alpha of 24° and in Fig. 27 for an alpha of 31°. The reader is referred to Fig. 9 for the location of these pressure orifices. At both angles-of-attack, the pressures measured on the windward surface are independent of the Reynolds number. Furthermore, there is reasonably good correlation between the values calculated using modified Newtonian theory and the experimental values obtained on the windward surface. As can be seen in Fig. 26a, the pressure measurements obtained on the leeward surface just upstream of the canopy are independent of Reynolds number at an alpha of 24°. Recall that a canopy-generated shock-wave was evident in the shadowgraphs for an alpha of 25°. Based on these two observations, i.e., the Reynolds-number independence of the pressure data and the existence of a shock wave, one would conclude that, at this alpha, the flow upstream of the canopy is characteristic of attached flow. The leeward pressures measured at x = 0.29L at an alpha of 24° exhibit some Reynolds-number dependence, although no definite relation between the leeward-surface pressure data and the Reynolds number is apparent. However, at an alpha of 31°, the surface-pressure measurements for the orifices located for $\phi > 90°$ show a definite Reynolds-number dependence at both stations. It is of interest to note that the surface oil-flow patterns indicate that the boundary layer does not actually separate until $\phi \approx 130°$. Therefore, even in the region between the chines and the separation location, the surface pressures exhibit a

Reynolds-number dependence. The nondimensionalized surface-pressure measure-ments decrease as the Reynolds number increases. The inverse Reynolds-number dependence is consistent with the lee-meridian pressure data of Hefner (Ref. 24).

Circumferential pressure-distributions for the UTN7* are presented in Fig. 28 for an alpha of roughly 23° and in Fig. 29 for an alpha of 30°. The reader is referred to Fig. 10 for the location of these pressure orifices. As was the case for the UTN2, the pressures measured on the windward surface are independent of Reynolds number and are in reasonably good agreement with the modified Newtonian values for both angles-of-attack. The variation in angle-of-attack which occurred for the two runs of Fig. 28 masks any Reynolds-number effect which may be present. However, at an alpha of 30°, the surface-pressure data for those orifices located for $\phi > 90°$ show a definite Reynolds-number dependence. The oil-flow patterns in this region indicate that the boundary layer does not actually separate until $\phi \approx 130°$. The inverse relation between the surface pressures in this region and the Reynolds number is consistent with the corresponding UTN2 data and with the leeward measurements of Hefner (Ref. 24).

The Leeward Flow-Field

Heat-transfer data. - The experimental heat-transfer distributions for the leeward pitch-plane are presented in Figs. 30 - 35 for angles-of-attack of 20°, 25°, 30°, 35°, 40°, and 50°. The oil-flow patterns for the leeward sur-face are included in Fig. 33, i.e., alpha of 35°. With the exception of the thermocouple nearest the apex, only the thermocouple on the forward-facing surface of the canopy recorded heating rates approaching the values measured on the windward surface.

For alphas of 20° and 25° (Figs. 30 and 31, respectively), the canopy has no apparent effect on the upstream flow-field, as indicated by the heating rates measured in the region x ≤ 0.16L. The upstream heat-transfer varies inversely with distance for the UTN7, while it is essentially constant for the UTN2 (at least for 0.06L ≤ x ≤ 0.16L). Recall that, in the region ahead of the canopy, the transverse radius of curvature at the plane-of-symmetry is much larger for the UTN2 than for the UTN7. Thus, the surface ahead of the UTN2 canopy (where the heat transfer is essentially constant) is relatively flat. The cross-sections ahead of the UTN7 canopy are elliptic. A canopy-generated shock-wave is evident in the shadowgraphs for alphas of 20° and of 25° (refer to Fig. 15). For both configurations, the heat transfer recorded by the thermocouple on the windshield is markedly greater than the value measured at the thermocouple just forward of the canopy. The heating perturbation, which is configuration-dependent and varies from a factor of 5 to a factor of 10, increases with Reynolds number and decreases with angle-of-attack. The heat transfer decreases significantly on the downstream surface of the canopy, reaching a minimum at x = 0.3L. Further downstream on the leeward surface of the fuselage, i.e., x ≥ 0.4L, the heat transfer exhibits only a weak dependence on Reynolds number or on position.

The heat-transfer distributions for the leeward pitch-plane are presented in Fig. 32 for an angle-of-attack of 30°. At this alpha, the canopy-generated flow-field perturbation causes the heat transfer to increase at thermocouples upstream of the canopy. It is interesting to note that this angle-of-attack is the lowest alpha at which the upstream perturbation was recorded and is also the lowest alpha for which no canopy-generated shock-wave was evident in the shadow-graphs (Fig. 16). The characteristics of the upstream perturbations differ for

the two configurations. For the UTN7, the heating perturbation is evident at only one thermocouple and increases with Reynolds number (as did the perturbation on the windshield). The canopy-induced perturbation for the UTN2 extends further upstream but causes only a slight heating increase, which is essentially independent of Reynolds number. The peak heat-transfer, which occurred on the windshield, was significantly greater for the UTN2 than for the UTN7 (which decreased rapidly for these alphas). Again, the minimum heat-transfer occurred at $x = 0.3L$. Further downstream, on the leeward surface of the fuselage, i.e., $x \geq 0.4L$, the heat transfer exhibits only a weak dependence on Reynolds number or on position.

The heat-transfer distributions for the leeward pitch-plane are presented in Fig. 33 for an angle-of-attack of 35°. Since the heat-transfer distributions are qualitatively similar for $30° \leq \alpha \leq 40°$, the objective of this figure is to relate the heat-transfer to the flow-field characteristics. Thus, the leeside oil-flow patterns are included. (Gravity, which acts downward relative to these photographs, may cause slight asymmetry in the oil-flow patterns.) The heat-transfer distributions are presented so that the measurement from a particular thermocouple can be readily compared with the oil-flow pattern for that location. Thus, the axial coordinate is distorted slightly in the nose region to compensate for the surface curvature.

The oil-flow pattern upstream of the canopy indicates the vanishing of the circumferential component of shear, while the longitudinal component of flow causes the oil to move over the nose along the plane-of-symmetry. Furthermore, the oil moves longitudinally along the circumferential separation curve (as is evident "below" the canopy of the UTN2). These oil-flow patterns are characteristic of the free-vortex-layer type of separation.

Whereas the oil has been scrubbed off the surface of the canopy wind-shield, the shear on the downstream side of the canopy is not sufficient to erase the brush strokes of application. Thus the oil-flow patterns on the canopy are consistent with the heat-transfer measurements in this region. Of the leeward heat-transfer measurements the maximum occurs on the windshield and the minimum occurs on the downstream surface of the canopy.

Downstream of the canopy, a viscous mechanism has brushed the oil in the vicinity of the plane-of-symmetry. Although the oil-flow pattern does not ex-hibit the "featherlike" characteristics described by the researchers at the Langley Research Center, the vortex is assumed to be the governing viscous mechanism for the present configurations also. Downstream of the canopy, the heat-transfer is only a weak function of position.

The heat-transfer distributions for the leeward pitch-plane are presented in Fig. 34 for an alpha of 40°. The distributions at this angle-of-attack are qualitatively similar to those obtained at 30° and at 35°.

The heat-transfer distributions for the leeward pitch-plane are presented in Fig. 35 for an alpha of 50°. The canopy-induced flow-field perturbation ex-tends well upstream, almost to the apex of the orbiter. As is the case for all angles tested, after reaching a maximum value on the windshield at $x = 0.2L$, the heat-transfer decreases to a minimum value on the downstream side of the canopy at $x = 0.3L$. Further downstream, on the leeward surface of the fuselage, i.e., $x \geq 0.4L$, the heat-transfer distributions exhibit variations with Reynolds number and with position which are greater than any recorded at the lower angles-of-attack. Although the nondimensionalized leeward heat-transfer $h/h_{t,R=1\ ft.}$ remains relatively low (no value above 0.01 was obtained in the present tests), the data suggest that changes occur in the leeward flow-field. Oil-flow patterns

which have been obtained in exploratory tests in the UT SWT indicate that the separation pattern for alphas in excess of 42° is different than that obtained for lower alphas. Since the UT SWT data are considered preliminary, additional data are needed before one can make definite conclusions about the separated flow-field. However, a possible explanation of the change is that the boundary-layer separation mechanism at the higher alphas includes a bubble-type separation (perhaps as part of a two stage separation, with the free-vortex-layer type upstream). This would be consistent with the calculations of Wang (see the Introduction, page 2).

The heat-transfer distributions from the leeward pitch-plane of the two present configurations are compared in Fig. 36. Except for the forward-facing surface of the canopy, the heat-transfer distributions are roughly the same for both configurations at all angles-of-attack. There are differences in the heat-transfer for thermocouples on the fuselage, i.e., $x \geq 0.4L$. However, the differences are relatively small and the heat-transfer in this region is relatively low for both configurations.

Also presented in Fig. 36 are the data obtained in the Langley 20-inch Mach 6 tunnel (Ref. 24) for a delta-wing orbiter (which had no canopy) and the data obtained in Tunnel B (Ref. 25) for the NAR 161B, a delta-wing orbiter with a canopy. The data were chosen so that the free-stream conditions were roughly the same for all four configurations, i.e., comparable values of Mach number and of free-stream Reynolds number based on model length. The maximum heat-transfer measured on the Langley configuration (using the phase-change-paint technique) is consistently higher than the peak value obtained in the present tests at the same alpha (noting that it is possible to miss the peak value since only a finite number of thermocouples are available). Of even more significance is the

fact that the heat transfer downstream of the canopy location is consistently lower at all alphas for the present models. Furthermore, for the present configurations the downstream heat-transfer is only weakly dependent on position (and on the Reynolds number), whereas a second heat-transfer peak is evident in this region of the Langley model and increases in severity as alpha increases. The heat-transfer rates measured downstream of the canopy of the NAR 161B compare favorably with the present data. Thus, it appears that the presence of a protuding cockpit changes the longitudinal component of flow, resulting in relatively low downstream heat-transfer.

The relation between alpha and the maximum lee-meridian heating rate measured in the present tests differed markedly from the correlation obtained for the Langley configuration, as can be seen in Fig. 37. Whereas the maximum heating rate measured in the leeward pitch-plane of the Langley orbiter increased as alpha increased, the peak value decreased as alpha increased for both of the present configurations. For the UTN7 the peak value decreased more rapidly with alpha for alpha from alphas from 20° to 30°, than at the higher alphas. For the UTN2, however, the peak value decreased most markedly as alpha was increased from 40° to 50°. The maximum lee-meridian heating rate was consistently greater for the UTN2. In addition, the position of the leeward peak heating was a function of the angle-of-attack for the Langley configuration. For the present tests, the maximum heat-transfer rate always occurred at the thermocouple on the canopy windshield. Therefore, alpha had no effect on the location of the peak heating.

Since the heat-transfer data presented in Fig. 37 are the maximum values measured along the leeward pitch-plane, these values reflect the canopy-induced

perturbation. Therefore, heat-transfer measurements for other lee-meridian thermocouples are presented as a function of alpha in Fig. 38. These thermocouples are located downstream of the canopy on the fuselage. Although the local heat-transfer varies with Reynolds number and with angle-of-attack, there appears to be no systematic correlation with these parameters. Furthermore, because the heating rates in this region are low, the experimental uncertainty approaches the Reynolds-number related variation observed for some conditions.

Surface-pressure data. - The pressure distributions for the leeward pitch plane of the UTN2 at an alpha of 31° are presented for several Reynolds numbers in Fig. 39. For a given Reynolds number, the surface-pressure distribution is qualitatively similar to the heat-transfer distribution (refer to Fig. 32). The pressure is constant on the relatively flat surface upstream of the canopy. As was the case with the heat transfer, the maximum pressure is measured on the canopy windshield, although the canopy-induced perturbation is evident at an upstream orifice. Downstream of the canopy, the pressure is relatively constant. Thus, there was no minimum as was observed in the heat transfer at $x = 0.3L$. The pressure measurements at the last two orifices are believed to be perturbed by the presence of the sting support. Unlike the Tunnel B heat-transfer data, these UT SWT pressure-data depend on the Reynolds number. Except for those orifices, where the pressure is affected by the canopy-induced flow-field perturbation, the pressure decreases as the Reynolds number increases. As noted previously, this inverse Reynolds-number correlation is consistent with the pressure data of Ref. 24.

The lee-meridian surface-pressure distributions for the UTN2 are presented for several angles-of-attack in Fig. 40. The maximum pressure (which occurs on the canopy windshield) varies inversely with the angle-of-attack.

The maximum lee-meridian heating rate and the maximum lee-meridian surface-pressure are presented in Fig. 41 for the UTN2. Although there are only limited data available at present, the two parameters exhibit a similar dependence on alpha. Thus, at least for this particular location (on the canopy windshield), there appears to be a relation, such as

$$\frac{h_{PK}}{h_{ref}} = A \left(\frac{P_{PK}}{P_{ref}} \right)^n ,$$

which describes the heating perturbation in terms of the pressure perturbation.

General comments. - A review of the aerothermodynamic measurements for the leeward surface of delta-wing orbiters would be beneficial at this point. The table below contains a brief summary of the test programs which have formed the principal data-base of the discussion.

	Tunnel B Heat-Transfer Program	UT SWT Pressure Program	Langley, Mach 6 20-inch Tunnel
Test conditions: M_∞ $Re_{\infty,L}$	8 1.6×10^6 to 7.8×10^6	5 6×10^6 to 12×10^6	6 1×10^6 to 7.7×10^6
Model: Length Notes	2.1 ft Cross-sections varied, but both have curvature on the windward surface Both configurations have canopies	0.5 ft	1.0 ft windward face is relatively flat. No canopy
Technique	Thin-skin thermocouple		Phase-change paint

The lee-meridian heat-transfer-rates obtained in the Langley program were Reynolds number dependent. However, the Tunnel B heat-transfer data were virtually independent of Reynolds number. For both programs, it was concluded that the leeward heat-transfer was due to the impingement of the vortices formed during separation. The presence of the canopy apparently reduced the longitudinal component of flow, reducing the downstream heat-transfer. As noted in the Introduction, Hefner and Whitehead (Ref. 13) reported that a configuration "with relatively large initial slope angle and sharp break in contour generated relatively low lee-surface heating." It was concluded that this lee-surface geometry encouraged the vortices to break away from the lee surface, significantly reducing the heating. Thus, the canopy and the abrupt change in contour have a similar effect on the leeward heat-transfer. No explanation can be given (based on available data) as to why the heat-transfer data for the configurations (plural) with a canopy are independent of Reynolds number, whereas the heat-transfer data for the configuration (singular) without a canopy are Reynolds-number dependent. It might be noted that the configuration for which the leeward heating was Reynolds-number dependent had neither a canopy nor an abrupt change in contour.

On the other hand, the surface pressures varied inversely with Reynolds number for both the UT SWT program and for the Langley program (Ref. 24). Lee-meridian surface-pressure data were reported by Hefner and Whitehead (Ref. 13) to be insensitive to the effects of vortices. The leeward surface pressures are believed to depend on the wake width. Therefore, a program is planned for the UT SWT to measure the width of the near wake as a function of Reynolds number.

CONCLUDING REMARKS

Based on the analysis of the data obtained in the present study, the following conclusions are made:

1. The comparison between the experimental and the theoretical heat-transfer distributions indicate that flow in the windward pitch-plane is two-dimensional at an alpha of 20° but exhibits cross flow at higher angles-of-attack. Perturbations (which were configuration dependent) in the heat-transfer and the surface-pressure distributions occurred in the vicinity of the windward-surface fairing which was required to mate the rounded nose to the flat underbelly of the windward fuselage.

2. The boundary-layer transition parameters based on the present data were consistently above the level predicted by industry-used shuttle criteria. This is somewhat surprising, since it was thought that the fairing-induced flow-field perturbation would promote transition and, hence, yield relatively low values for the transition parameters. Thus, the fact that the present transition values are slightly above the industry correlations indicates that the carefully designed windward surface (to eliminate bow-shock inflections) and the absence of surface joints in the model serve to delay transition.

3. Over the range of alpha tested ($20° \le \alpha \le 50°$), separation was of the free-vortex-layer type. Thus, even in the separated region, there is a strong component of the longitudinal flow.

Although the cross-sections of the two models differ markedly, the separation surfaces for an alpha of 35° (as determined from the oil flow patterns) were roughly the same. The oil-flow patterns show evidence of vortex scrubbing in the leeward pitch-plane of the current configurations.

4. Of the thermocouples on the leeward surface, those (and only those) on the forward-facing surface of the canopy recorded heating rates approaching the values measured on the windward surface. The windshield heat-transfer was highest at an alpha of 20°, but remained high (with the canopy-influence extending upstream) for alphas from 30° to 50°. A canopy-generated shock-wave was evident in the shadowgraph for an alpha of 25°, but no shock-wave appeared in the shadowgraphs for higher angles-of-attack. On the canopy, the perturbed values of the non-dimensionalized heat-transfer, $h/h_{t, R = 1 ft.}$, increased with Reynolds number.

5. Over the angle-of-attack range $20° \leq \alpha \leq 50°$, the heat-transfer data for the leeward pitch-plane are significantly less for the current configurations than for a Langley delta-wing orbiter (which had no canopy protuberance). Thus, the cockpit apparently changes the longitudinal flow-component. Downstream of the canopy location, the present data were only weakly dependent on the Reynolds number, whereas the Langley data in this region were very sensitive to Reynolds number.

REFERENCES

1. P. K. Chang: Separation of Flow, Chapter 1, Pergamon Press, Oxford, Great Britain, 1970.

2. K. C. Wang: "Three-Dimensional Boundary Layer Near the Plane of Symmetry of a Spheroid at Incidence", Journal of Fluid Mechanics, Vol. 43, Part I, August 1970, pp. 187-209.

3. K. C. Wang: "Separation Patterns of Boundary Layer Over an Inclined Body of Revolution", AIAA Paper No. 71-130, presented at the 9th Aerospace Sciences Meeting, January 1971.

4. K. C. Wang: "Separation Patterns of Boundary Layer Over an Inclined Body of Revolution", AIAA Journal, Vol. 10, No. 8, August 1972, pp. 1044-1050.

5. K. F. Stetson and E. G. Friberg: "Surface Correlations in the Leeward Region of a Blunt Cone at Angle of Attack in Hypersonic Flow", ARL-69-0114, July 1969, Aerospace Research Labs., Wright-Patterson Air Force Base, Ohio.

6. K. F. Stetson: "Experimental Results of Laminar Boundary Layer Separation on a Slender Cone at Angle of Attack at $M_\infty = 14.2$", ARL 71-0127, August 1971, Aerospace Research Labs., Wright-Patterson Air Force Base, Ohio.

7. K. F. Stetson: "Boundary-Layer Separation on Slender Cones at Angle of Attack", AIAA Journal, Vol. 10, No. 5, May 1972, pp. 642-648.

8. K. F. Stetson and E. G. Friberg: "Communication Between Base and Leeward Region of a Cone at Angle of Attack in Hypersonic Flow", ARL 69-0115, July 1969, Aerospace Research Labs., Wright-Patterson Air Force Base, Ohio.

9. R. H. Feldhuhn, A. E. Winkelmann, and L. Pasiuk: "An Experimental Investigation of the Flow Field Around a Yawed Cone", AIAA Journal, Vol. 9, No. 6, June 1971, pp. 1074-1081.

10. G. Maise: "Leeside Heating Investigations, Part II - Leeside Heating Investigations of Simple Body-Like Configurations", NASA Space Shuttle Technology Conference, Volume I - Aerothermodynamics, Configurations, and Flight Mechanics, TM X-2272, April 1971, NASA.

11. A. H. Whitehead, Jr.: "Effect of Vortices on Delta Wing Lee-Side Heating at Mach 6", AIAA Journal, Vol. 8, No. 3, March 1970, pp. 599-600.

12. J. N. Hefner and A. H. Whitehead, Jr.: "Lee Side Investigation, Part I - Experimental Lee-Side Heating Studies on a Delta-Wing Orbiter", NASA Space Shuttle Technology Conference, Volume I - Aerothermodynamics, Configurations, and Flight Mechanics, TM X-2272, April 1971, NASA.

13. J. N. Hefner and A. H. Whitehead, Jr.: "Lee-Side Flow Phenomena on Space Shuttle Configurations at Hypersonic Speeds, Part II - Studies of Lee-Surface Heating at Hypersonic Mach Numbers", Space Shuttle Aerothermodynamics Technology Conference, Volume II - Heating, TM X-2507, February 1972, NASA.

14. A. H. Whitehead, Jr., J. N. Hefner, and D. M. Rao: "Lee-Surface Vortex over Configurations in Hypersonic Flow", AIAA Paper No. 72-77, presented at the 10th Aerospace Sciences Meeting, San Diego, January 1972.

15. D. M. Rao: "Hypersonic Lee-Surface Heating Alleviation on Delta Wing by Apex-Drooping", AIAA Journal, Vol. 9, No. 9, September 1971, 1875-1876.

16. A. H. Whitehead, Jr., and M. H. Bertram: "Alleviation of Vortex-Induced Heating to the Lee Side of Slender Wings in Hypersonic Flow", AIAA Journal, Vol. 9, No. 9, September 1971, 1970-1872.

17. J. J. Bertin, J. P. Lamb, J. L. Zickler, and W. D. Goodrich: "Flow Field Measurements for Space-Shuttle-Related Cylindrical Configurations in Hypersonic Streams", AIAA Paper No. 72-294, presented at the 7th Thermophysics Conference, San Antonio, April 1972.

18. C. H. Young, D. C. Reda, and A. M. Roberge: "Hypersonic Flow Field and Heat Transfer Studies on a Lifting Entry Vehicle at Angles of Attack from 0° to 60°", GDC-ERR-1418, September 1970, General Dynamics, Convair Division.

19. C. H. Young, D. C. Reda, and A. M. Roberge: "Hypersonic Transitional and Turbulent Flow Studies on a Lifting Entry Vehicle", AIAA Paper No. 71-100, presented at the 9th Aerospace Sciences Meeting, New York, January 1971.

20. Y. S. Touloukian and E. H. Buyeo: Thermophysical Properties of Matter, Vol. 4, Specific Heat: Metallic Elements and Alloys, IFI/Plenum, New York, 1970.

21. F. L. Guard and H. D. Schultz: "Space Shuttle Aerodynamic Heating Considerations", ASME Paper No. 70-HT/SpT-16, presented at the Space Technology and Heat Transfer Conference, Los Angeles, California, June 1970.

22. C. B. Johnson: "Boundary-Layer Transition and Heating Criteria Applicable to Space Shuttle Configurations from Flight and Ground Tests", NASA Space Shuttle Technology Conference, Volume I - Aerothermodynamics, Configurations, and Flight Mechanics, TM X-2272, April 1971, NASA.

23. J. J. Bertin, J. P. Lamb, K. R. Center, and B. W. Graumann: "Flow Measurements for Cylindrical Configurations in a Hypersonic Wind Tunnel:Windward and Leeward Flow Fields", Aerospace Engineering Report 71007, December 1971, The University of Texas at Austin.

24. J. N. Hefner: "Lee-Surface Heating and Flow Phenomena on Space Shuttle Orbiters at Large Angles of Attack and Hypersonic Speeds," TN D-7088, November 1972, NASA.

25. J. D. Warmbrod, W. R. Martindale, and R. K. Mathews: "Heat Transfer Rate Measurements on North American Rockwell Orbiter (161B) at Nominal Mach Number of 8," DMS-DR-1177, Volume III, December 1971, Arnold Engineering Development Center.

26. M. L. Rasmussen: "On Hypersonic Flow Past an Unyawed Cone", AIAA Journal, Vol. 5, No. 8, August 1967, pp. 1495-1497.

27. R. K. Matthews, R. H. Eaves, Jr., and W. R. Martindale: "Heat Transfer and Flow Field Tests of the McDonnell-Douglas: Martin-Marietta Space Shuttle Configurations", TR in preparation, February 1973, AEDC.

28. R. L. Stallings, Jr.: "Experimentally Determined Local Flow Properties and Drag Coefficients for a Family of Blunt Bodies at Mach Numbers from 2.49 to 4.63", TR R-274, October 1967, NASA.

29. G. Moretti: "Inviscid Blunt Body Shock Layers", Pibal Report No. 68-15, June 1968, Polytechnic Institute of Brooklyn.

30. A. C. Thomas and A. Perlbachs: "Application of Ground Test Data to Reentry Vehicle Design", AFFDL-TR-66-229, January 1967, Flight Dynamics Laboratory, Wright-Patterson Air Force Base, Ohio.

31. A. L. Fehrman and R. V. Masek: "Study of Uncertainties of Predicting Space Shuttle Thermal Environment", Report MDC E0639, June 1972, McDonnell-Douglas Astronautics Company.

32. C. A. Scottoline: "Determination of Aerothermodynamic Uncertainties with Application to Space Shuttle Vehicles", NASA Space Shuttle Aerothermodynamics Technology Conference, Volume II-Heating, TM X-2507, February 1972, NASA.

33. E. R. G. Eckert: "Engineering Relations for Friction and Heat Transfer to Surfaces in High Velocity Flow", Journal of the Aeronautical Sciences, Vol. 22, No. 8, August 1955, pp. 585-587.

34. D. B. Spalding and S. W. Chi: "The Drag of a Compressible Turbulent Boundary Layer on a Smooth Flat Plate with and without Heat Transfer", Journal of Fluid Mechanics, Vol. 18, Part I, January 1964, pp. 117-143.

35. R. Vaglio-Laurin: "Laminar Heat Transfer on Three Dimensional Blunt Nosed Bodies in Hypersonic Flow", ARS Journal, Vol. 29, No. 2, February 1959, pp. 123-129.

36. R. Vaglio-Laurin: "Turbulent Heat Transfer on Blunt Nosed Bodies in Two-Dimensional and General Three-Dimensional Hypersonic Flow", Journal of the Aero-Space Sciences, Vol. 27, No. 1, January 1960, pp. 27-36.

37. J. C. Adams, Jr., and W. R. Martindale: "Hypersonic Lifting Body Windward Surface Flow-Field Analysis for High Angles of Incidence", TR in preparation, February 1973, AEDC.

Table 1. - Run schedule for the entry configuration
tests in Tunnel B of AEDC

(a)   Heat-transfer runs

(i)   UTN2

Group	α (deg)	M_∞	$Re_{\infty,L}$ ($\times 10^{-6}$)	P_{t2} (psia)	T_t ($^\circ R$)
35	20	7.92	1.565	1.329	1245
36	30	7.92	1.552	1.319	1244
37	40	7.92	1.577	1.335	1242
38	50	7.92	1.561	1.320	1240
34	30	7.96	3.007	2.590	1265
28	20	7.97	4.113	3.615	1282
29	25	7.97	3.967	3.615	1314
30	30	7.97	4.059	3.610	1293
31	35	7.97	4.132	3.620	1279
32	40	7.97	4.182	3.650	1277
33	50	7.97	4.117	3.640	1288
27	30	7.98	5.685	5.150	1311
26	30	8.00	6.799	6.150	1314
20	20	8.01	7.801	7.270	1343
24	20	8.00	6.895	7.310	1460
21	30	8.01	7.778	7.280	1346
22	40	8.01	7.793	7.310	1347
23	50	8.01	7.770	7.290	1348
25	50	8.00	7.747	7.310	1350

(ii) <u>UTN7</u>

Group	α (deg)	M_∞	$Re_{\infty, L}$ $(\times 10^{-6})$	P_{t2} (psia)	T_t (°R)
15	20	7.93	1.656	1.330	1201
16	30	7.93	1.637	1.323	1206
19	35	7.93	1.613	1.330	1222
17	40	7.93	1.634	1.331	1212
18	50	7.93	1.623	1.330	1217
14	30	7.96	2.963	2.615	1284
8	20	7.98	4.044	3.600	1295
9	25	7.98	4.053	3.605	1295
10	30	7.98	4.065	3.605	1292
11	35	7.98	4.078	3.615	1293
12	40	7.98	4.078	3.610	1292
13	50	7.98	4.053	3.608	1295
7	30	7.99	5.666	5.140	1313
6	30	8.00	6.568	6.140	1343
1	20	8.01	7.784	7.310	1349
3	30	8.01	7.857	7.315	1341
4	30	8.01	7.789	7.260	1343
5	40	8.01	7.770	7.280	1348
2	50	8.01	7.799	7.305	1347

(b) Oil-flow runs

Conf.	α (deg)	M_∞	$Re_{\infty, L}$ $(\times 10^{-6})$	P_{t2} (psia)	T_t (°R)
UTN2	35	7.92	1.6	1.33	1220
UTN7	35	7.93	1.6	1.33	1220
UTN7	20	7.93	1.6	1.33	1220

Table 2. - Run schedule for the pressure models of the

nose configurations tested in the UT SWT

(a) UTN2

Run No.	α (deg)	M_∞	$Re_{\infty, L}$ $(x\ 10^{-6})$	P_{t2} (psia)	T_t ($^\circ$R)
2-11-29	32	4.97	6.58	13.99	+No HT
2-12-5	45	4.97	6.63	13.79	+No HT
1-12-4	22.5	4.97	6.73	13.99	+No HT
1-11-30	31	4.97	6.83	16.14	582
1-12-6	45	4.97	6.83	16.08	582
3-12-6	25	4.97	6.91	16.08	578
2-12-1	43	4.97	8.11	19.11	582
1-12-1	19.5	4.97	8.13	18.92	578
1-11-29	31	4.97	8.13	18.92	578
1-12-12	24	4.97	8.21	19.11	580
2-12-6	46	4.97	10.80	25.18	572
2-11-30	31.5	4.97	11.00	25.24	572
1-17-5	24	4.97	11.13	25.41	572

+ Air in reservoir was at ambient temperature

Table 2. - Run schedule for the pressure models of the

nose configurations tested in the UT SWT

(b) UTN7*

Run No.	α (deg)	M_∞	$Re_{\infty,L}$ ($\times 10^{-6}$)	P_{t2} (psia)	T_t (°R)
1-10-17	30	4.97	6.65	14.93	No HT
2-10-18	22	4.97	6.79	15.19	No HT
1-10-18	23	4.97	8.41	18.85	578
1-10-6	30	4.97	8.43	18.85	578
1-10-12	30	4.97	11.42	25.17	572
2-10-17	20	4.97	11.43	25.23	572

*The leeward surface of the UT pressure model differed slightly from the AEDC heat-transfer model as noted in the section "Experimental Program".

45

Table 3. – Transition-related parameters

Conf	α (deg)	M_∞	$Re_{\infty,L}$ $(\times 10^{-6})$	x_{tr} (ft)	M_e	Re/ft $(\times 10^{-6})$	$Re_{x,tr}$ $(\times 10^{-6})$	Re_θ	$\dfrac{Re_\theta}{M_e}$
UTN2	20°	8.01	7.801	.8553	3.967	4.271	3.653	1260	254
UTN2	30°	8.01	7.778	.7510	2.778	2.928	2.199	691	249
UTN2	40°	8.01	7.793	.5632	1.938	1.990	1.121	476	245
UTN2	50°	8.00	7.747	.5632	1.280	1.289	0.726	339	265
UTN2	30°	7.97	4.059	1.043	2.775	1.531	1.597	757	270
UTN2	40°	7.97	4.182	.8344	1.937	1.038	0.866	424	219
UTN2	50°	7.97	4.117	.8344	1.279	0.671	0.560	312	244
UTN7	20°	8.01	7.784	1.043	3.967	4.269	4.453	1378	347
UTN7	30°	8.01	7.857	.9596	2.778	2.939	2.810	851	306
UTN7	40°	8.01	7.770	.8970	1.938	1.990	1.785	642	331
UTN7	50°	8.01	7.799	.8970	1.280	1.299	1.165	495	386
UTN7	20°	7.98	4.044	1.2516	4.004	2.263	2.832	1102	275
UTN7	30°	7.98	4.065	1.2516	2.804	1.548	1.937	907	323
UTN7	40°	7.98	4.078	1.356	2.005	1.076	1.459	663	331
UTN7	50°	7.98	4.053	1.356	1.336	0.702	0.952	527	394
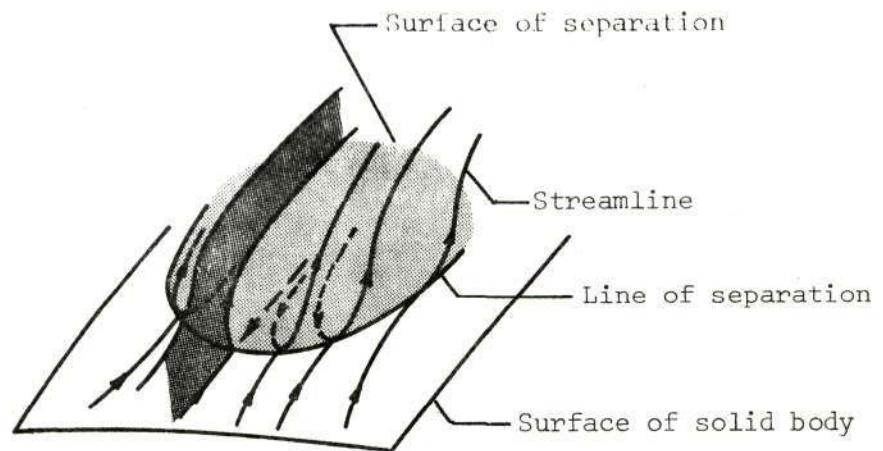
(a) Separation bubble; basic pattern
    presented by Wang (Ref. 3)
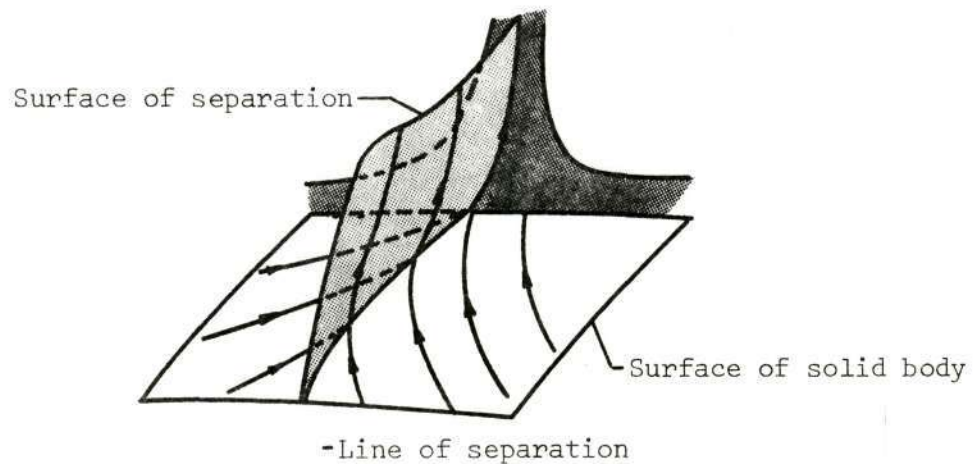
(i) Basic pattern presented by Wang (Ref. 3)
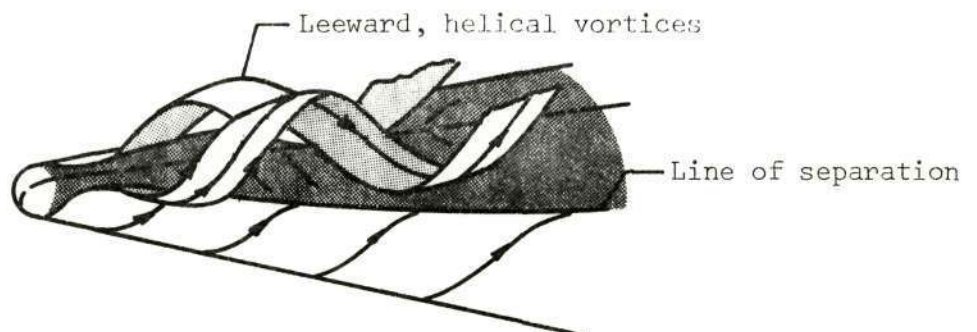
(ii) Model of Stetson (Ref. 6) for a cone

(b) Free-vortex layer

Figure 1. - Sketches of separation patterns.

24.99
(L)

15.14

10.34

1.94

y

z

x

z

Λ

Note: All dimensions in inches
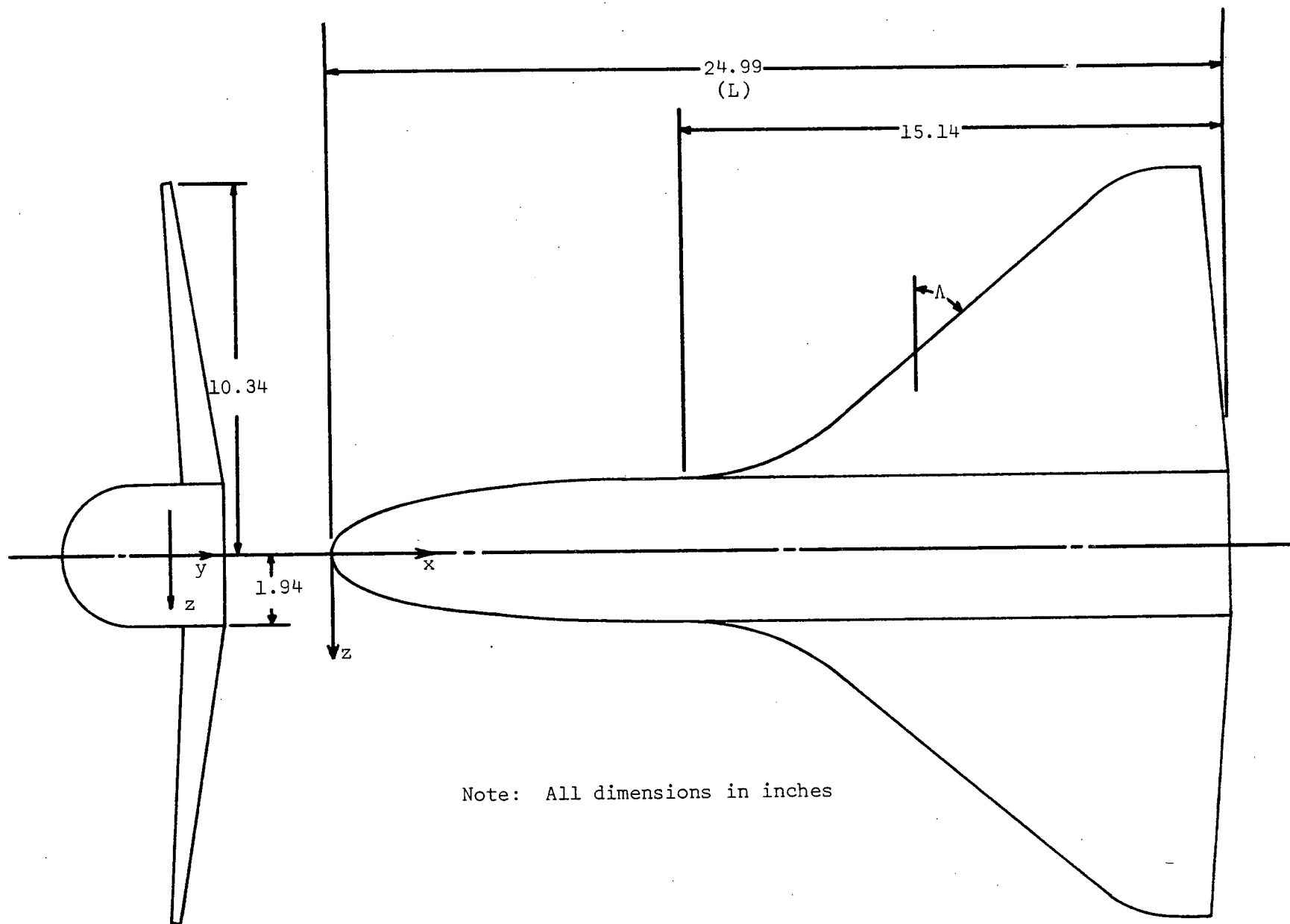
Figure 2.   -   Sketch of models used in Tunnel B (AEDC) test program.

(a) Top view

$\frac{x}{L}$

0.1   0.2   0.3   0.4   0.5   0.6   0.7   0.8   0.9

A   B   C   D   E   F

A   B   C   D   E   F
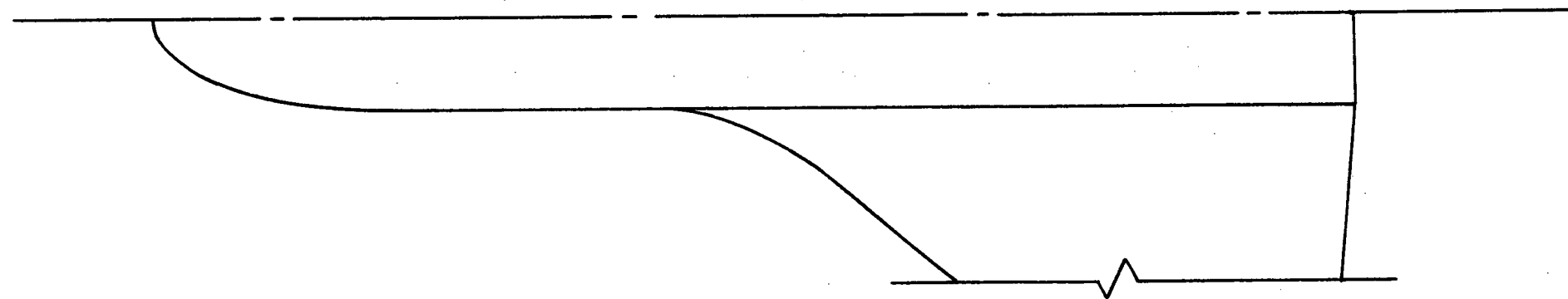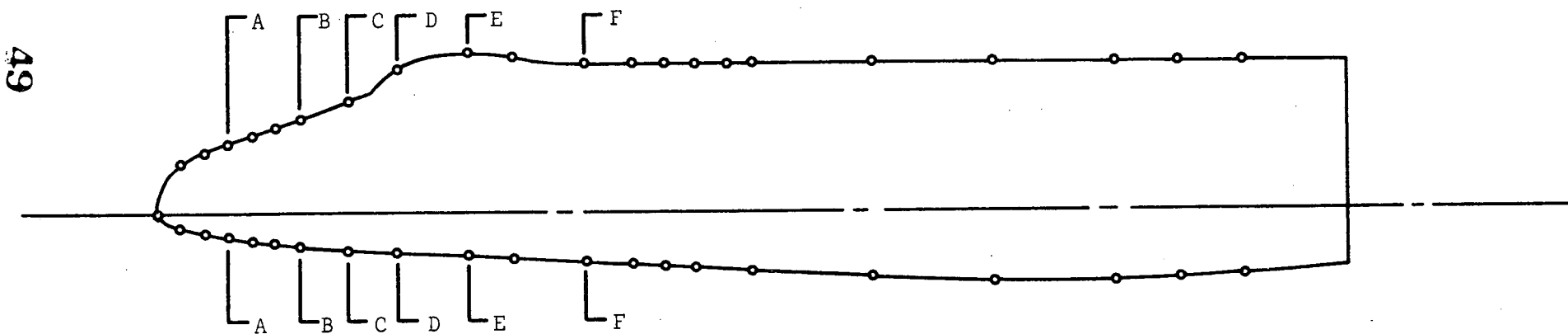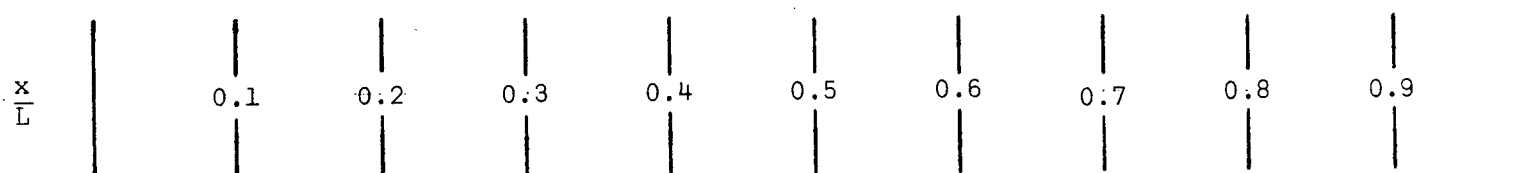
(b) Side view

Figure 3. - Sketch of UTN2 configuration for AEDC tests indicating thermocouple locations.

Section AA

x = 0.06L

Section BB

x = 0.12L

Section CC

x = 0.16L

Section DD

x = 0.20L

Section EE

x = 0.26L
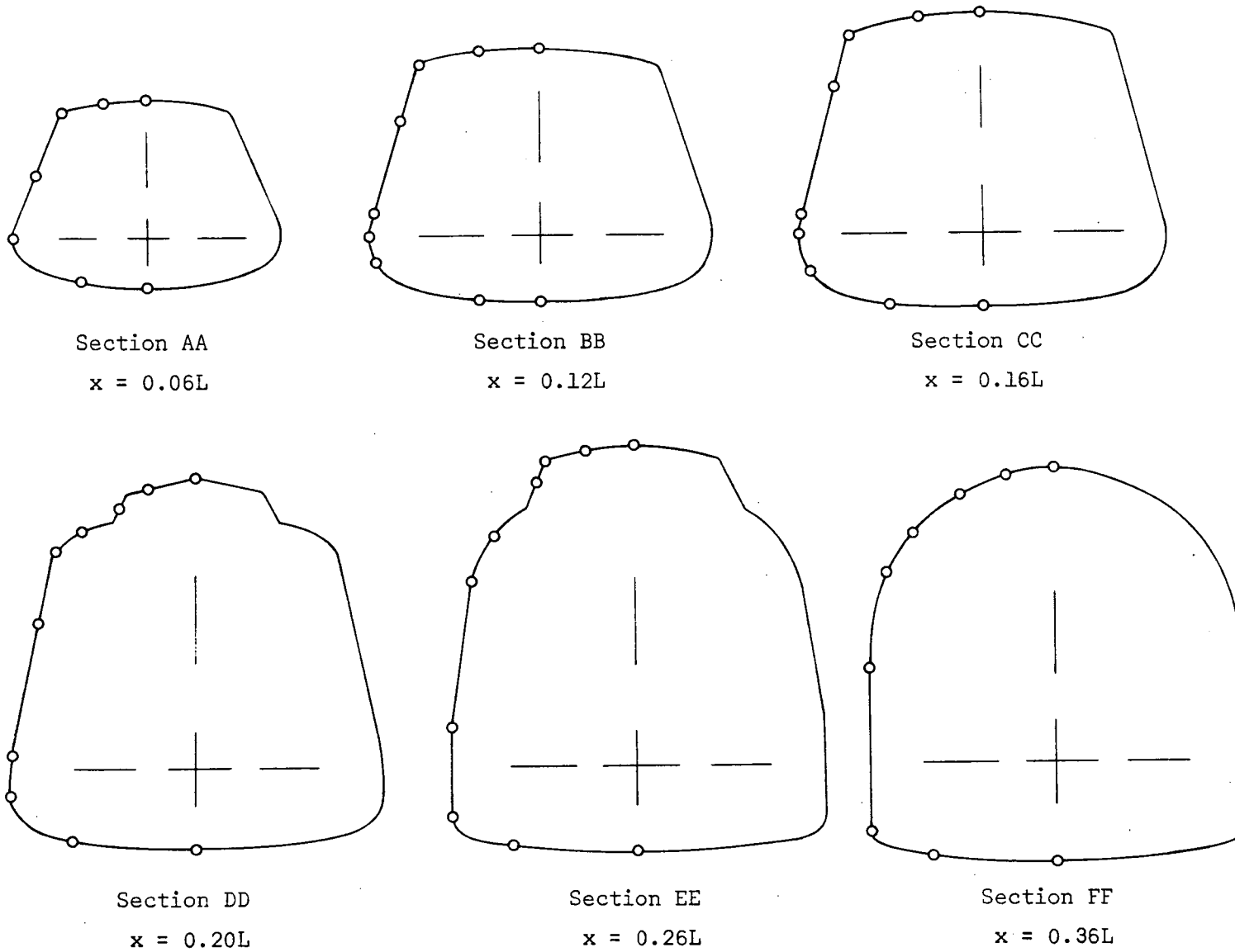
Section FF

x = 0.36L

Figure 3. - Concluded

50

(a) Top View

$\frac{x}{L}$ 0.1   0.2   0.3   0.4   0.5   0.6   0.7   0.8   0.9

A   B   C   D   E   F   G

A   B   C   D   E   F   G
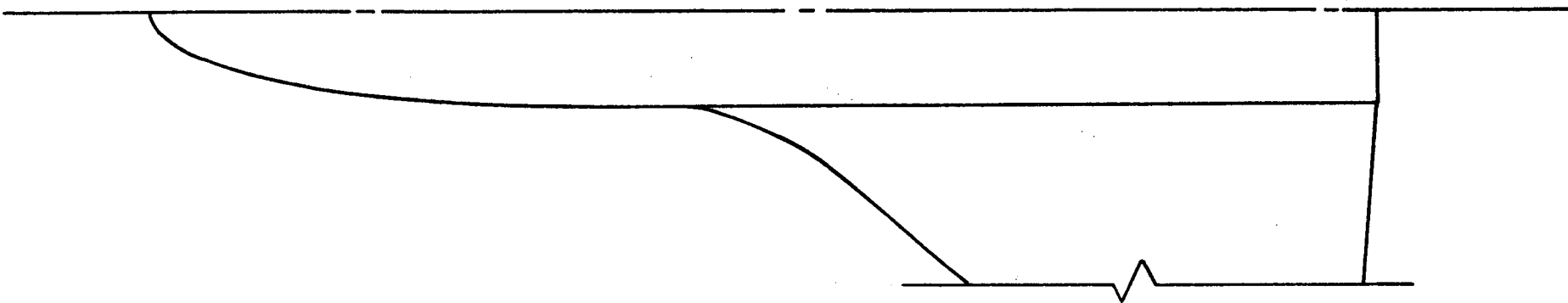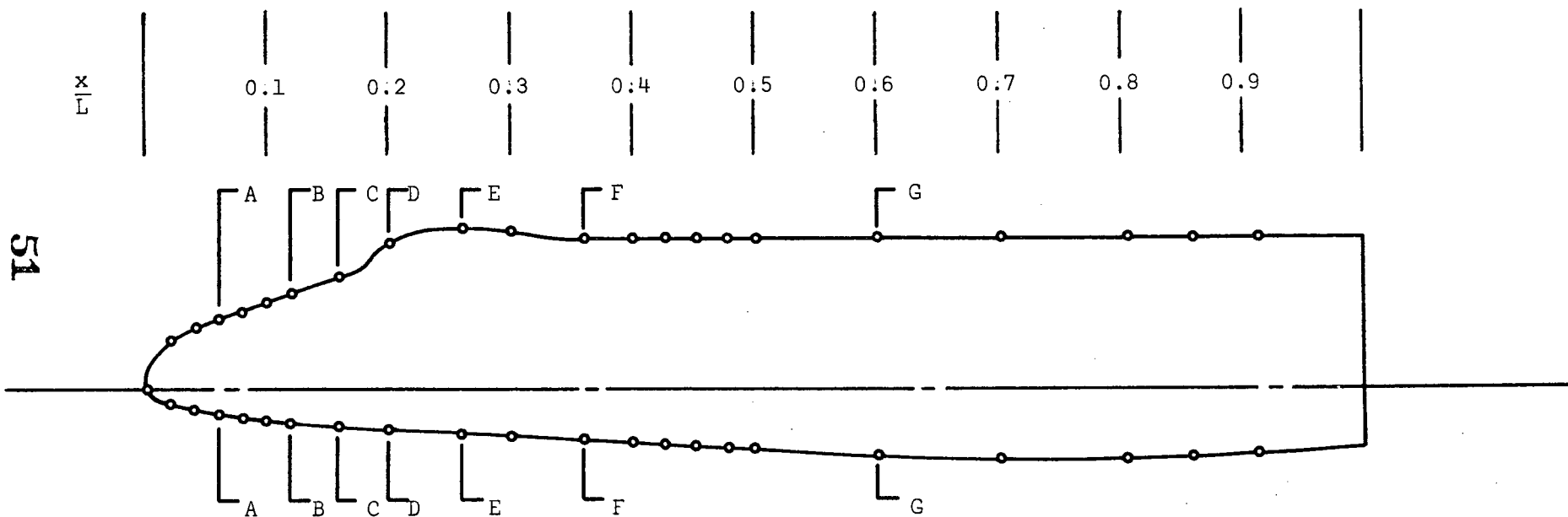
(b) Side view

Figure 4. - Sketch of the UTN7 configuration for AEDC tests indicating thermocouple locations.
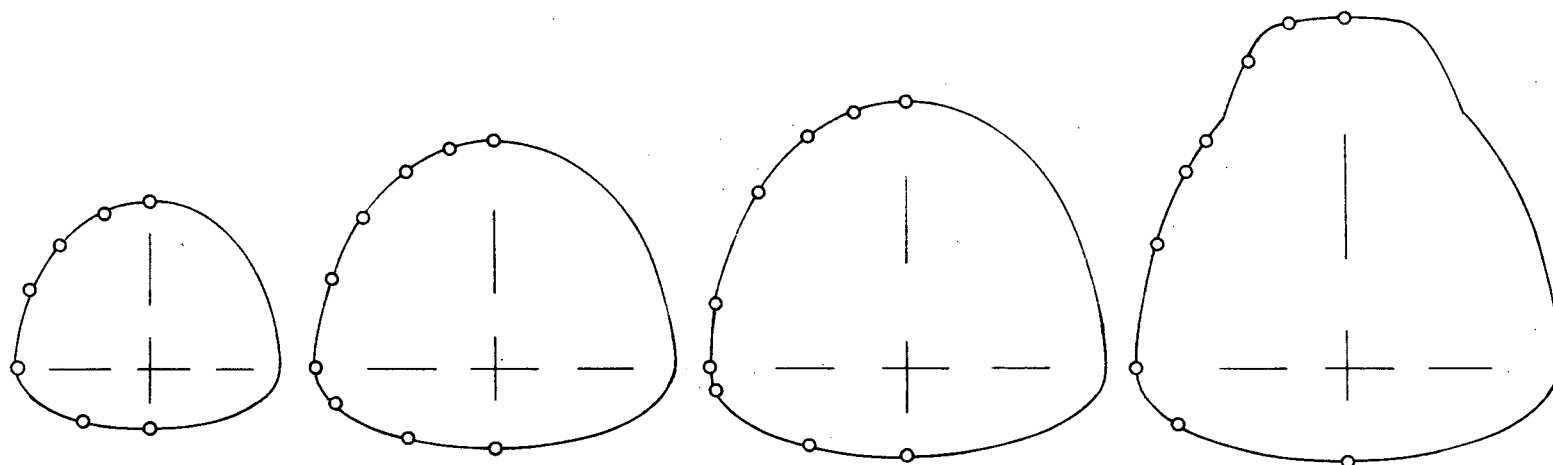
Section AA
x = 0.06L

Section BB
x = 0.12L

Section CC
x = 0.16L
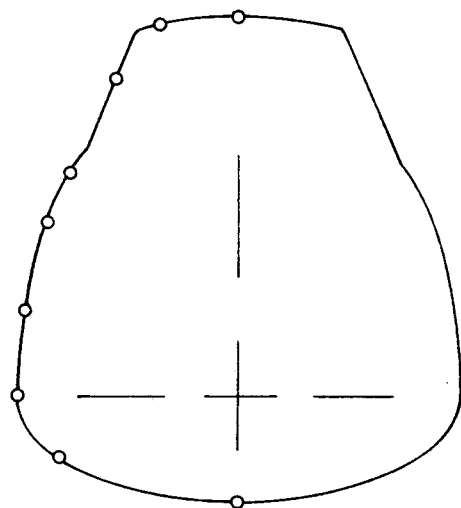
Section DD
x - 0.20L
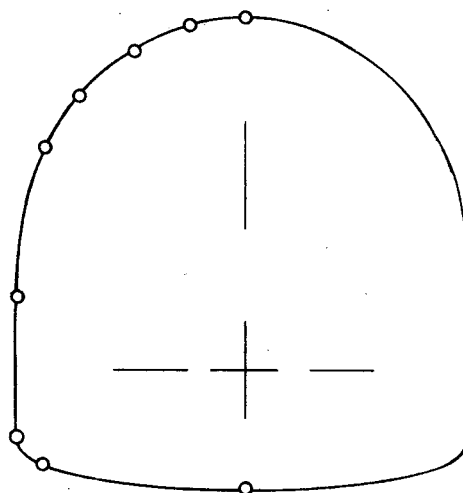
Section EE
x = 0.26L
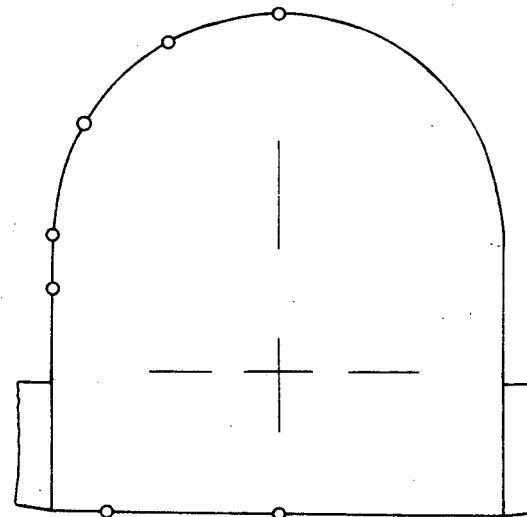
Section FF
x = 0.36L

Section GG
x = 0.60L

Figure 4. - Concluded

52
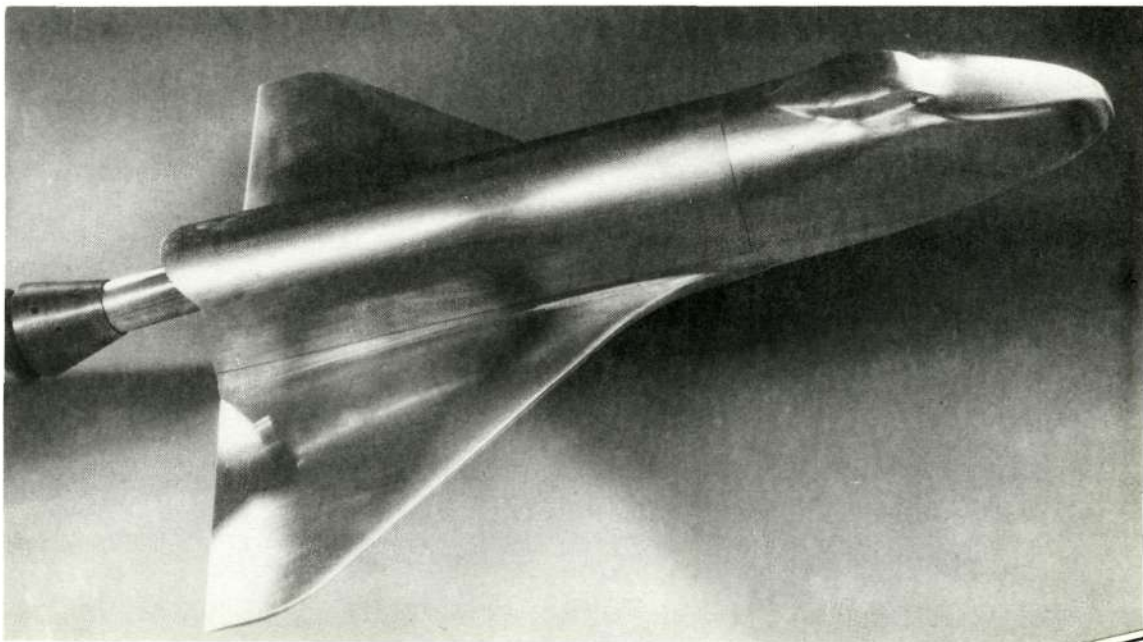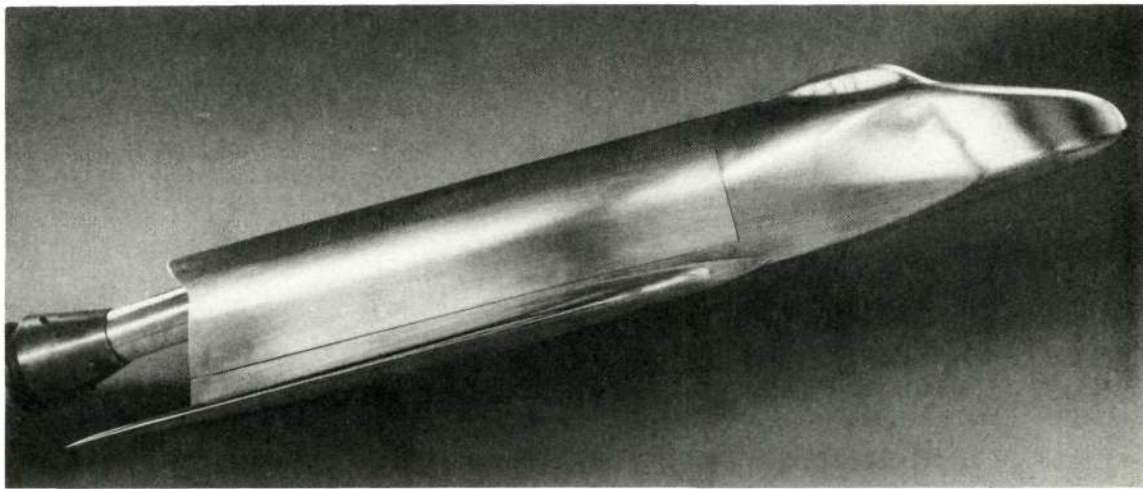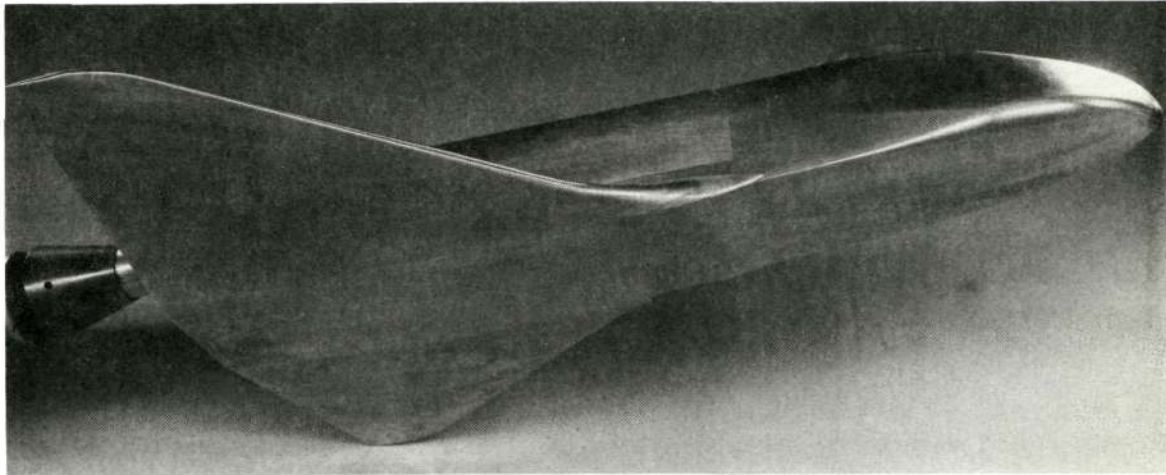
(a) UTN2

Figure 5.- Photographs of the two 0.019-scale models
tested in Tunnel B.

53
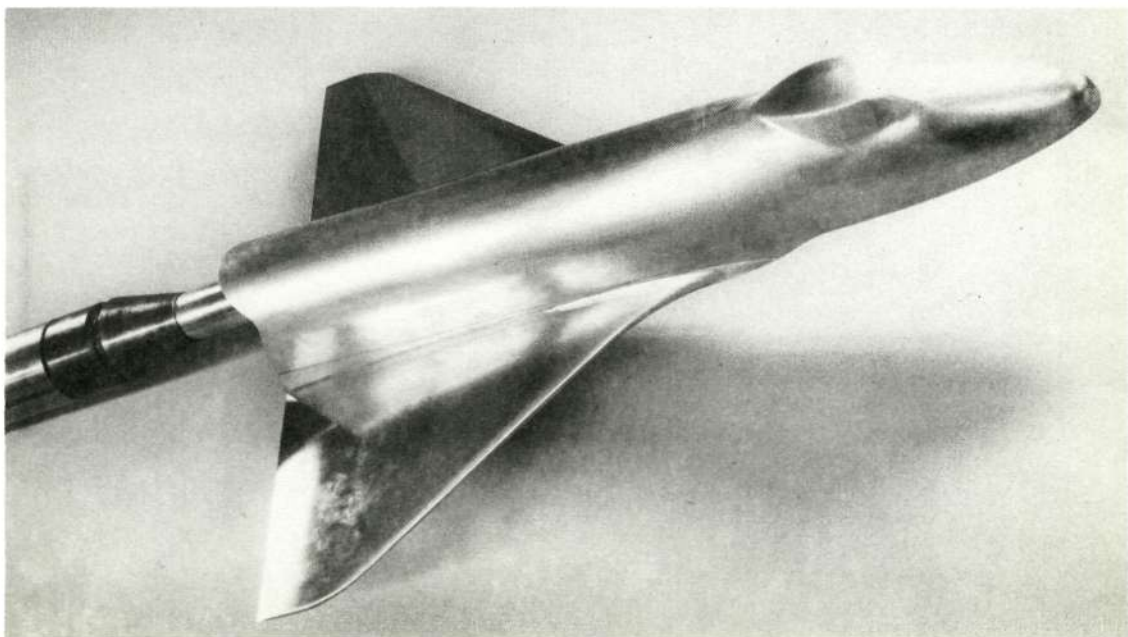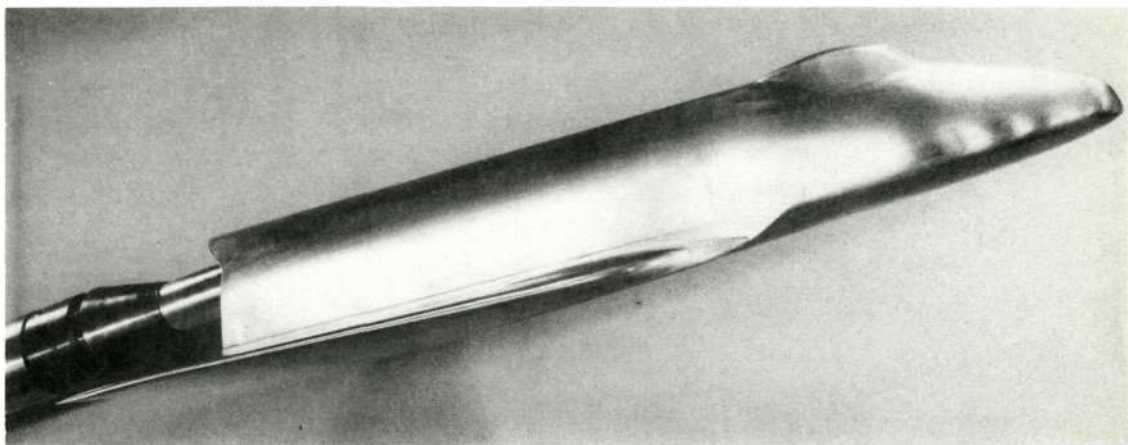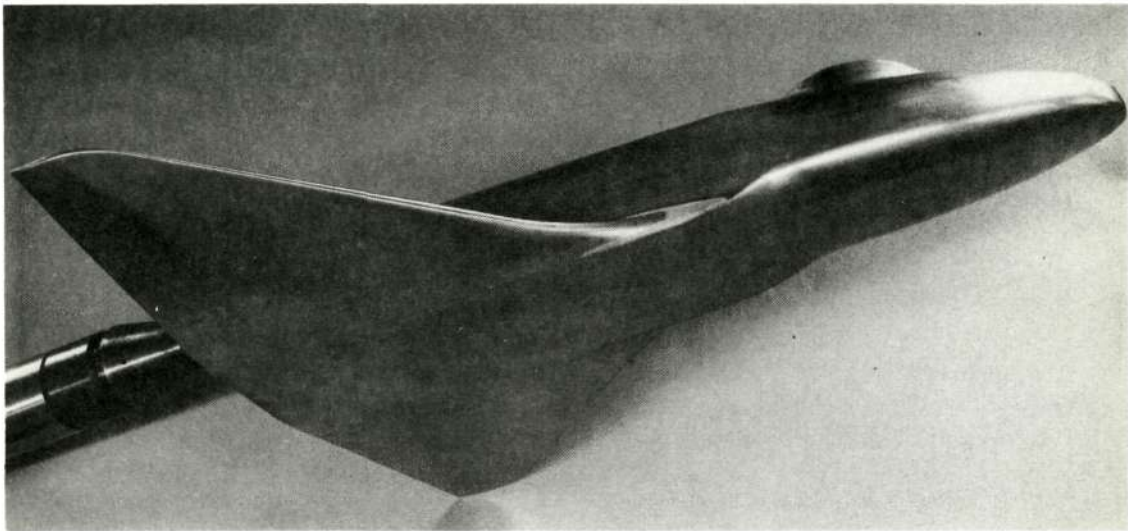
(b) UTN7

Figure 5.- Concluded.

54
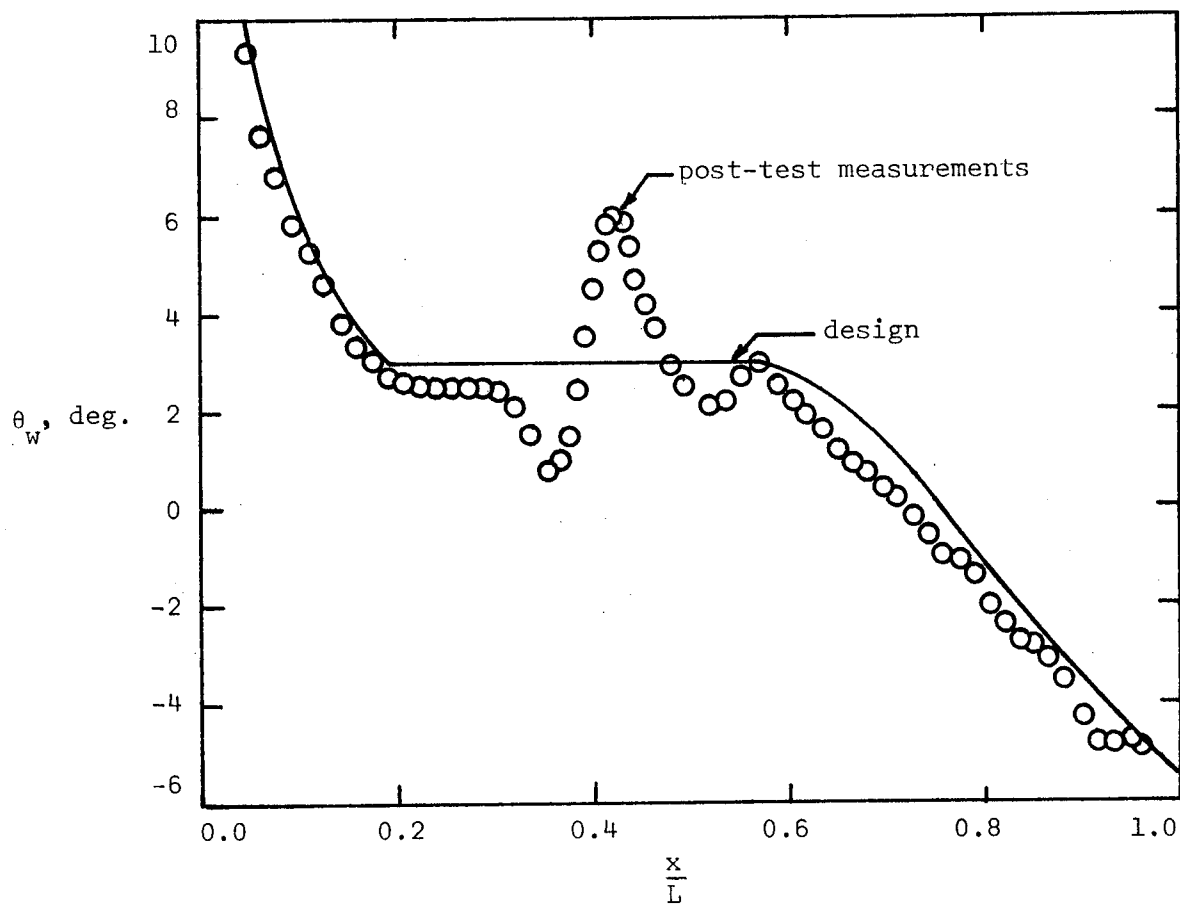
Figure 6. - Comparison of post-test measurements
of windward-surface angles with the design
value for the UTN2

55
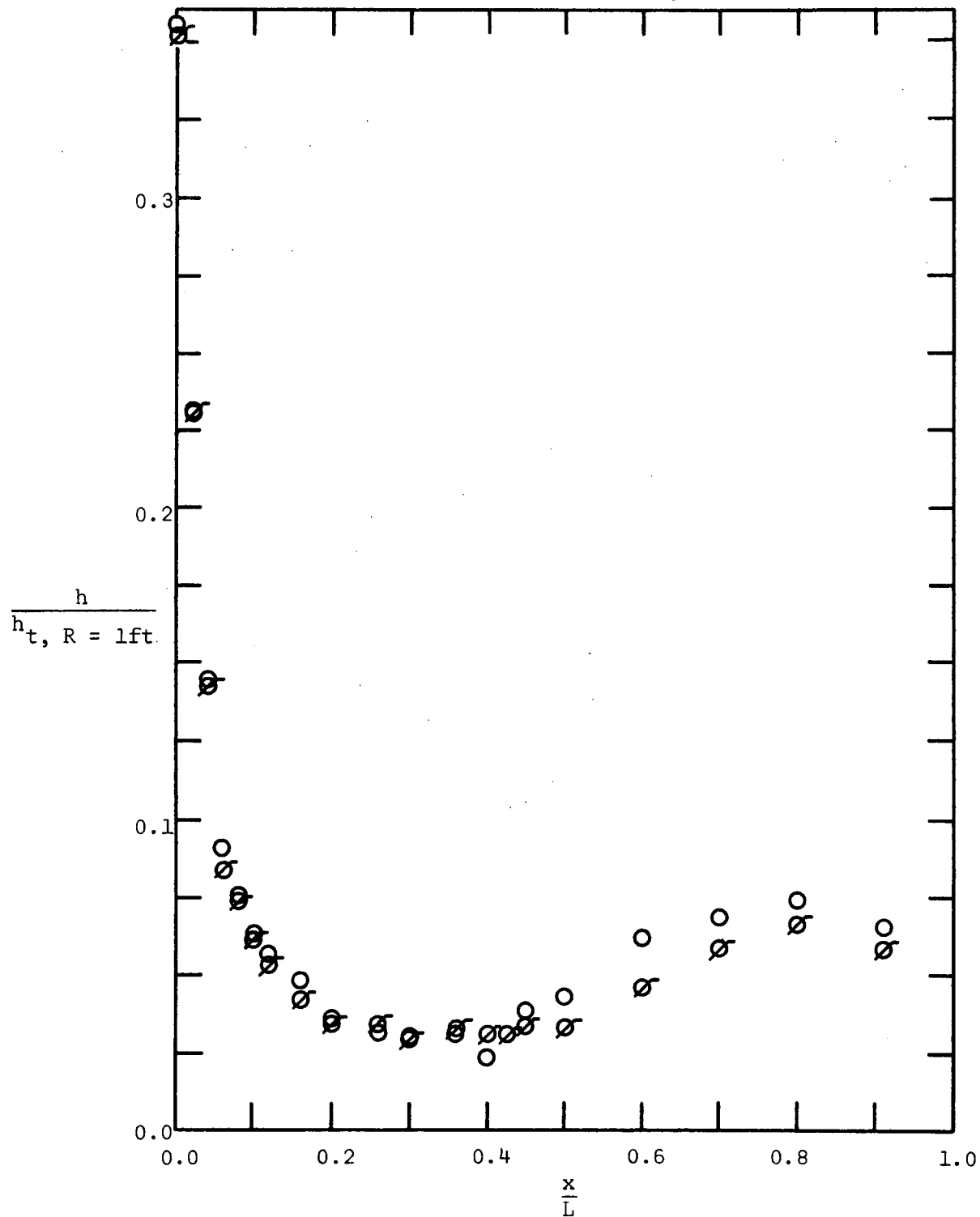
(a) $\alpha = 20°$

Figure 7. - Heat-transfer distribution for the windward pitch-plane of the UTN2, as affected by the surface change.

56

Group 23: $\oslash$ $M_\infty = 8.01$, $Re_{\infty,L} = 7.770 \times 10^6$

Group 25: $\bigcirc$ $M_\infty = 8.00$, $Re_{\infty,L} = 7.747 \times 10^6$
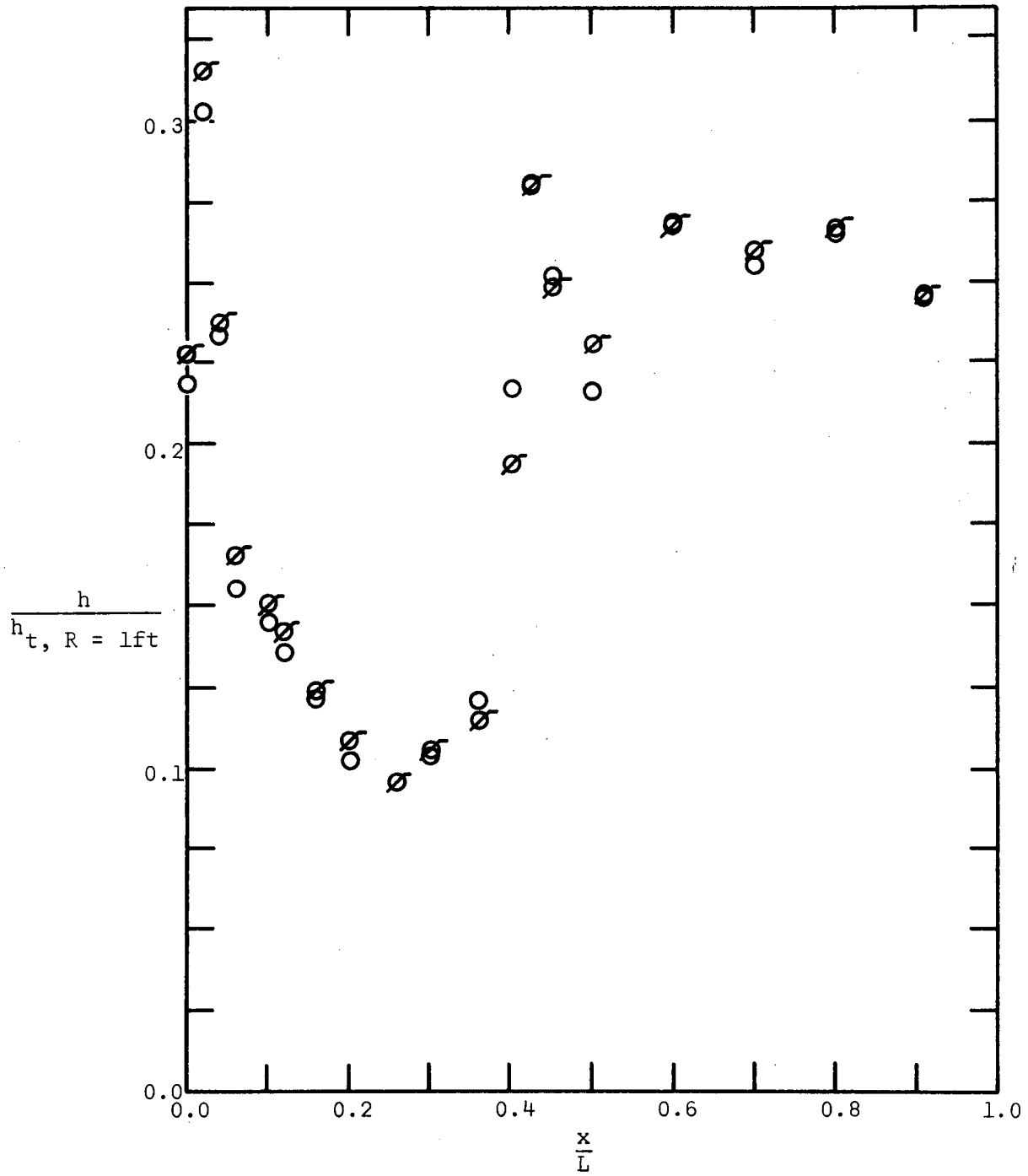
$$\frac{h}{h_{t,\ R\ =\ 1ft}}$$

$$\frac{x}{L}$$

(b) $\alpha = 50°$

Figure 7. - Concluded.
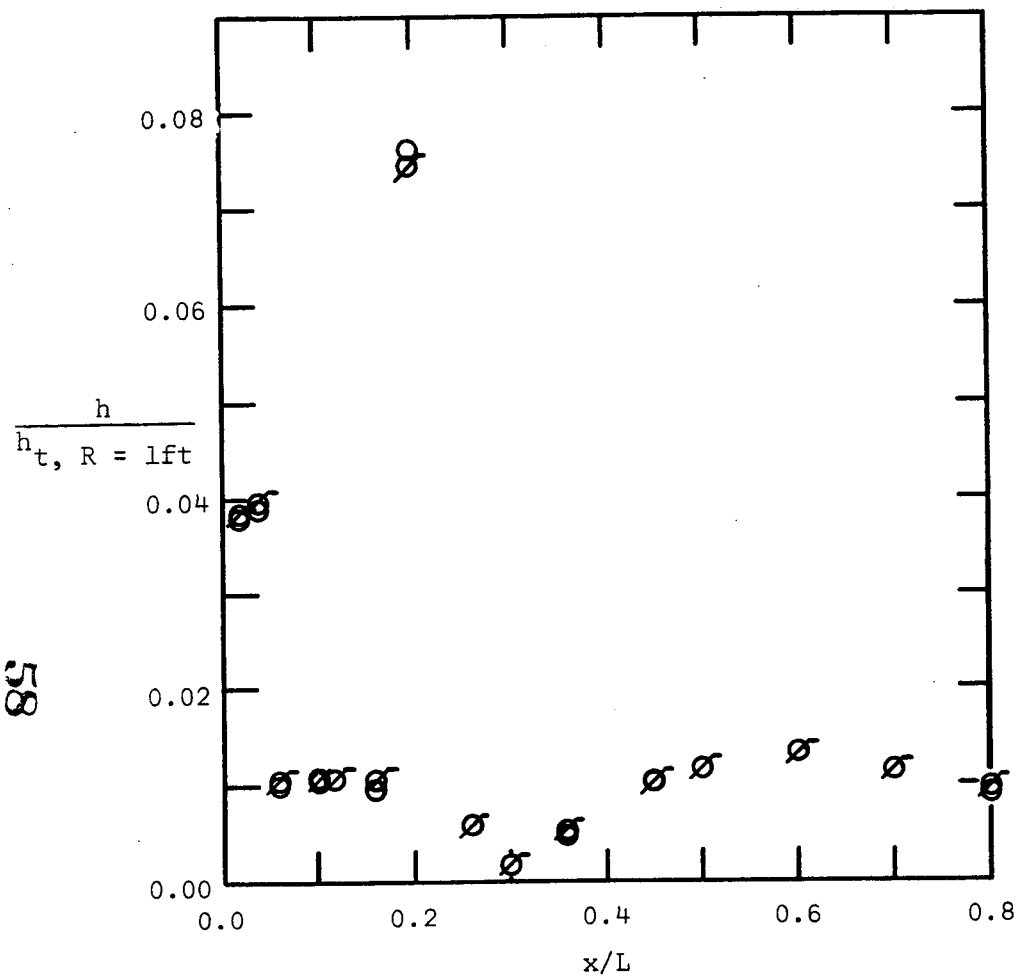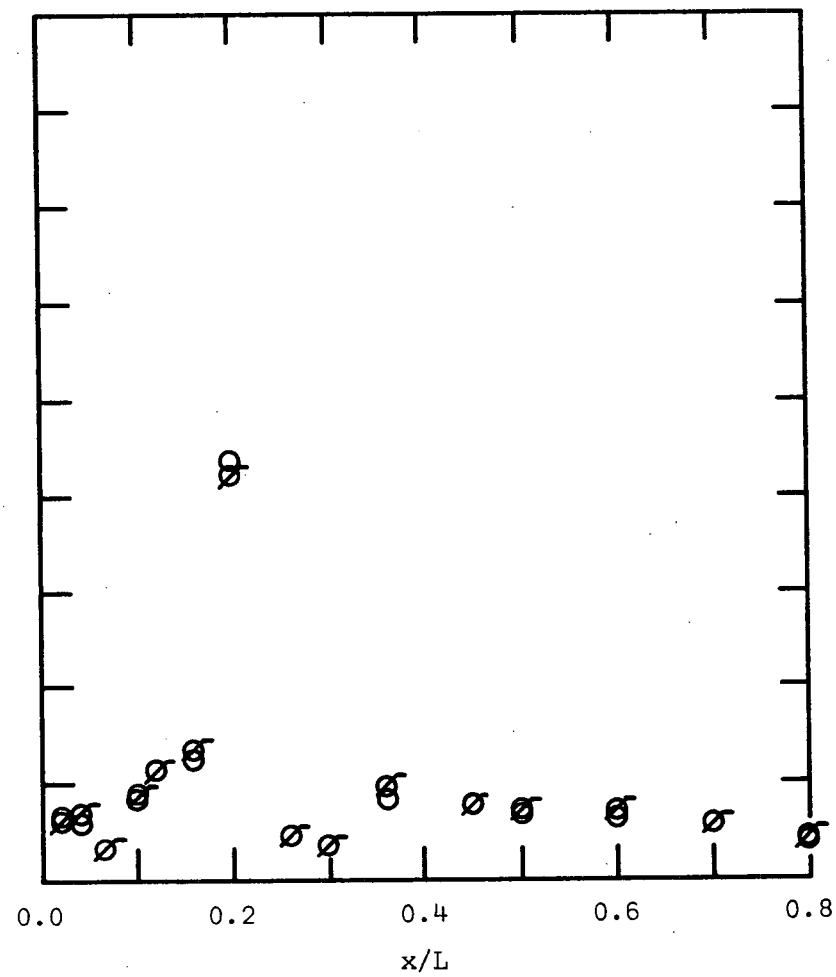
Figure 8. - Heat-transfer distribution for the leeward pitch-plane of the UTN2.
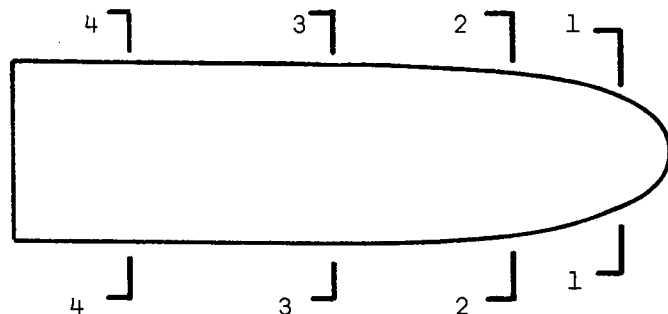
(a) Top view
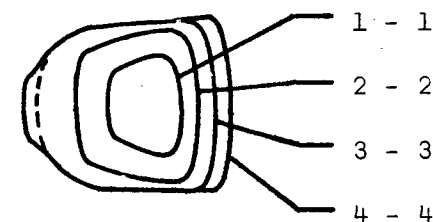
(b) Front-view sections
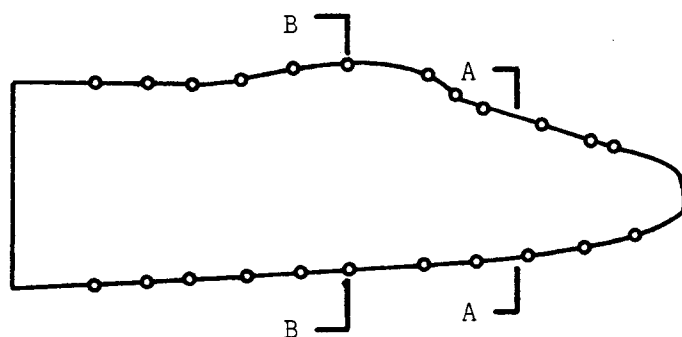
Model length = 3.45 in.

Effective length = 5.91 in.
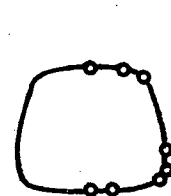
(c) Side view

Section AA
x = 0.14L

Section ʙB
x = 0.29L

(d) Instrumented cross-sections

Figure 9. - Sketch of UTN2 configuration used in UT SWT indicating
pressure-orifice locations.
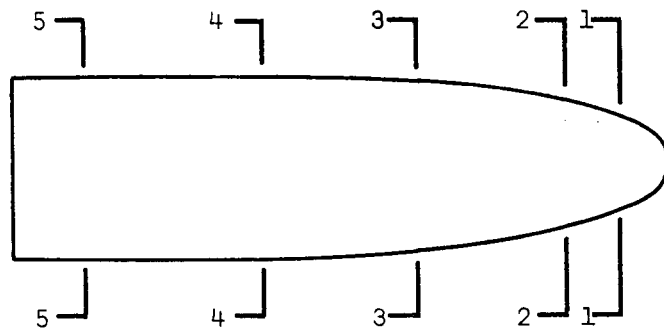
(a) Top view
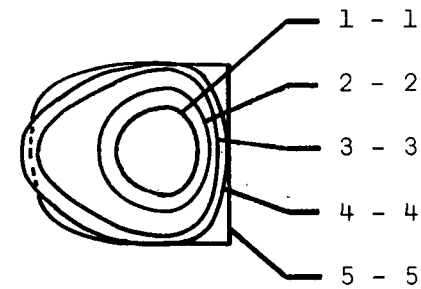
(b) Front-view sections

Model length   = 3.4 in.

Effective length = 6.13 in.
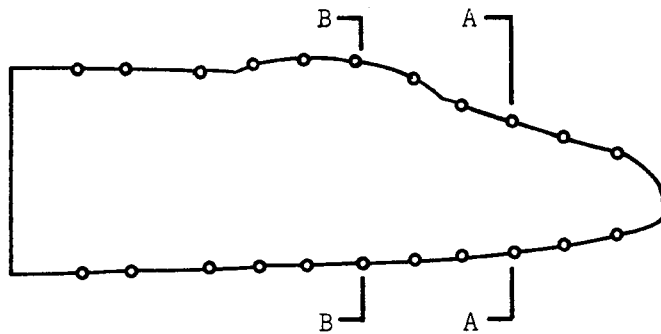
(c) Side view
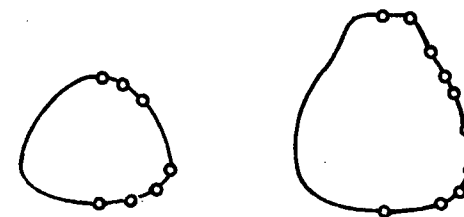
Section AA

x = 0.12L

Section BB

x = 0.26L

(d) Instrumented cross-sections

Figure 10. - Sketch of UTN7*configuration used in UT SWT indicating
     pressure-orifice locations.
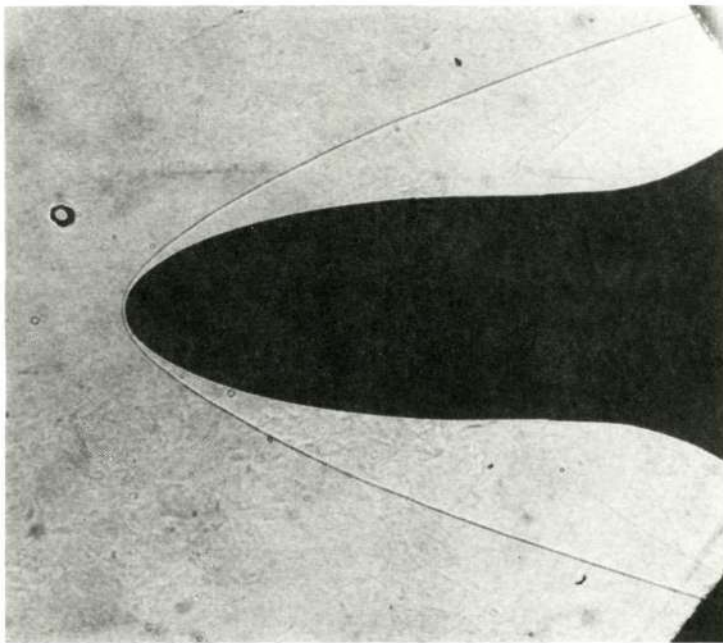
(a) Shadowgraph
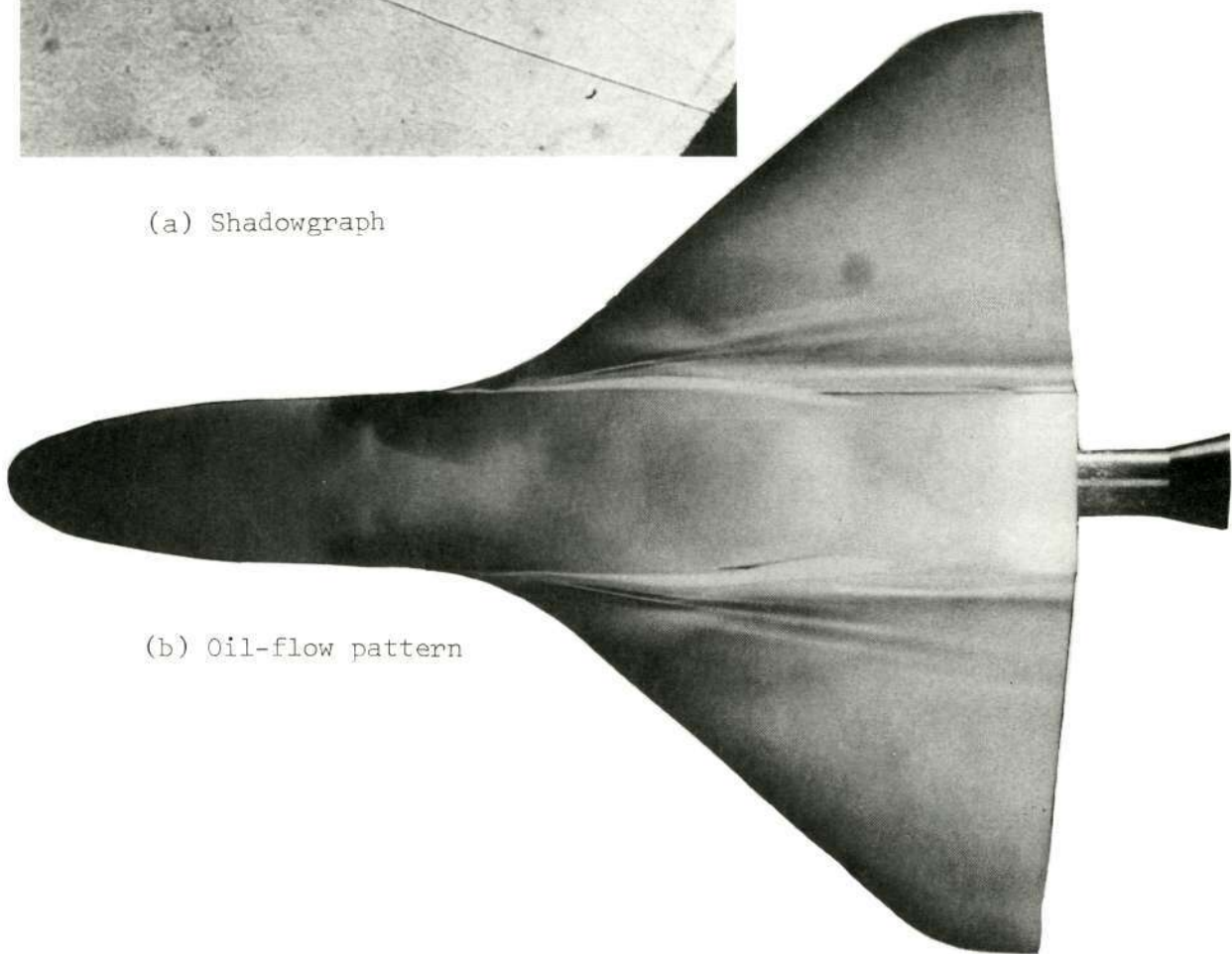
(b) Oil-flow pattern

Figure 11.- Flow-visualization photographs for the windward surface of the
UTN7 at an alpha of 35°, $M_\infty = 7.93$, $Re_{\infty,L} = 1.6 \times 10^6$.

61

$Re_{\infty,L} = 6.65 \times 10^6$

$Re_{\infty,L} = 8.43 \times 10^6$

$Re_{\infty,L} = 11.42 \times 10^6$

$Re_{\infty,L} = 1.637 \times 10^6$

$Re_{\infty,L} = 2.963 \times 10^6$

$Re_{\infty,L} = 4.065 \times 10^6$

$Re_{\infty,L} = 5.666 \times 10^6$

$Re_{\infty,L} = 6.568 \times 10^6$

$Re_{\infty,L} = 7.789 \times 10^6$

66

$\dfrac{p}{p_{t2}}$

1.0
0.8
0.6
0.4
0.2
0.0

0.0 0.2 0.4 0.6

$\dfrac{x}{L}$

$\dfrac{h}{h_{t,R=1\ ft.}}$

0.25
0.20
0.15
0.10
0.05
0.00

0.0 0.2 0.4 0.6 0.8

$\dfrac{x}{L}$
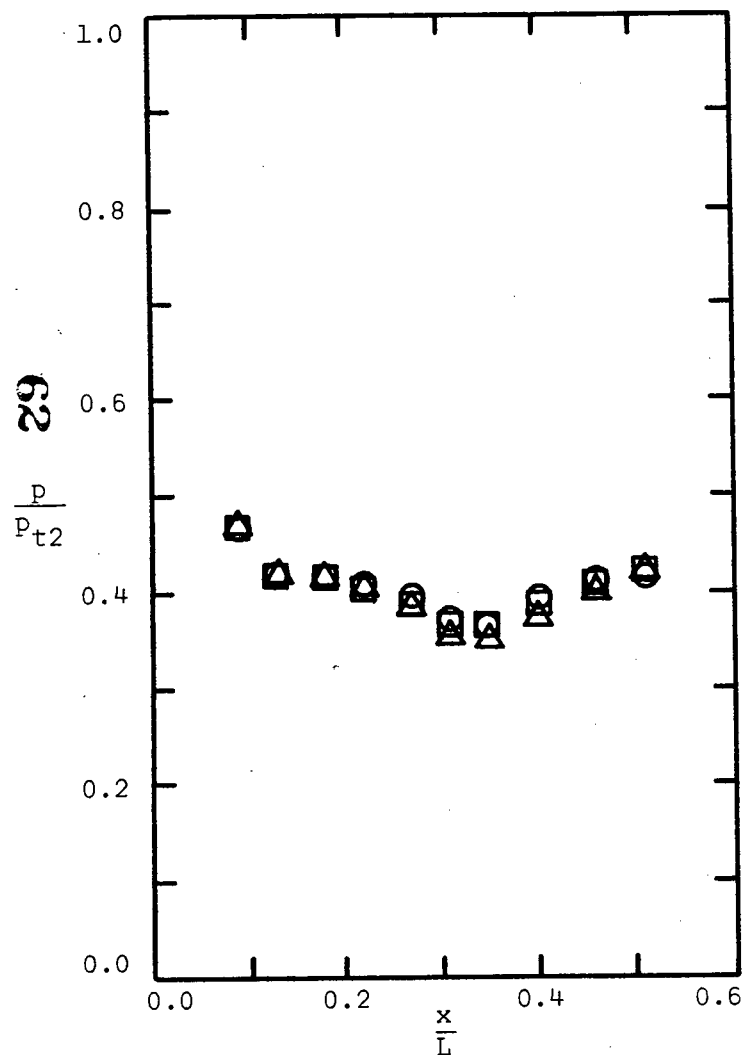
(a) Surface-pressure from UT SWT
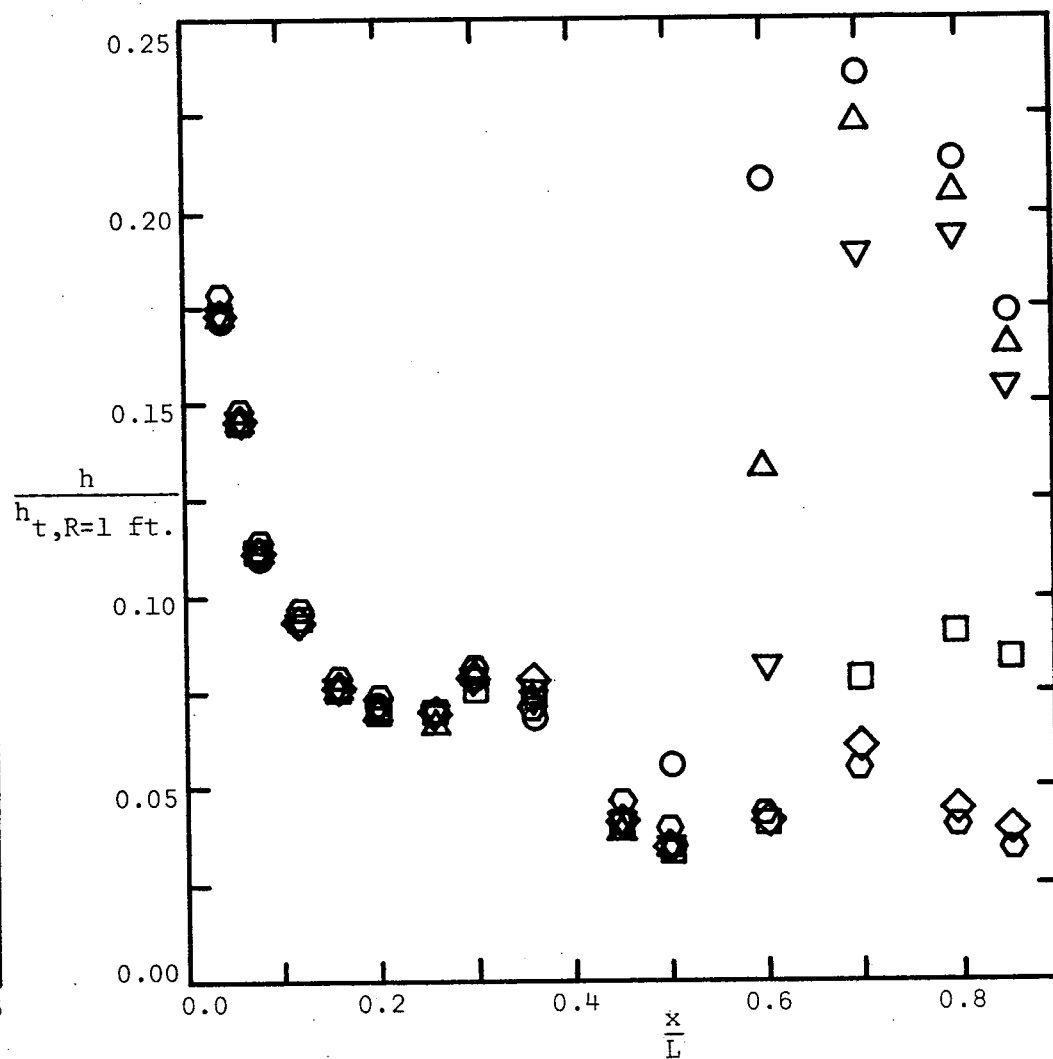
(b) Heat-transfer from AEDC Tunnel B

Figure 12. - Data from the windward pitch-plane of the UTN7 at a nominal alpha of 30°.
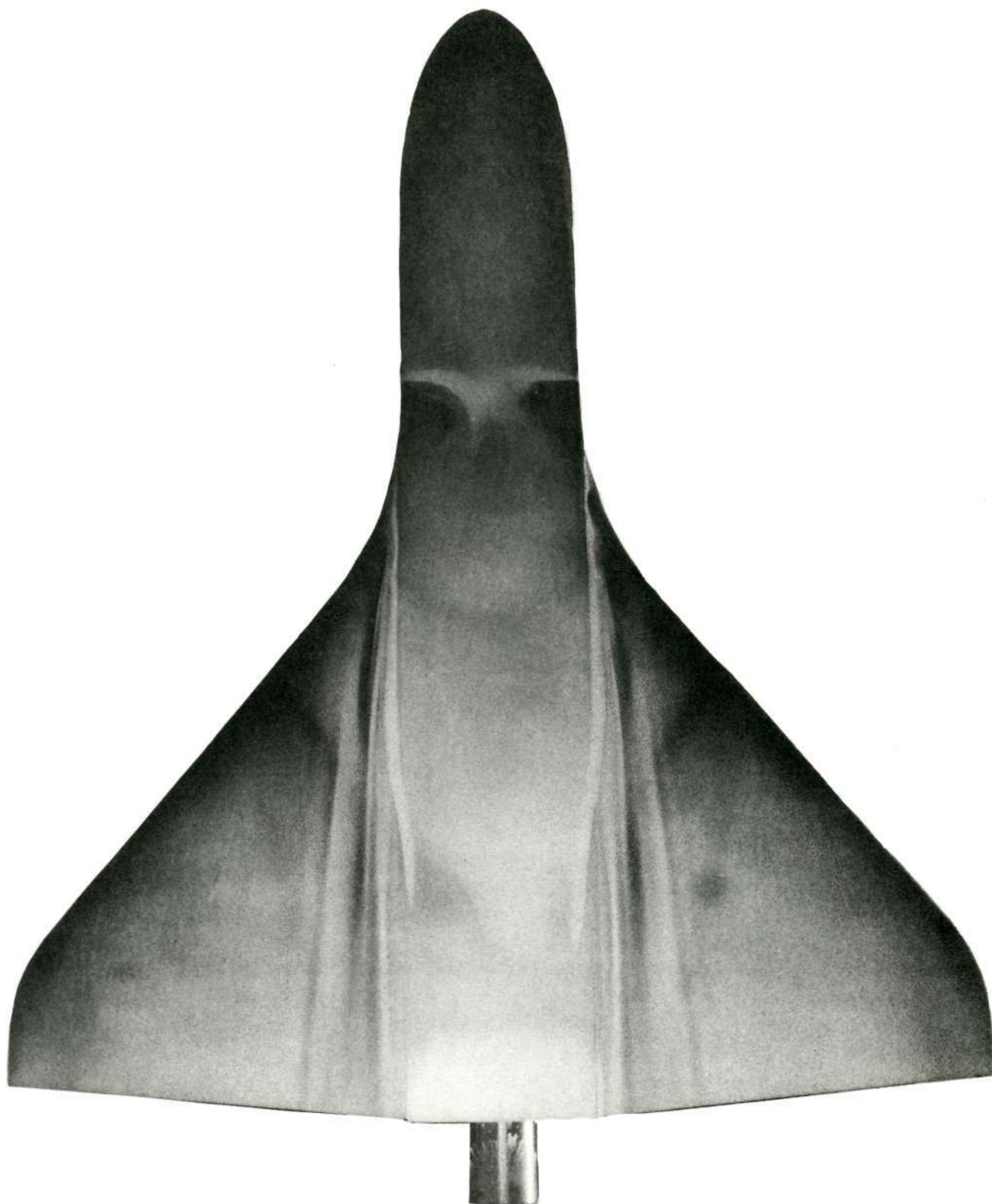
Figure 13.- Oil-flow pattern for the windward surface of the UTN2 at an alpha of 35°, $M_\infty = 7.92$, $Re_{\infty,L} = 1.6 \times 10^6$.
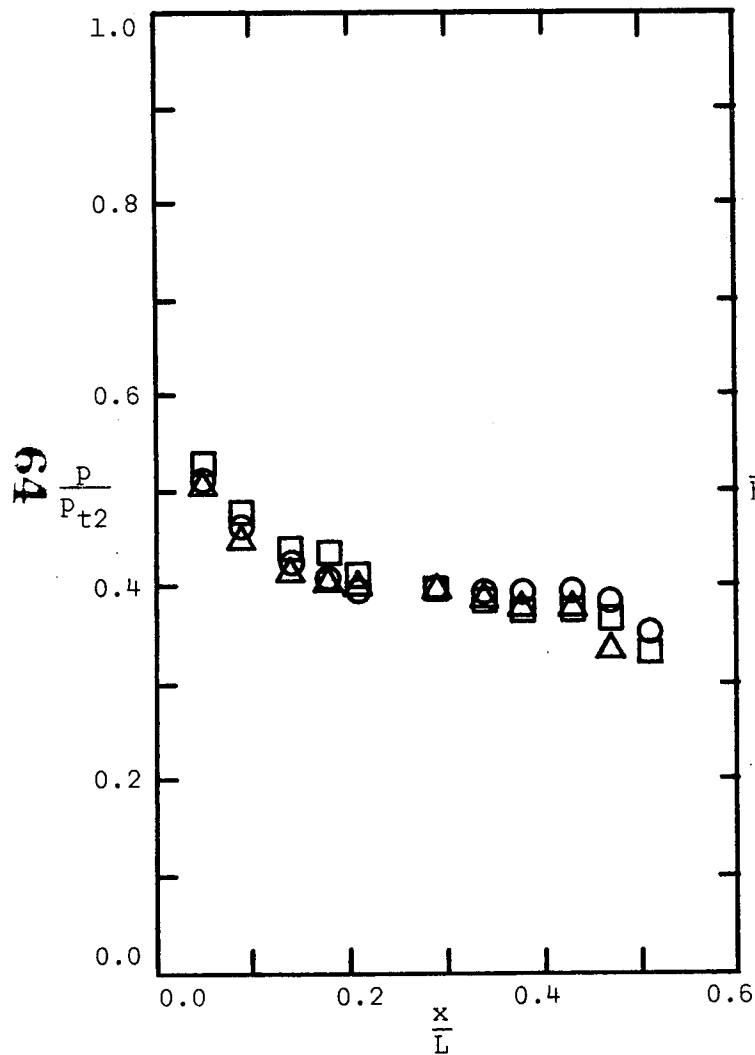
(a) Surface-pressure from UT SWT
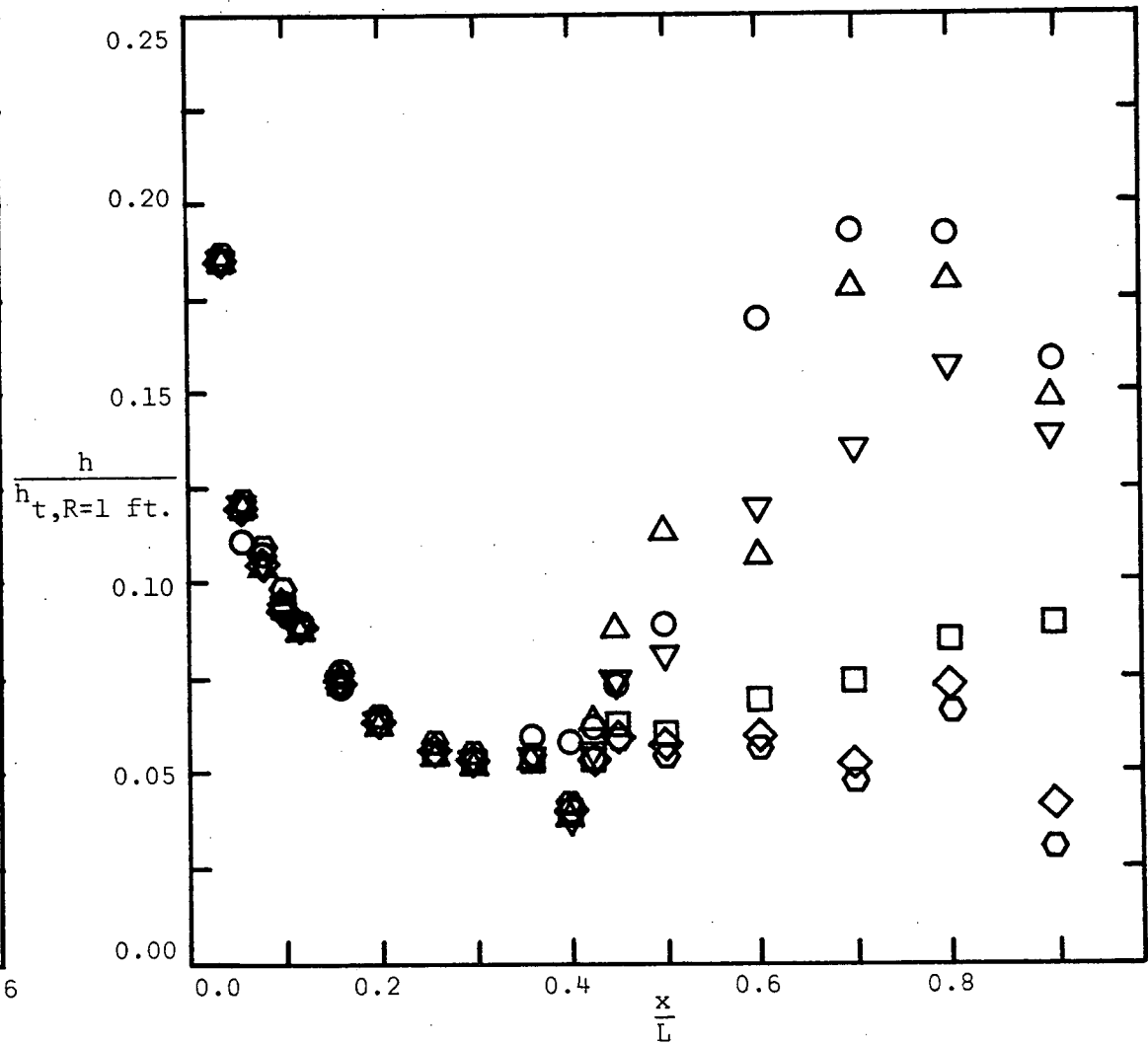
(b) Heat-transfer from AEDC Tunnel B

Figure 14. – Data from the windward pitch-plane of the UTN2 at a nominal alpha of 30°.

64
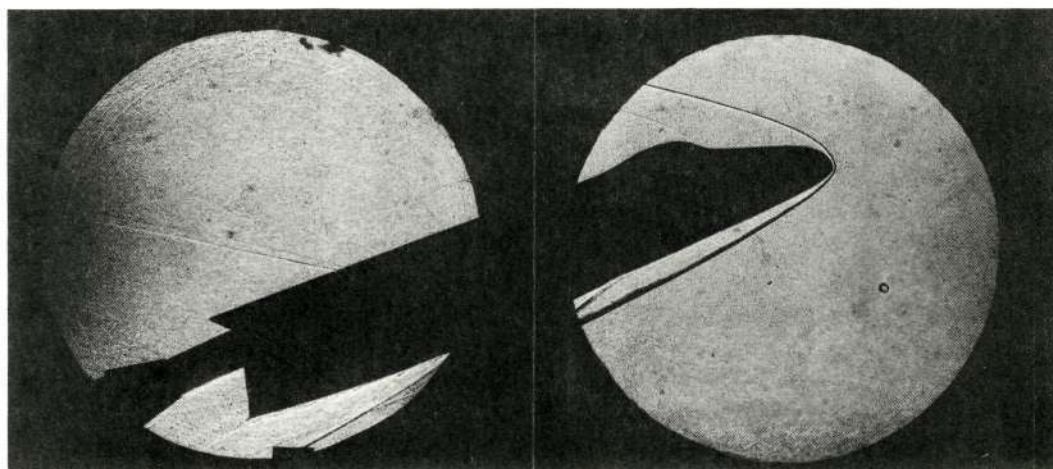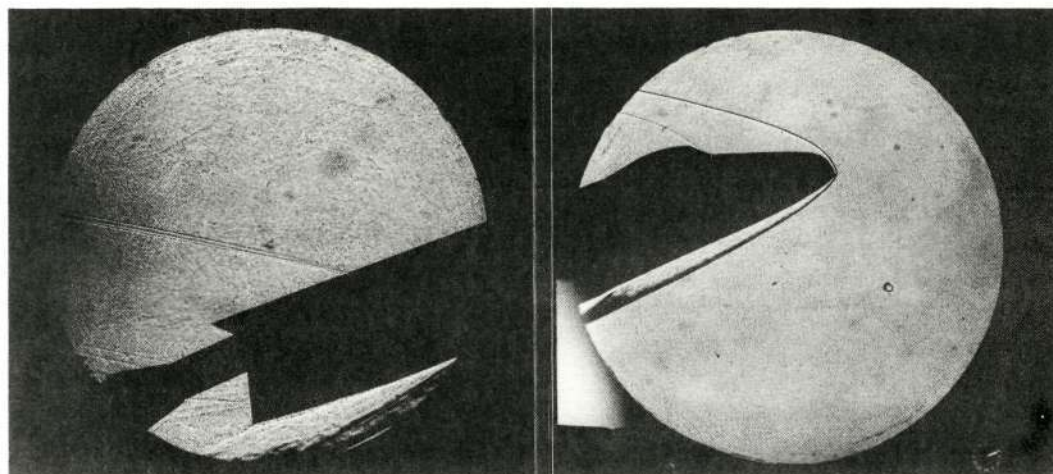
(a) UTN2

(b) UTN7

Figure 15.- Pitch-plane shadowgraph for an alpha of 20°.
$M_\infty = 8.0$, $Re_{\infty,L} = 7.8 \times 10^6$.

65
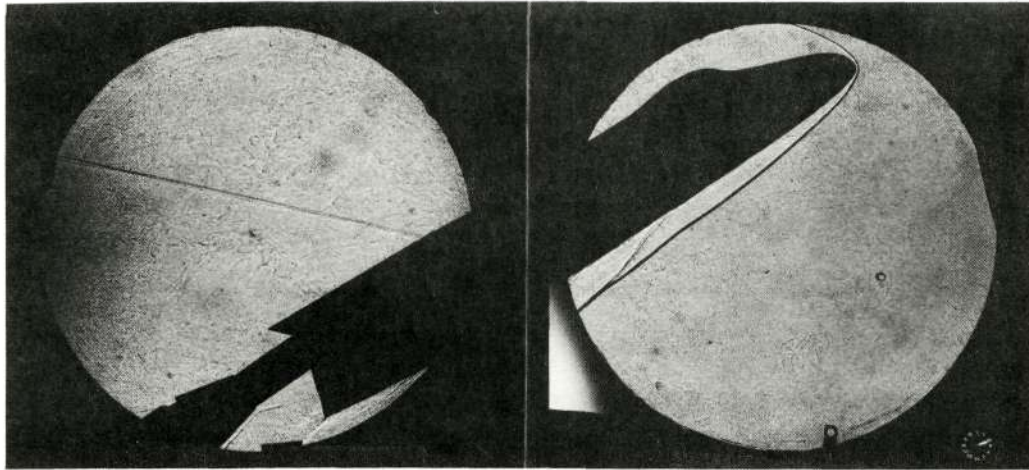
(a) UTN2
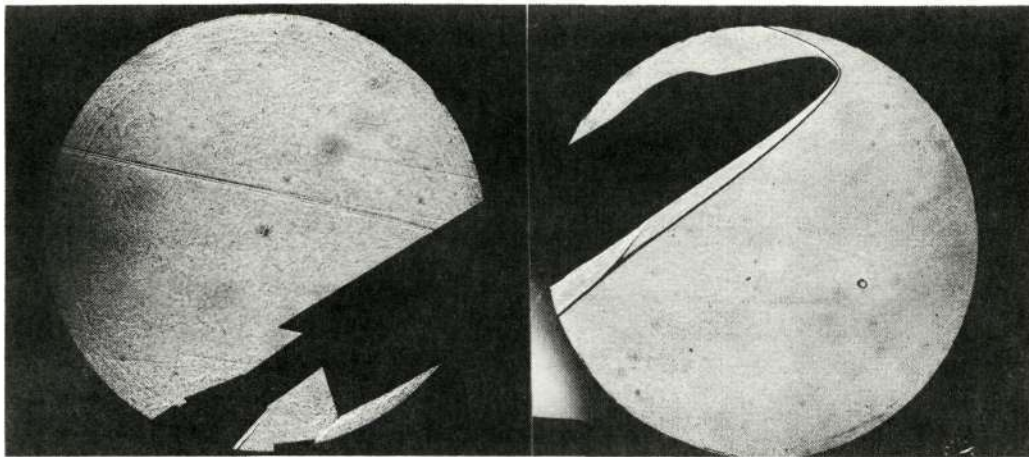
(b) UTN7

Figure 16.- Pitch-plane shadowgraphs for an alpha of 30°.
$M_{\infty} = 8.0$, $Re_{\infty,L} = 7.8 \times 10^{6}$.

66
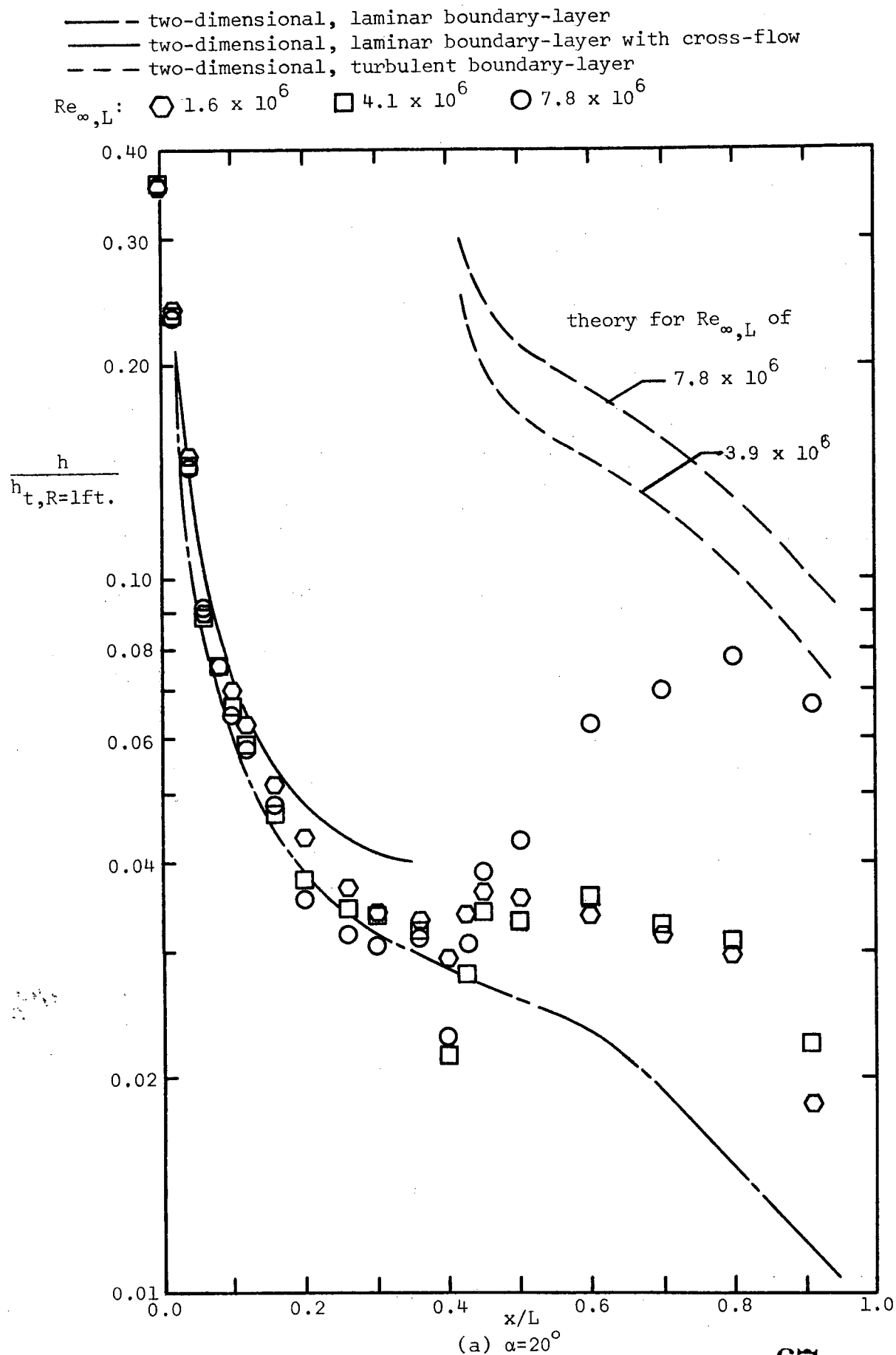
Figure 17.-Heat-transfer distribution for the windward pitch-plane of the UTN2.

(b) α=30°

68

Figure 17.-Continued.

Figure 17.-Continued.

69

two-dimensional, laminar boundary-layer
two-dimensional, laminar boundary-layer with cross-flow
two-dimensional, turbulent boundary-layer

$Re_{\infty,L}$: ⬡ 1.6×10^6 ⬜ 4.1×10^6 ◯ 7.8×10^6

theory for $Re_{\infty,L}$ of
7.8 × 10^6
3.9 × 10^6

$\dfrac{h}{h_{t,R=1ft.}}$

x/L_o

(d) $\alpha = 50^{\circ}$

70
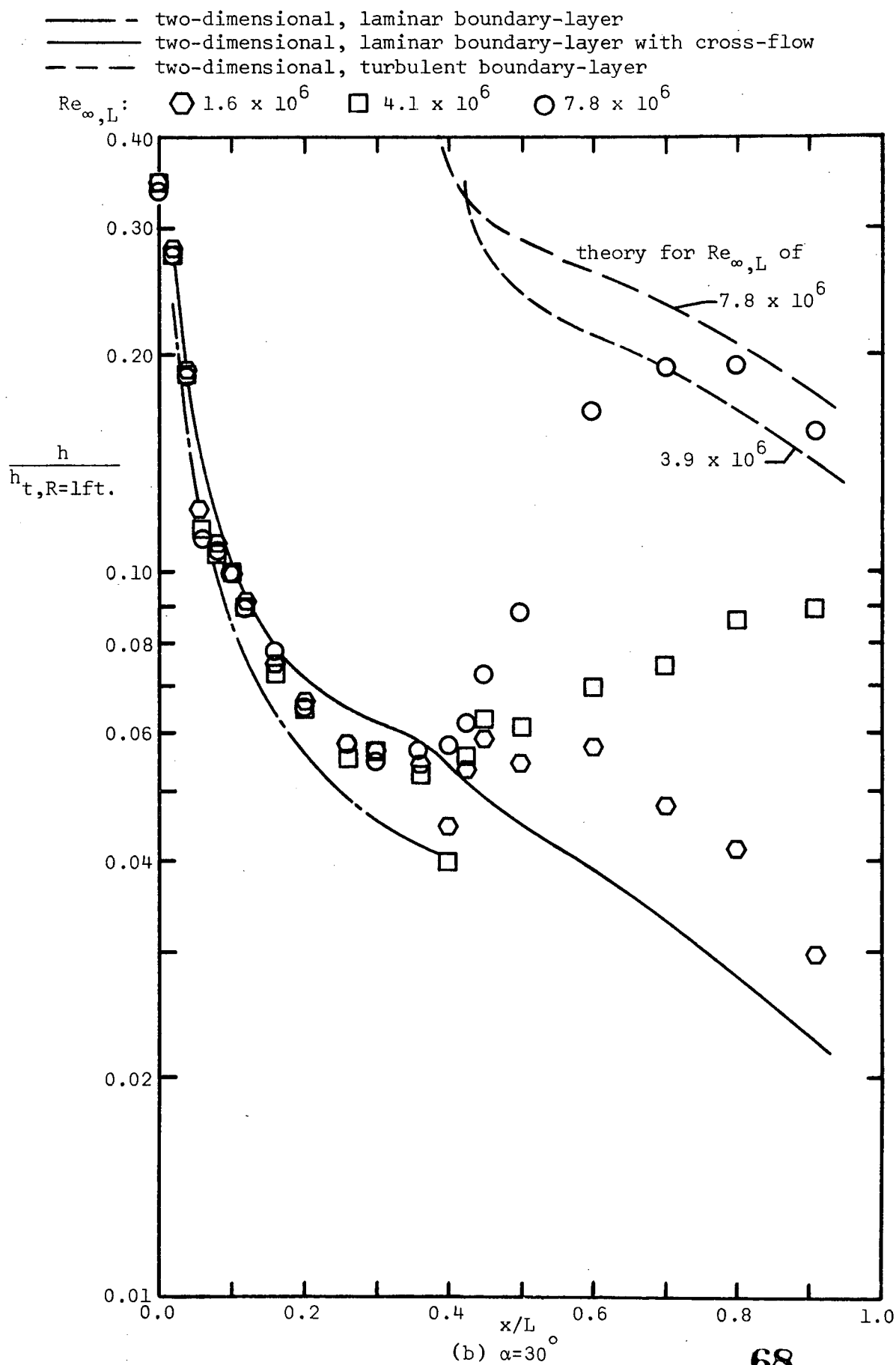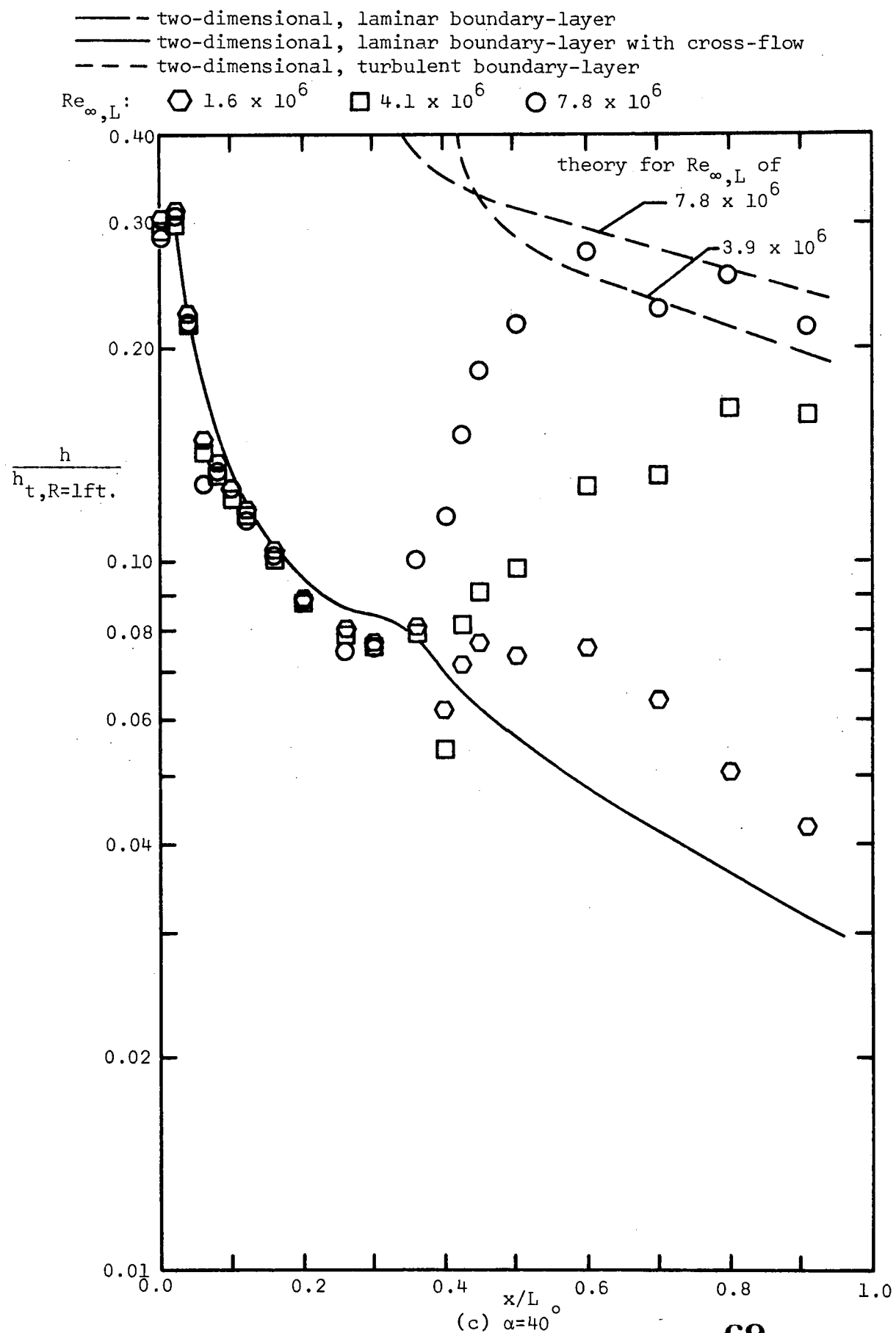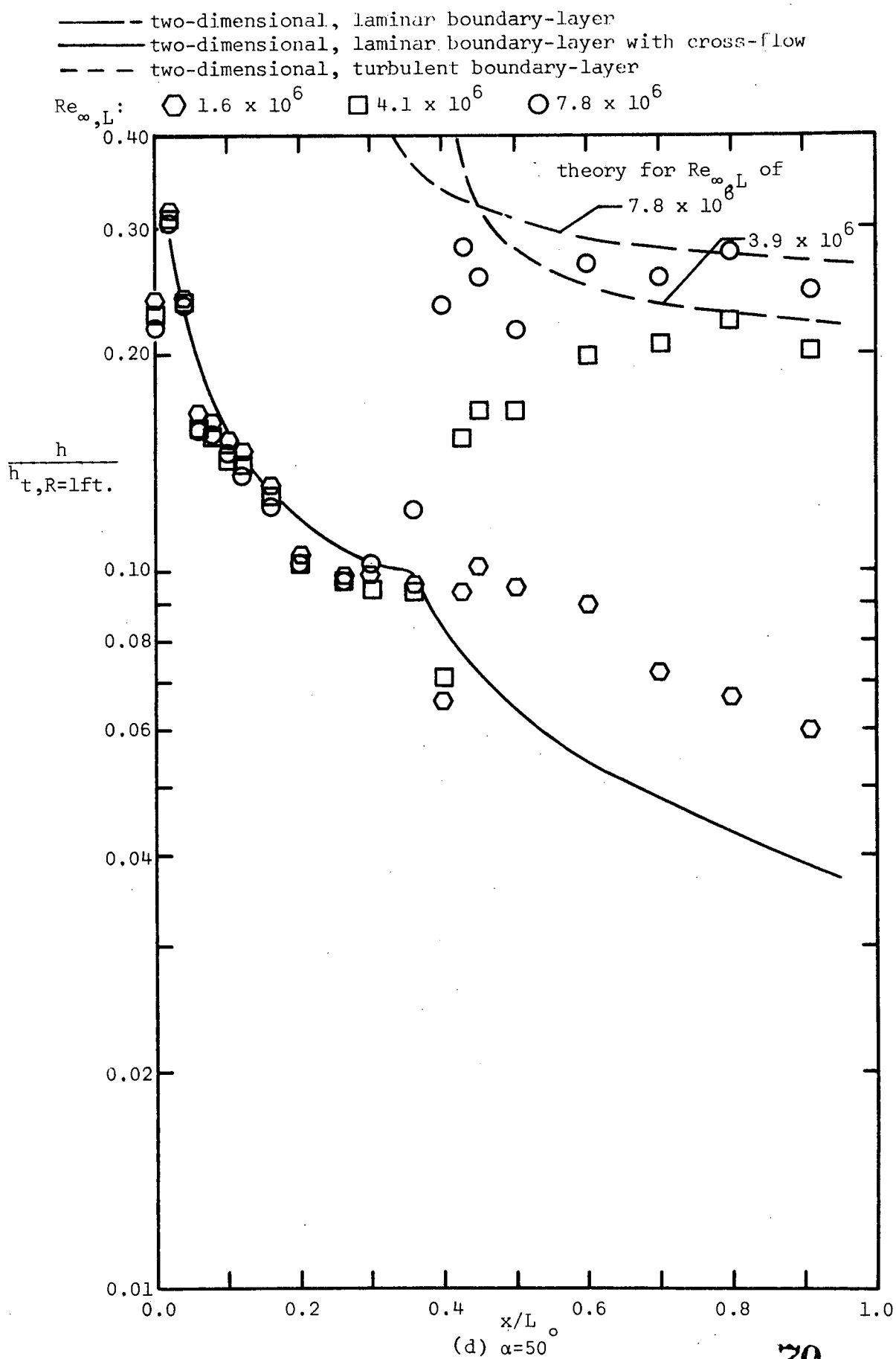
Figure 17.-Concluded.
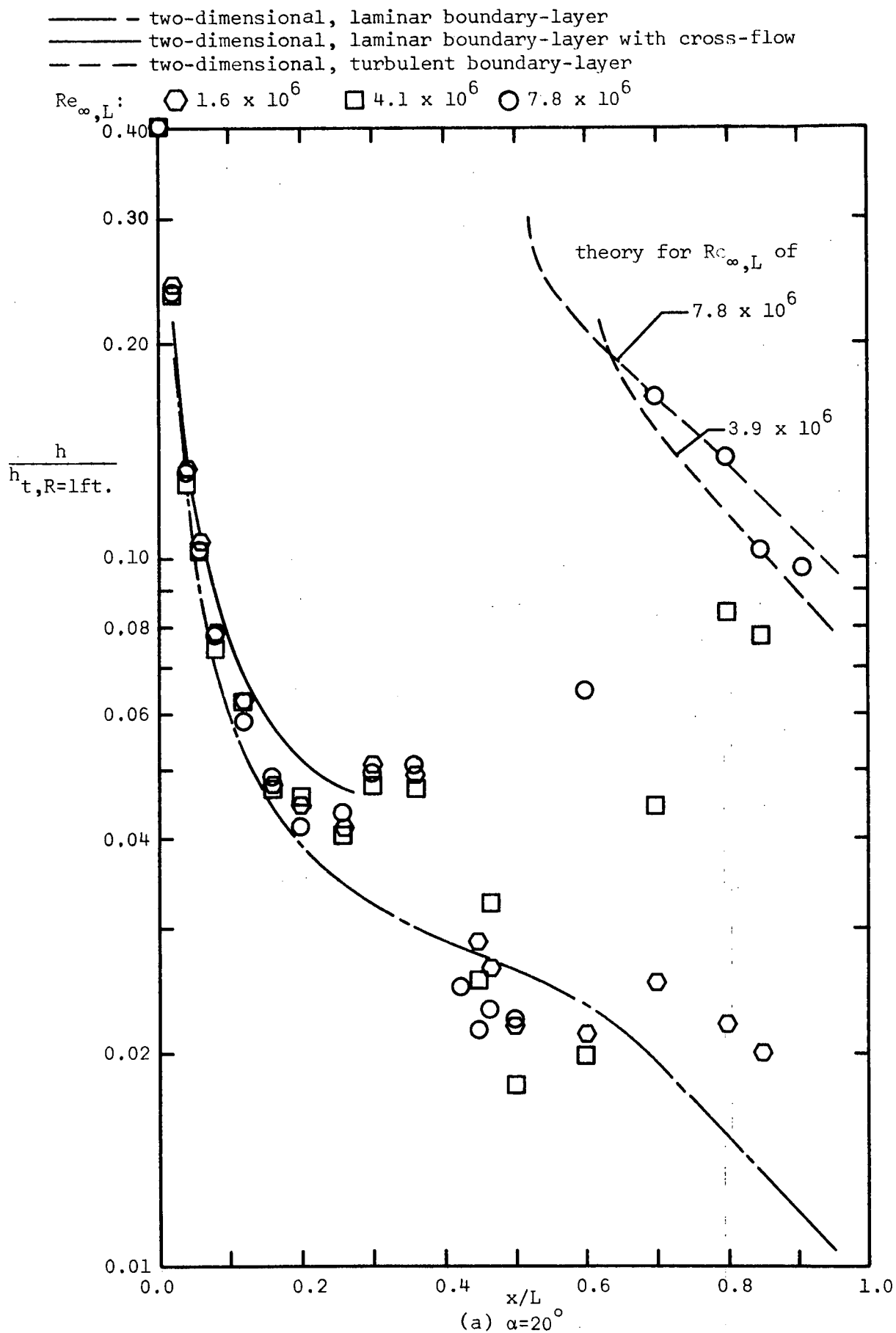
Figure 18. - Heat-transfer distribution for the windward pitch-plane of the UTN7.

71

Figure 18.-Continued.

72

two-dimensional, laminar boundary-layer
two-dimensional, laminar boundary-layer with cross-flow
two-dimensional, turbulent boundary-layer

$Re_{\infty,L}$: ⬡ 1.6×10^6 □ 4.1×10^6 ◯ 7.8×10^6

theory for $Re_{\infty,L}$ of
7.8×10^6
3.9×10^6

$\dfrac{h}{h_{t,R=1ft.}}$

(c) $\alpha = 40°$

Figure 18.-Continued.

73

(d) $\alpha = 50^\circ$
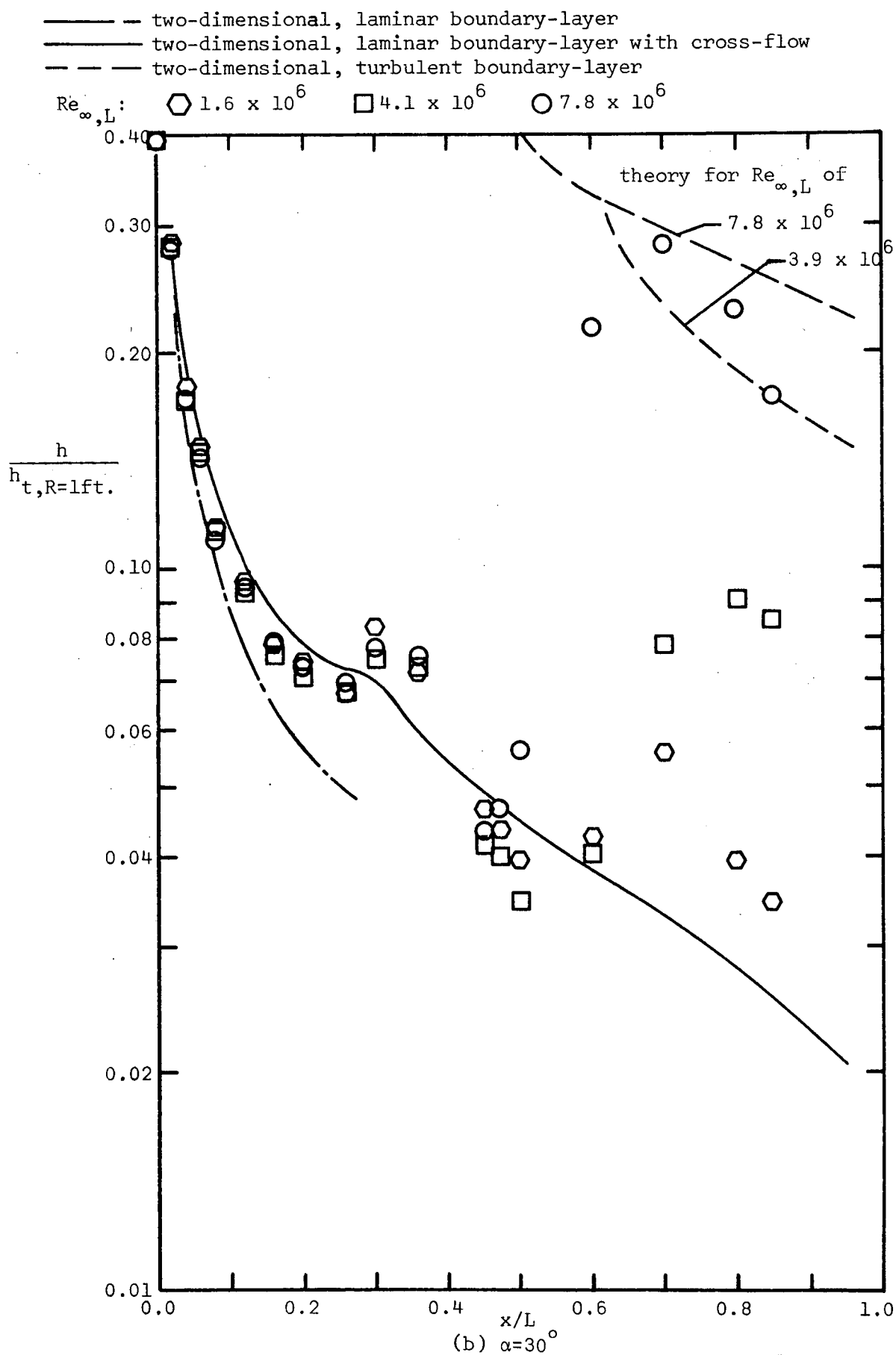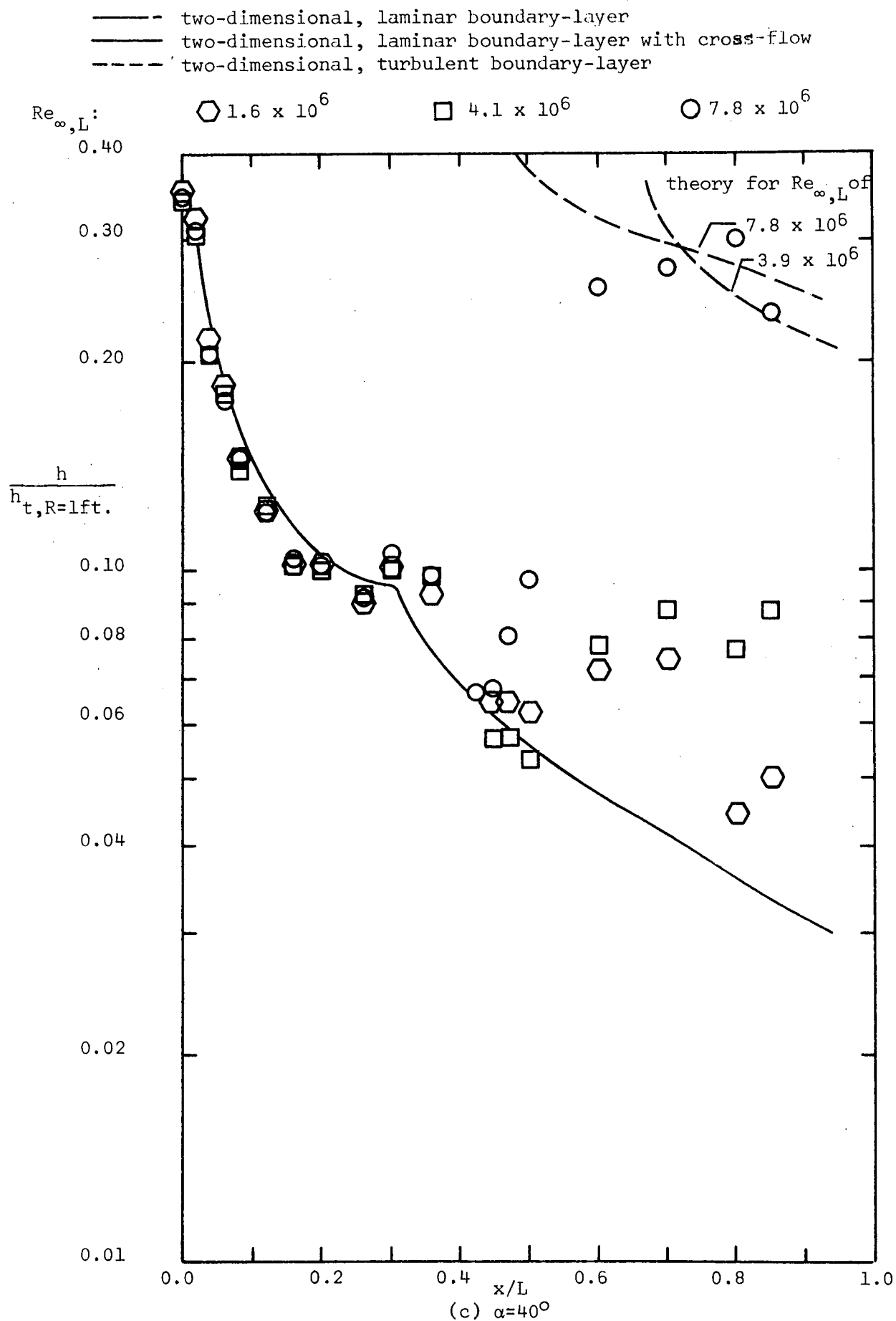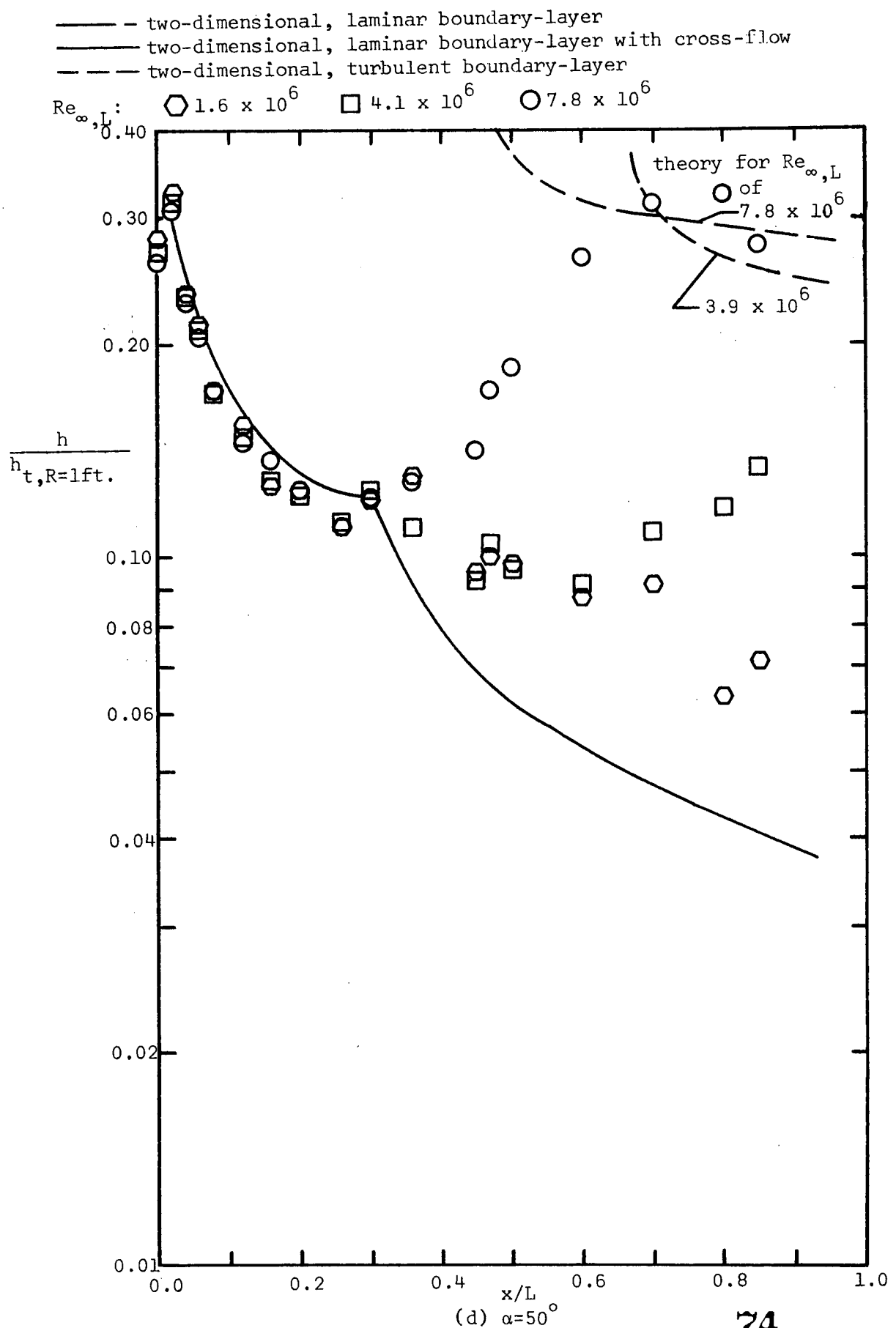
Figure 18.-Concluded.

74
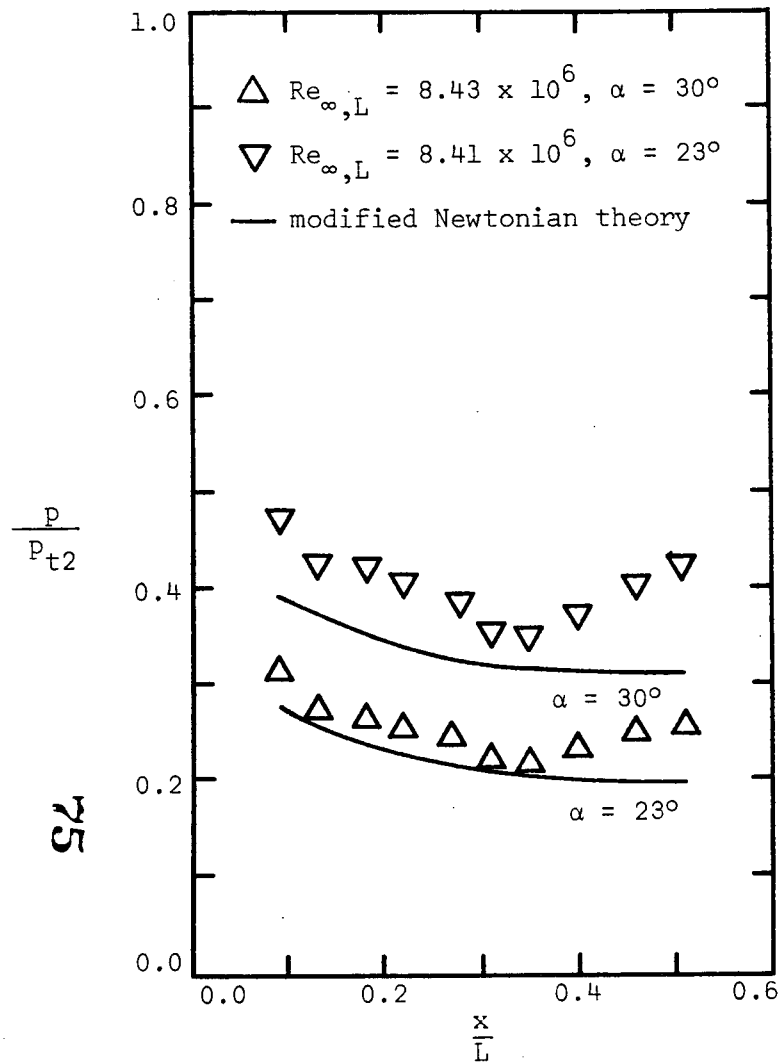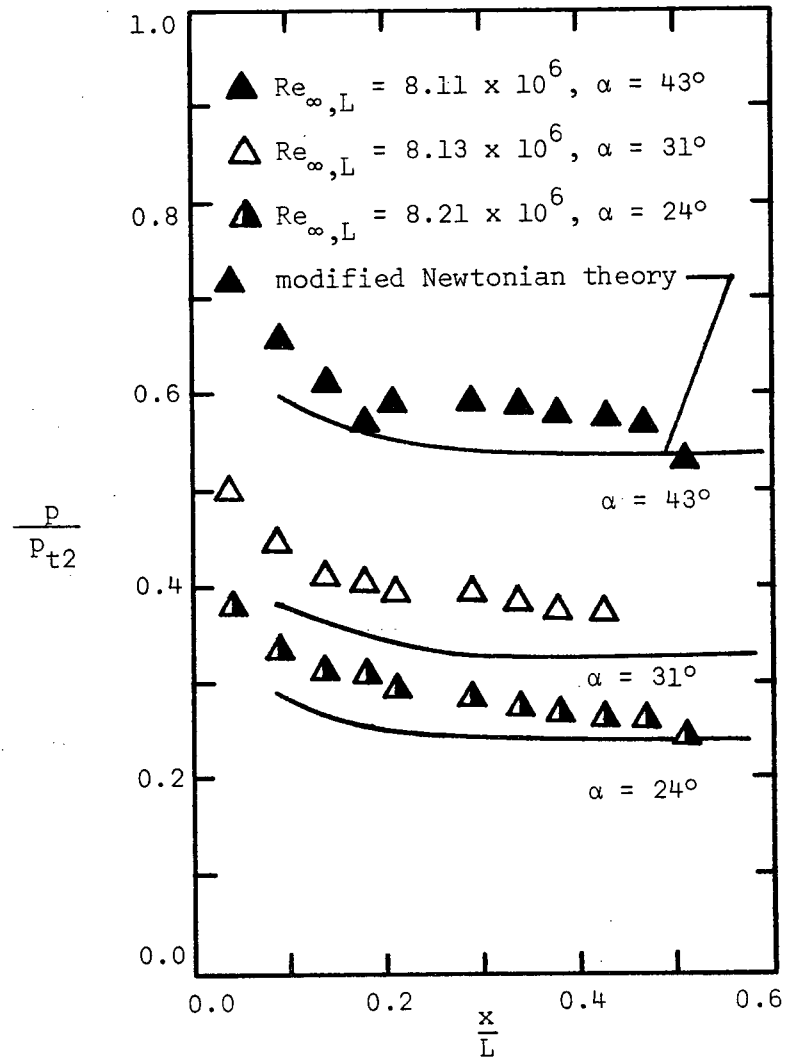
(a) UTN7   (b) UTN2

Figure 19. - Correlation of pressure distribution from the windward pitch-
plane as a function of alpha.

○ UTN2   □ UTN7

Open symbol, $Re_{\infty,L} = 4.1 \times 10^6$

Filled symbol, $Re_{\infty,L} = 7.8 \times 10^6$

▦ Data band, as presented in Ref. 22

── NAR criterion, as presented in Ref. 22
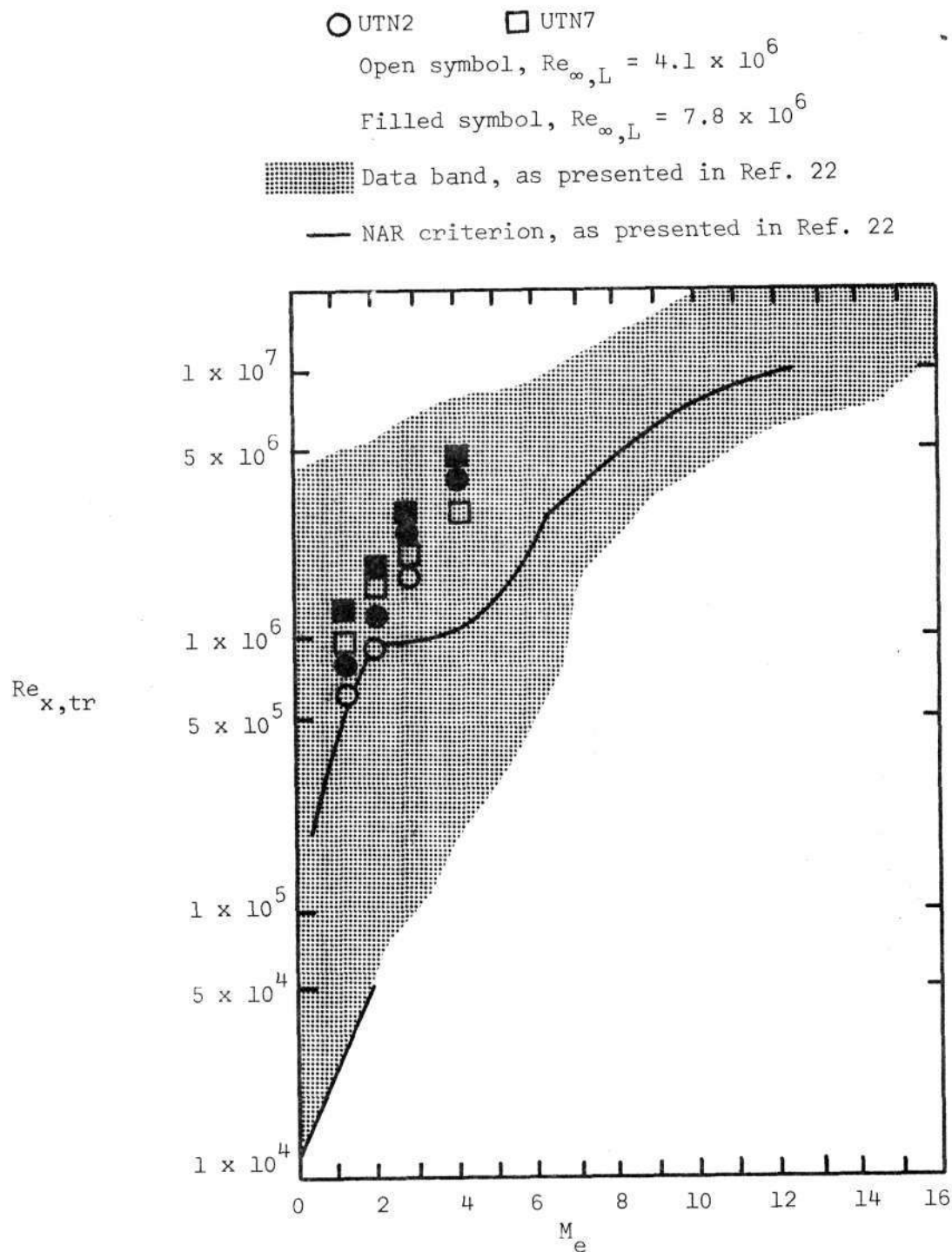
Figure 20. - The local Reynolds number at transition as a function of the local Mach number.

76
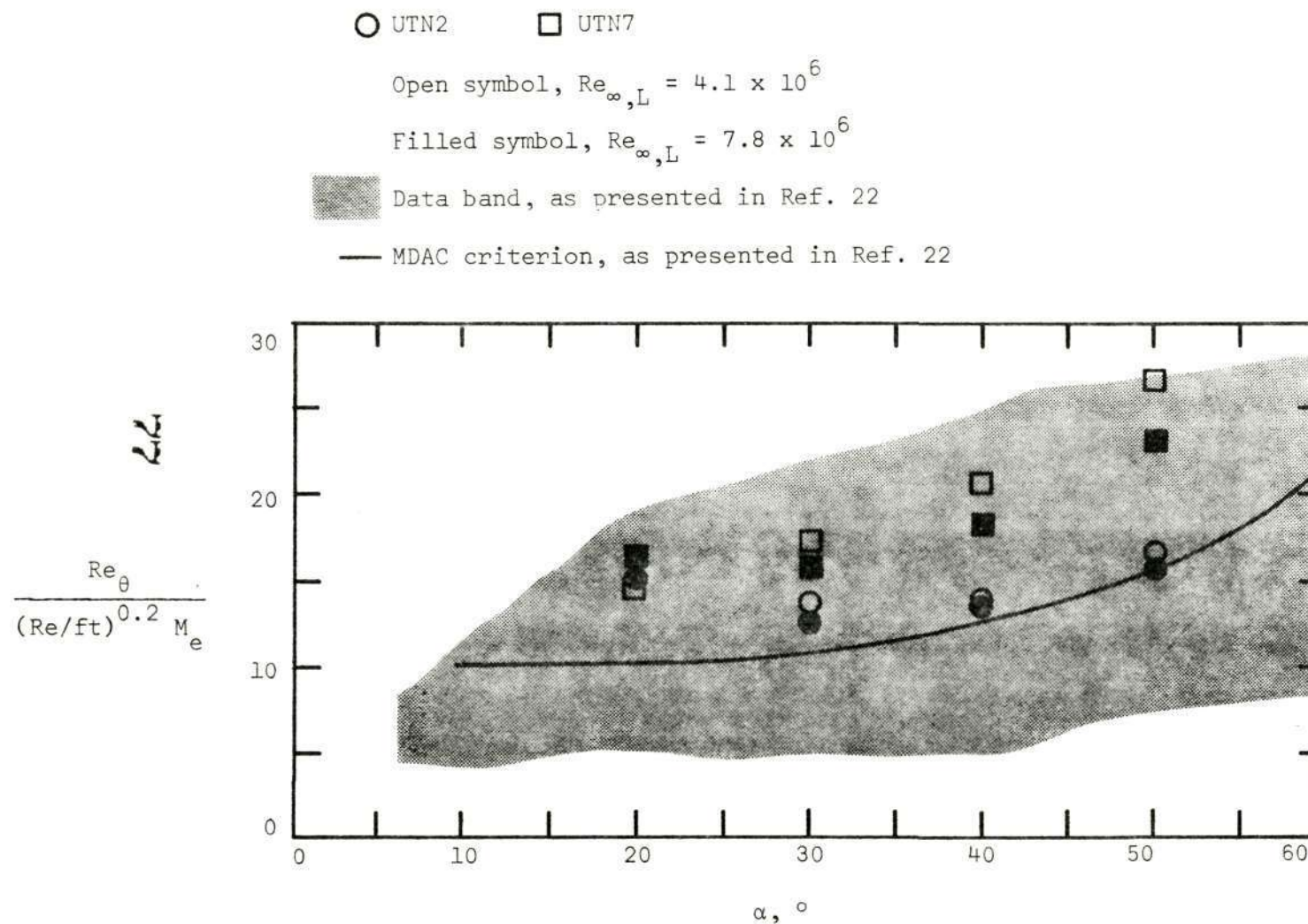
Figure 21. - Current transition results presented in terms of the McDonnell-Douglas correlation parameter.
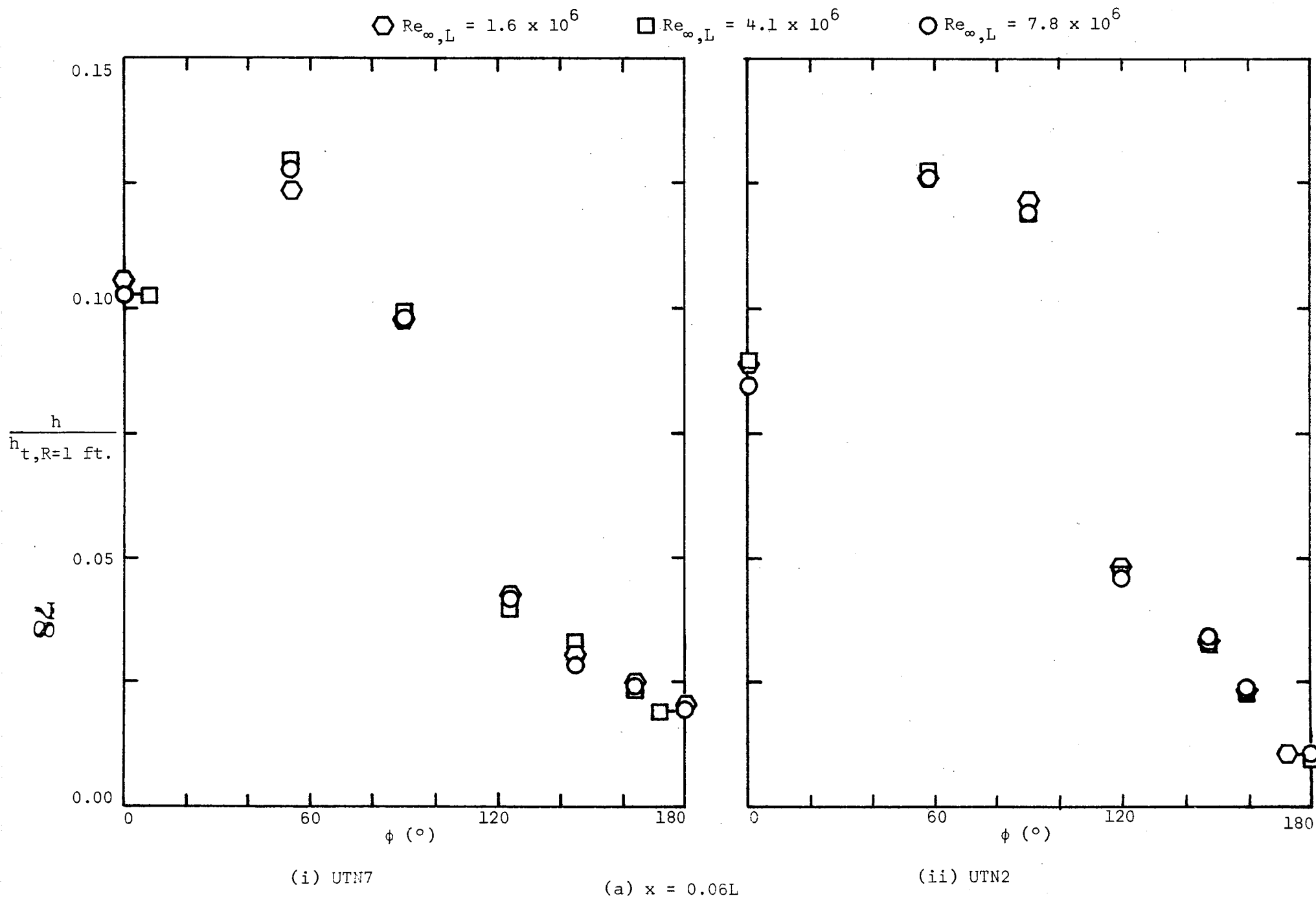
Figure 22. - Circumferential heat-transfer distributions for alpha of 20°.
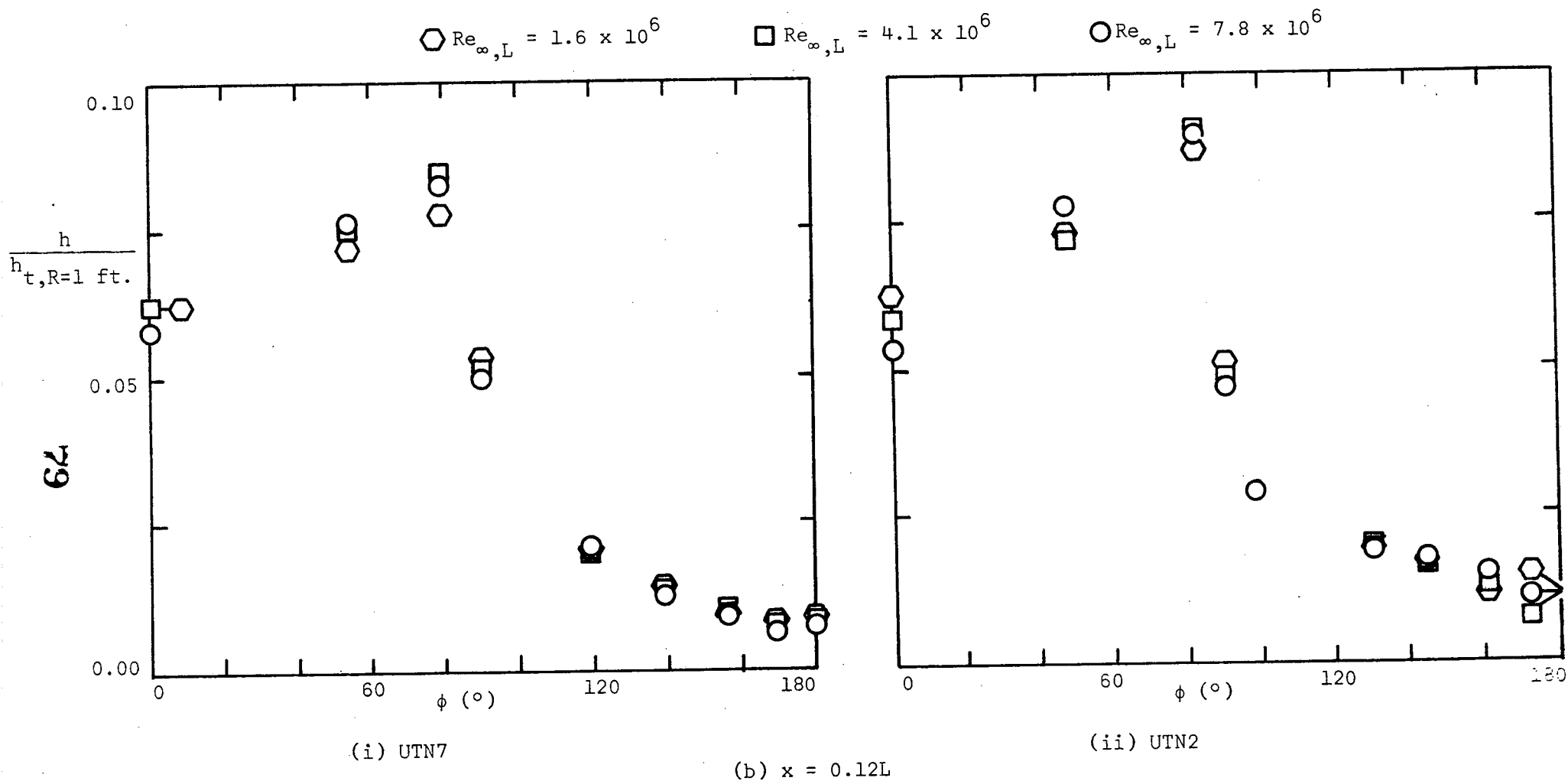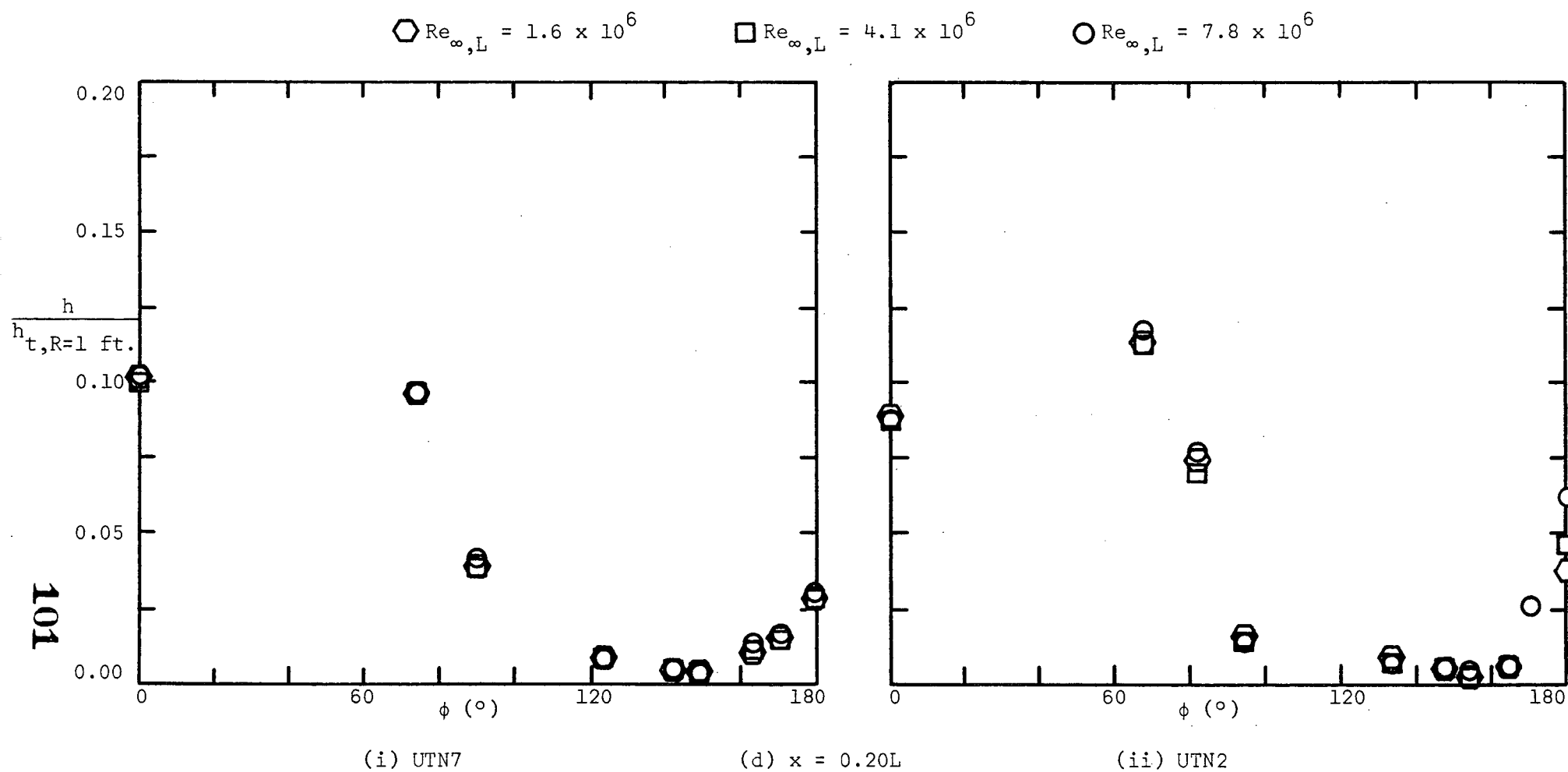
Figure 22. - Continued.
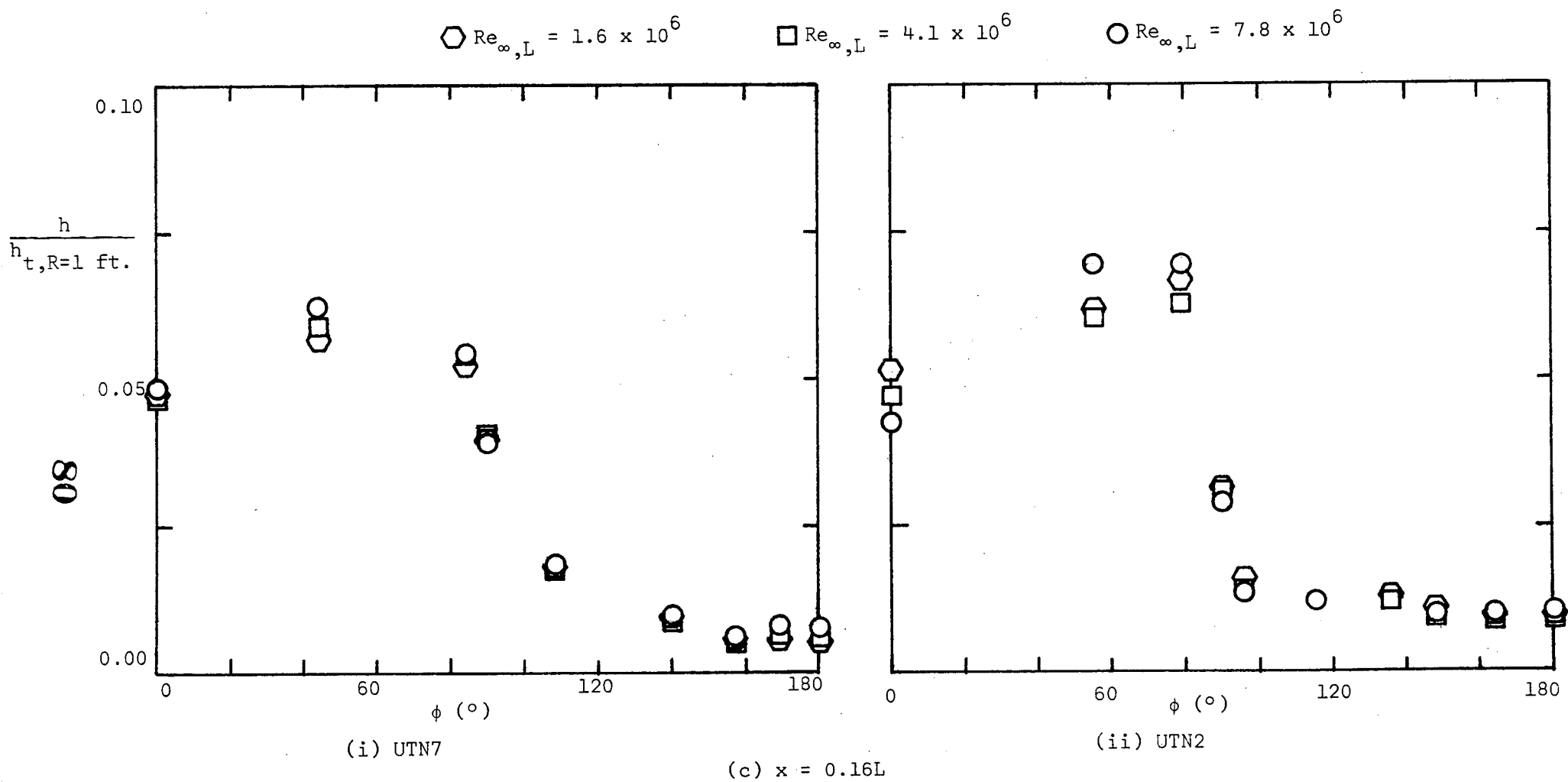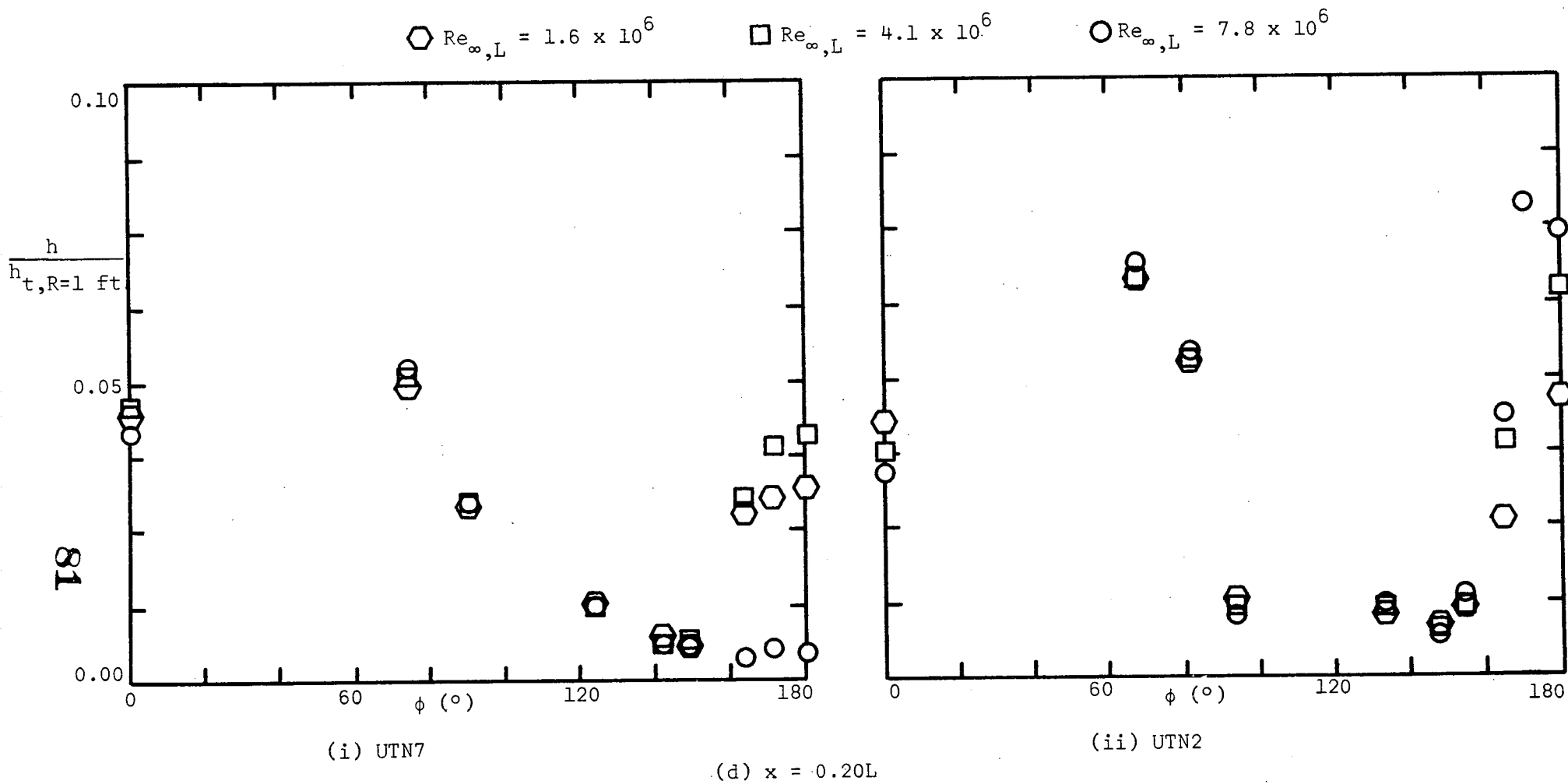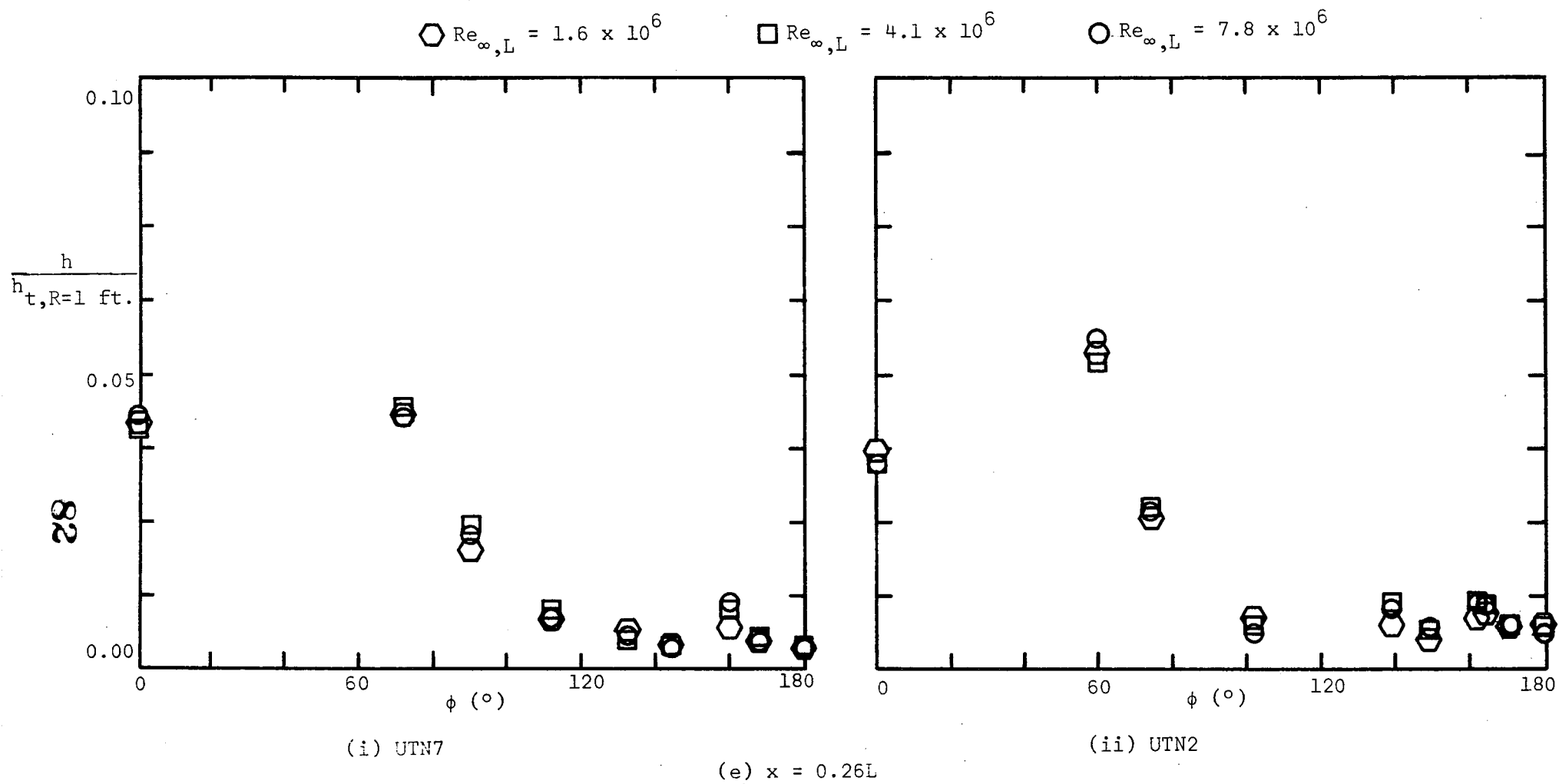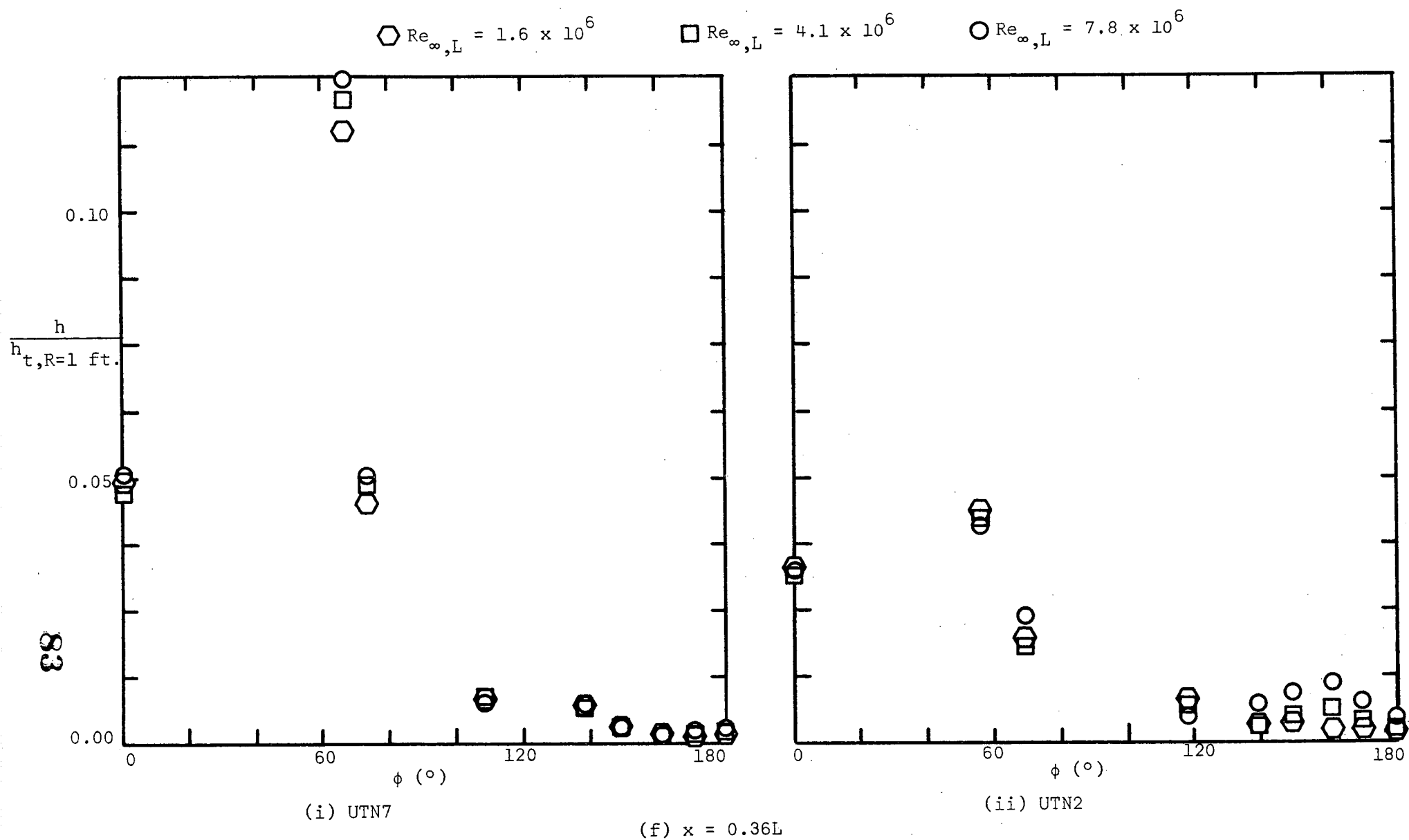
Figure 22. - Continued.

$$\hexagon \ Re_{\infty,L} = 1.6 \times 10^6 \qquad \square \ Re_{\infty,L} = 4.1 \times 10^6 \qquad \bigcirc \ Re_{\infty,L} = 7.8 \times 10^6$$

(i) UTN7

(ii) UTN2

(d) x = 0.20L

Figure 22. - Continued.
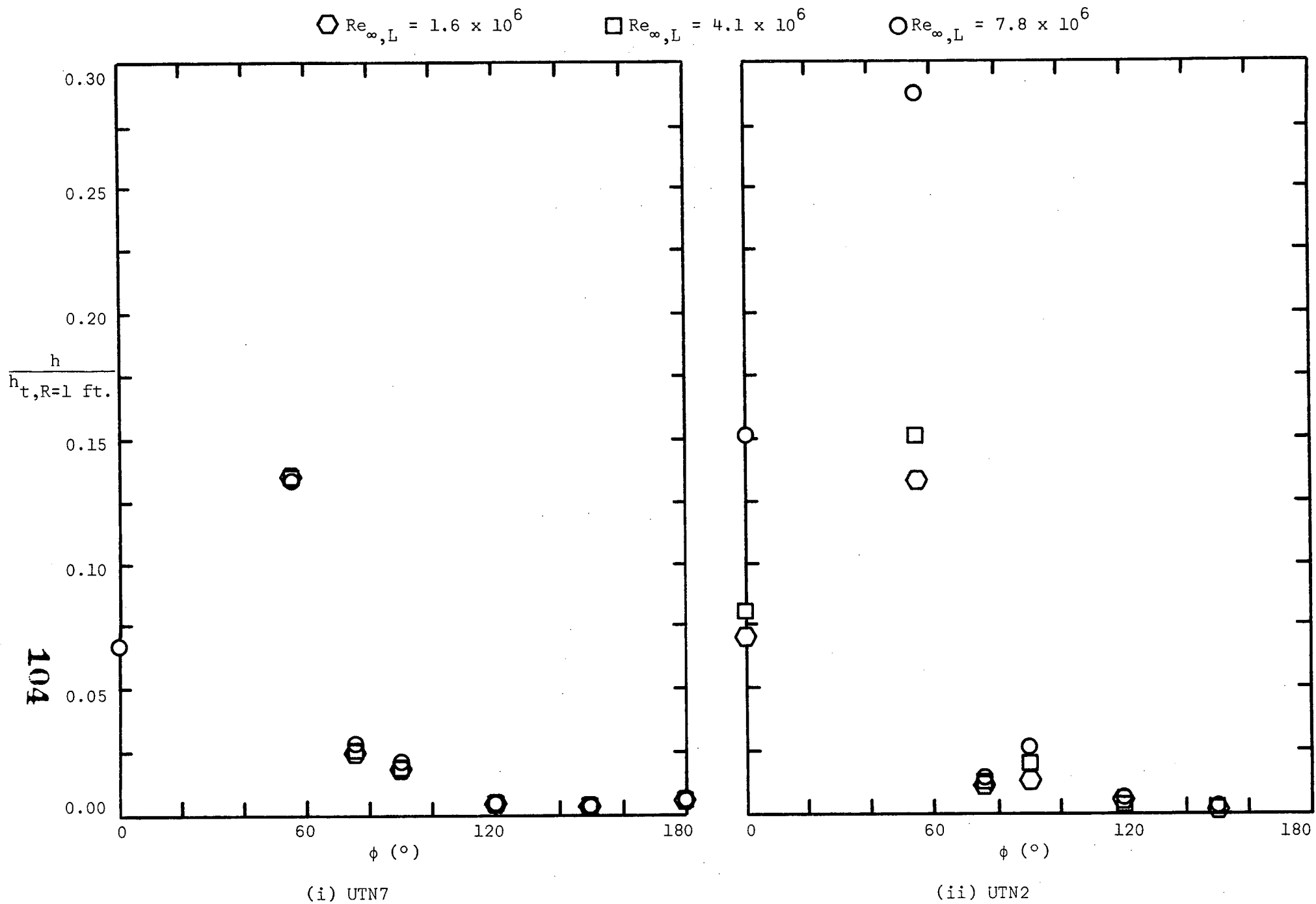
81

Figure 22. - Continued.

Figure 22. - Continued.

$\bigcirc$ Re$_{\infty,L}$ = 1.6 x 10^6 $\square$ Re$_{\infty,L}$ = 4.1 x 10^6 $\bigcirc$ Re$_{\infty,L}$ = 7.8 x 10^6

$\dfrac{h}{h_{t,R-1\ ft.}}$

0.10

0.05

0.00

ϕ (°)

(i) UTN7

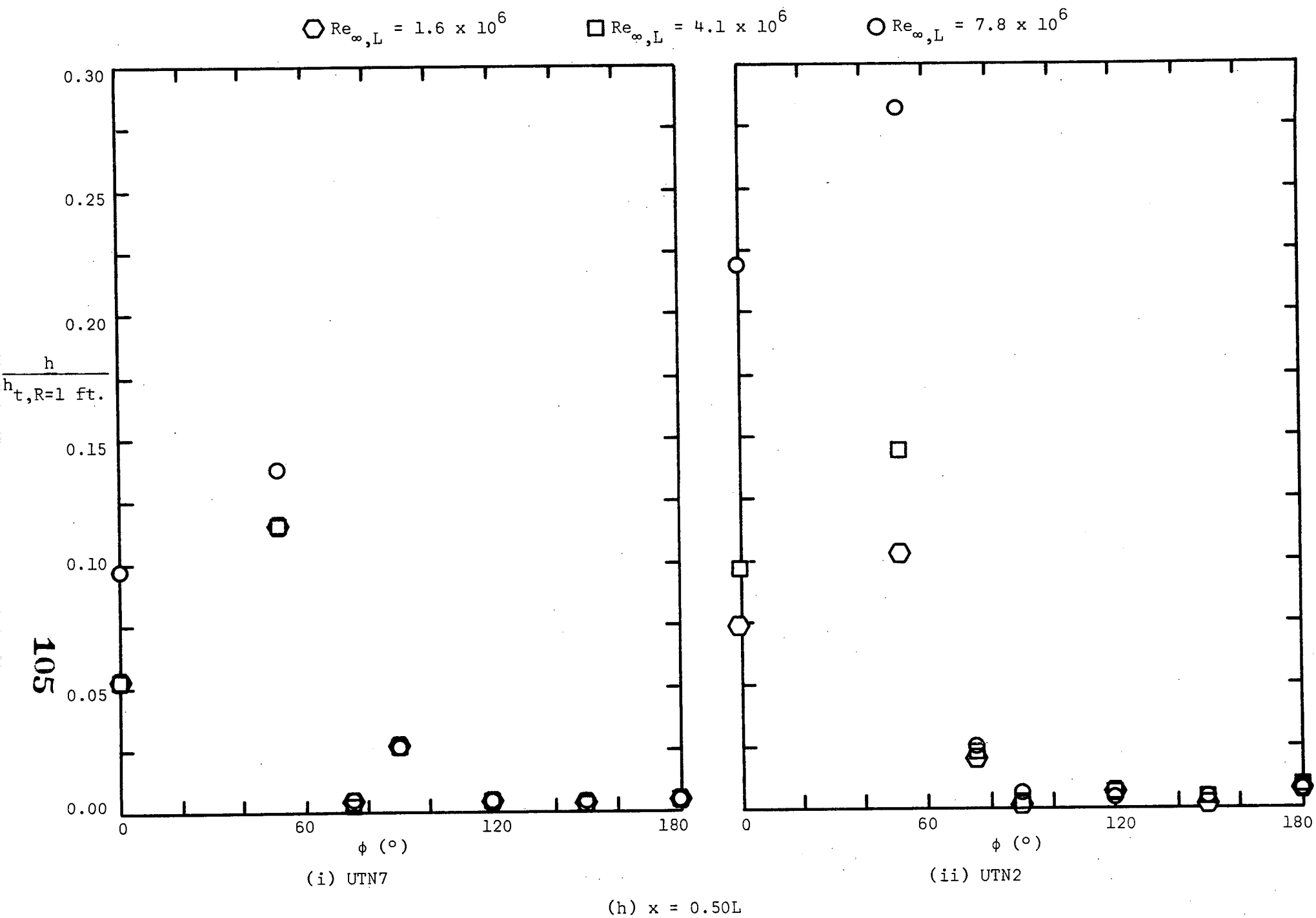(ii) UTN2

(g) x = 0.425L
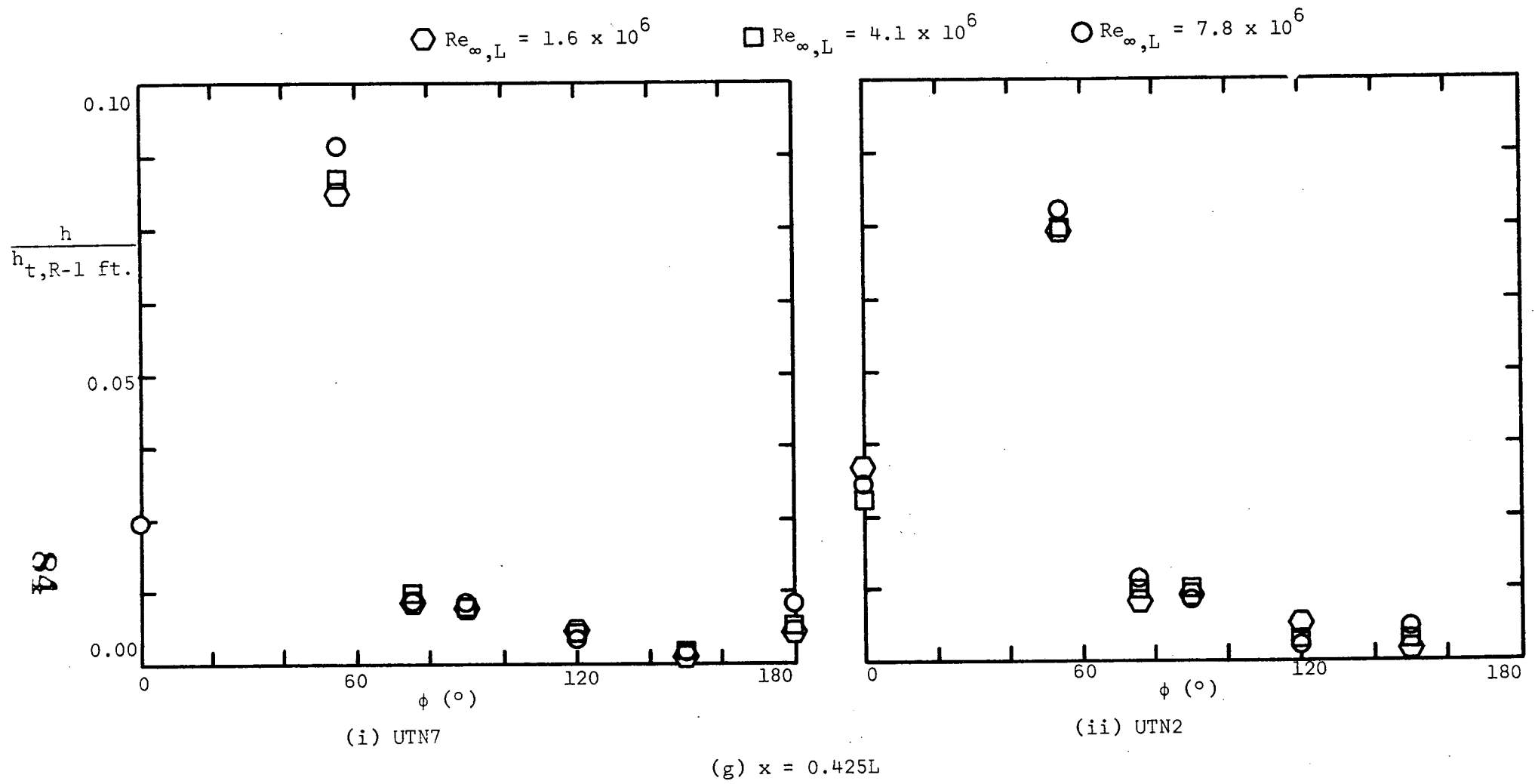
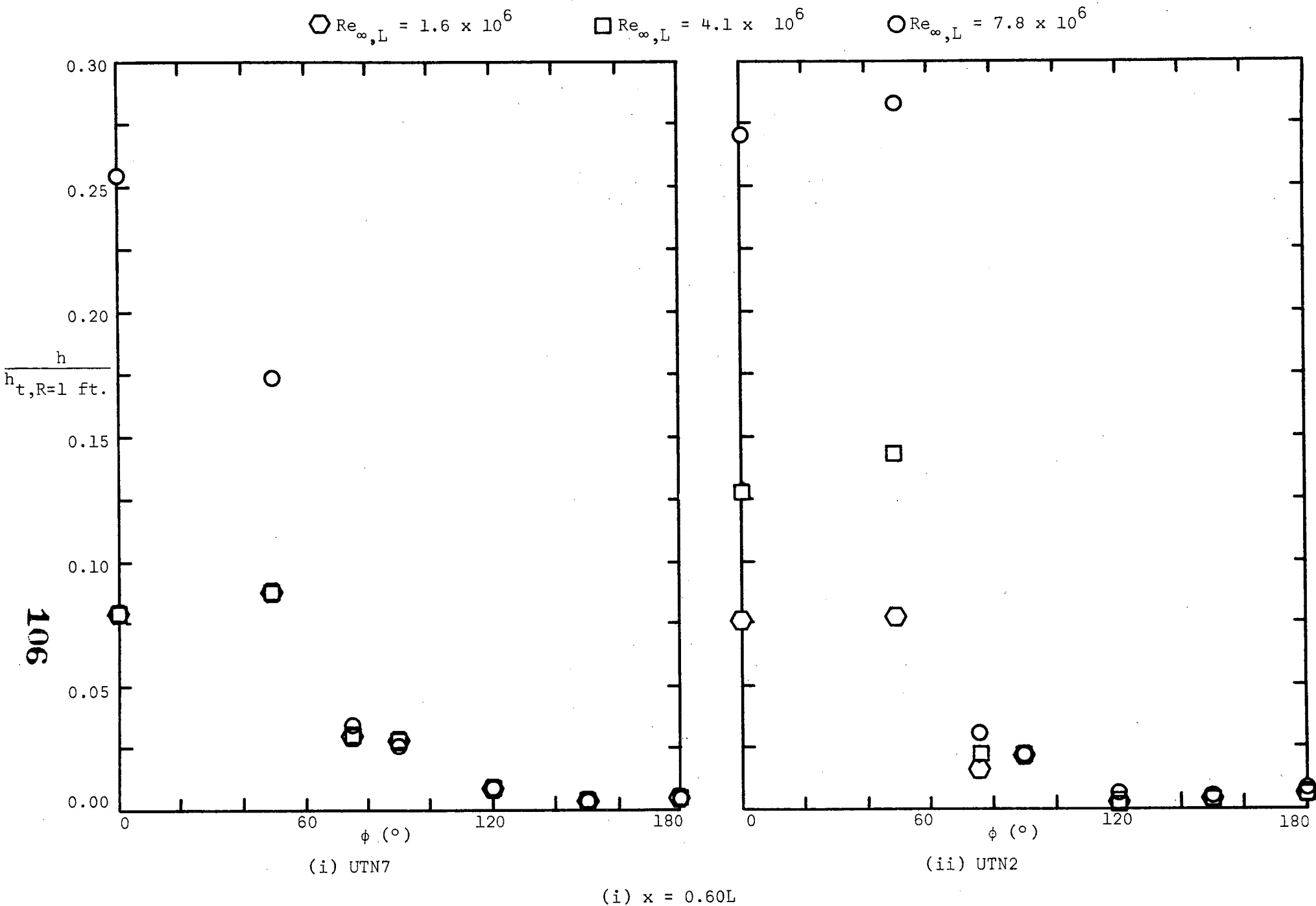Figure 22. - Continued.
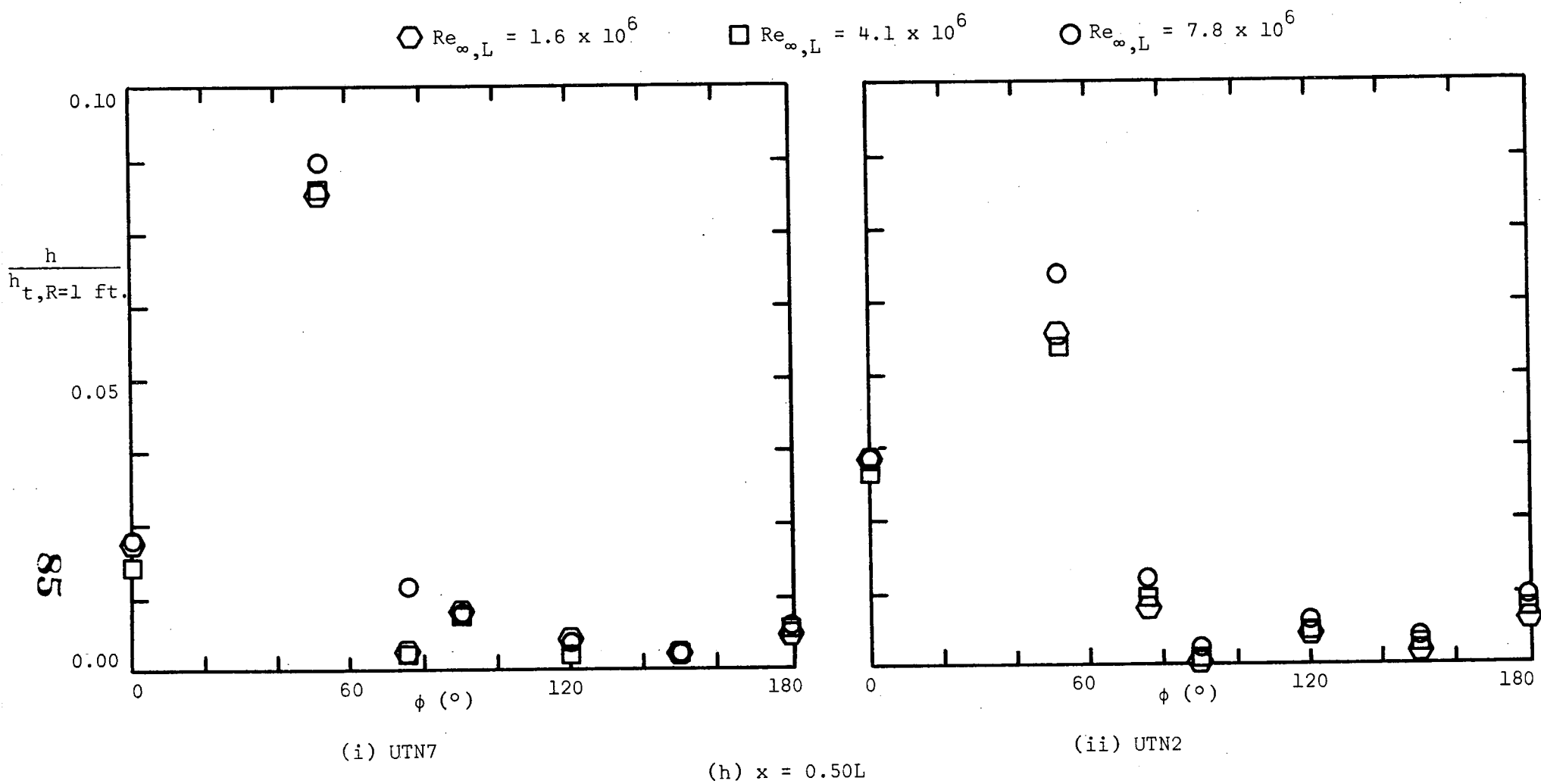
Figure 22. - Continued.
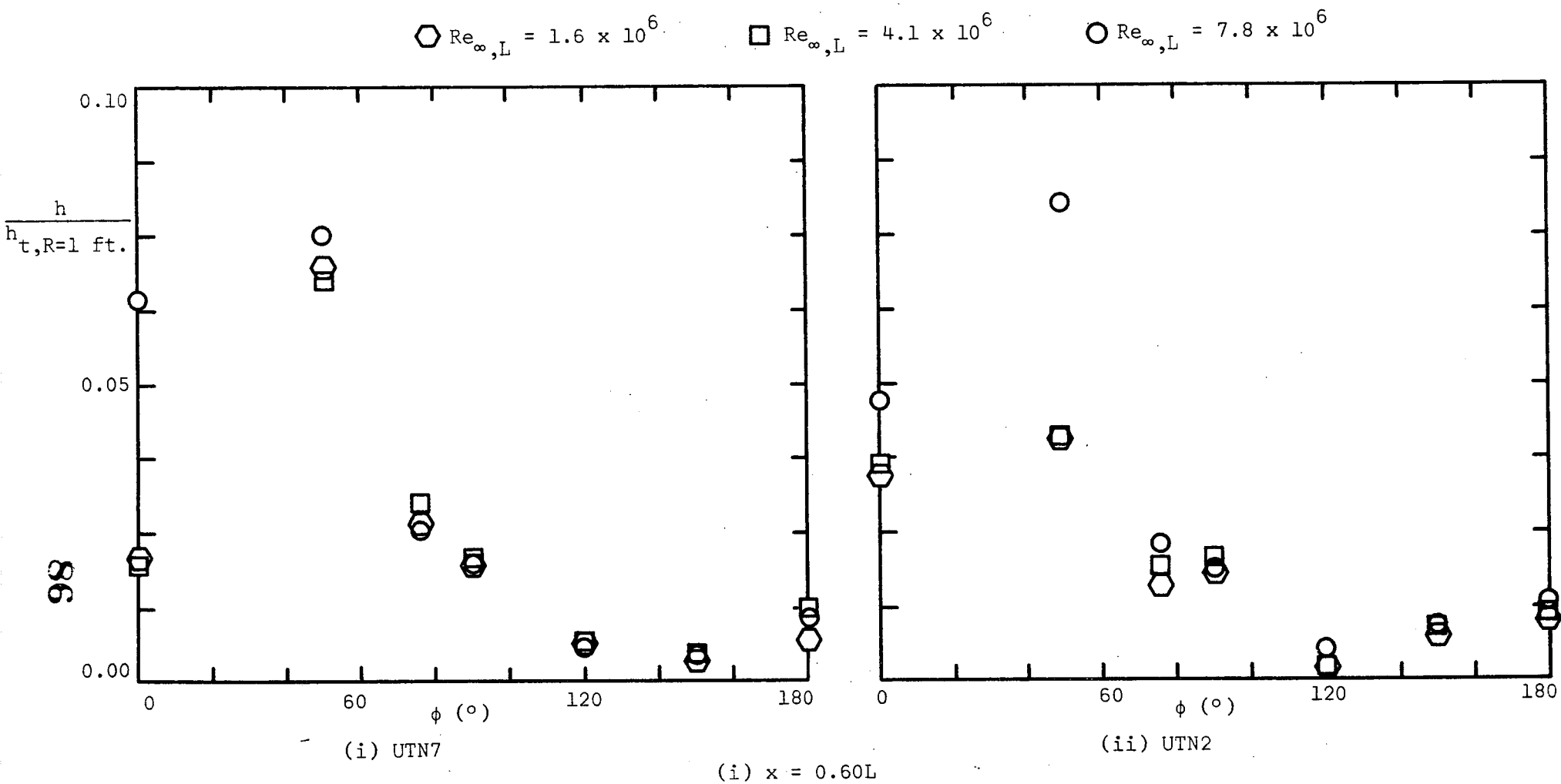
Figure 22. - Continued.
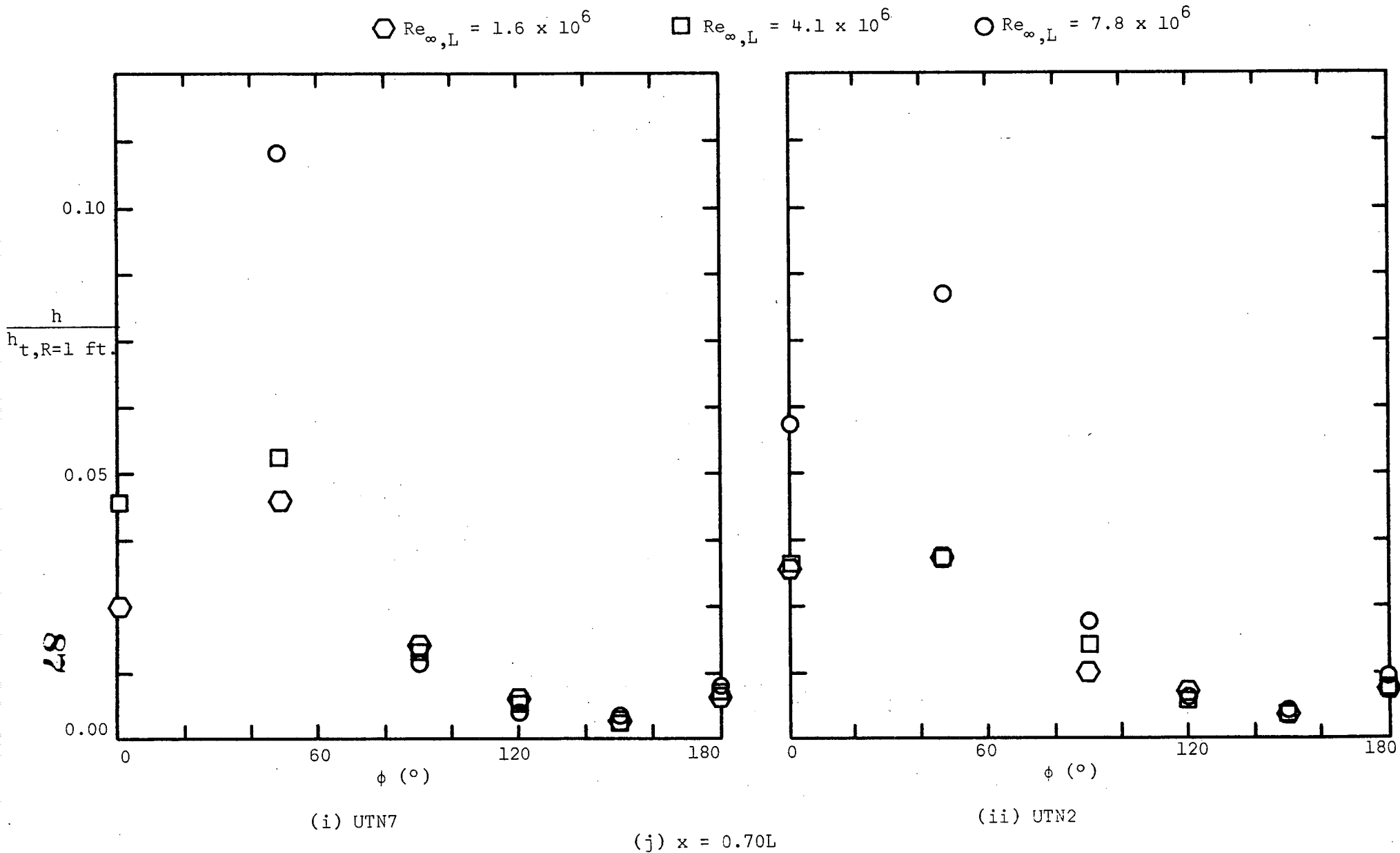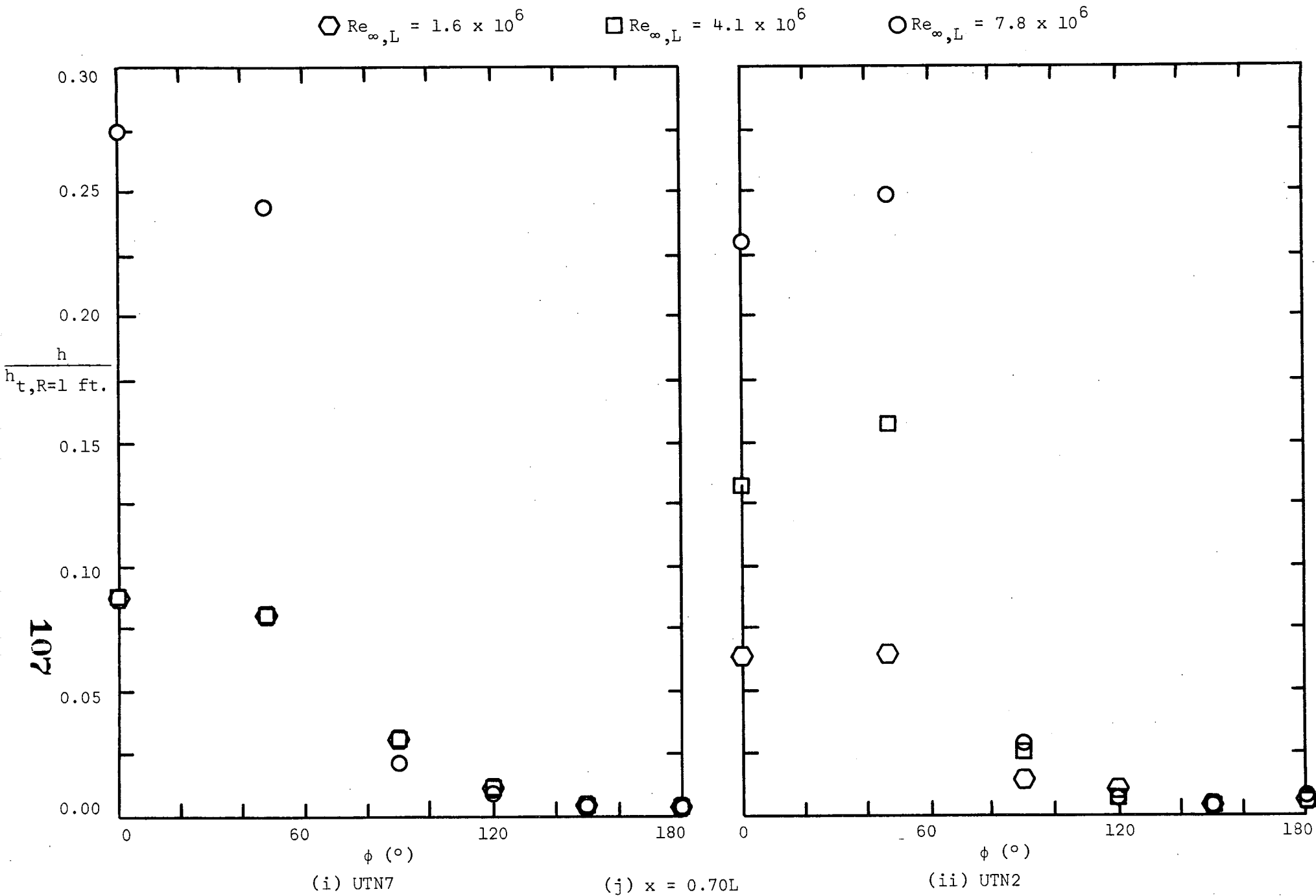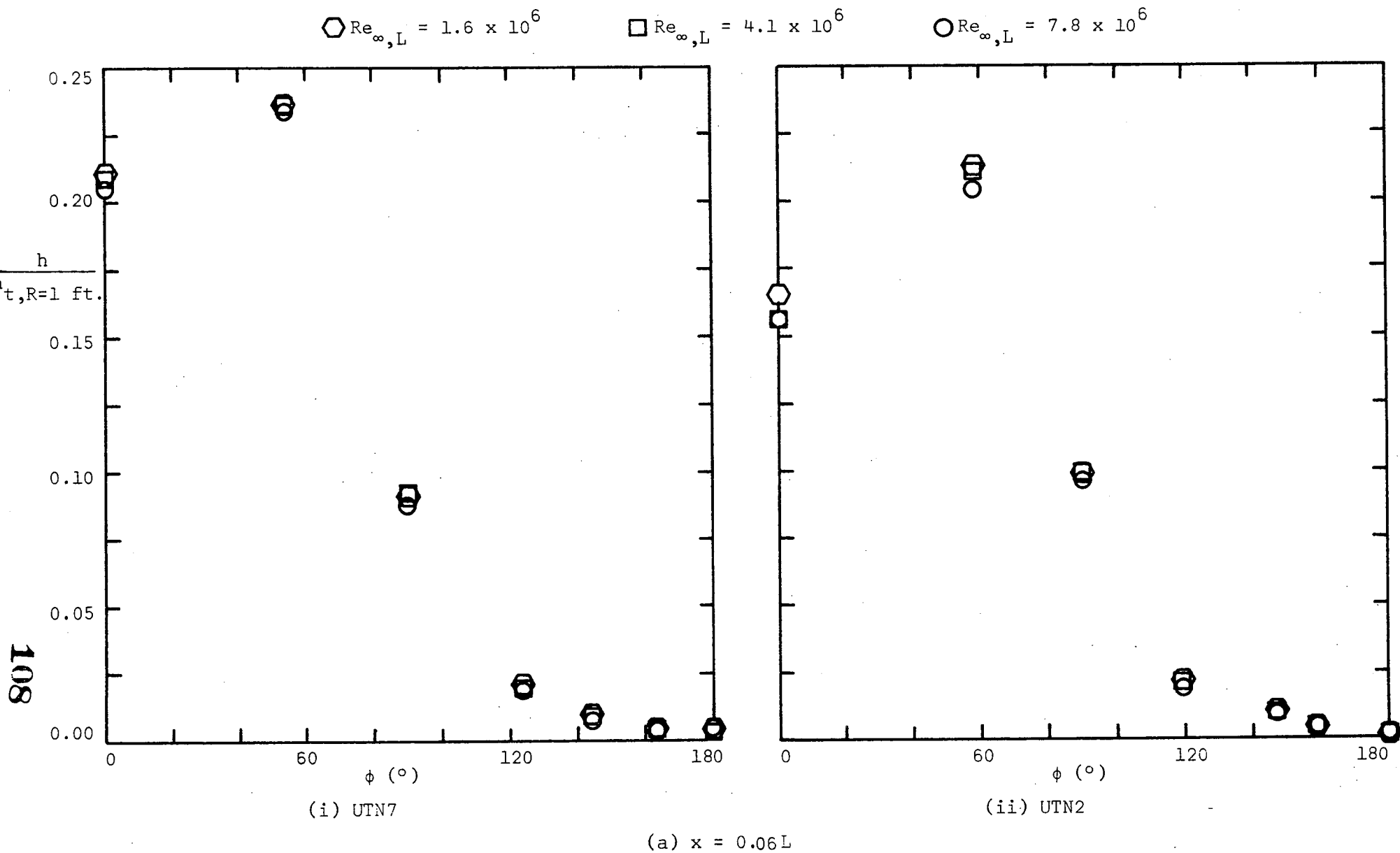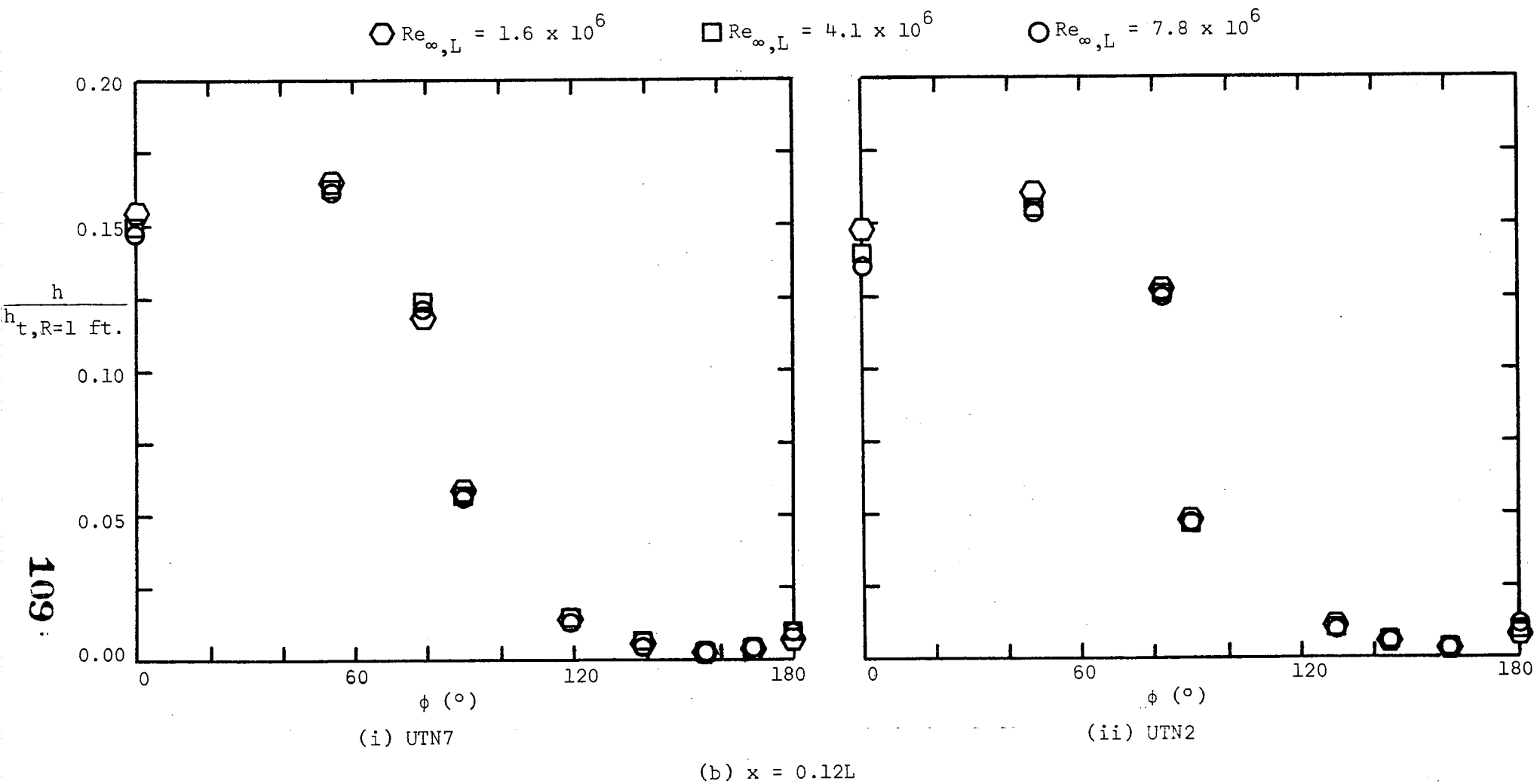
Figure 22. - Concluded.
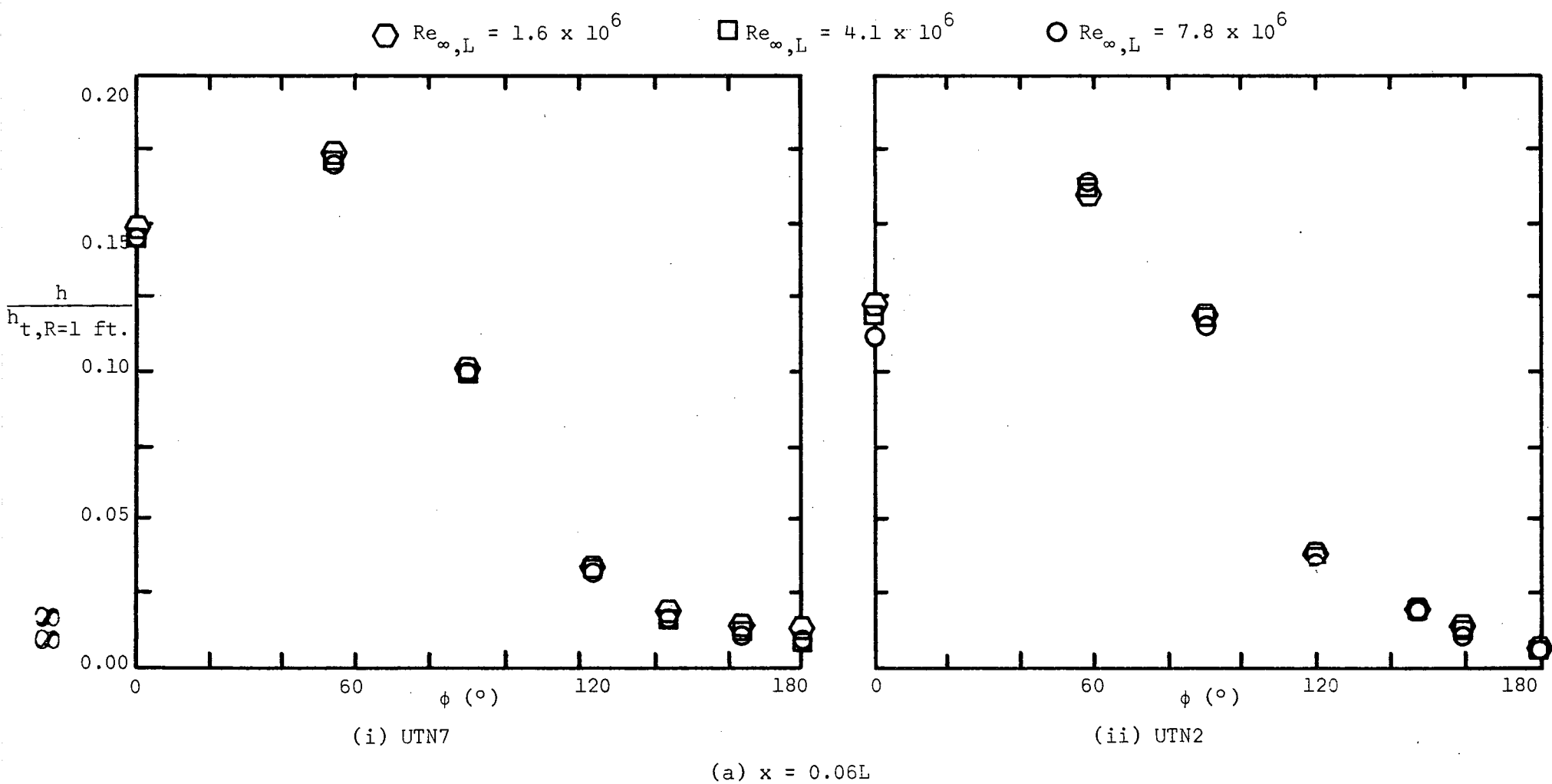
Figure 23. - Circumferential heat-transfer distributions for alpha of 30°.

$\bigcirc$ $Re_{\infty,L} = 1.6 \times 10^6$ $\square$ $Re_{\infty,L} = 4.1 \times 10^6$ $\bigcirc$ $Re_{\infty,L} = 7.8 \times 10^6$

$\dfrac{h}{h_{t,R=1\ ft.}}$

ϕ (°)

(i) UTN7

(ii) UTN2

(b) x = 0.12L

Figure 23. – Continued.

68

$\text{Re}_{\infty,L} = 1.6 \times 10^6 \qquad \text{Re}_{\infty,L} = 4.1 \times 10^6 \qquad \text{Re}_{\infty,L} = 7.8 \times 10^6$

(i) UTN7

(ii) UTN2

(c) x = 0.16L

Figure 23. - Continued.

(d) x = 0.20L

Figure 23. – Continued.

(e) x = 0.26L

Figure 23. - Continued.

92
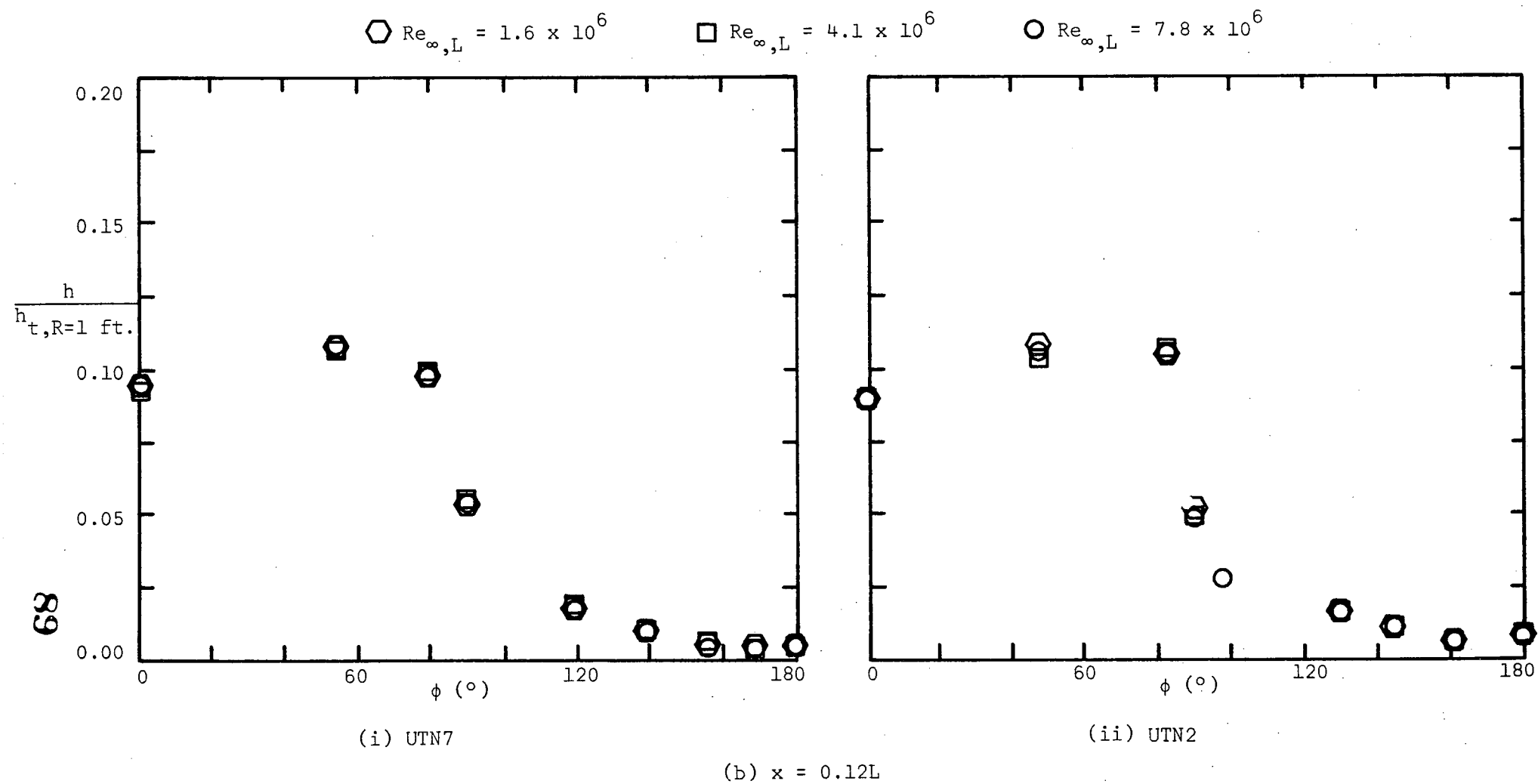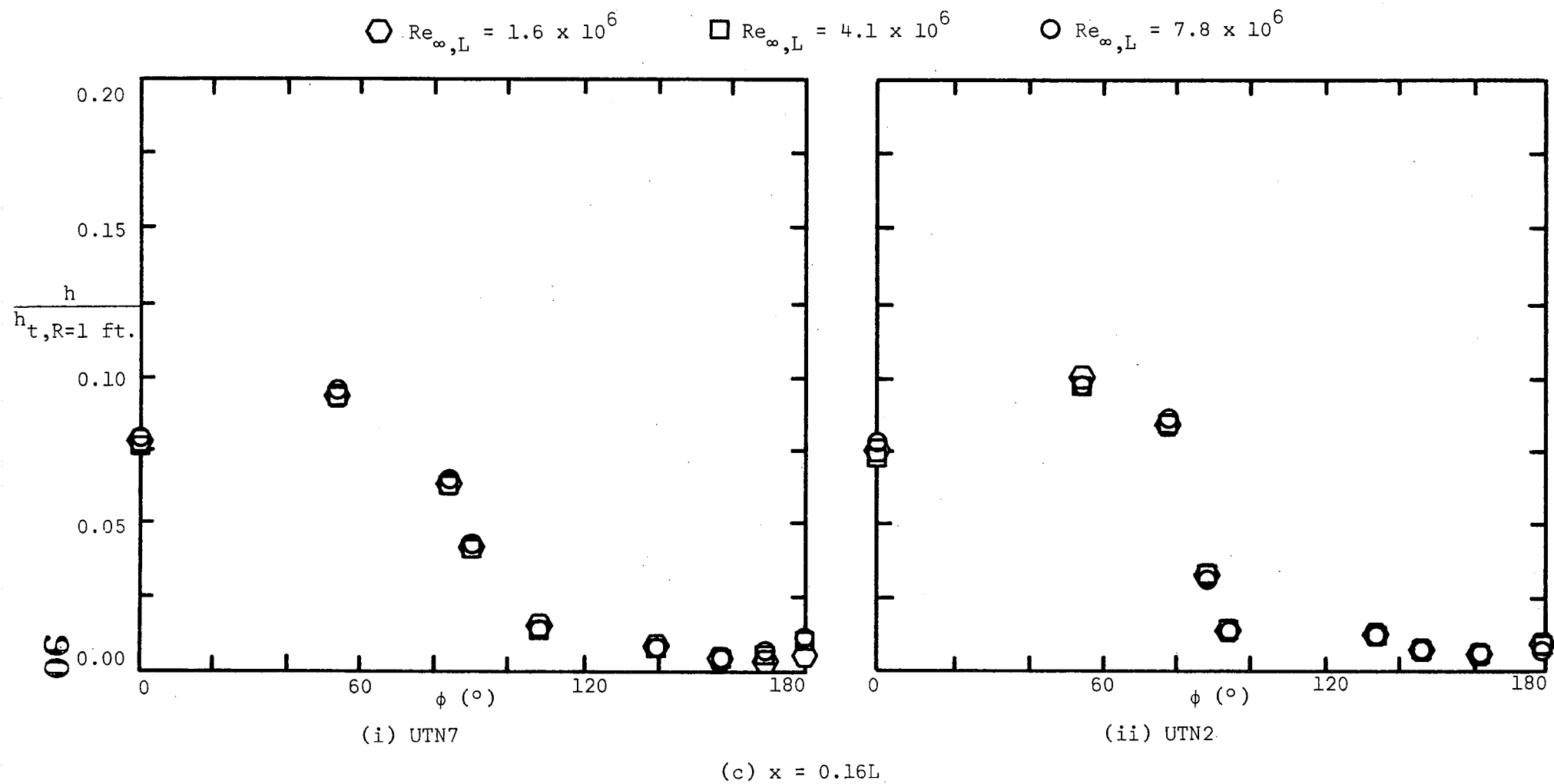
Figure 23. - Continued.

Figure 23. - Continued.

$Re_{\infty,L} = 1.6 \times 10^6$ $Re_{\infty,L} = 4.1 \times 10^6$ $Re_{\infty,L} = 7.8 \times 10^6$

$\dfrac{h}{h_{t,R=1\ ft.}}$

(i) UTN7

(ii) UTN2

(h) x = 0.50L

Figure 23. - Continued.

95
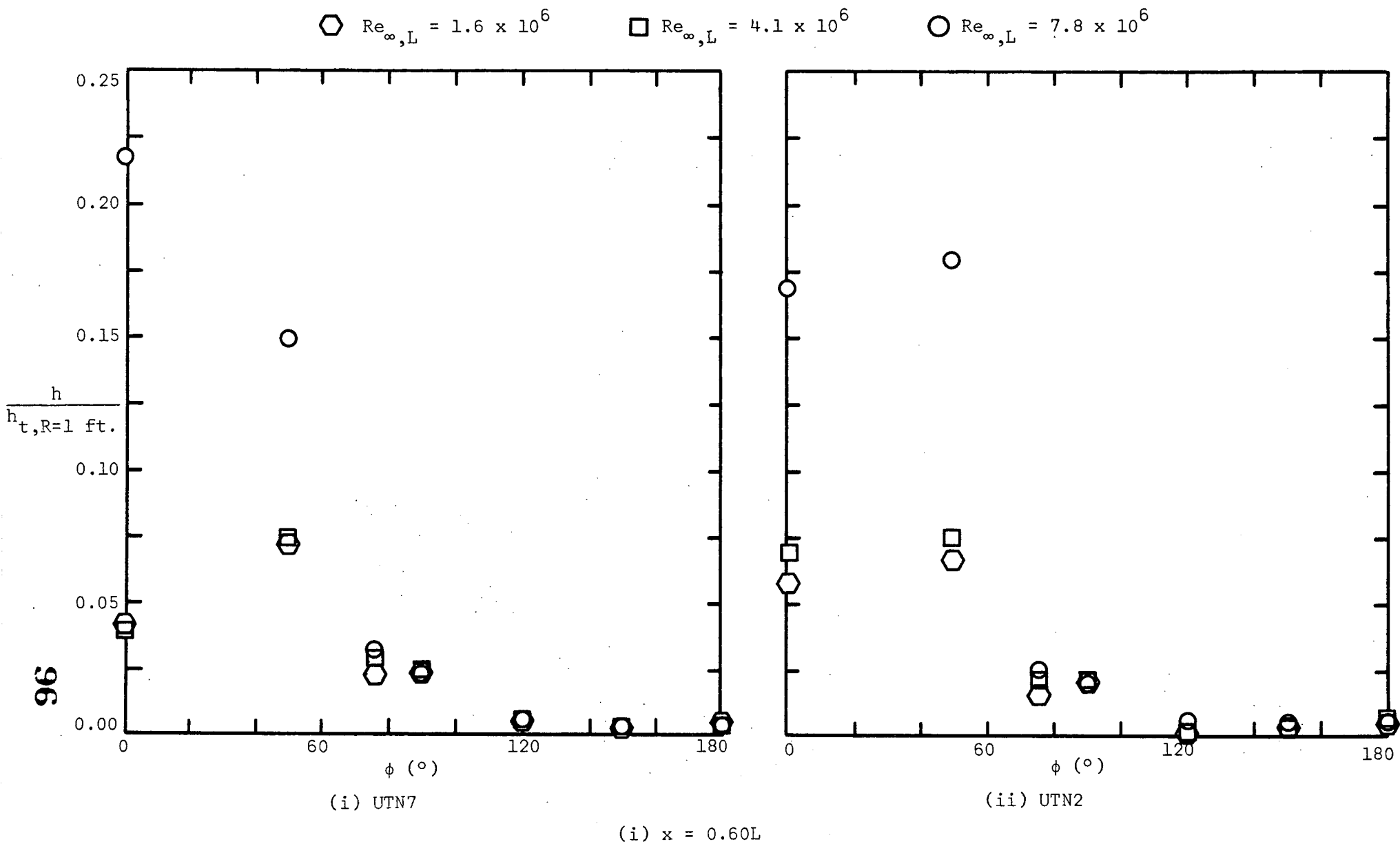
Figure 23. - Continued.
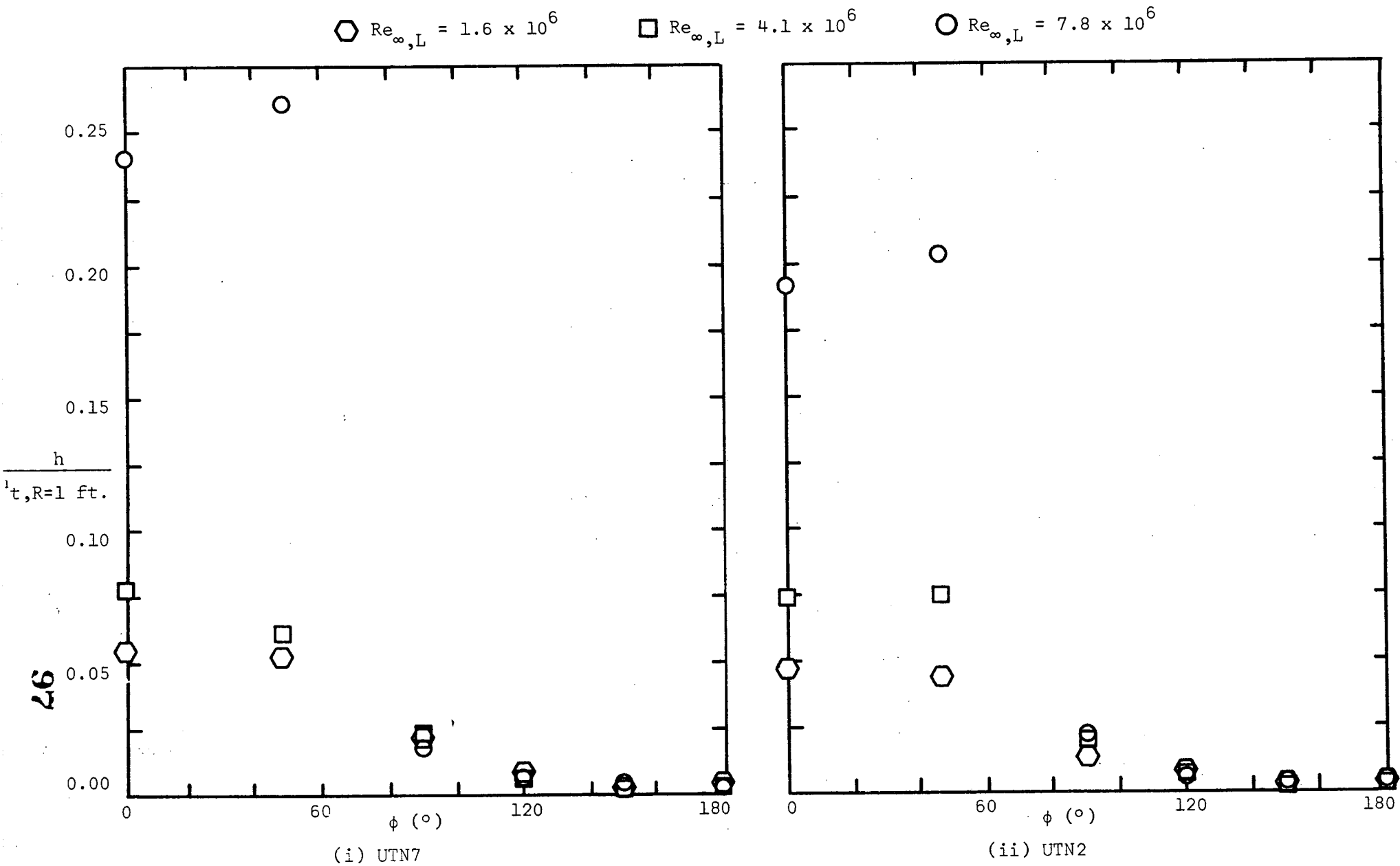
(j) x = 0.7L

Figure 23. - Concluded.
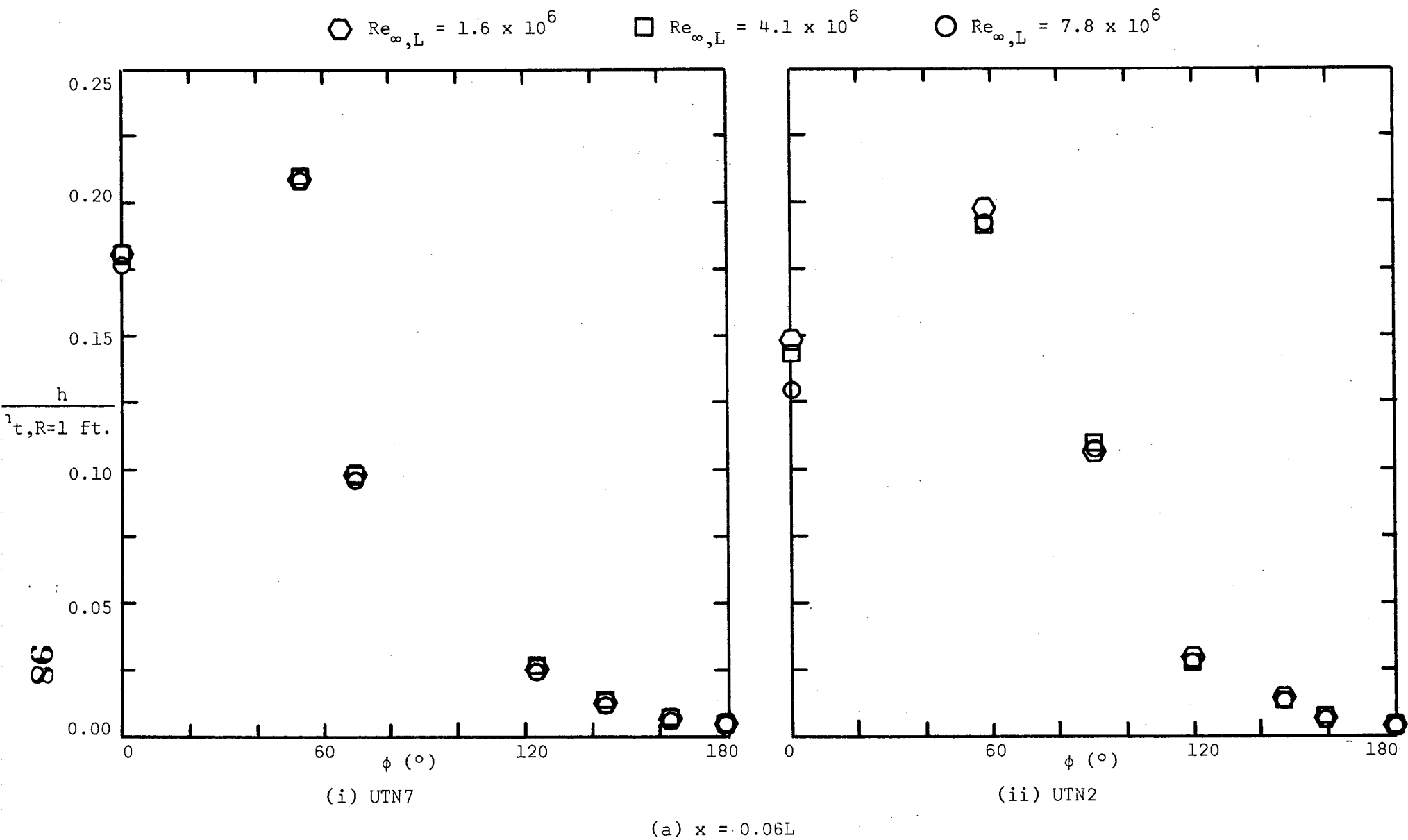
Figure 24. – Circumferential heat-transfer distributions for alpha of 40°.
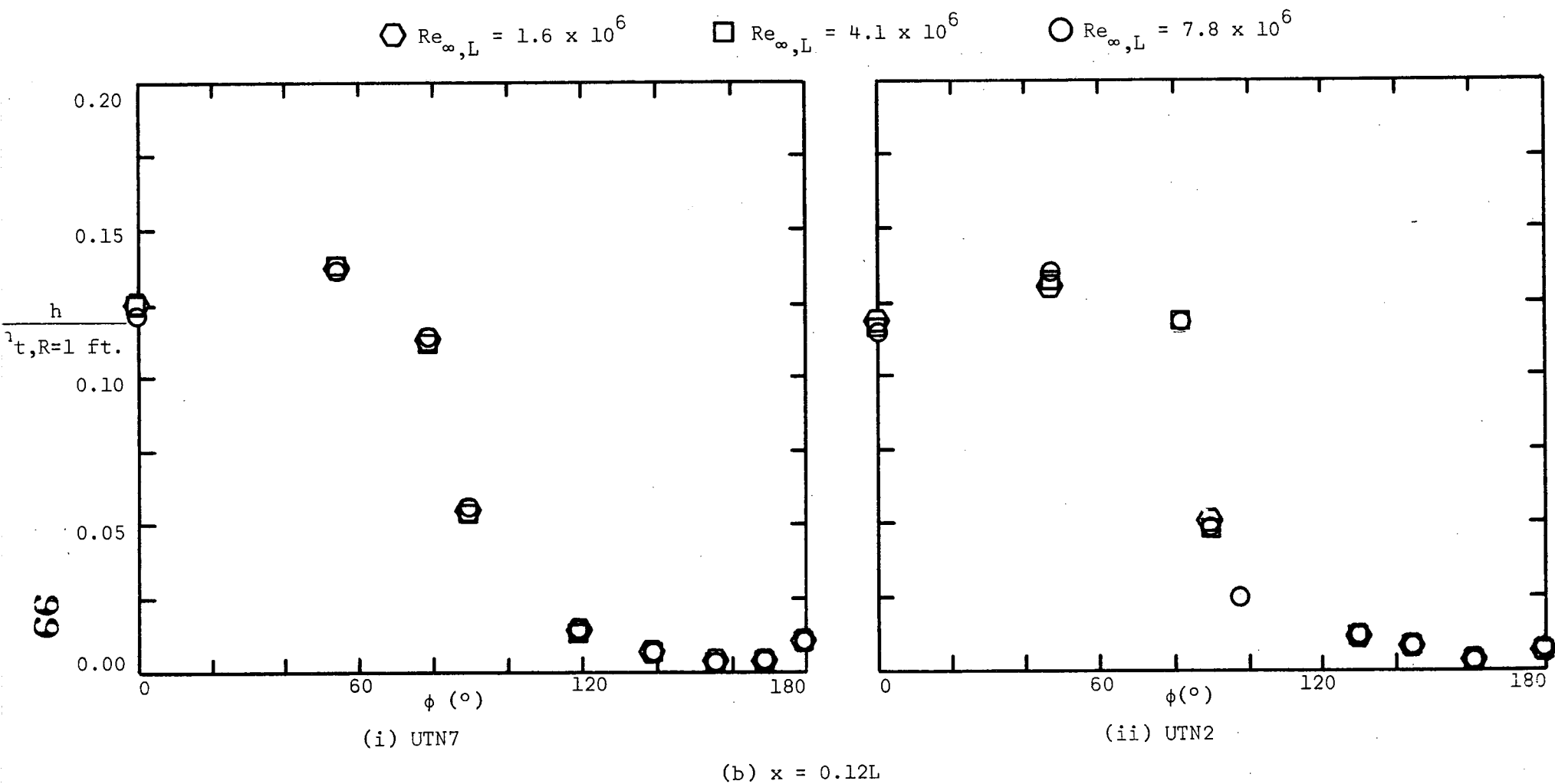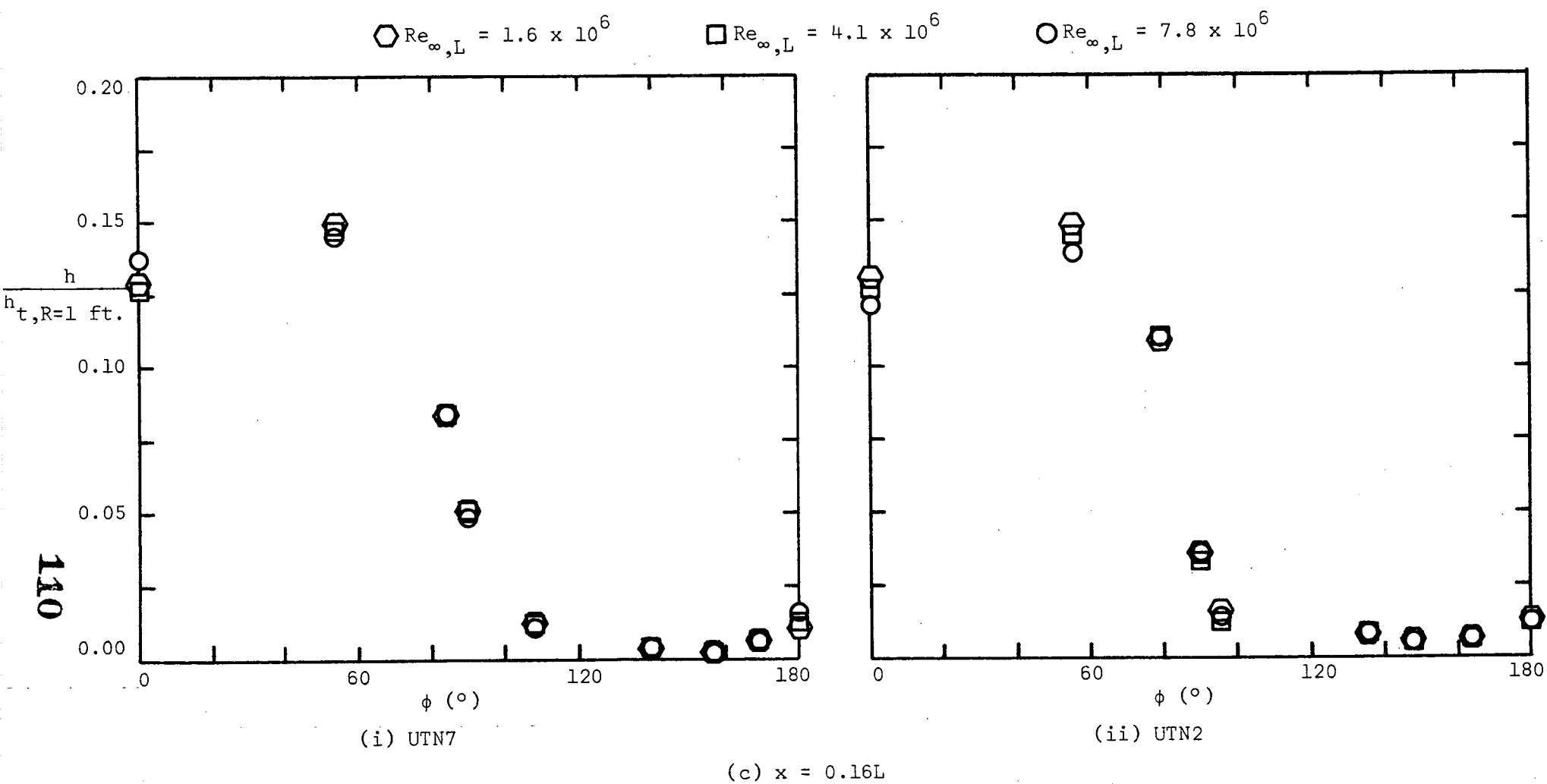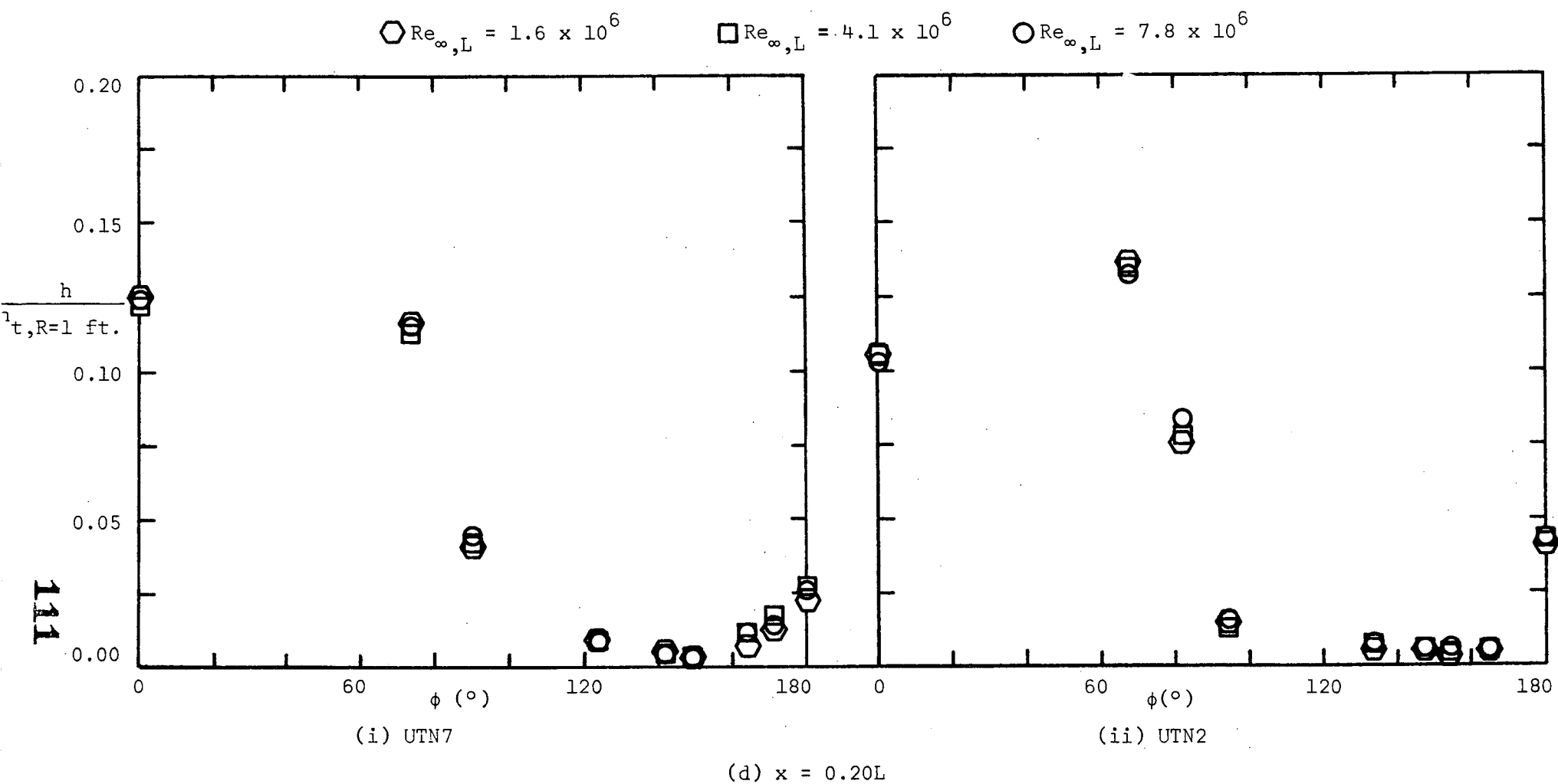
Figure 24. – Continued.
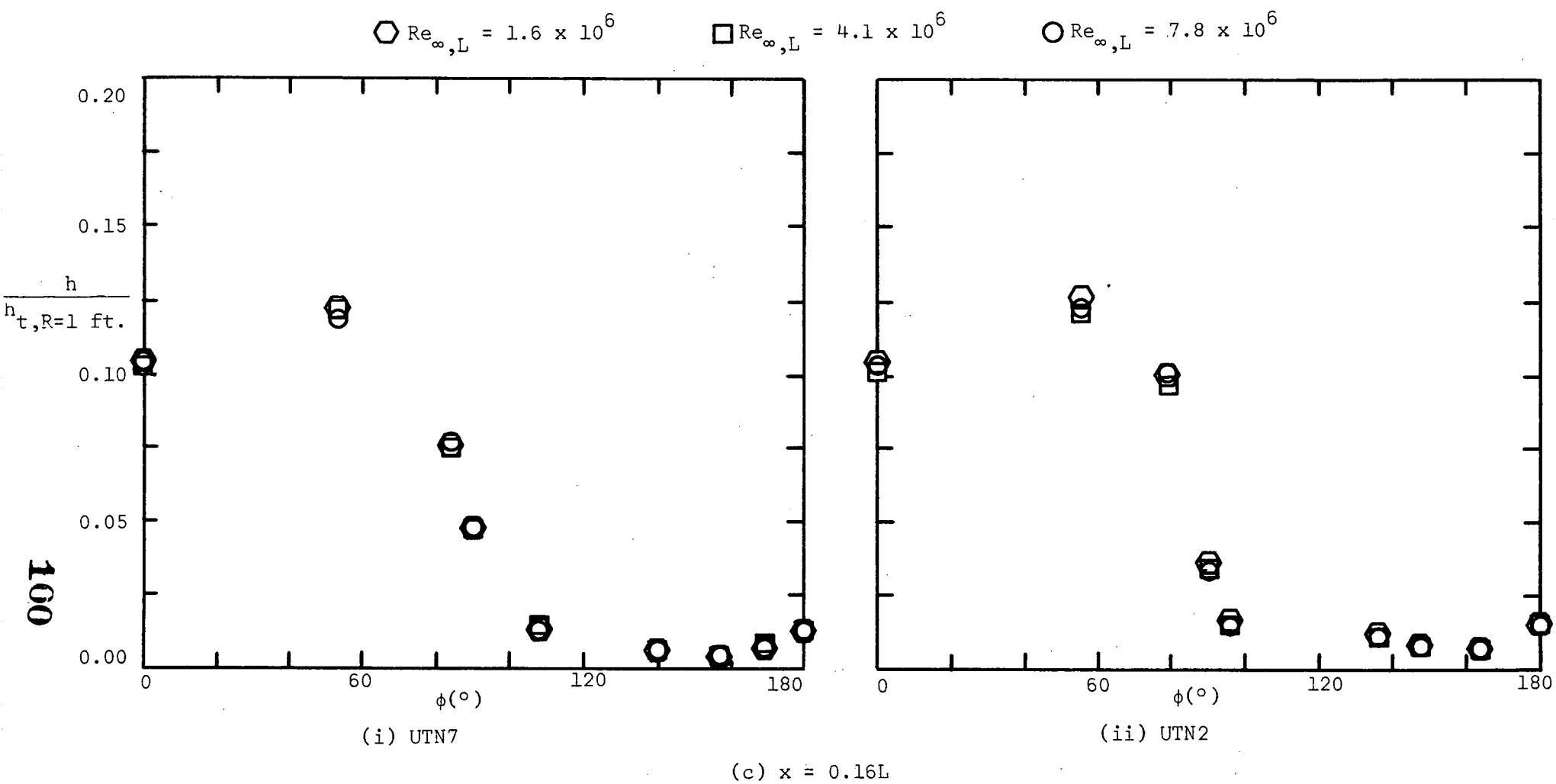
Figure 24. - Continued.

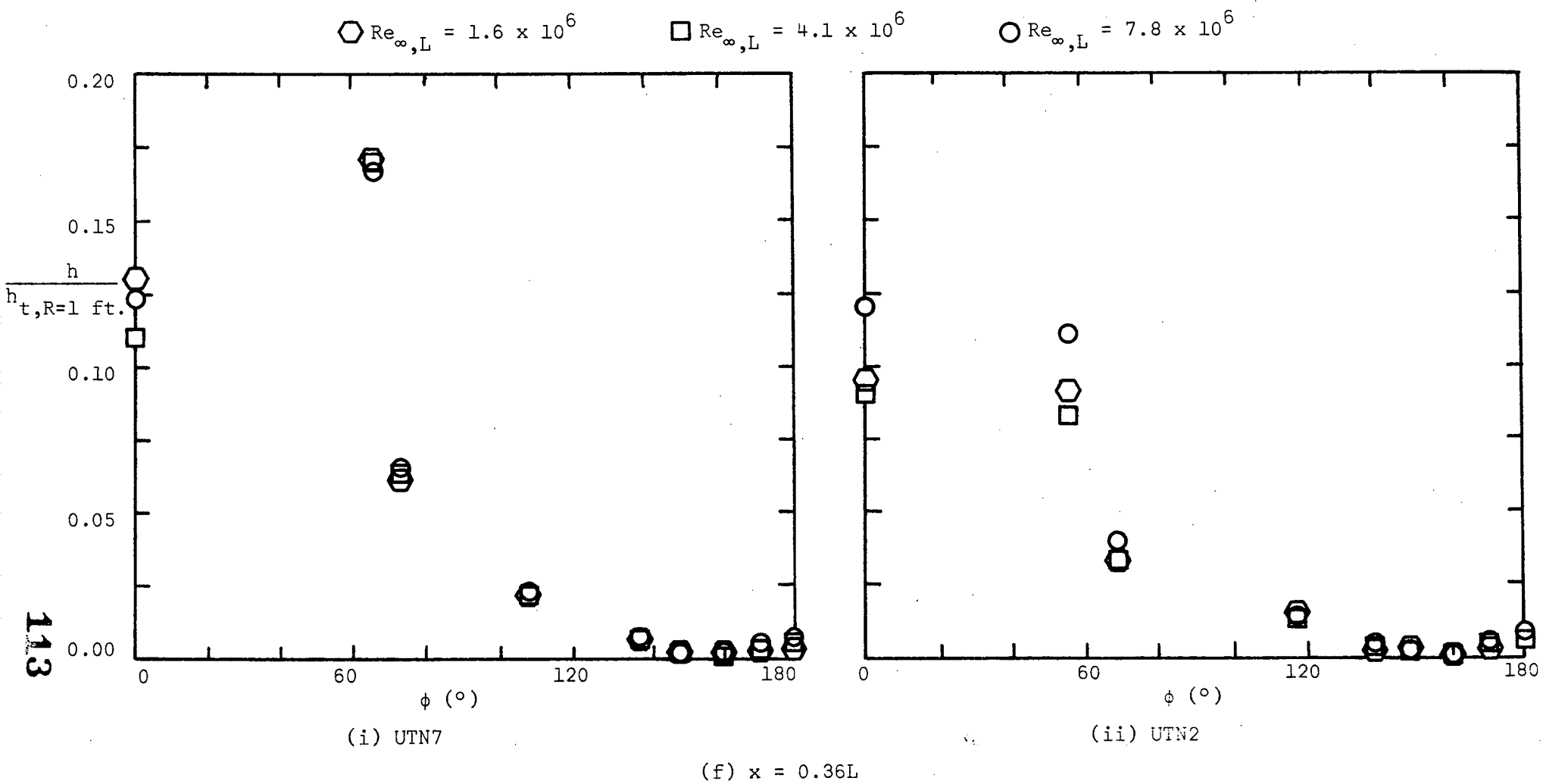$\bigcirc Re_{\infty,L} = 1.6 \times 10^6$ $\square Re_{\infty,L} = 4.1 \times 10^6$ $\bigcirc Re_{\infty,L} = 7.8 \times 10^6$

(i) UTN7   (d) x = 0.20L   (ii) UTN2

101

Figure 24. - Continued.

$$\bigcirc Re_{\infty,L} = 1.6 \times 10^6 \qquad \square Re_{\infty,L} = 4.1 \times 10^6 \qquad \bigcirc Re_{\infty,L} = 7.8 \times 10^6$$

(i) UTN7

(ii) UTN2

(e) x = 0.26L

Figure 24. - Continued.

102

$$\mathrm{O}\, \mathrm{Re}_{\infty,\mathrm{L}} = 1.6 \times 10^6 \qquad \square\, \mathrm{Re}_{\infty,\mathrm{L}} = 4.1 \times 10^6 \qquad \mathrm{O}\, \mathrm{Re}_{\infty,\mathrm{L}} = 7.8 \times 10^6$$

(i) UTN7

(ii) UTN2

(f) x = 0.36L

Figure 24. - Continued.

103

(i) UTN7

(ii) UTN2
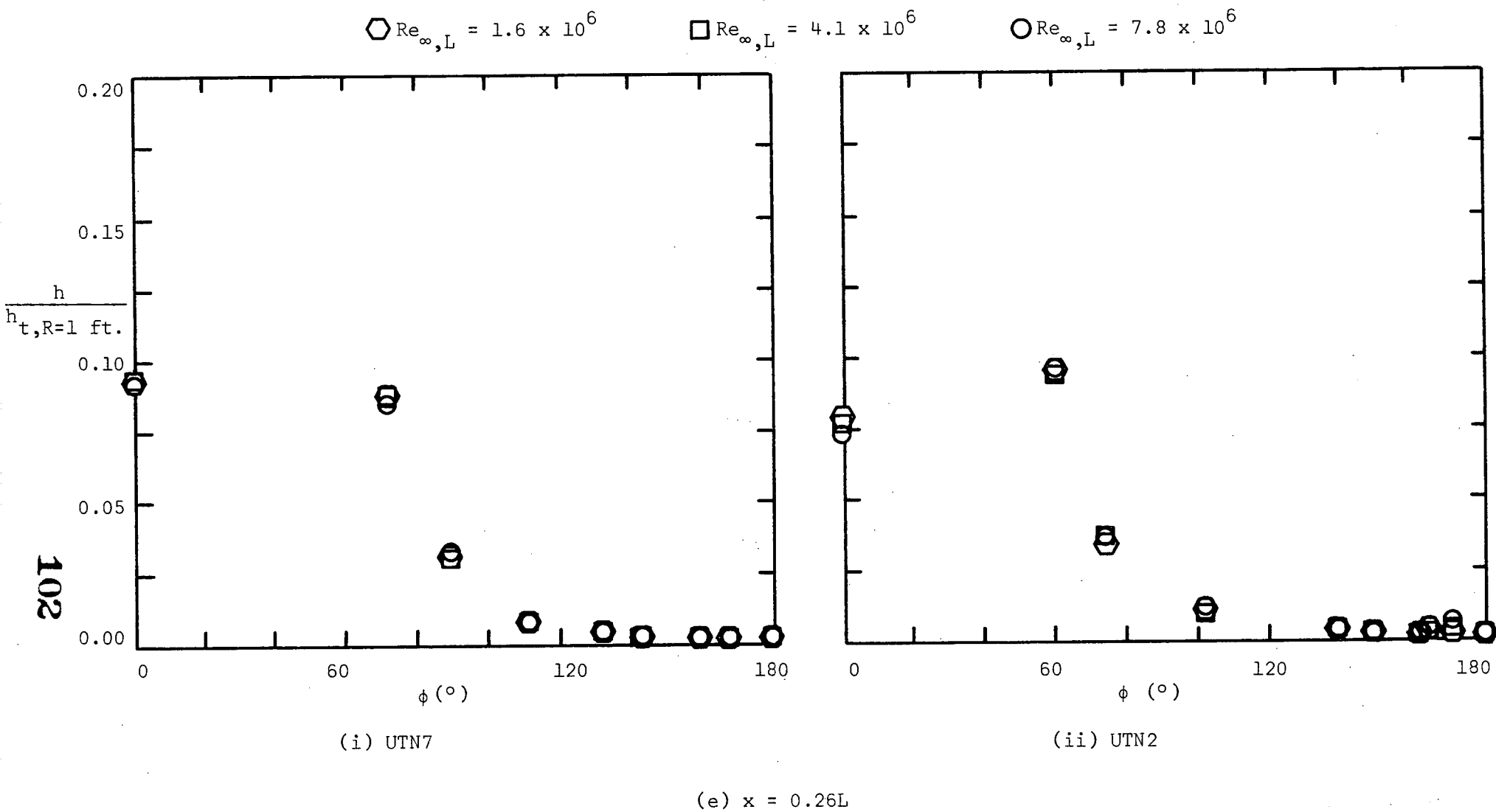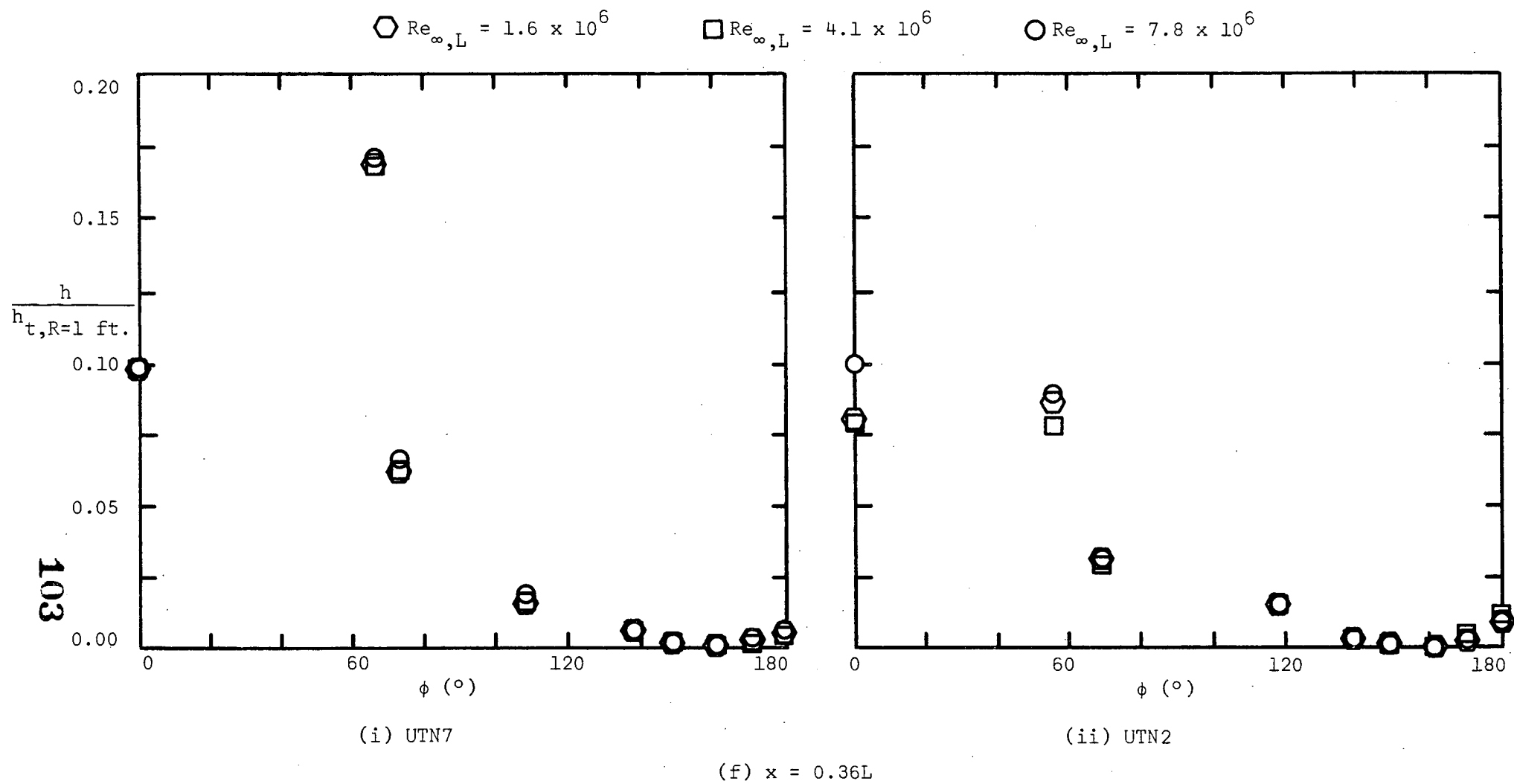
(g) x = 0.425L

Figure 24. – Continued.

$Re_{\infty,L} = 1.6 \times 10^6$ $Re_{\infty,L} = 4.1 \times 10^6$ $Re_{\infty,L} = 7.8 \times 10^6$
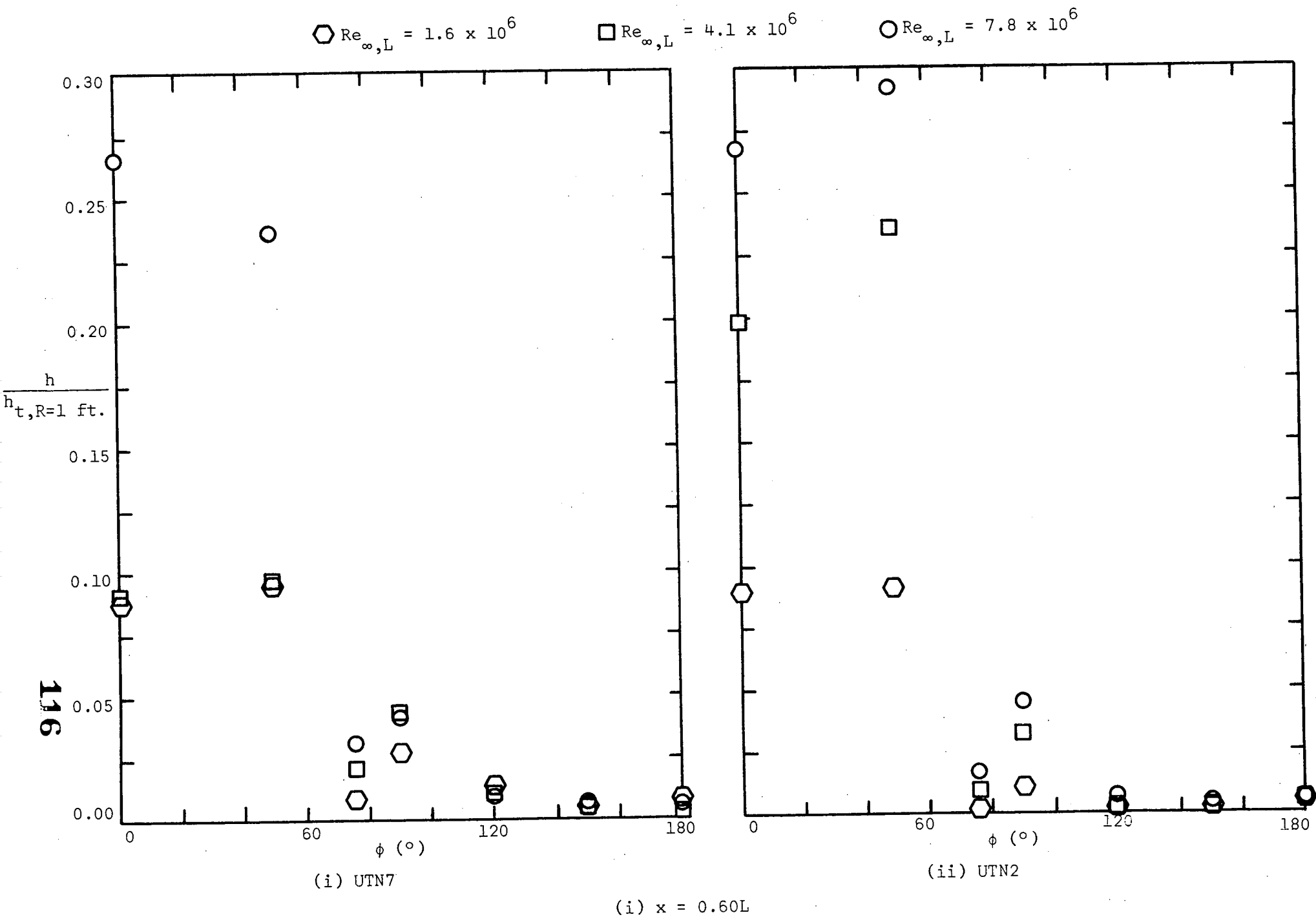
(i) UTN7

(ii) UTN2

(h) x = 0.50L

105

Figure 24. - Continued.

Figure 24. - Continued.

Figure 24. - Concluded.

Figure 25. - Circumferential heat-transfer distributions for alpha of 50°.
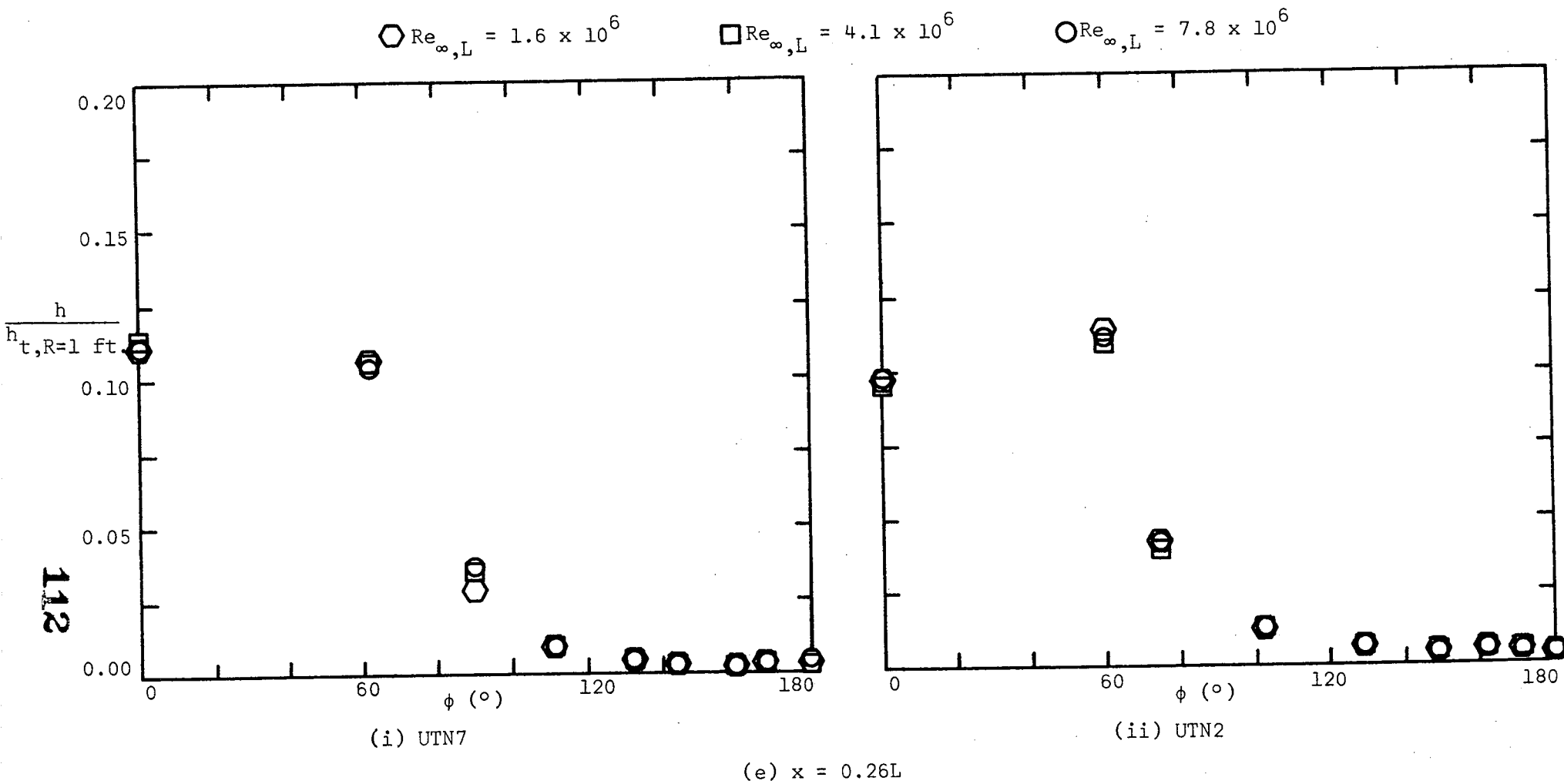
108

(b) x = 0.12L

Figure 25. - Continued.

$\bigcirc \mathrm{Re}_{\infty,L} = 1.6 \times 10^{6}$ $\square \mathrm{Re}_{\infty,L} = 4.1 \times 10^{6}$ $\bigcirc \mathrm{Re}_{\infty,L} = 7.8 \times 10^{6}$

$\dfrac{h}{h_{t,R=1\ ft.}}$

$\phi\ (°)$

(i) UTN7

$\phi\ (°)$

(ii) UTN2

(c) x = 0.16L

Figure 25. - Continued.

$\bigcirc Re_{\infty,L} = 1.6 \times 10^6$ $\square Re_{\infty,L} = 4.1 \times 10^6$ $\bigcirc Re_{\infty,L} = 7.8 \times 10^6$

$\dfrac{h}{h_{t,R=1\ ft.}}$

ϕ (°)

(i) UTN7

(ii) UTN2

(d) x = 0.20L

111

Figure 25. - Continued.

$\hexagon Re_{\infty,L} = 1.6 \times 10^6 \qquad \square Re_{\infty,L} = 4.1 \times 10^6 \qquad \bigcirc Re_{\infty,L} = 7.8 \times 10^6$

112

(i) UTN7

(ii) UTN2

(e) x = 0.26L

Figure 25. - Continued.

$Re_{\infty,L} = 1.6 \times 10^6$ $Re_{\infty,L} = 4.1 \times 10^6$ $Re_{\infty,L} = 7.8 \times 10^6$

$\dfrac{h}{h_{t,R=1 \text{ ft.}}}$

(i) UTN7

(ii) UTN2

(f) x = 0.36L

Figure 25. - Continued.

Figure 25. - Continued.

Figure 25. - Continued.

Figure 25. - Continued.

$\hexagon$ $Re_{\infty,L} = 1.6 \times 10^6$ $\square$ $Re_{\infty,L} = 4.1 \times 10^6$ $\bigcirc$ $Re_{\infty,L} = 7.8 \times 10^6$

(i) UTN7

(ii) UTN2

(j) x = 0.70L
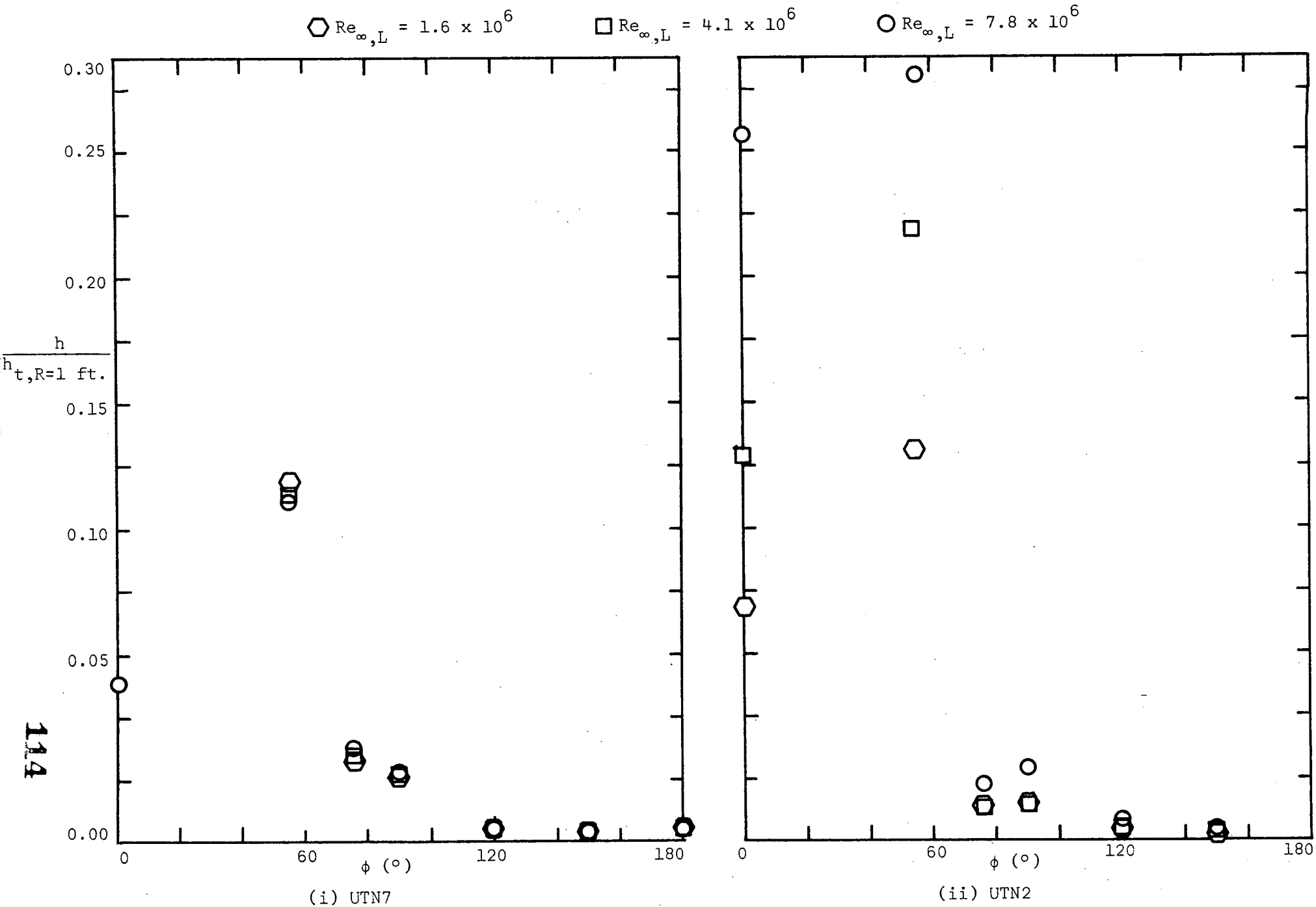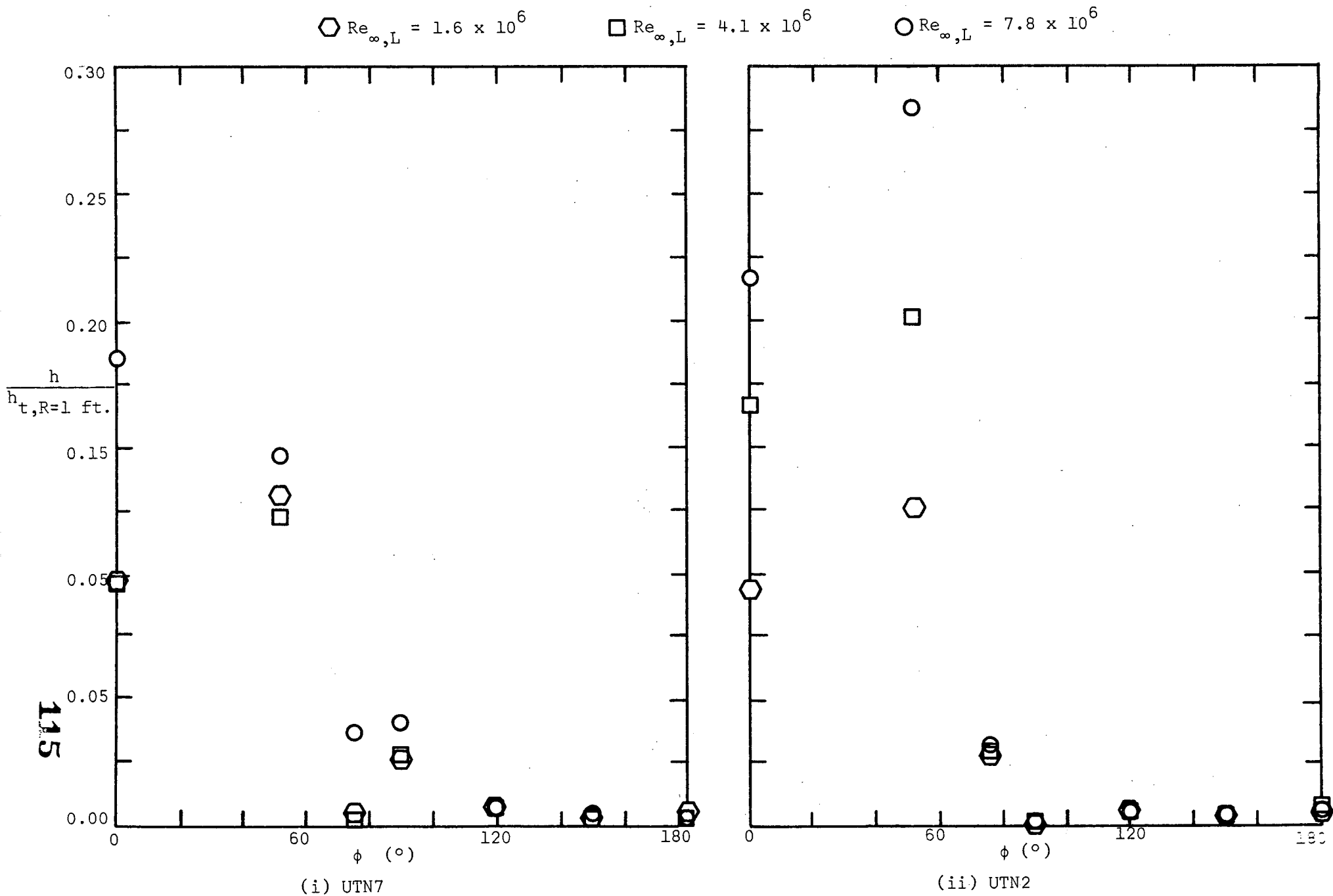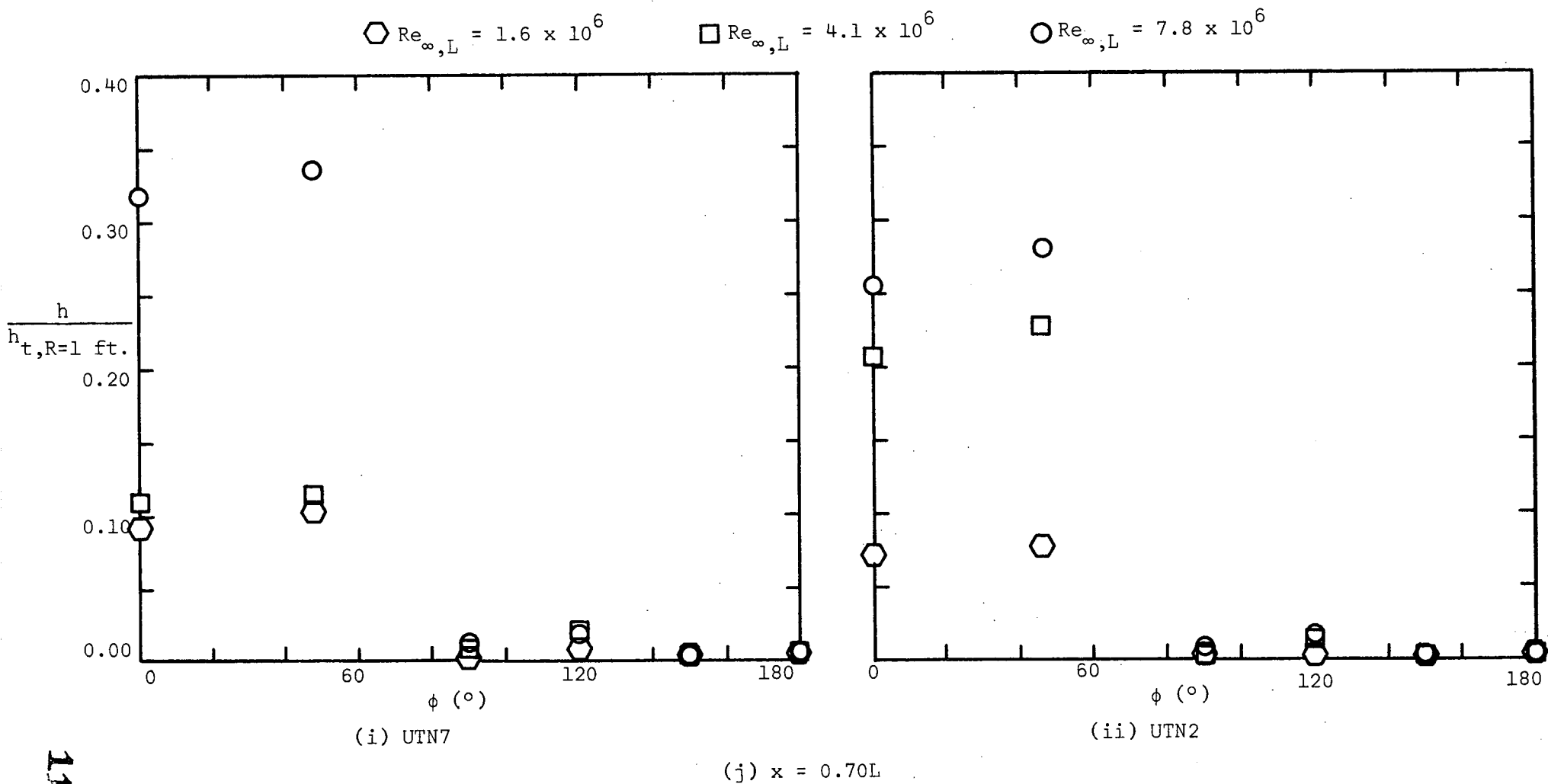
Figure 25. - Concluded.
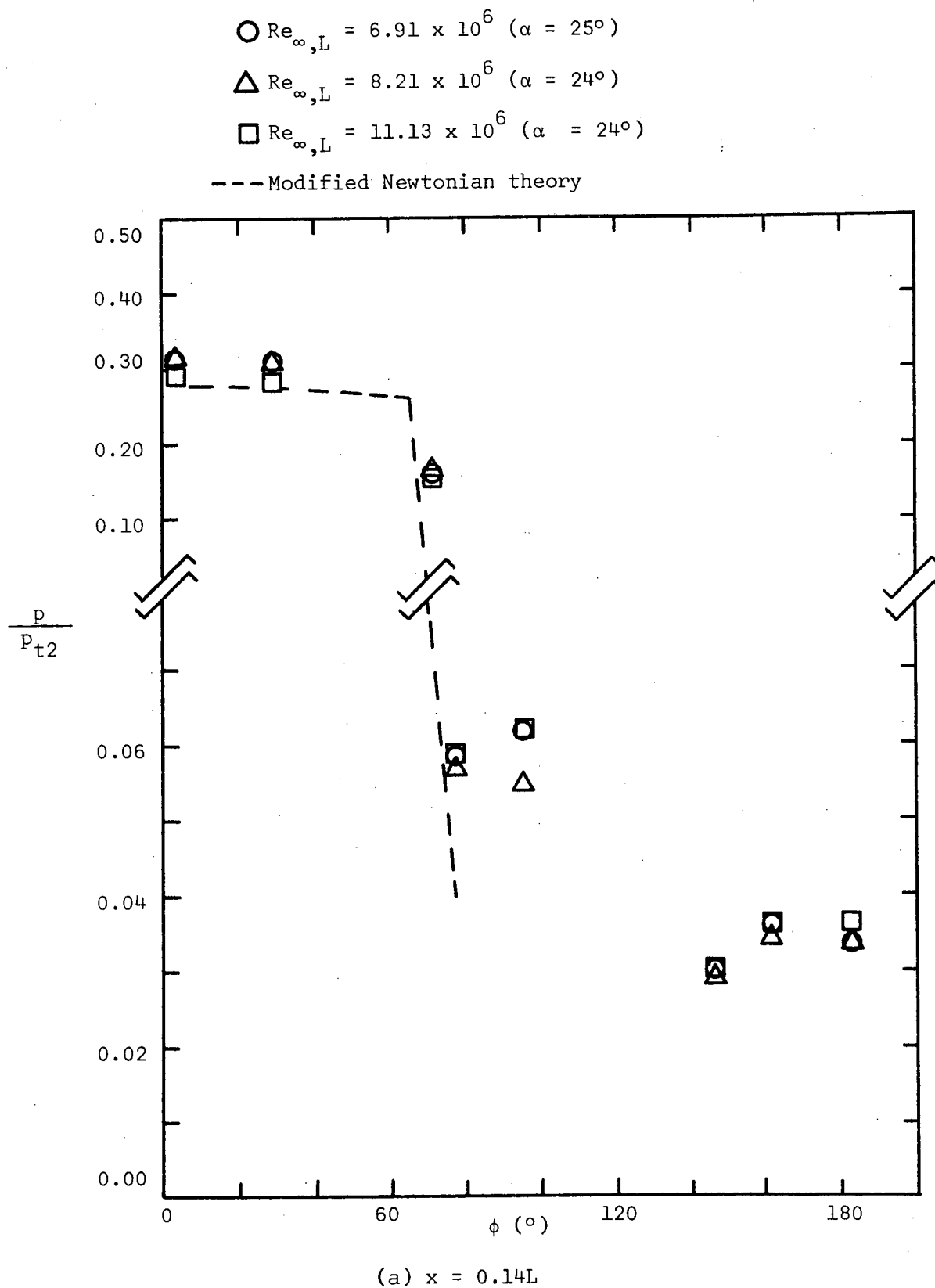
Figure 26. – Circumferential pressure-distribution for the UTN2 at an alpha of 24°.

118

$\bigcirc \mathrm{Re}_{\infty,L} = 6.91 \times 10^6 \ (\alpha = 25°)$

$\triangle \mathrm{Re}_{\infty,L} = 8.21 \times 10^6 \ (\alpha = 24°)$

$\square \mathrm{Re}_{\infty,L} = 11.13 \times 10^6 \ (\alpha = 24°)$

———Modified Newtonian theory
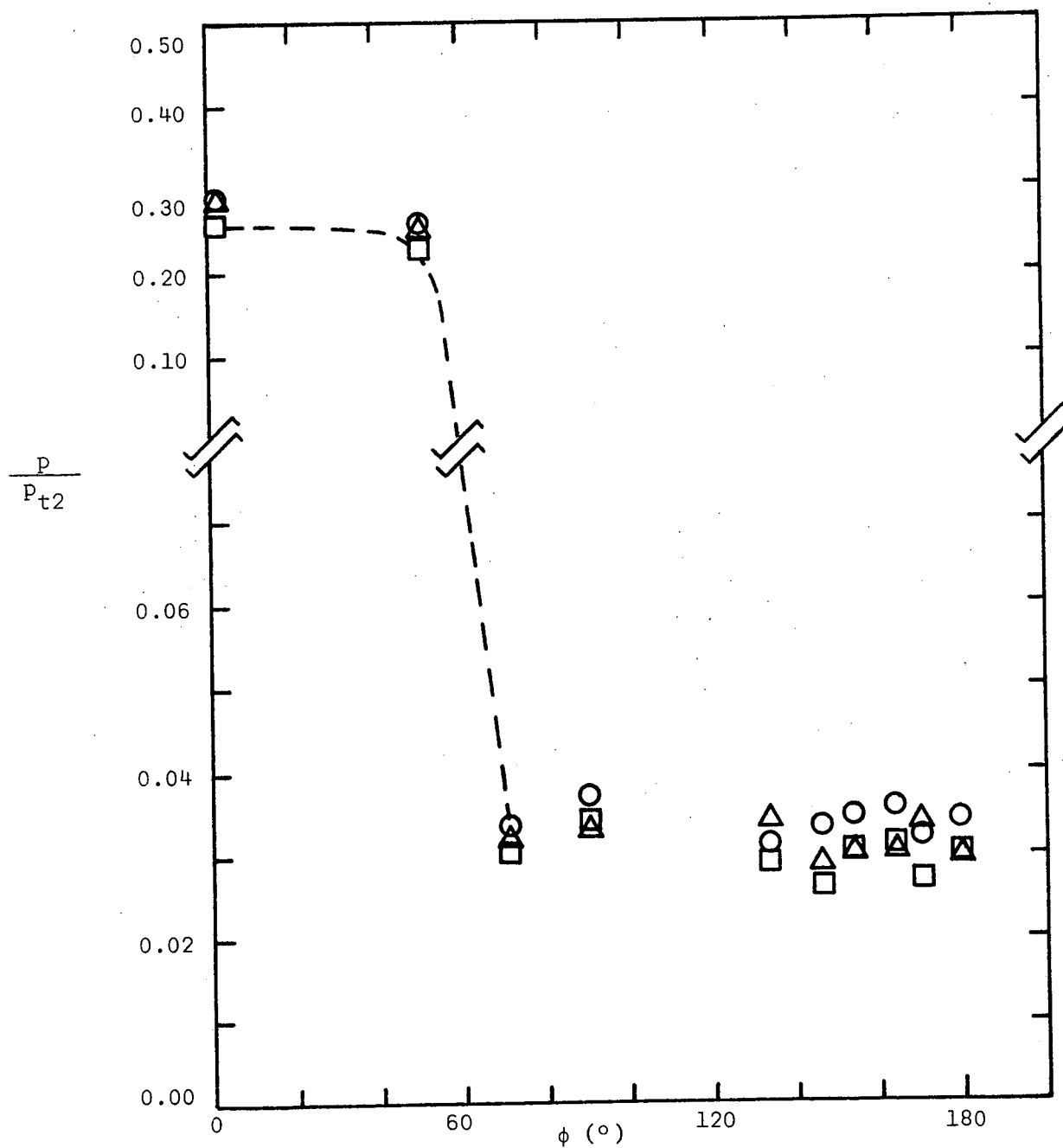
(b) x = 0.29L

Figure 26. - Concluded.

$\bigcirc \, Re_{\infty,L} = 6.83 \times 10^6 \; (\alpha = 31°)$

$\triangle \, Re_{\infty,L} = 8.13 \times 10^6 \; (\alpha = 31°)$

$\square \, Re_{\infty,L} = 11.00 \times 10^6 \; (\alpha = 31.5°)$

− − −Modified Newtonian theory

(a) x = 0.14L
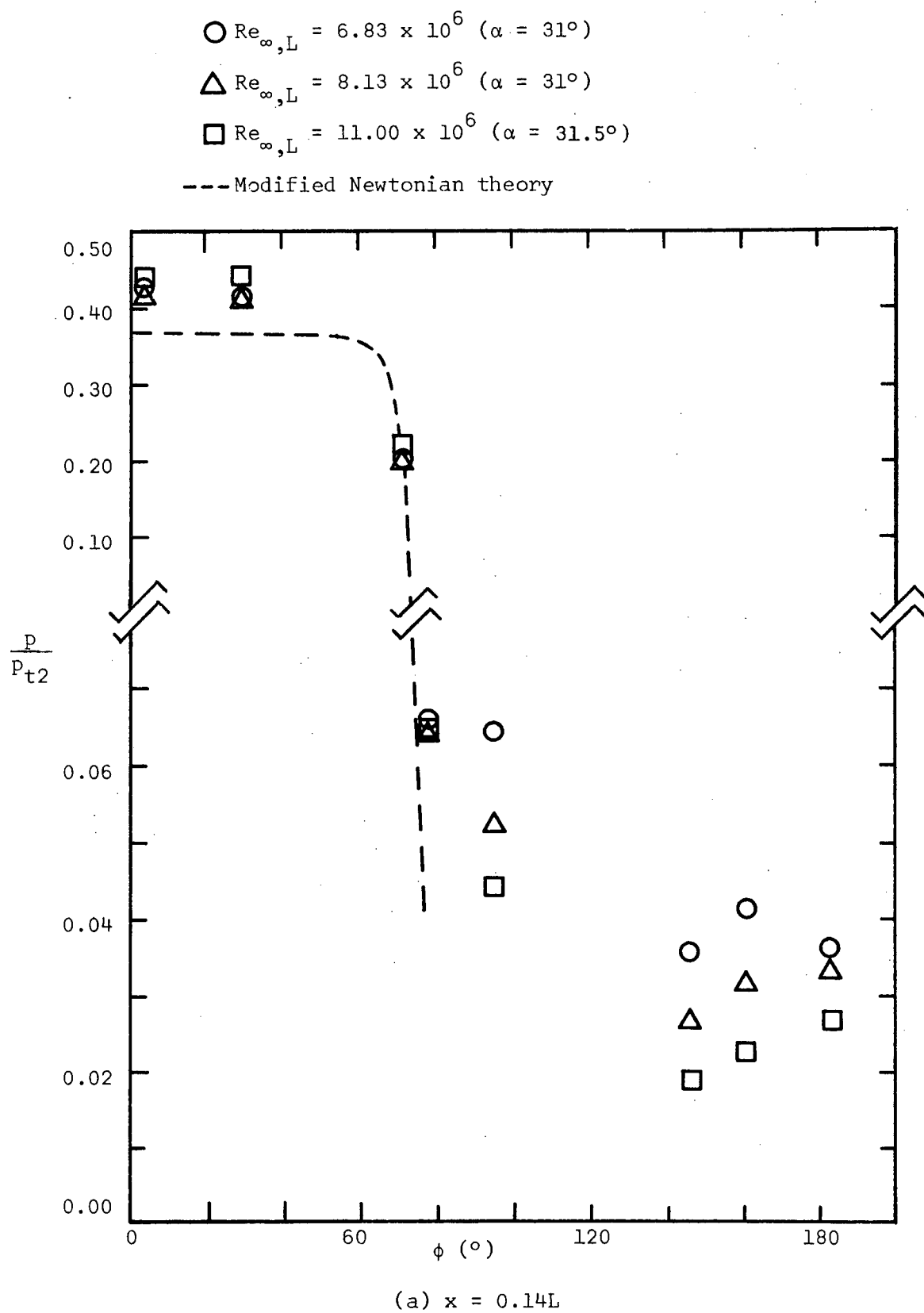
Figure 27. - Circumferential pressure-distribution for the UTN2 at an alpha of 31°.

120

$\bigcirc \ Re_{\infty,L} = 6.83 \times 10^6 \ (\alpha = 31^\circ)$

$\triangle \ Re_{\infty,L} = 8.13 \times 10^6 \ (\alpha = 31^\circ)$

$\square \ Re_{\infty,L} = 11.00 \times 10^6 \ (\alpha = 31.5^\circ)$

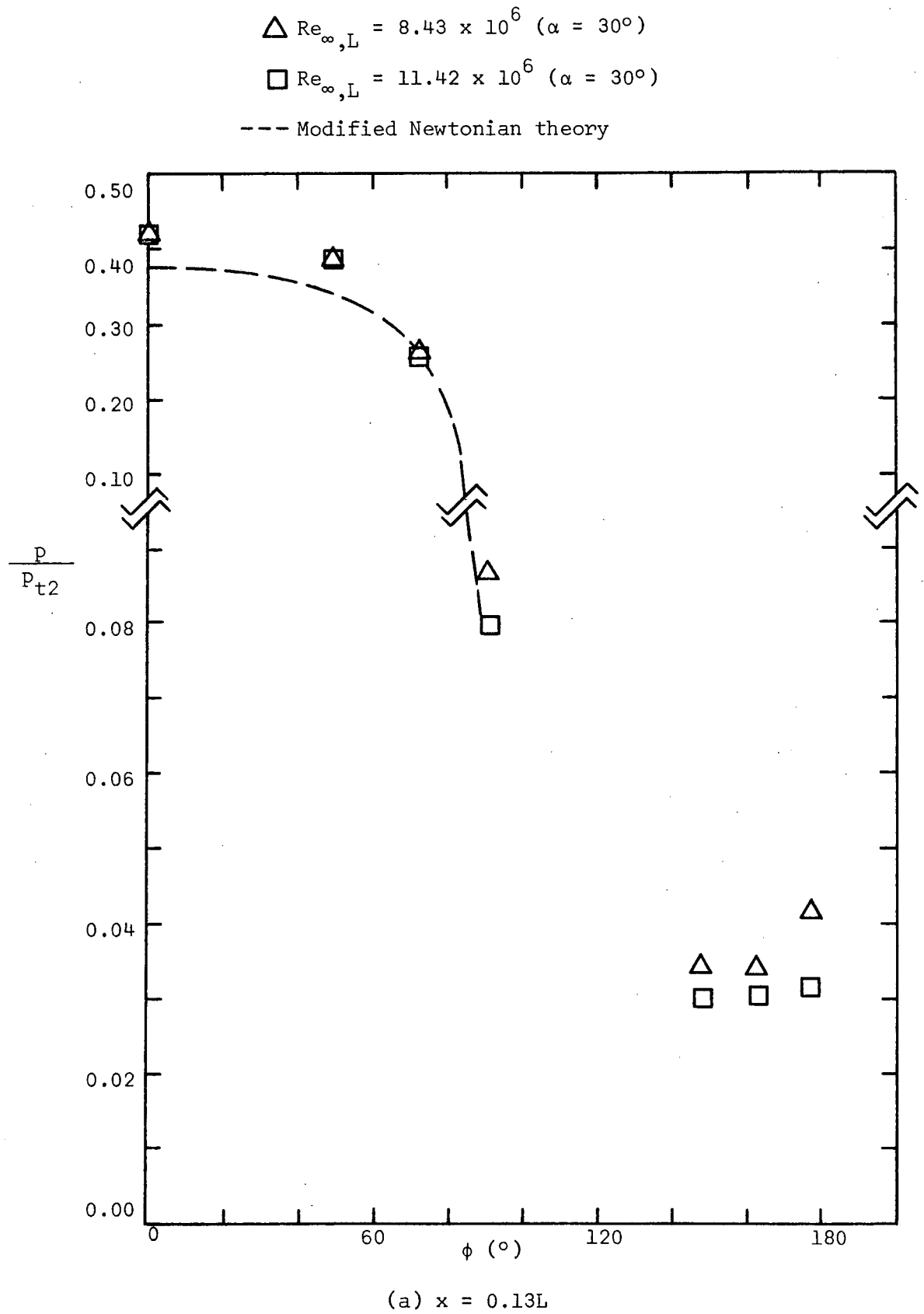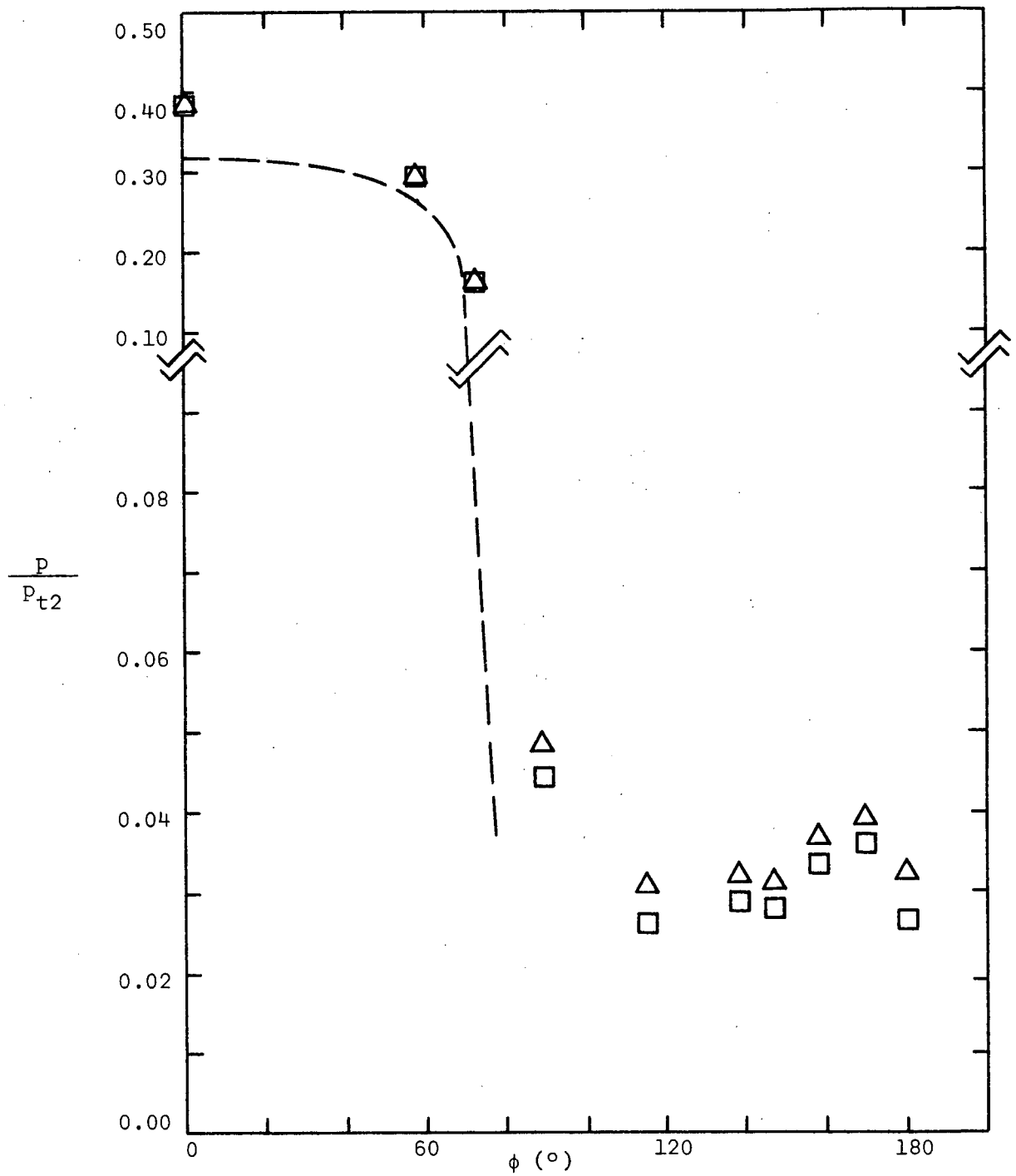---- Modified Newtonian theory
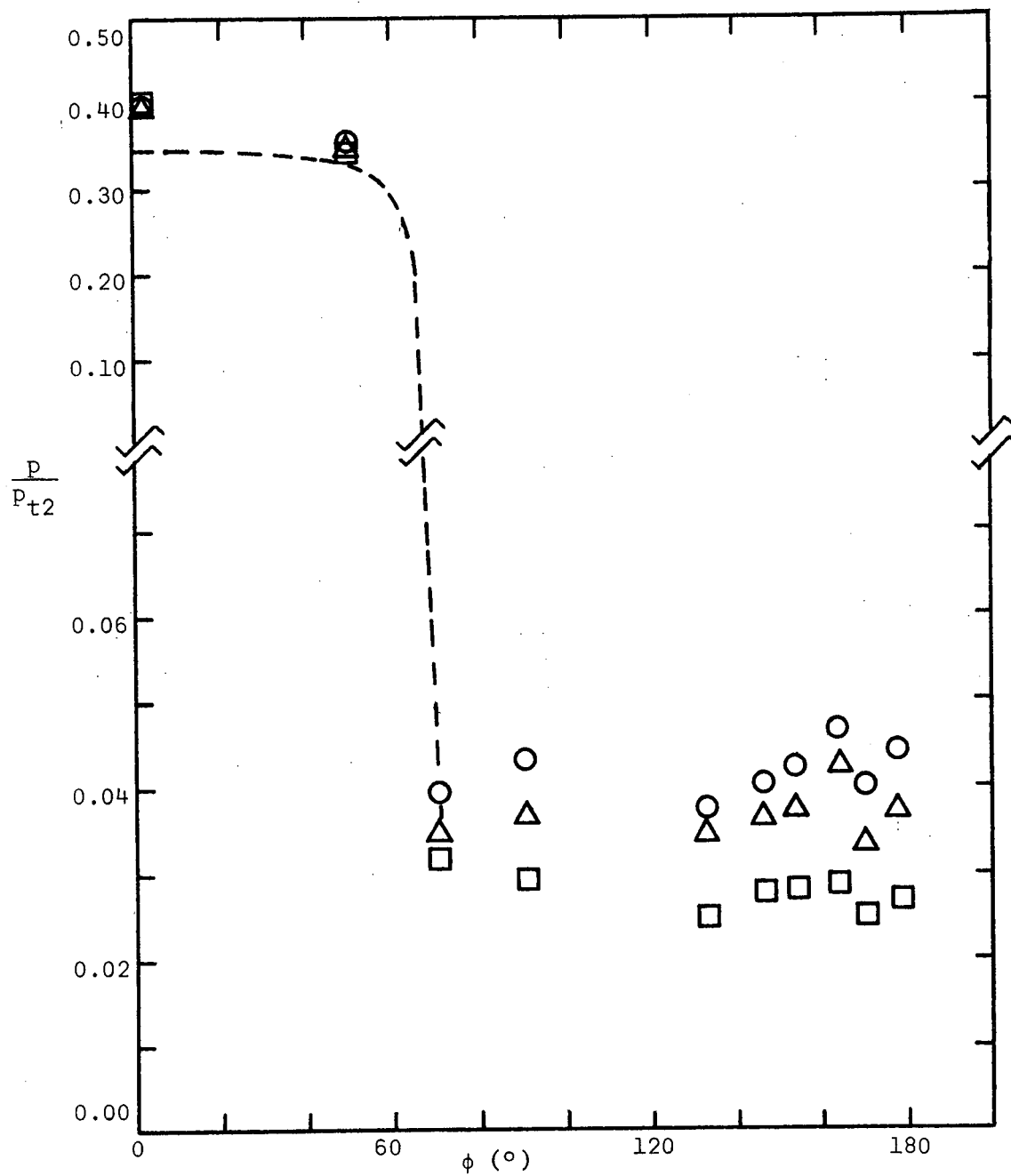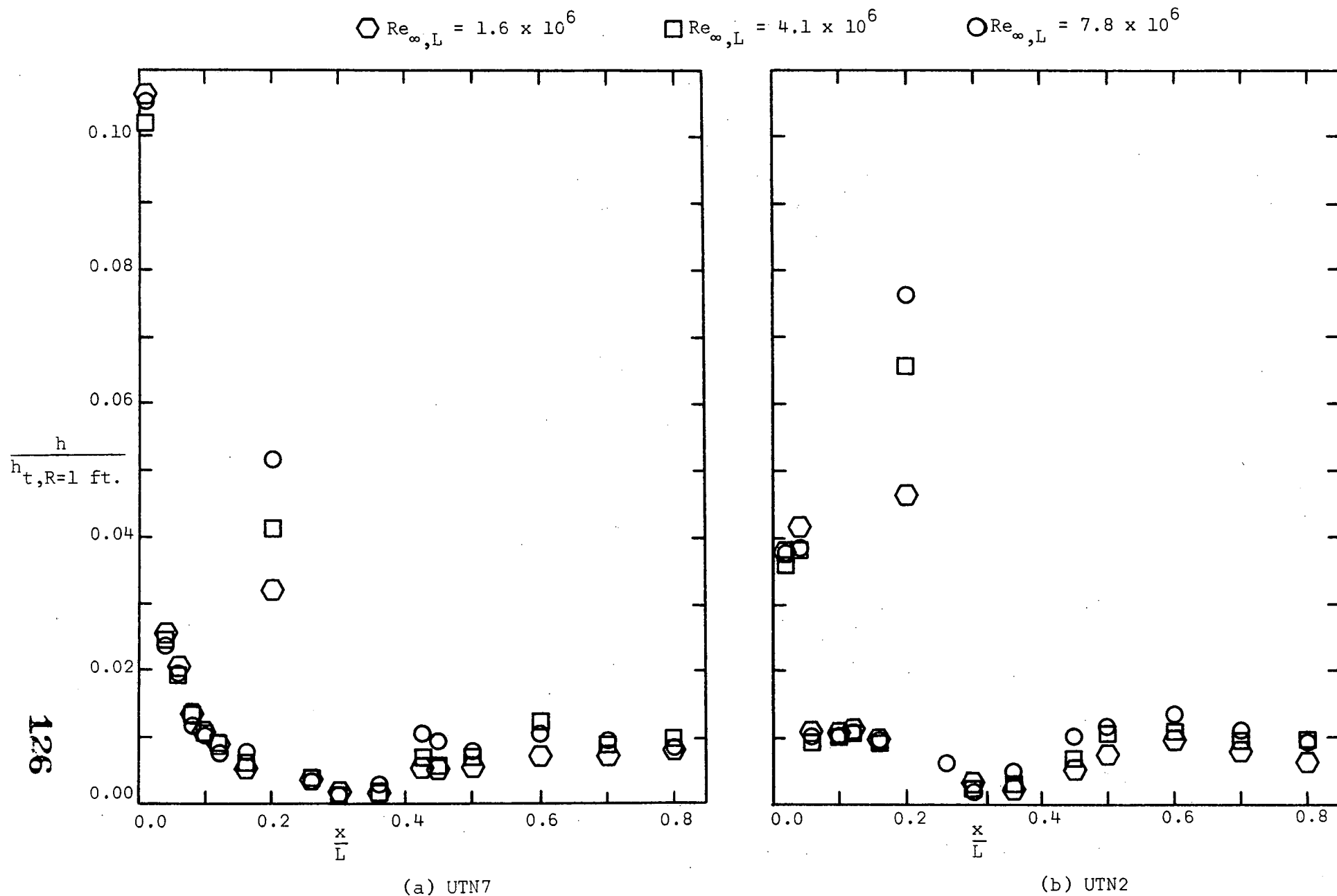
(b) x = 0.29L

Figure 27. - Concluded.
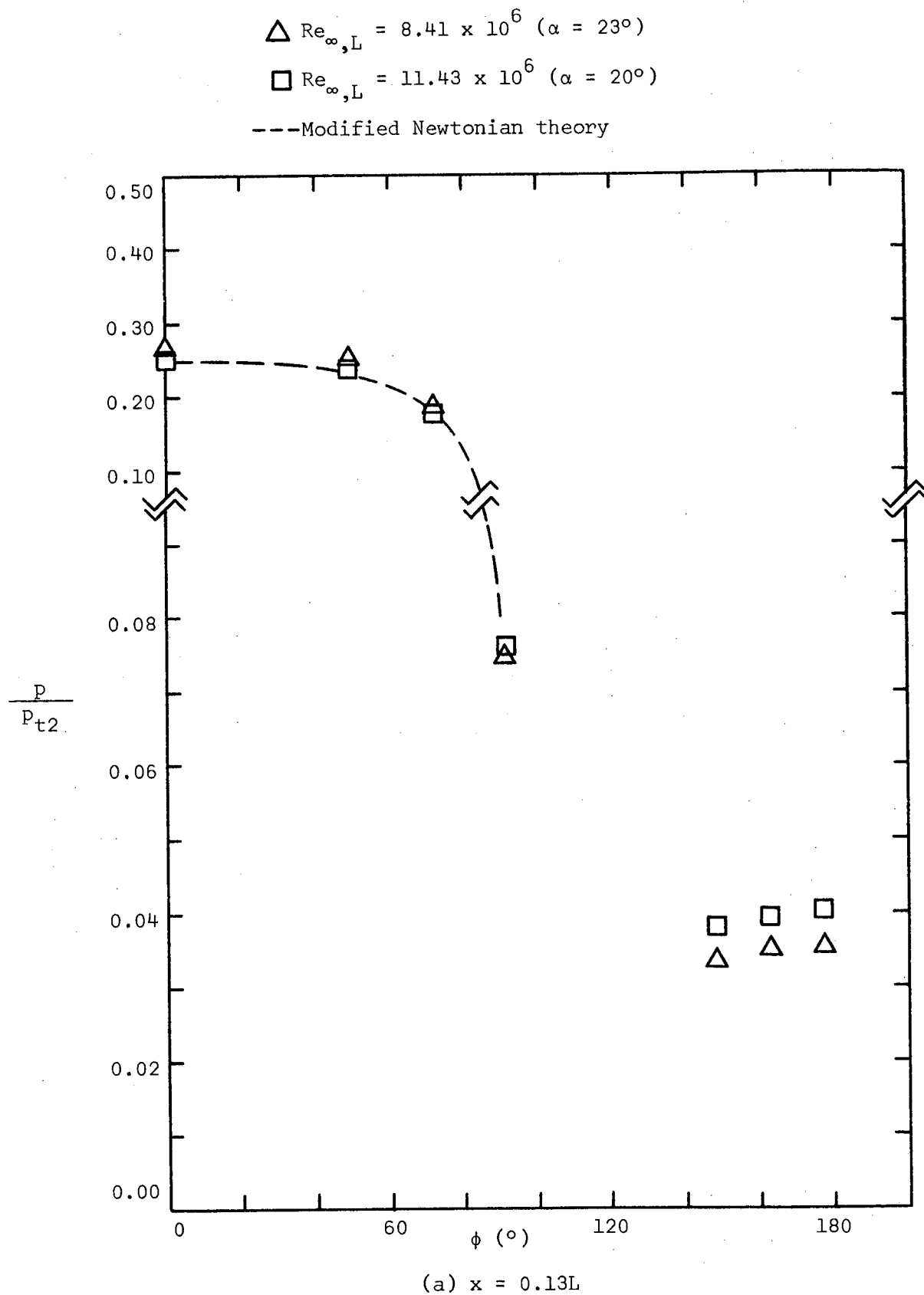
Figure 28. - Circumferential pressure-distribution for the UTN7* at an alpha of 23° (roughly).

122

$\triangle \ Re_{\infty,L} = 8.41 \times 10^6 \ (\alpha = 23°)$

$\square \ Re_{\infty,L} = 11.43 \times 10^6 \ (\alpha = 20°)$

--- Modified Newtonian theory
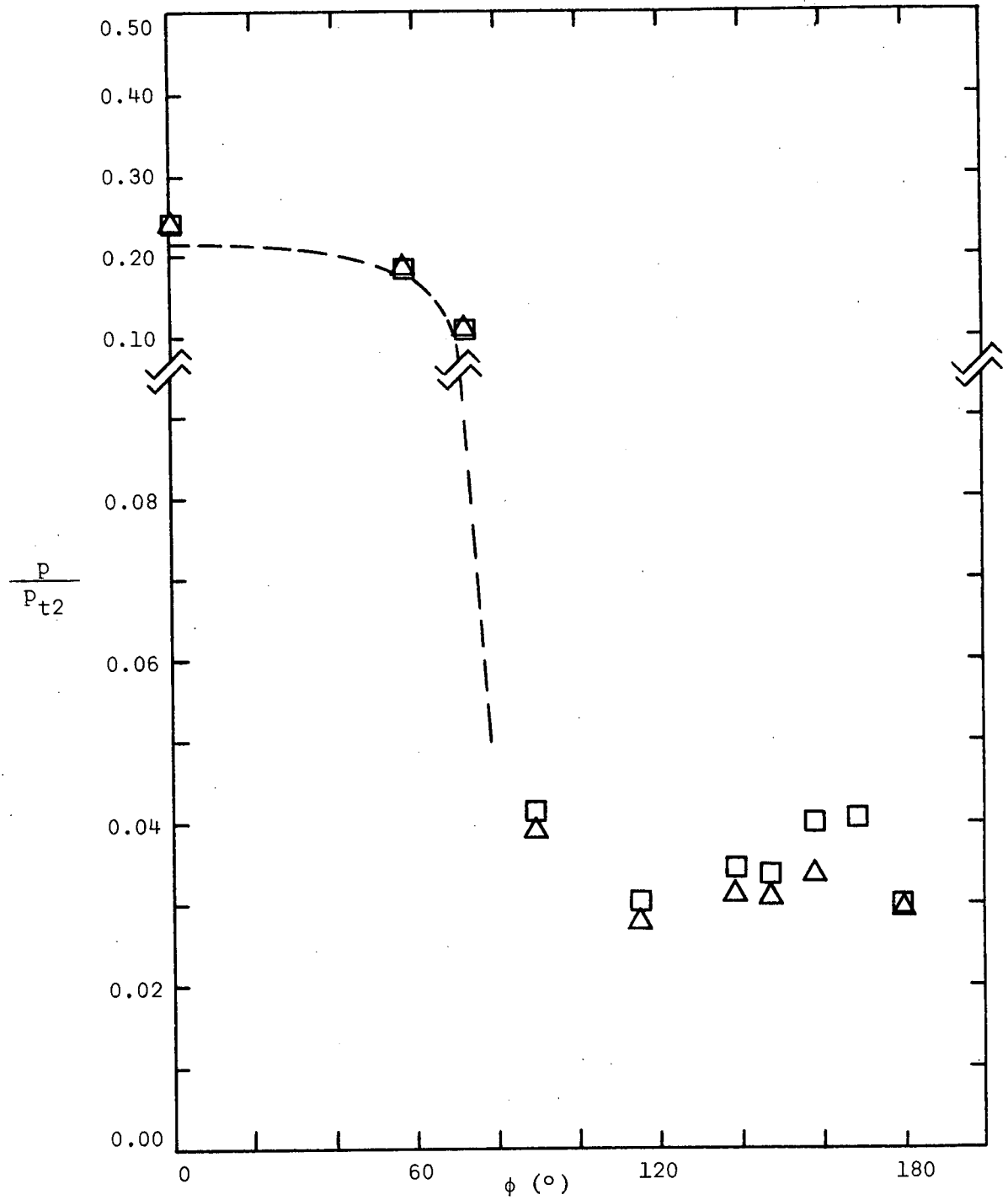
(b) x = 0.27L

Figure 28. - Concluded.

123

$\triangle$ $Re_{\infty,L}$ = 8.43 x 10^6 (α = 30°)

$\square$ $Re_{\infty,L}$ = 11.42 x 10^6 (α = 30°)

- - - Modified Newtonian theory
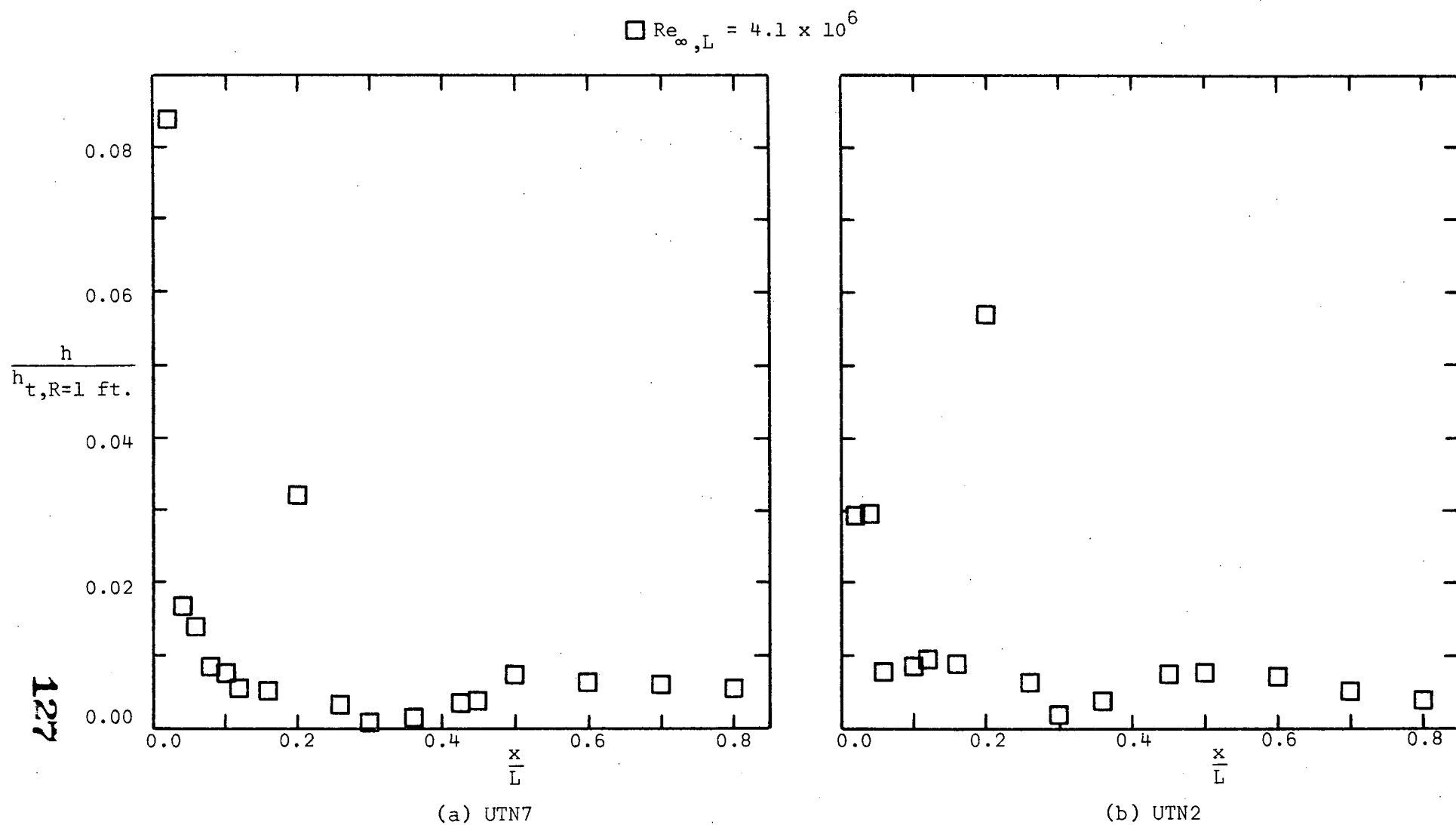
(b) x = 0.27L

Figure 29. - Concluded.

125

Figure 30. - The heat-transfer distribution for the leeward pitch-plane for
the orbiters at an alpha of 20°.

$$\square \, Re_{\infty,L} = 4.1 \times 10^6$$

(a) UTN7

(b) UTN2

Figure 31. - The heat-transfer distribution for the leeward pitch-plane for the orbiters at an alpha of 25°.

127

Figure 32. - The heat-transfer distribution for the leeward pitch-plane
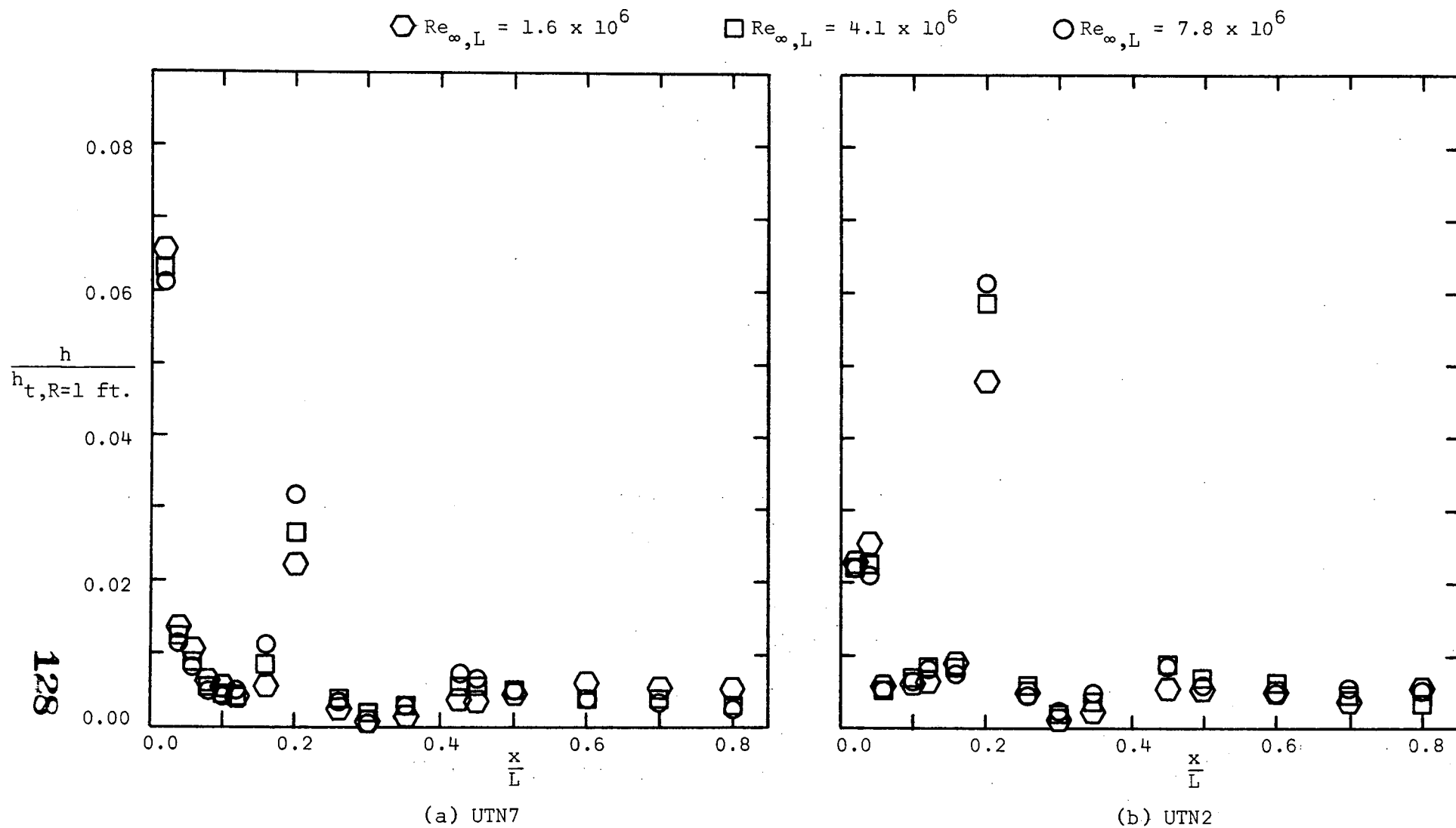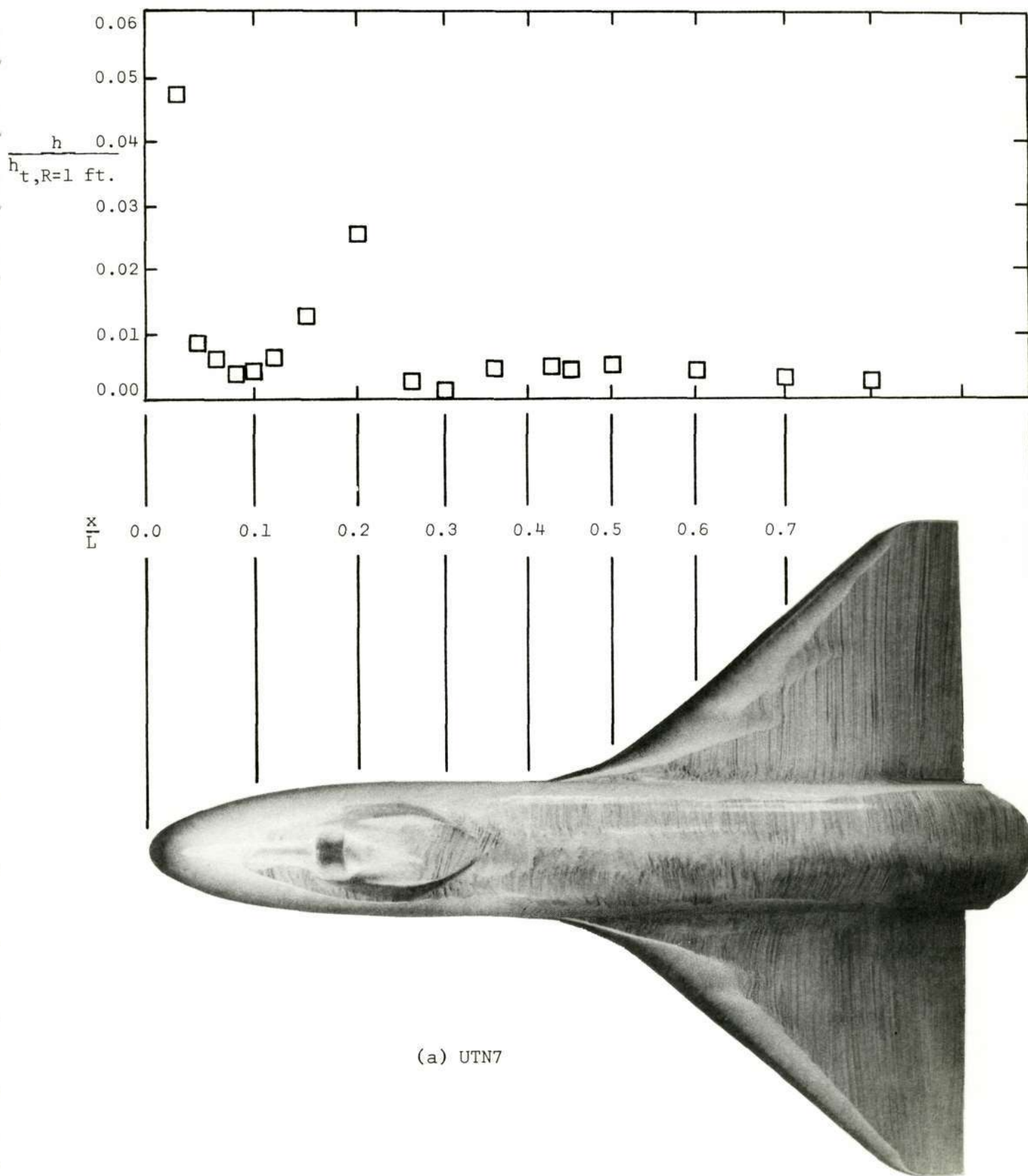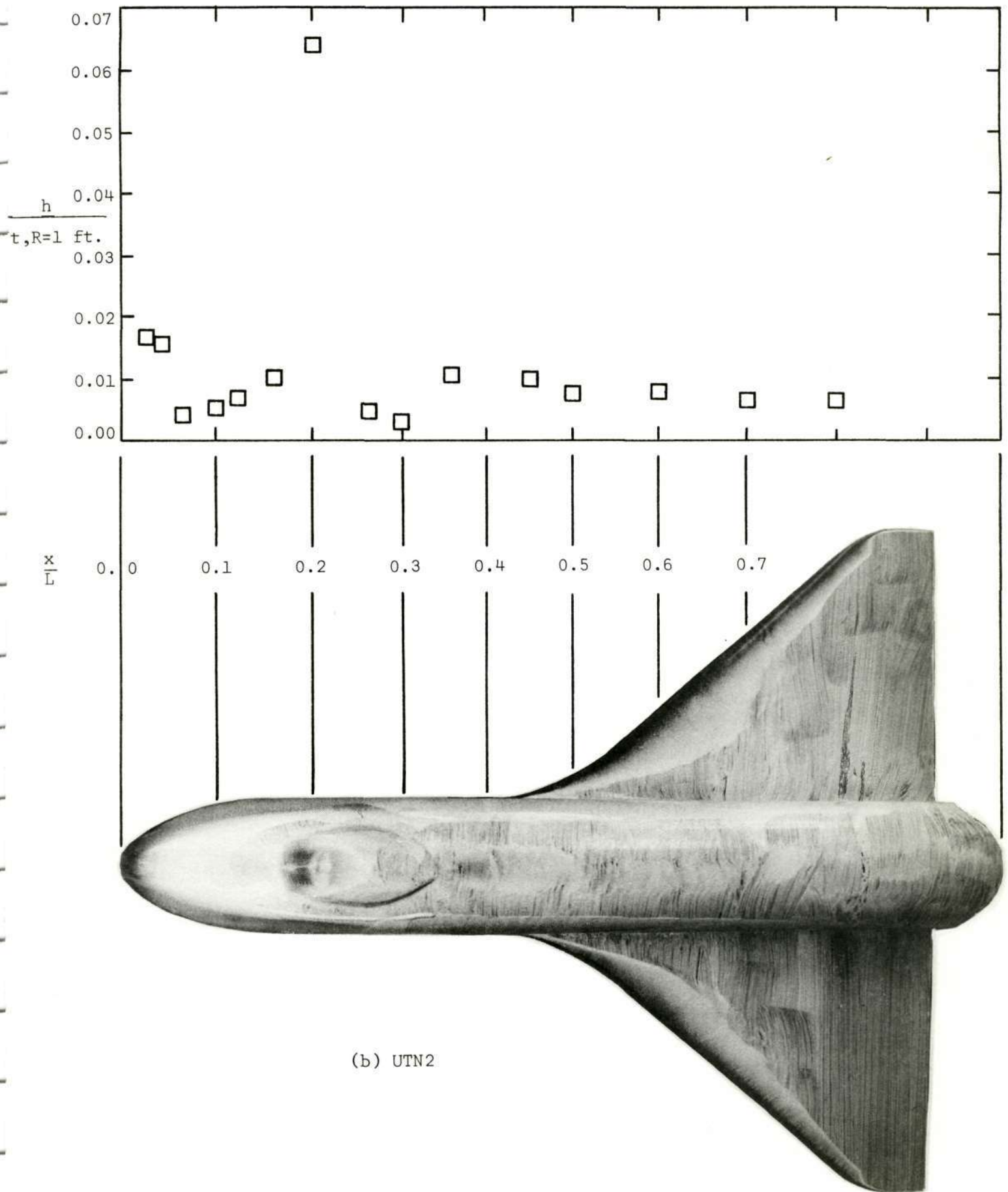for the orbiters at an alpha of 30°.

Figure 33. - The heat-transfer distribution for the leeward
pitch plane and the oil-flow pattern for the orbiters at
an alpha of 35°. ($Re_{\infty,L}$ = 4.1 x 10^6 for data)
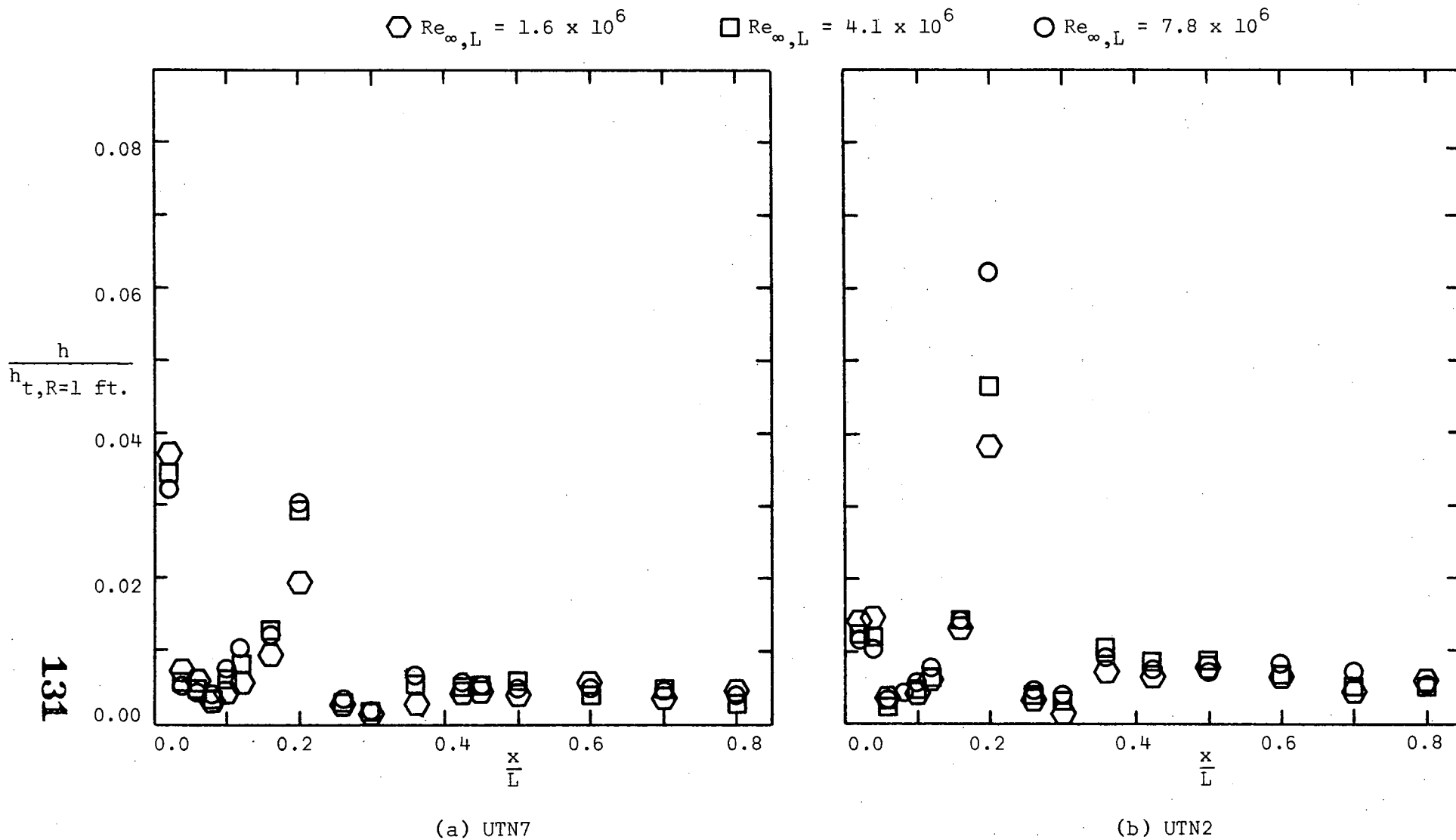
129

(b) UTN2

Figure 33. - Concluded.

Figure 34. - The heat-transfer distribution for the leeward pitch-plane for
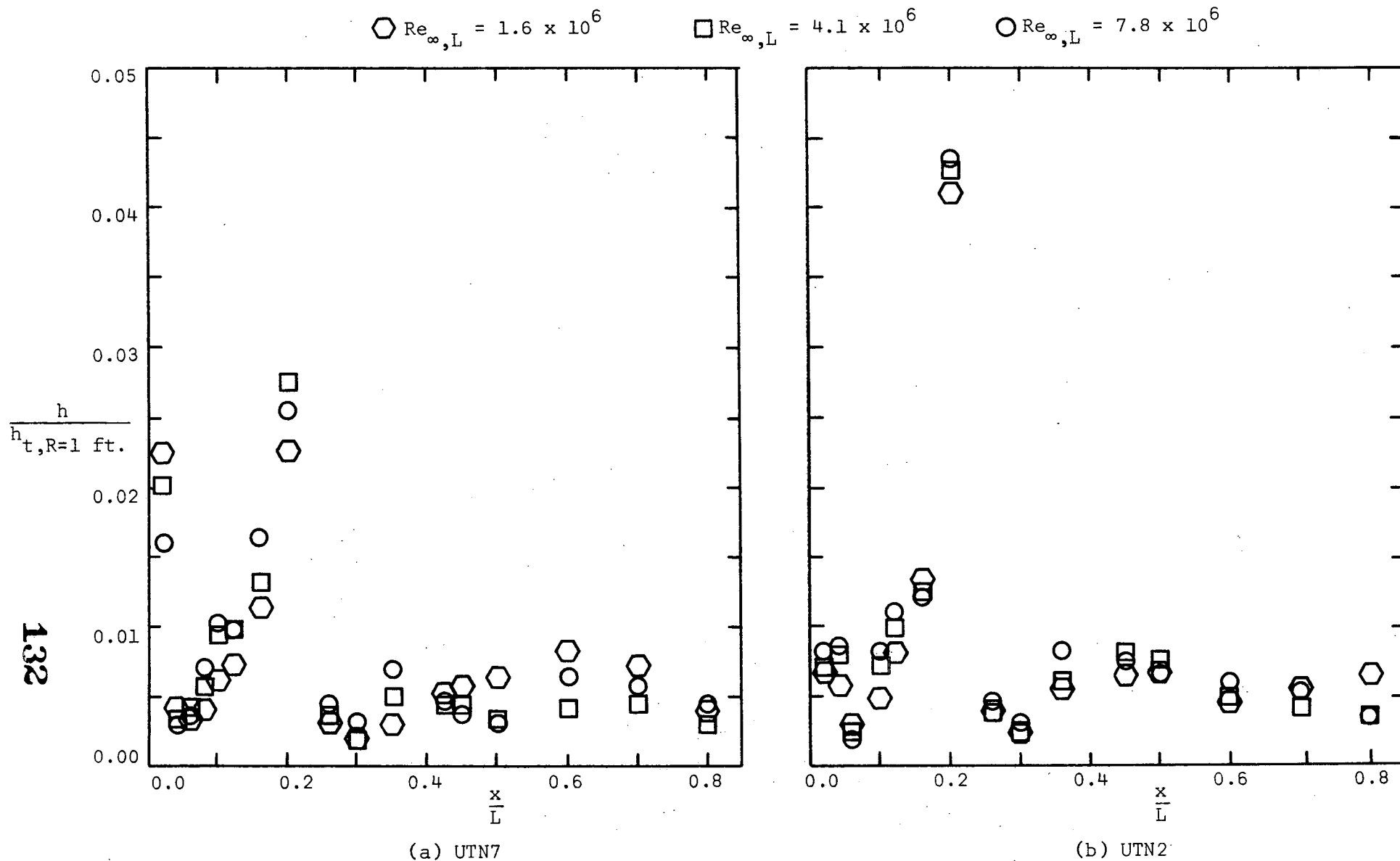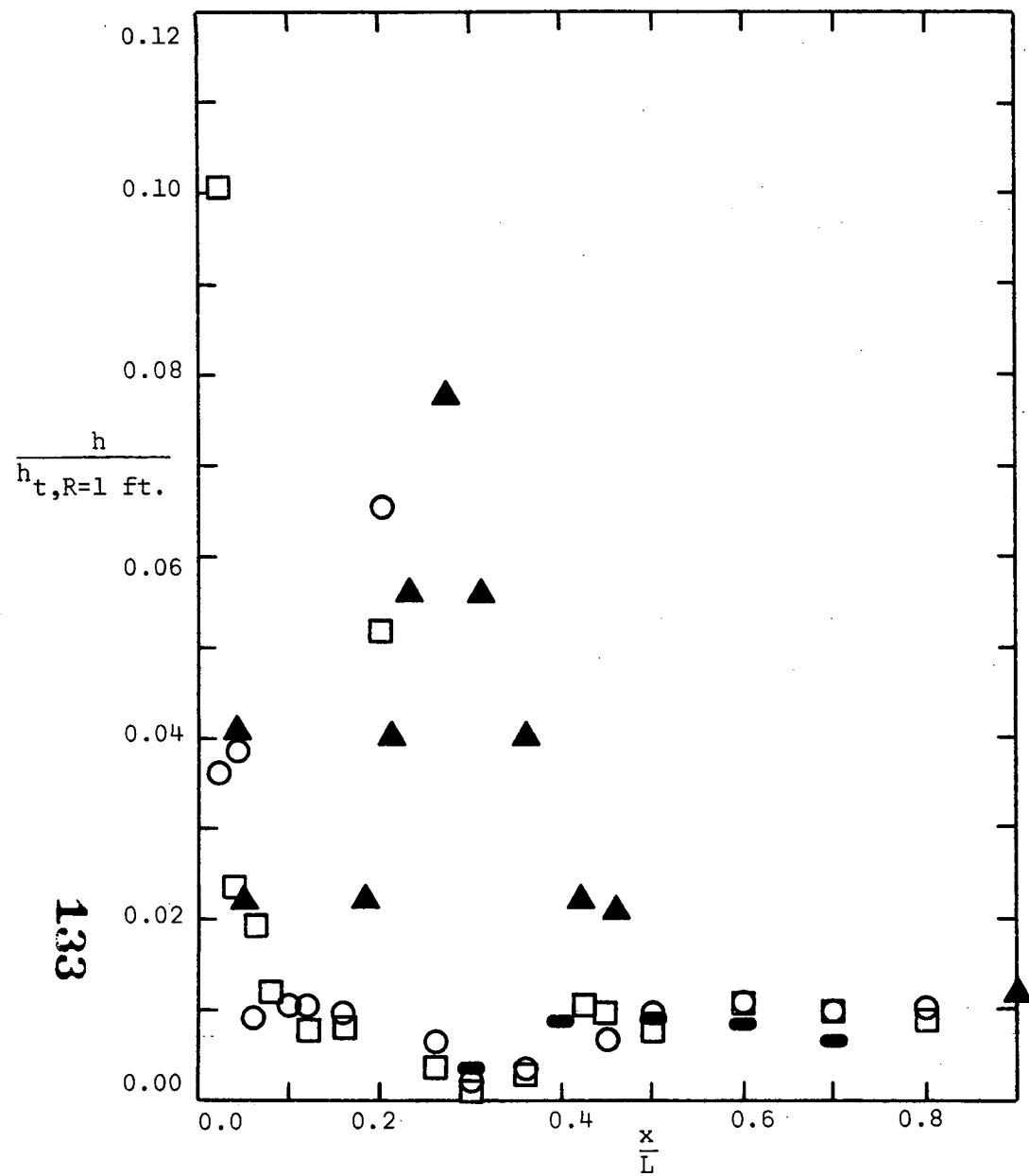the orbiters at an alpha of 40°.

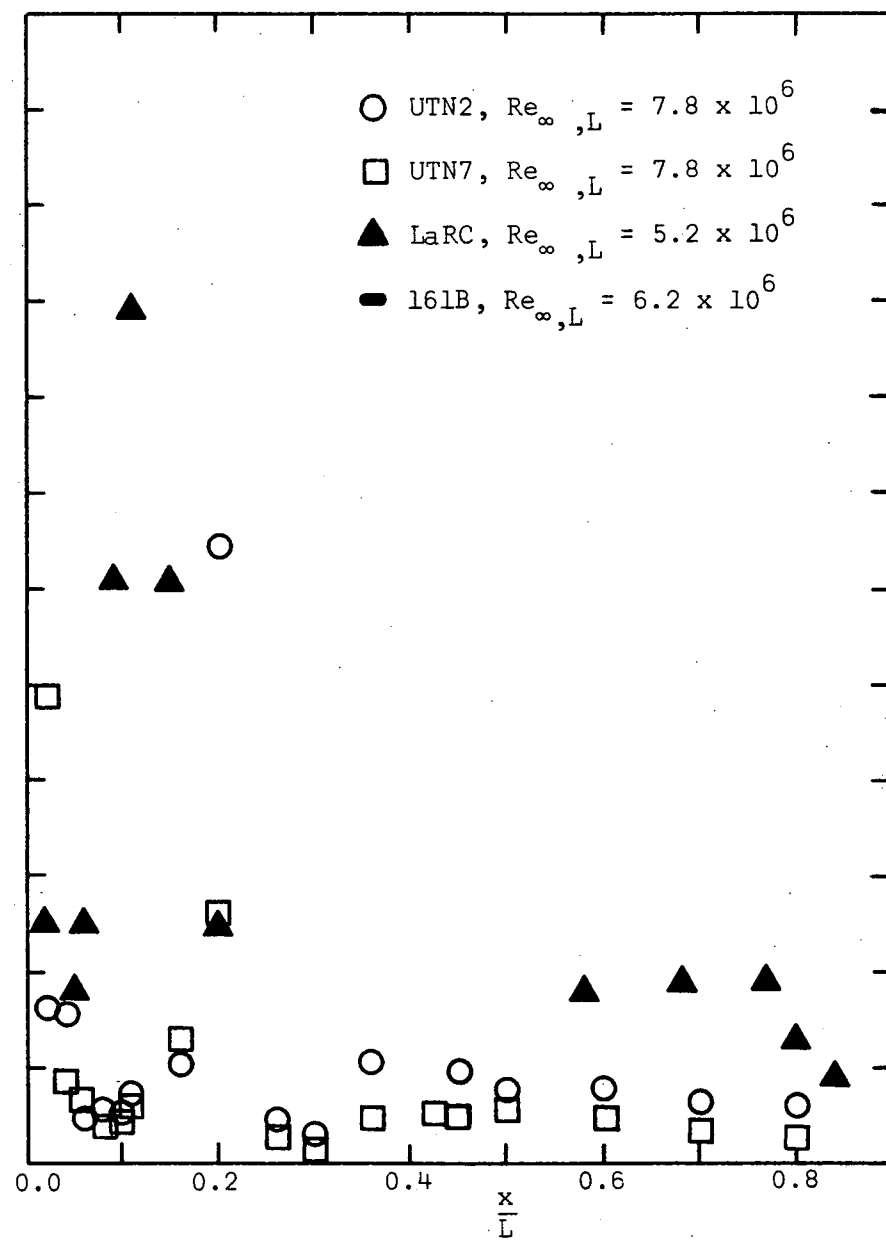Figure 35. - The heat-transfer distribution for the leeward pitch-plane
for the orbiters at an alpha of 50°.

132

(a) $\alpha = 20°$

(b) $\alpha = 35°$

Figure 36.- A comparison of the heat-transfer distributions in
the leeward pitch plane for delta-wing orbiters.

The vertical axis label reads $\dfrac{h}{h_{t,R=1\ \text{ft.}}}$ with values 0.00, 0.02, 0.04, 0.06, 0.08, 0.10, 0.12.

The horizontal axis label reads $\dfrac{x}{L}$ with values 0.0, 0.2, 0.4, 0.6, 0.8.

Legend:
- ○ UTN2, $Re_{\infty,L} = 7.8 \times 10^{6}$
- □ UTN7, $Re_{\infty,L} = 7.8 \times 10^{6}$
- ▲ LaRC, $Re_{\infty,L} = 5.2 \times 10^{6}$
- ◖ 161B, $Re_{\infty,L} = 6.2 \times 10^{6}$

(c) $\alpha = 40°$

(d) $\alpha = 50°$

134
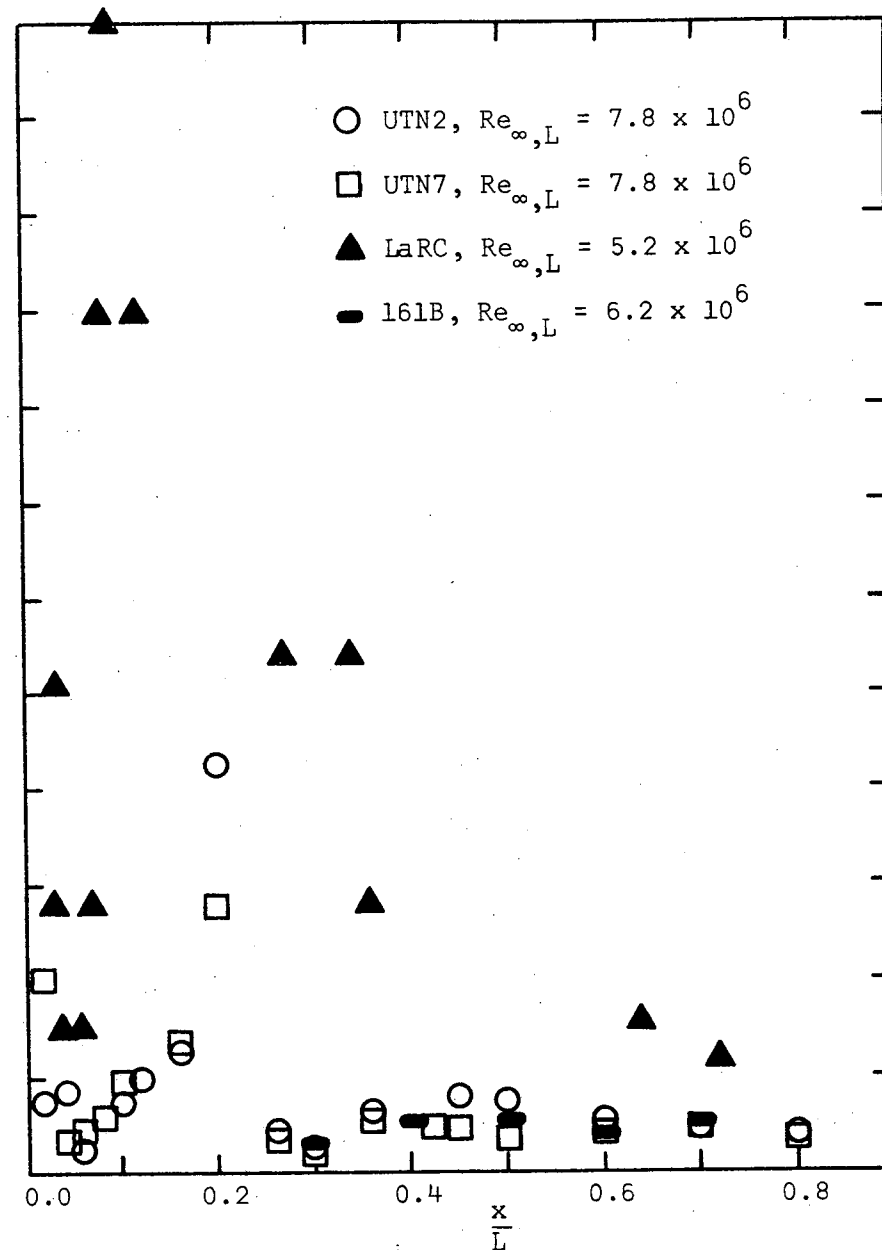
Figure 36. - Concluded.

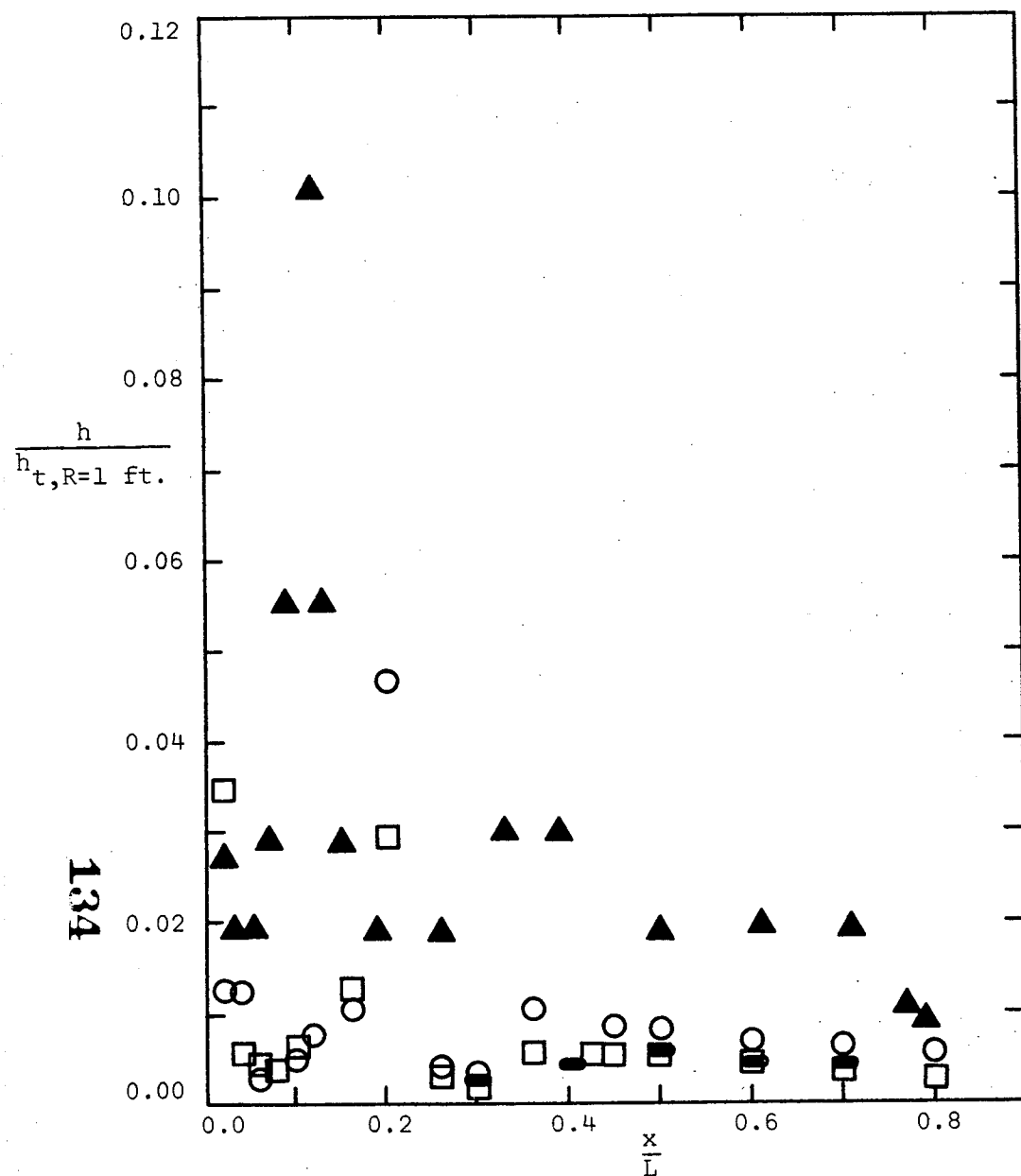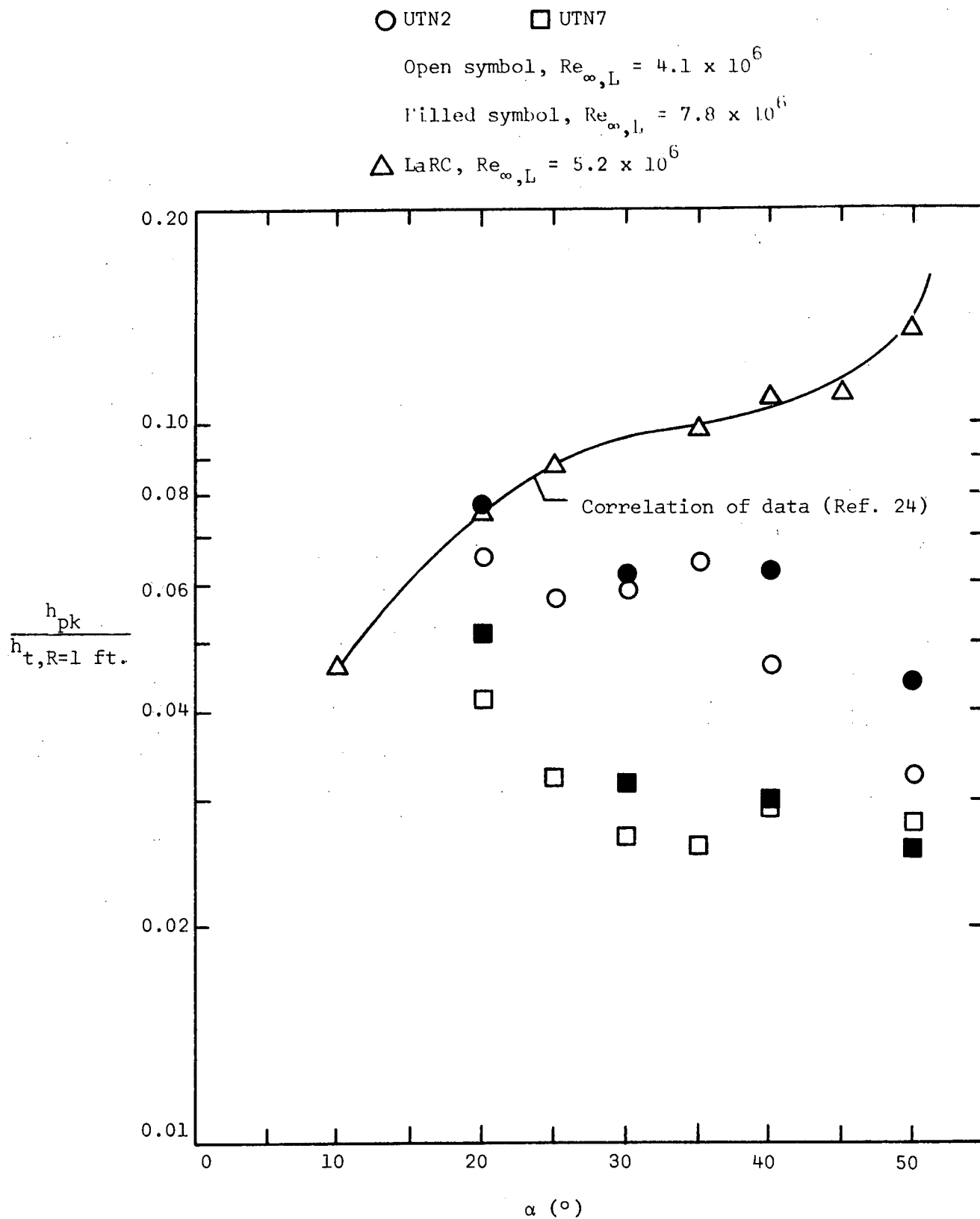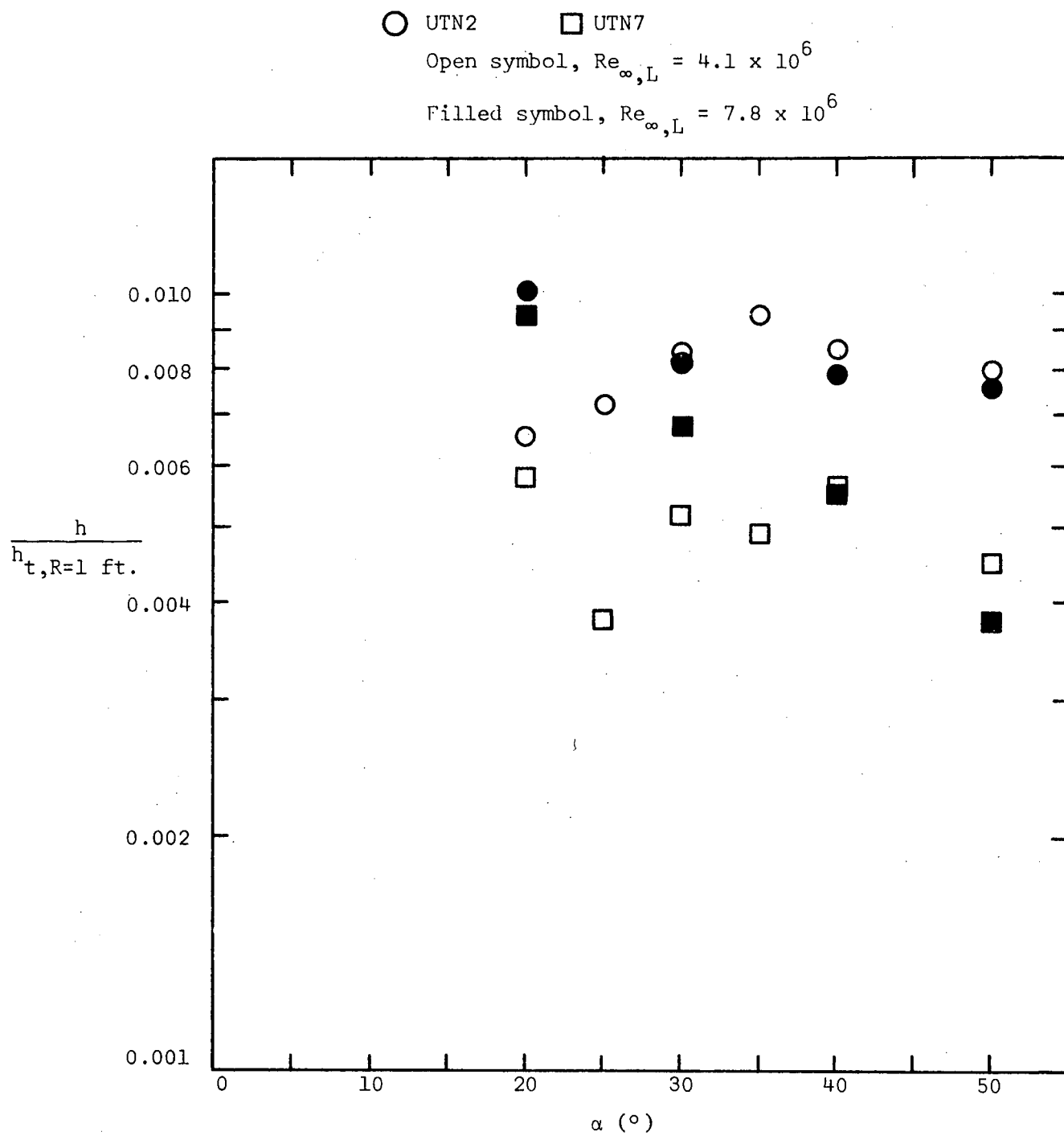Figure 37. - Effect of alpha on the peak heat-transfer measurement in the leeward pitch-plane of delta-wing orbiters.

(a) x = 0.45L

Figure 38. - The local lee-meridian heat-transfer rates for the fuselage as a function of alpha.

136
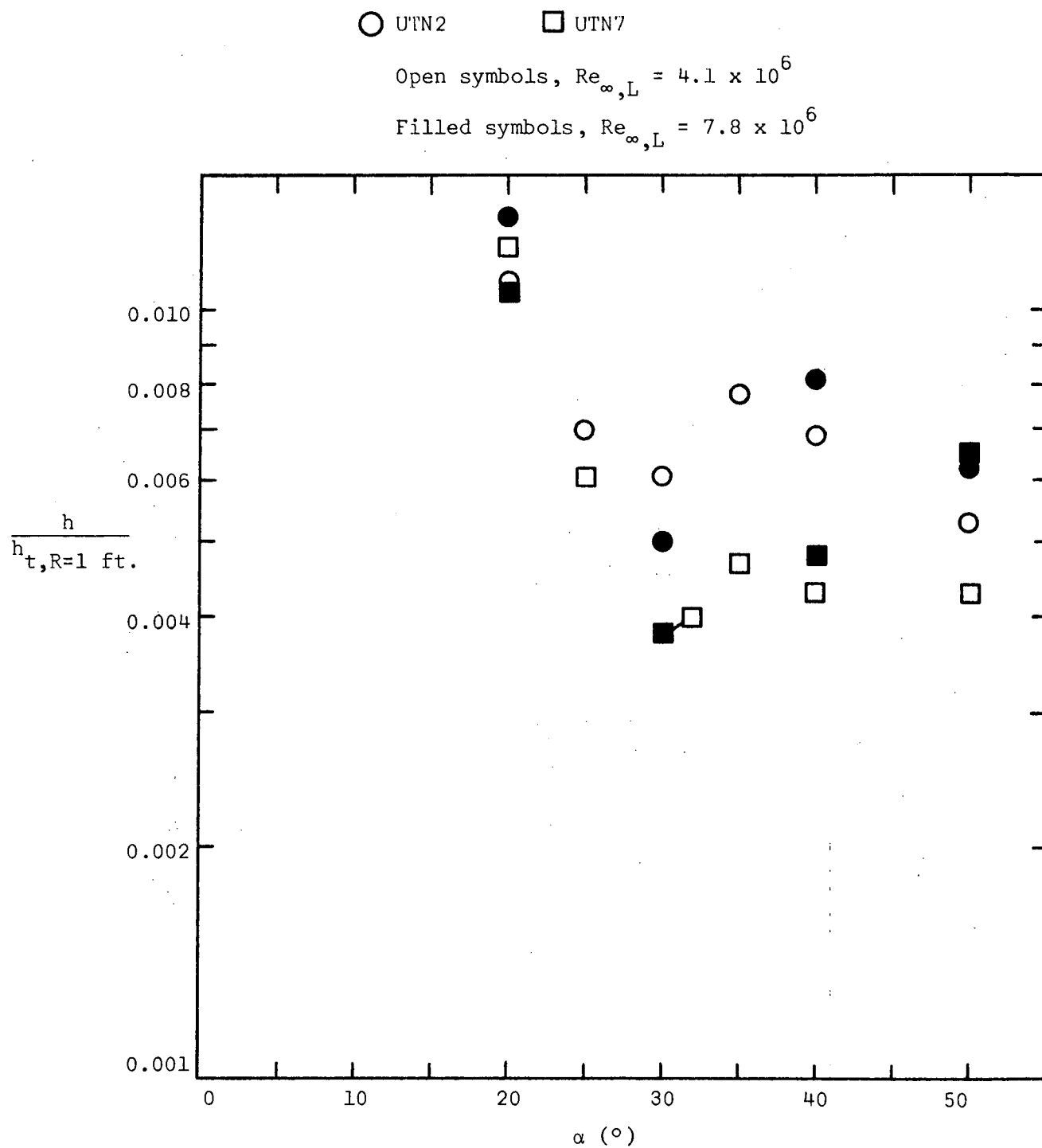
(b) x = 0.60L

Figure 38. - Concluded.

137
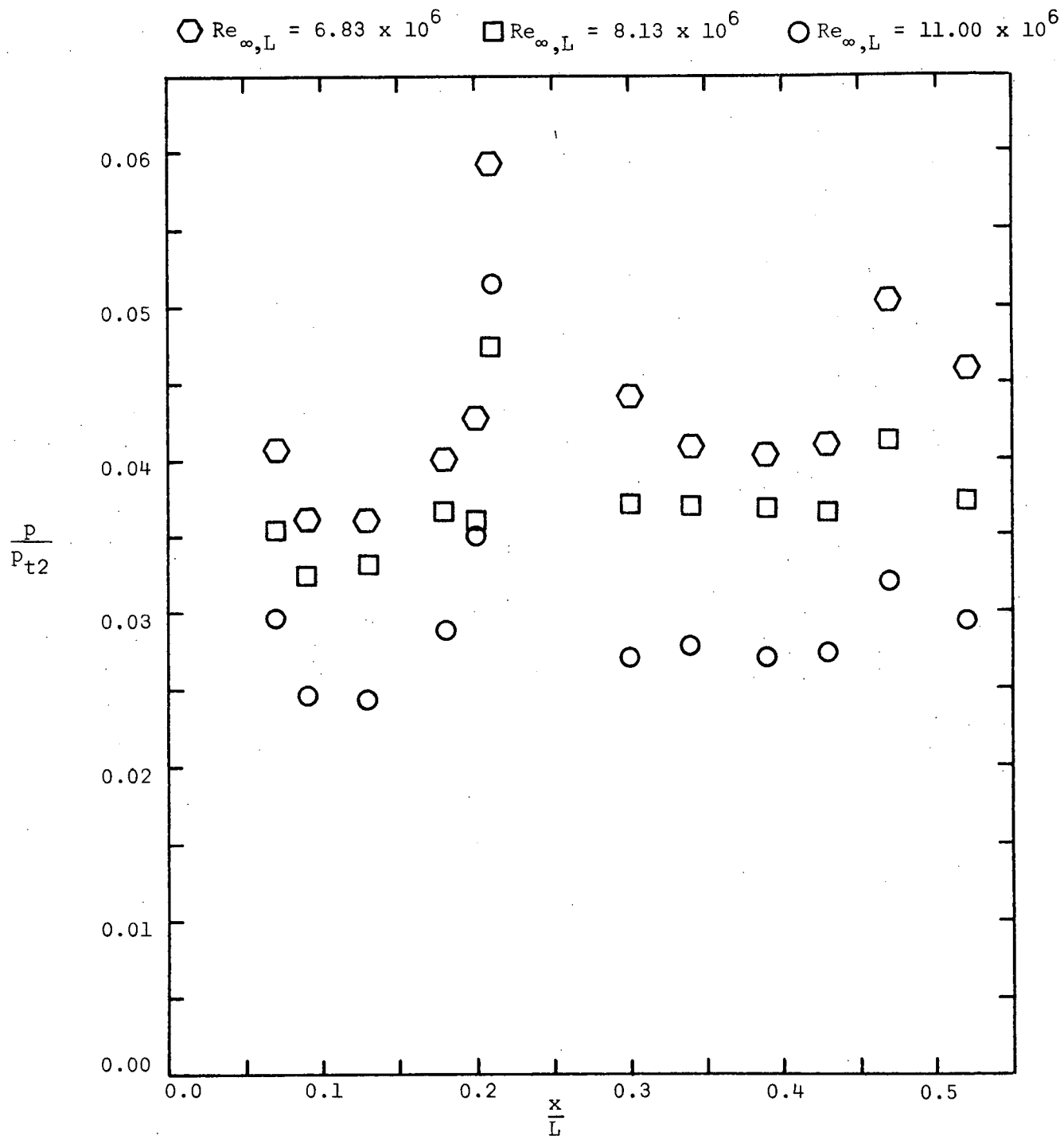
Figure 39. - Pressure-distribution for the leeward pitch-
plane of the UTN2 as a function of Reynolds number.
Alpha of 31°.

Angle-of-attack

◯ = 19.5°   ☐ = 24°   △ = 31°   ⬡ = 43°

Figure 40. - Pressure-distribution for the leeward pitch-plane of the UTN2 as a function of alpha. $Re_{\infty,L} = 8.1 \times 10^6$.

139

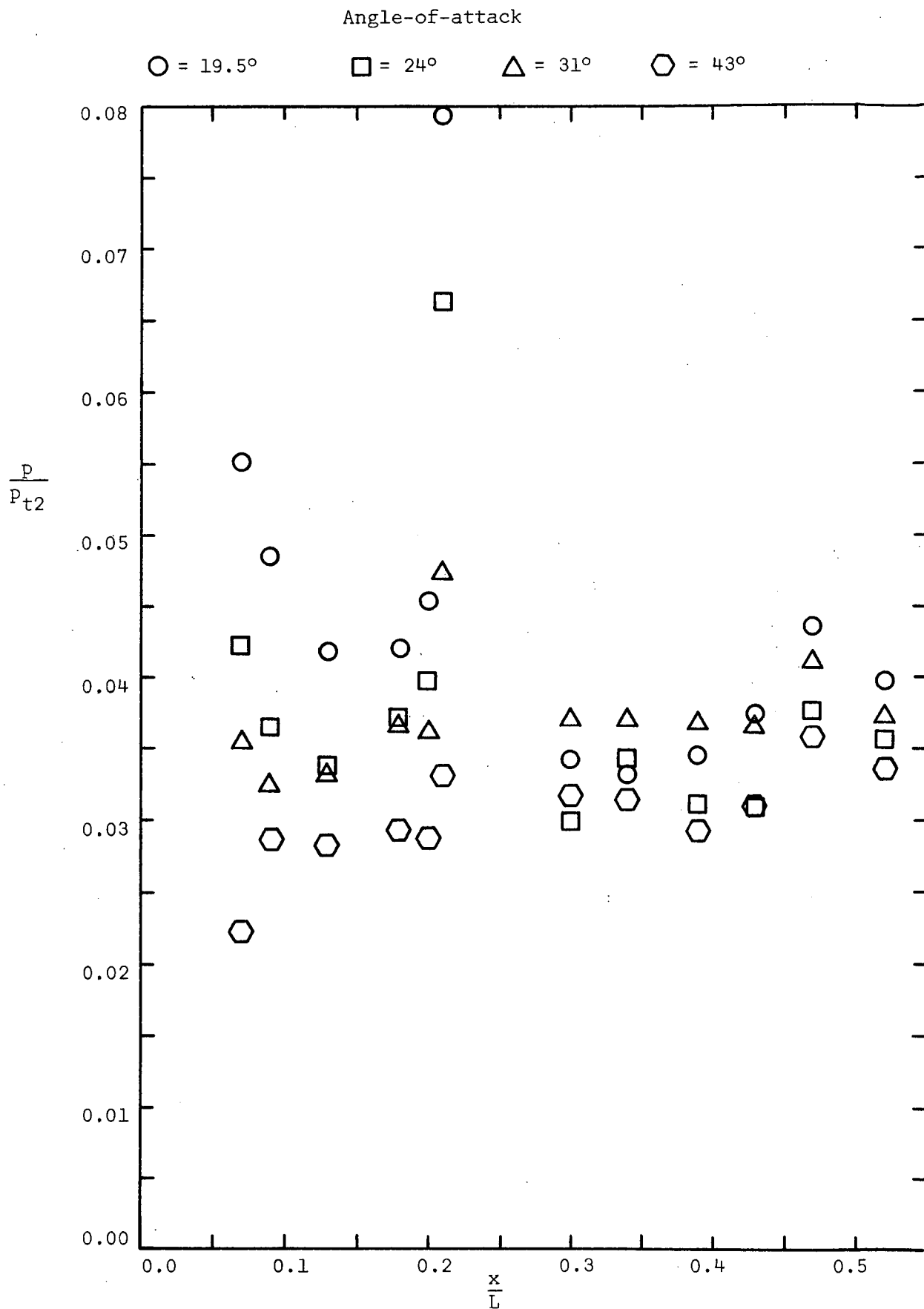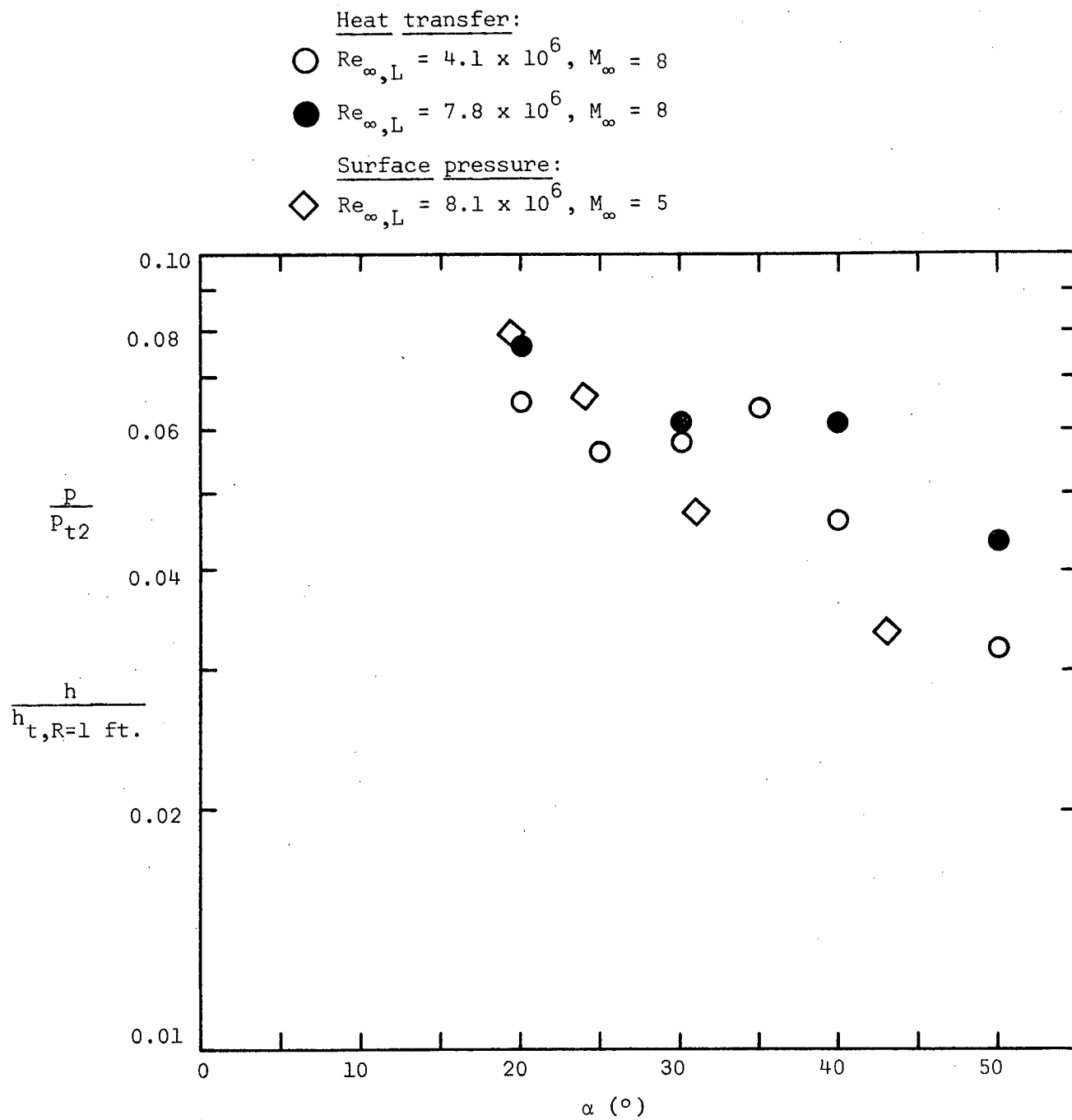Figure 41. - The maximum lee-meridian heating rate and the maximum lee-meridian surface-pressure as a function of alpha for the UTN2.

140

APPENDIX A - GEOMETRY OF THE UTN2 AND THE UTN7

SECTIONS (WITHOUT CANOPIES)

Since both models have geometrically identical side views, this appendix will be divided into three parts. The first part will contain a description of the side view geometry. The planform and cross-section criteria for the UTN2 and for the UTN7 will be described in the other two parts.

The coordinate system used to describe the models is a right-hand system in which "x" lies along the longitudinal axis of the model; "y" describes the vertical axis, such that the windward surface is positive; and "z", the width axis. (Refer to Figs. 2, A-1, and A-2.) The coordinate system origin is located at the apex of the nose (station 200). Note: all dimensions have been nondimensionalized using the nominal length of the AEDC models, i.e., 25 inches, as a reference. Therefore, when a coordinate parameter such as x is used in this appendix, it corresponds to x/L as used in the body of this report.

Both nose sections are mated with the same fuselage at x = 0.38 (station 700). The mating cross section is made up of a flat horizontal bottom with vertical linear sides and topped by a tangent semicircle. Both nose sections are modified to fair "smoothly" into the common aft-fuselage.

Side-View Geometry

The side view of the present configurations (Fig. A-1) is similar to that configuration 040A. The contour can be described by a series of elementary curves which are tangent to each other. The geometry can be described as follows.

141

Above the chine (y < 0), i.e., the leeward pitch-plane:

Region I (0 $\leq$ x $\leq$ 0.04)

The leeward pitch-plane in this section is defined by an ellipse whose

equation is: y = - (1.89755 - 0.714369 (1.629805 - 25.x)^2)$^{\frac{1}{2}}$/25.   (Region I)

Region II (0.04 $\leq$ x $\leq$ 0.1881)

The surface is linear in this region with the same slope as the 040A, i.e.,

a slope of 20°. The governing equation is: y = - (8.853x + 0.91639)/25.
                                                                    (Region II)

Region III (0.1881 $\leq$ x $\leq$ 0.3036)

This is the canopy region for the 040A and for the present configurations.

Without the canopy, this region is described by an ellipse, which is tangent to

the two linear segments bounding it. The governing equation for the ellipse is:

y = -((125.13142 - 1.30743 (7.5905 - 25.x)^2)$^{\frac{1}{2}}$ - 8.10774)/25.   (Region III)

Region IV (0.3036 $\leq$ x $\leq$ 0.38)

The surface in Region IV is a horizontal linear segment, as was the case

for the 040A. Thus, y = - 0.12316   (Region IV)

Below the chine (y > 0); i.e., the windward pitch-plane:

One of the mating requirements is that the model bottom have a slope of -3.°

at x = 0.38 (station 700). It was decided that the windward pitch-plane would be

defined by an ellipse followed by a linear element of slope -3.°.

Region V (0 $\leq$ x $\leq$ 0.19)

Region V is an ellipse whose equation is:

y = (0.819 - 0.0107 (8.75 - 25.x)^2)$^{\frac{1}{2}}$/25.   (Region V)

At x = 0.19 the slope is -3.°.

142

Region VI $(0.19 \leq x \leq 0.38)$

This is the straight line whose slope is -3.°. The equation of the line

is: $y = (0.80512 + 0.05241 (25.x - 4.75))/25.$ (Region VI)

Planform and Cross-Section Criteria for the UTN2

Planform:

The forward part of the planform of the UTN2 is an ellipse whose axes ratio

is 5:2. The aft part of the planform is linear and tangent to the points of

maximum width of the forward ellipse. Refer to Fig. A-2. The governing relations

are:

Forward, $0 \leq x \leq 0.19$:

$\pm z = (1.936^2 - (1.936/4.75)^2 (4.75 - 25.x)^2)^{\frac{1}{2}}/25.$ (a-1)

Aft, $0.19 \leq x \leq 0.38$:

$\pm z = 0.0774$ (a-2)

Cross sections:

Below the chine $(y \geq 0)$, i.e., the windward surface:

The criteria in the design of the lower cross sections is that any section

taken in a horizontal plane (x - z plane) has the same geometry as the planform.

To obtain the surface coordinates, the planform outline is translated axially and

vertically so as to satisfy the side view geometry requirements. This results in

a cross section which is much "blunter" than an elliptic section. Refer to Figs.

A-2 and A-3,

To avoid a surface discontinuity about the point at which the side view be-

comes linear (x = 0.19, station 450) the horizontal cross sections below the

143

y-coordinate at x = 0.19 are not required to match the planform silhouette. Instead, a "fill-in" ellipse in the y - z plane tangent to the model sides at the depth of the y-coordinate at x = 0.19 is used to complete the cross section. Refer to Fig. A-4.

Above the chine (y ≤ 0), i.e., the leeward surface:

For x ≤ 0.19 the cross section is composed of a circular arc, a linear element ("fall away" side), and a cap ellipse. In the region x < 0.04 the height of the circular arc and the depth of the elliptic section are 0.004. The fall-away angle of the linear side is given by (as illustrated in Fig. A-3):

$$ANGLE = 25. - (10./3.5) (25.x - 0.5) \text{ degrees} \tag{a-3}$$

The fall-away angle is the acute angle between a vertical and the linear element of the cross section. The circular arc, the linear element, and the elliptic section are mated such that the slope is continuous.

For the region 0.04 ≤ x < 0.19 the height of the circular arc (CIR) is (see Fig. A-3):

$$CIR = (0.1 + 0.05 (25.x - 1.))/25. \tag{a-4}$$

and the depth of the cap ellipse (ELL) is:

$$ELL = (25.y_{cl} - 1.17051 - 0.3041 (25x - 1)/25. \tag{a-5}$$

"y_{cl}" is the surface coordinate of the leeward pitch plane at the axial point of interest. For x < 0.16 the fall away angle is given by:

$$ANGLE = 25. - (10./3.5) (25.x - 0.5) \text{ degrees} \tag{a-6}$$

For x ≥ 0.16 the fall away angle changes to:

$$ANGLE = 15. - (15./5.5) (25.x - 4.) \text{ degrees} \tag{a-7}$$

At x = 0.19 a vertical flat side is initiated to accomodate mating with the fuselage at x = 0.38. This vertical flat surface lengthens as x increases.

144

For $0.19 \leq x < 0.25$ the cross section is composed of a vertical flat element, a circular arc, a linear fall away element, and a cap ellipse. Refer to Fig. A-4. The governing relations are:

Height of the vertical flat side (yf):

$$yf = 1.14293 \ (25.x - 4.75)/118.7 \tag{a-8}$$

And the height of the circular section:

$$CIR = 0.1 + 0.05 \ (25.x - 1.) - yf \tag{a-9}$$

The fall away angle:

$$ANGLE = 15. - (15./5.5) \ (25.x - 4.) \ degrees \tag{a-10}$$

Depth of the cap ellipse section:

$$ELL = (25.y_{cl} - 2.310885 + 1.167955 \ (25.x - 4.75)/4.75)/25. \tag{a-11}$$

Note that the height of the circular section is reduced by the length of the vertical flat side. In the region $0.19 \leq x < 0.25$ the slope is continuous.

At $x = 0.25$ the height of the circular section becomes zero. Hence, for $0.25 \leq x \leq 0.38$ the cross section is composed of a vertical flat side, a linear fall away element, and a cap ellipse. The slope is continuous except at the intersection of the vertical flat side and the linear fall away element. At this intersection the slope changes by an amount "ANGLE", i.e., the fall away angle. Refer to Fig. A-5. The governing relations are:

Height of vertical flat:

$$yf = 1.14293 \ (25.x - 4.75)/118.7 \tag{a-12}$$

Fall away angle:

$$ANGLE = 15. - (15./5.5) \ (25.x - 4.) \ degrees \tag{a-13}$$

And depth of cap ellipse:

$$ELL = (y_{cl} - 2.310885 + 1.167955 \ (25.x - 4.75)/4.75)/25. \tag{a-14}$$

145

At x = 0.38 these relations yield a cross section composed of a vertical flat side tangent to a circular section, as desired for fuselage mating.

Planform and Cross Section Criteria for the UTN7

Planform:

The forward part of the N7 planform is an ellipse of axes ratio 8:2. The aft part of the planform is linear and tangent to the points of maximum width of the forward ellipse. Refer to Fig. A-6. The governing relations are:

Forward, $0. \leq x \leq 0.304$:

$$\pm z = (1.936^2 - 1.936^2 (7.6 - 25.x)^2/7.6)^{\frac{1}{2}}/25. \qquad \text{(a-15)}$$

Aft, $0.304 \leq x \leq 0.38$:

$$\pm z = 0.0774 \qquad \text{(a-16)}$$

Cross sections:

For $0. \leq x \leq 0.304$ the cross sections are composed of two elliptic halves for which the ratio of axes satisfies the planform and the side-view coordinates and which intersect with a vertical slope at the chine. Refer to Fig. A-7.

For $0.304 \leq x \leq 0.38$ the cross sections are formed by a growing vertical flat side (to satisfy fuselage mating requirements) and two elliptic halves such the planform and side view are satisfied. The relations governing the size of the vertical flat follow;

The distance from the chine to the upper end of the vertical flat (yu) is:

$$yu = 1.14293 (25.x - 7.6)/47. \qquad \text{(a-17)}$$

And the distance from the chine to the lower end of the vertical flat (yl) is:

$$yl = 0.34978 (25.x - 7.6)/25. \qquad \text{(a-18)}$$

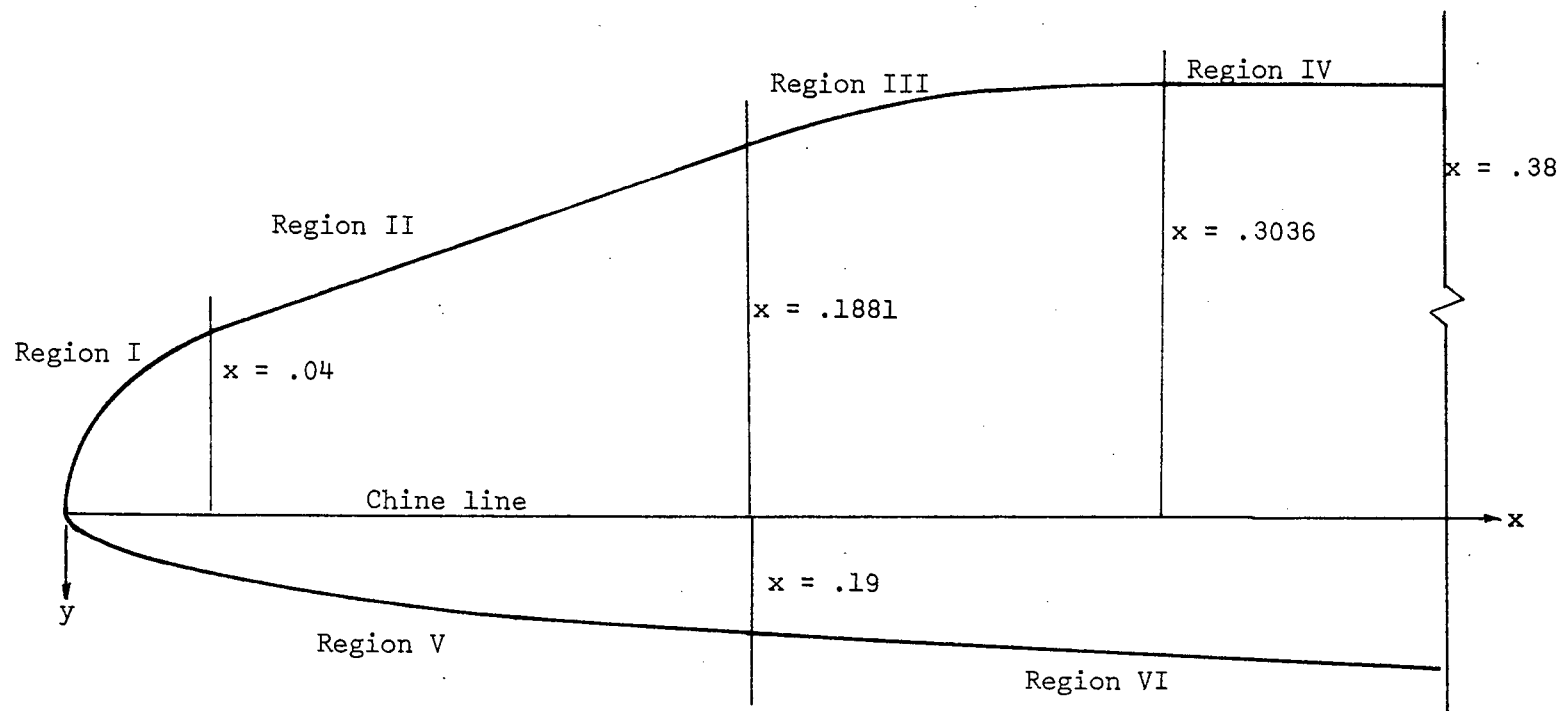The slopes are continuous for all points of the cross sections. Refer to Fig. A-8.

Figure A - 1. - Common side view for the UTN2 and the UTN7 configurations without canopy. (0.75-scale)
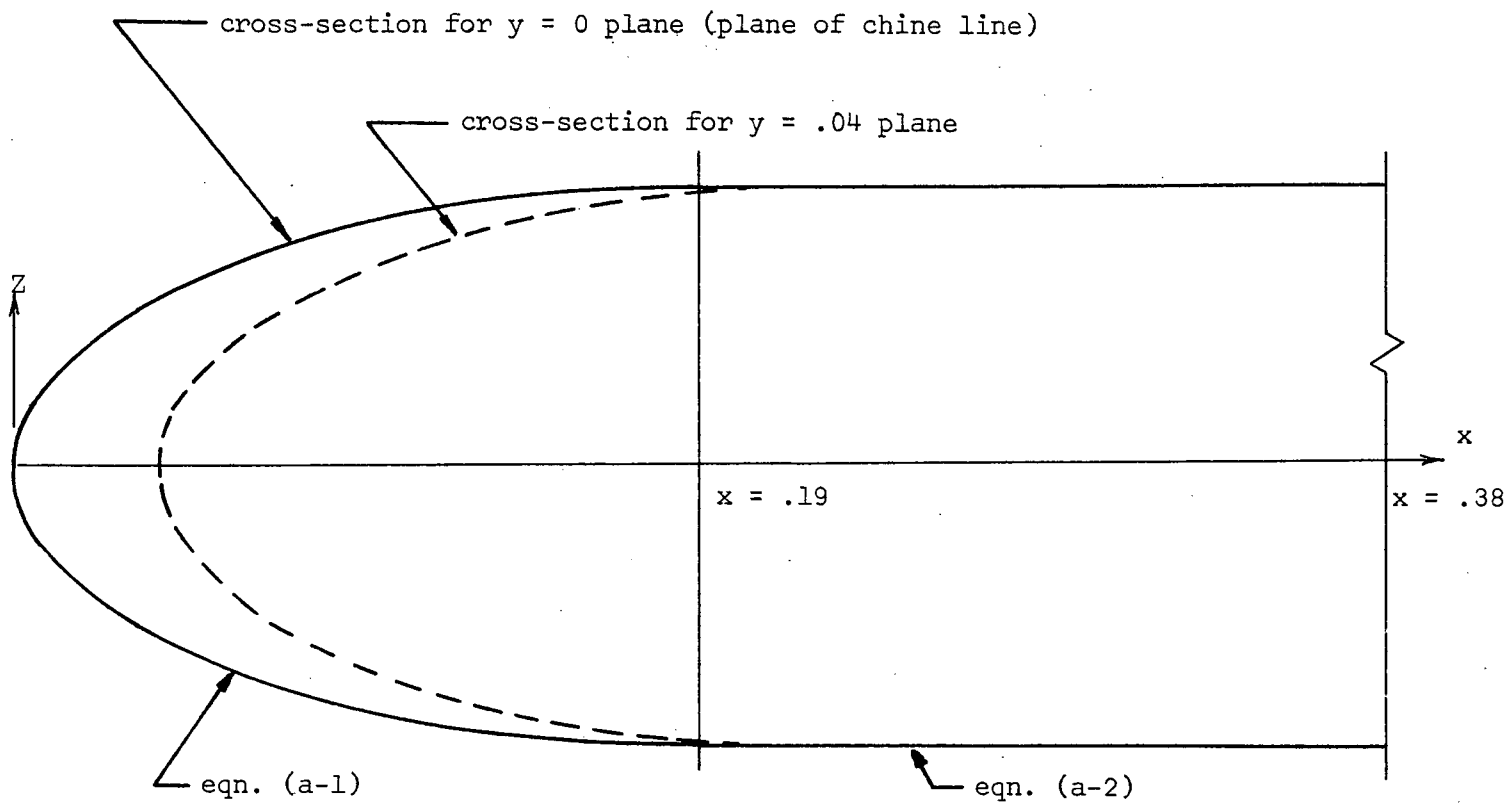
147

cross-section for y = 0 plane (plane of chine line)

cross-section for y = .04 plane

z

x

x = .19

x = .38

eqn. (a-1)

eqn. (a-2)

Figure A - 2. - Planform for the UTN2. (0.75-scale)

shallow cap ellipse, eq. (a-5)

linear "fall-away" element

"Fall-away" angle, eq. (a-6)

Circular arc, eq. (a-4)

The windward surface is defined by the translated elliptic planforms

149
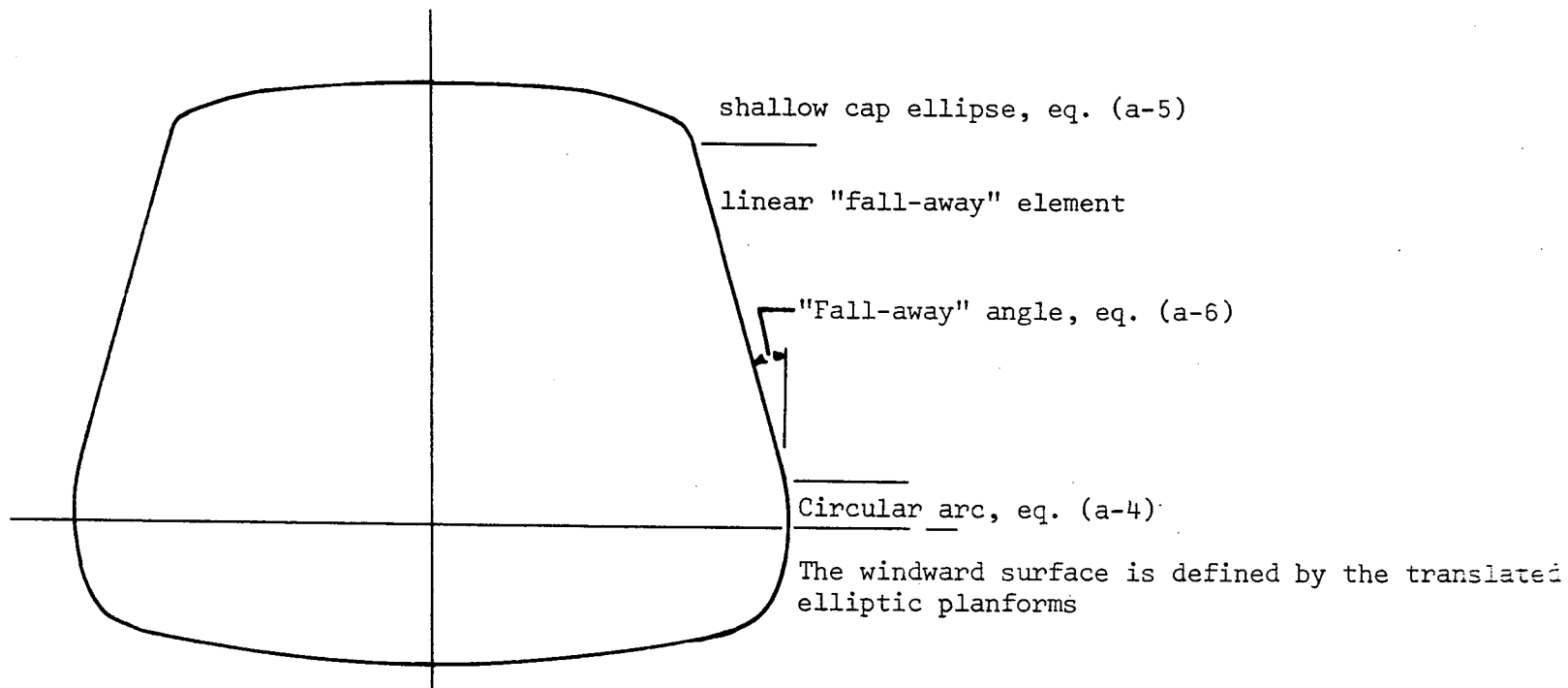
Figure A-3. - Cross-section of the UTN2 at x = .16.
    (full scale)

150

Cap ellipse, eq. (a-11)

linear "fall-away" side, eq. (a-10)

"fall-away" angle

Circular arc

Vertical flat-side for fuselage mating,
that part above the chine (eq. a-8)

Cross-section necessary to fair into
aft fuselage cross-section
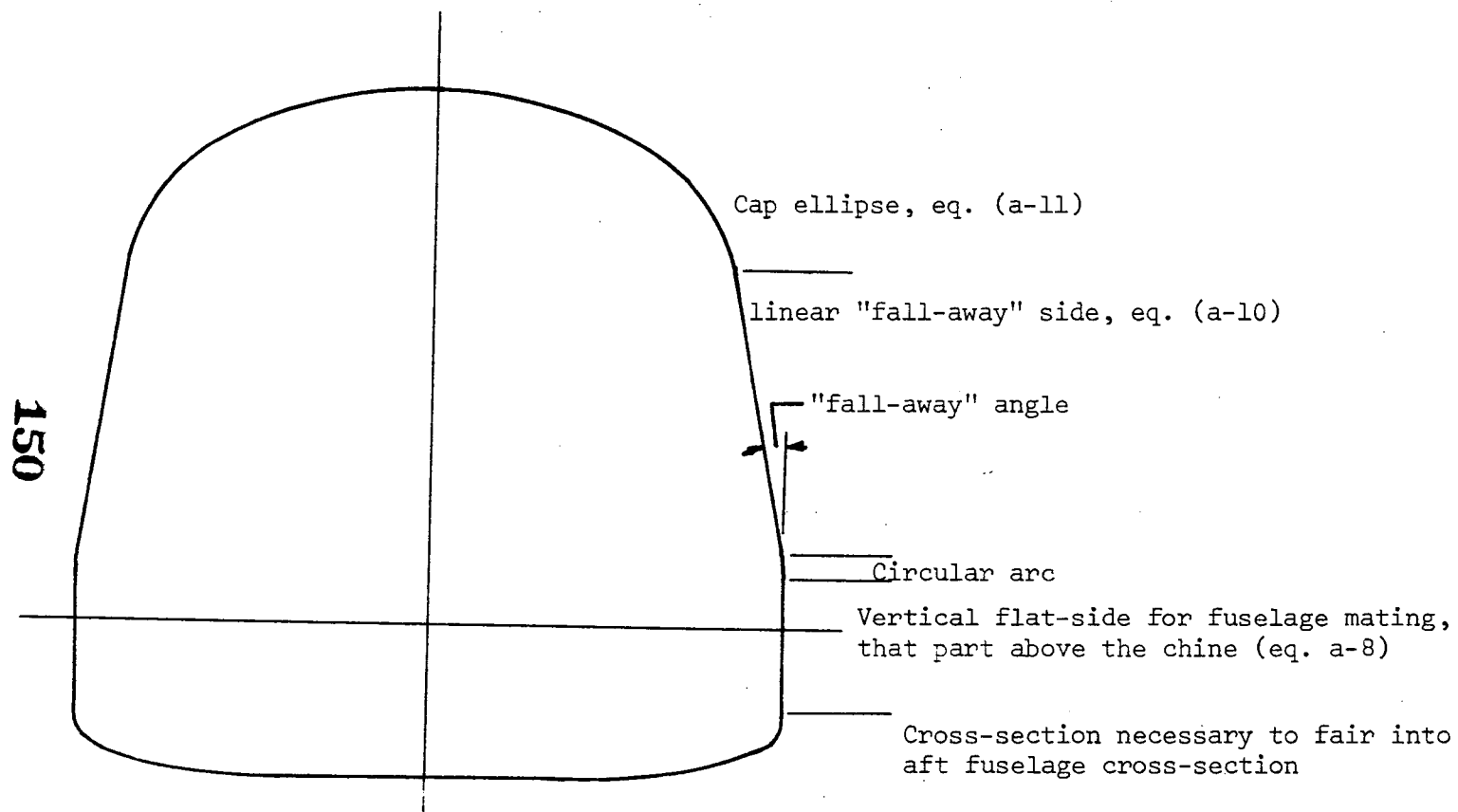
Figure A-4. - Cross-section of the UTN2 at x = .24.
(full scale)

Cap ellipse, eq. (a-14)

linear "fall-away" side, eq. (a-13)

vertical flat side for fuselage mating, which is defined by eq. (a-12)
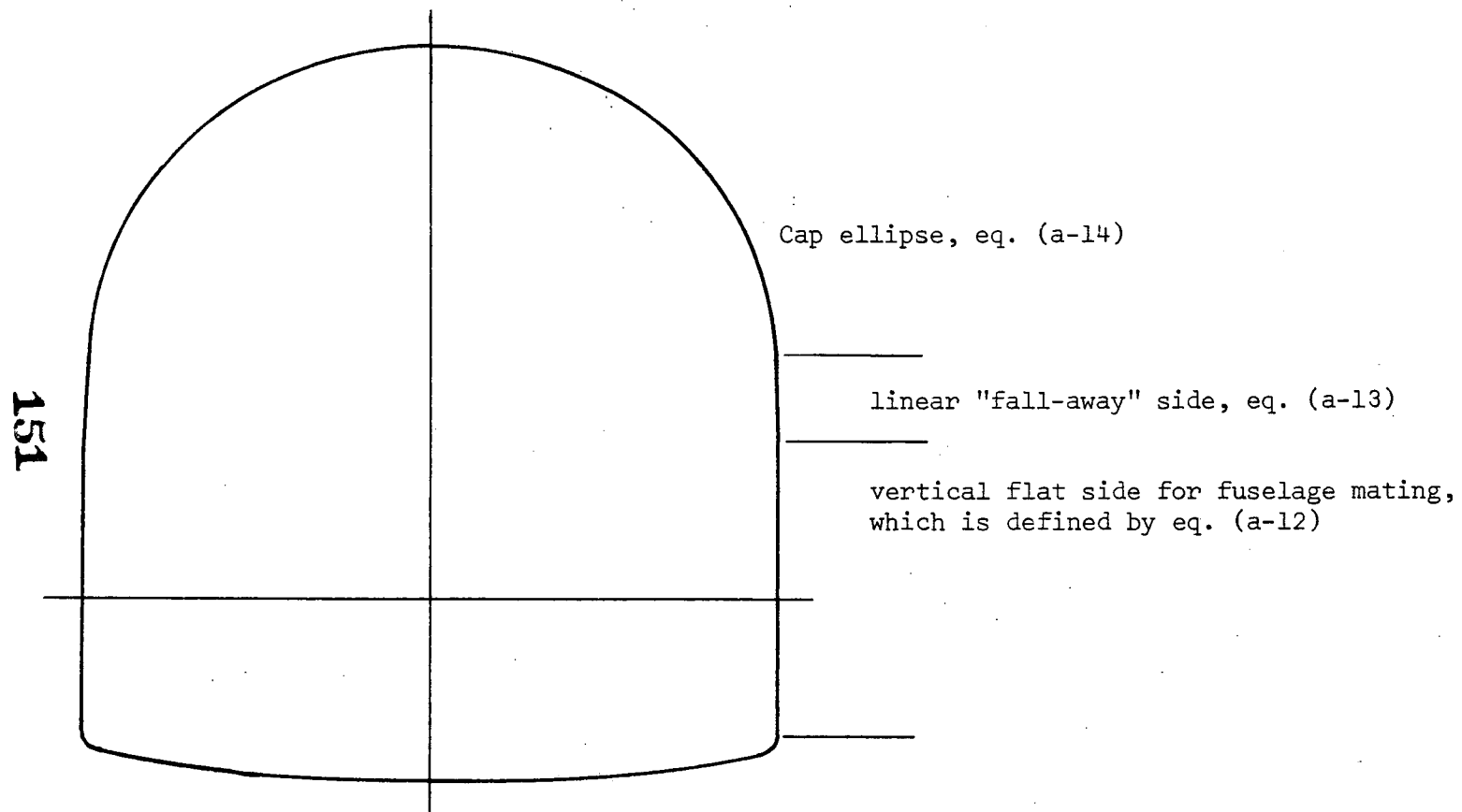
Figure A-5. – Cross-section of the UTN2 at x = .34. (full scale)
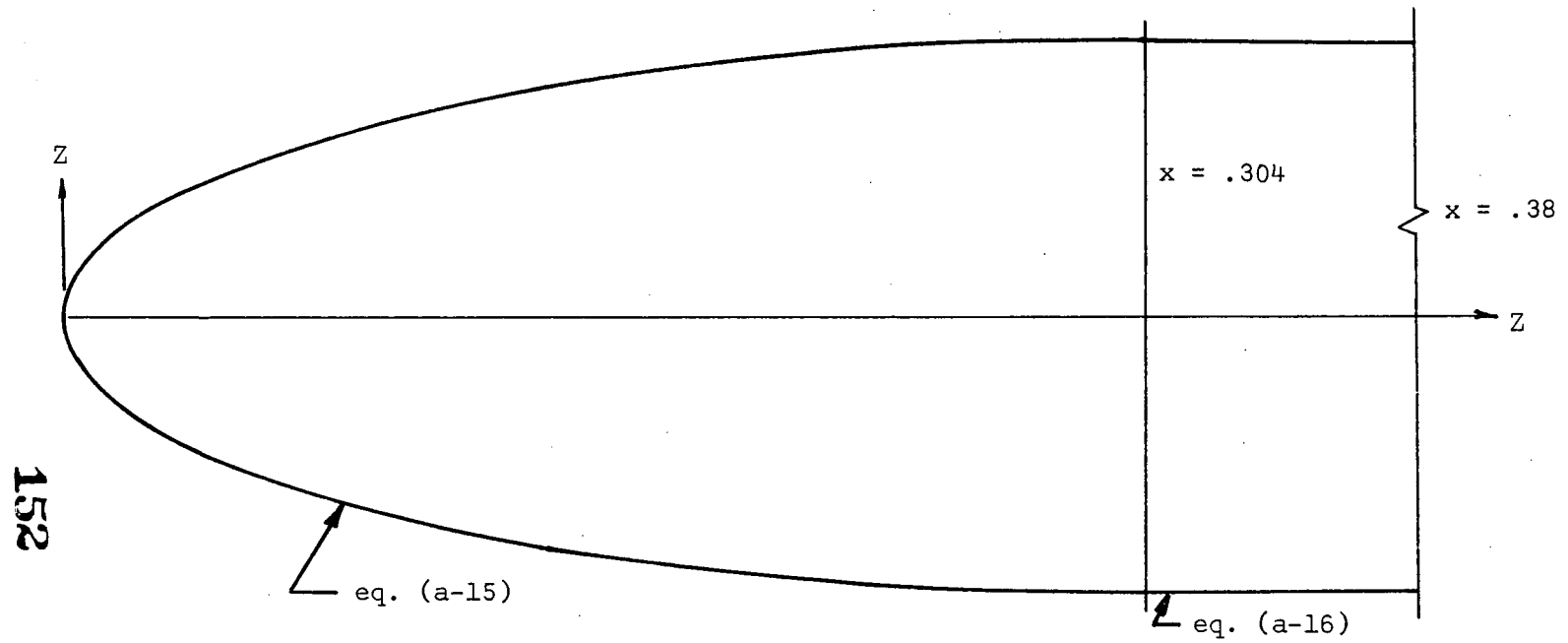
Figure A-6. - Planform of the UTN7. (0.75-scale)

leeward ellipse

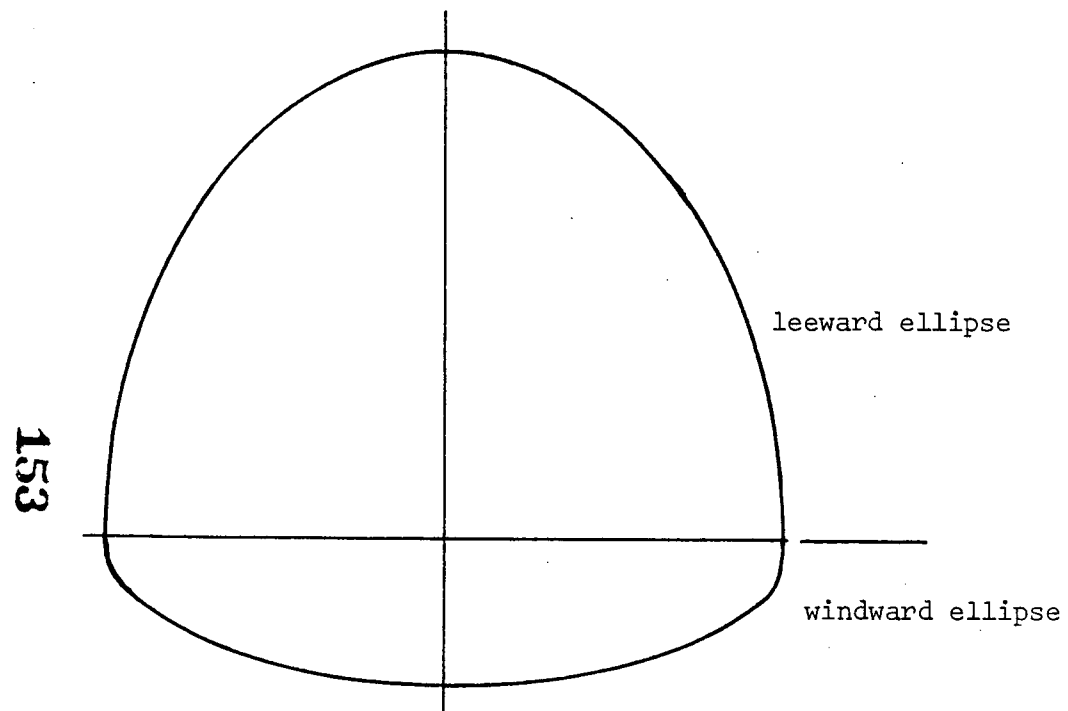windward ellipse

Figure A-7. - Cross-section of the UTN7 at x = .18.
    (full-scale)

leeward ellipse

growing vertical flat for fuselage mating,
which is described by eq. (a-17) above the
chine and by eq. (a-18) below the chine
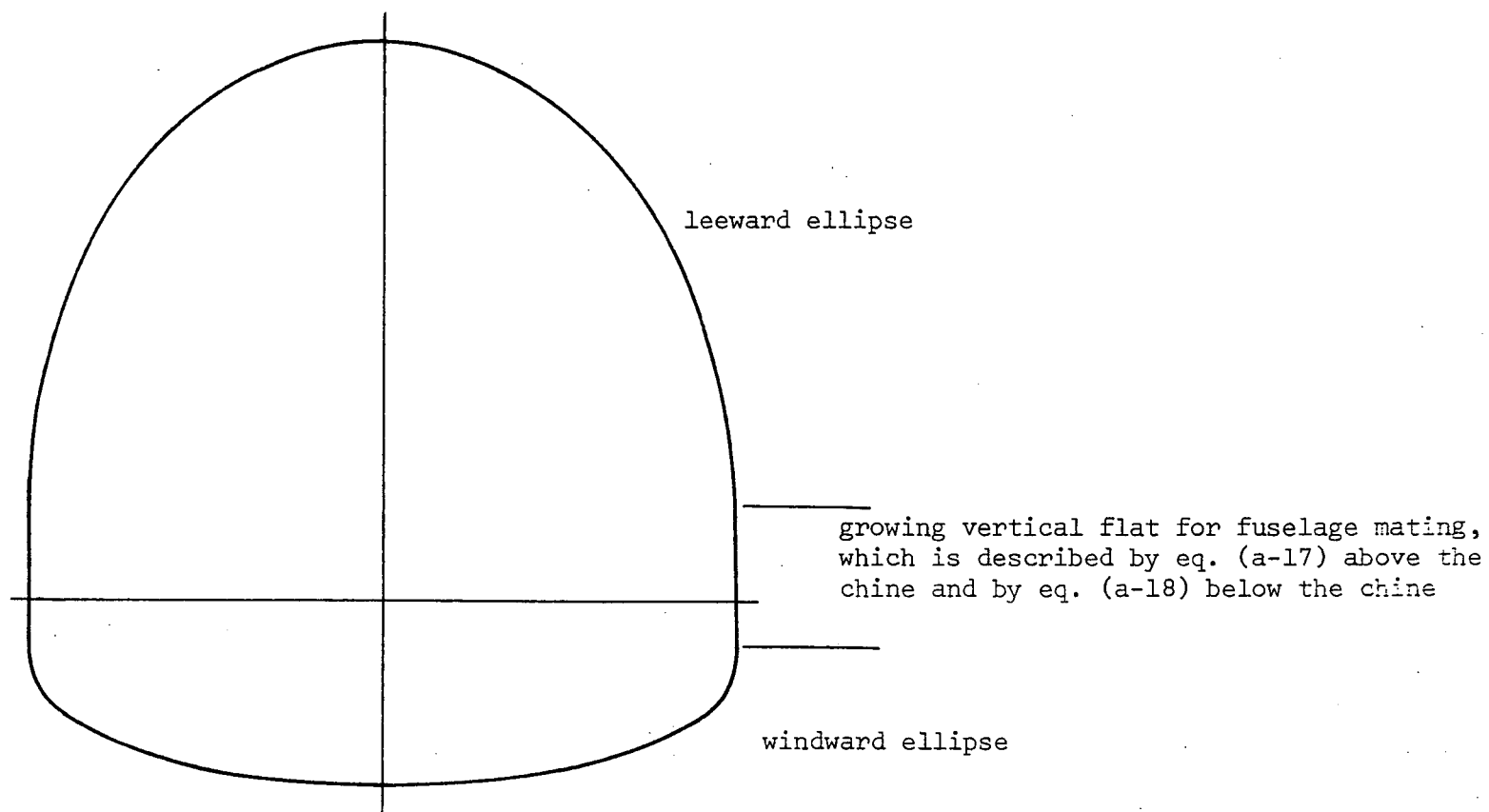
windward ellipse

Figure A-8. - Cross-section of the UTN7 at x = .34.
  (full-scale)

APPENDIX B - FLOW-FIELD TECHNIQUES

Inviscid Flow-Field

The local shock angles taken from shadowgraph photographs are compared with tangent wedge, tangent cone, and parallel shock values in Fig. B-1. Though there is considerable scatter in the measured shock-angles, the tangent cone values are seen to best represent the results. The tangent cone values shown in Fig. B-1 were computed using the following equation from Ref. 26

$$\frac{\sin \theta_s}{\sin \alpha_1} = \left[\frac{\gamma + 1}{2} + \frac{1}{(M_\infty \sin \alpha_1)^2} \right]^{0.5} \tag{b-1}$$

Centerline surface pressure measurements for Phase B space shuttle configurations indicate surface pressures are generally between tangent cone and modified Newtonian theory. Examples of these data for the McDonnell Douglas Phase B orbiter are shown in Fig. B-2 which were taken from Ref. 27 Modified Newtonian theory was used to define the pressure distributions in the present calculations of the inviscid flow-field. With both shock angle and surface pressure calculated all other properties at the boundary-layer edge were determined by crossing the shock using the oblique shock relations followed by an isentropic compression to surface pressure.

Cross sections for the nose region of the UTN2 were approximated by double radius blunt bodies and the crossflow velocity gradient obtained from Fig. 20 of Ref.28. The crossflow flow velocity gradient for the elliptical cross sections of the UTN7 were obtained by using the shock standoff distances of Ref.29 and Equation (B-2) from Ref. 28. These crossflow velocity gradients were then applied over the following regions in the boundary-layer calculations based on the oil flow photographs.

155

Configuration	Crossflow Region
UTN2	$0 < x/L \leq 0.36$
UTN7	$0 < x/L \leq 0.30$

Results obtained from the delta-wing flow-field correlations of Ref. 30 indicate that true crossflow is not achieved on a 49-deg sweep delta wing at angles of attack of 50 deg or less. Furthermore, it was shown in Ref. 21 that streamline divergence effects are significant on delta wing centerline heating only at values of angle of attack significantly greater than the apex angle, or in the case of the present wing, 41 deg. For these reasons no crossflow or streamline divergence was applied to the centerline boundary layer calculations in the aft region.

Boundary-Layer Calculations

The boundary-layer calculations in the present report use the basic methods which have become typical in data comparisons by Space Shuttle Contractors (see Refs. 31 and 32). These are the Eckert Reference Enthalpy method (Ref. 33) for laminar flow and the Spalding-Chi method (Ref. 34) for turbulent flow. Crossflow corrections for nose region were obtained using the crossflow velocity gradients as outlined and equations for equivalent surface distances from Refs. 35 and 36. The differences between the theoretical heat-transfer distributions for the UTN2 and for the UTN7 (Figs. 17 and 18, respectively) when the boundary layer is turbulent are due primarily to differences in the virtual origin, i.e., the onset of transition.

A comparison of present results for heat transfer rates and momentum thickness Reynolds number with those obtained using a nonsimilar numerical calculation (Ref. 37) and the same edge conditions are shown in Fig. B-3. The heating rate comparison is good but a significant difference between the methods occurs in the momentum thickness Reynolds number at the rear of the body.
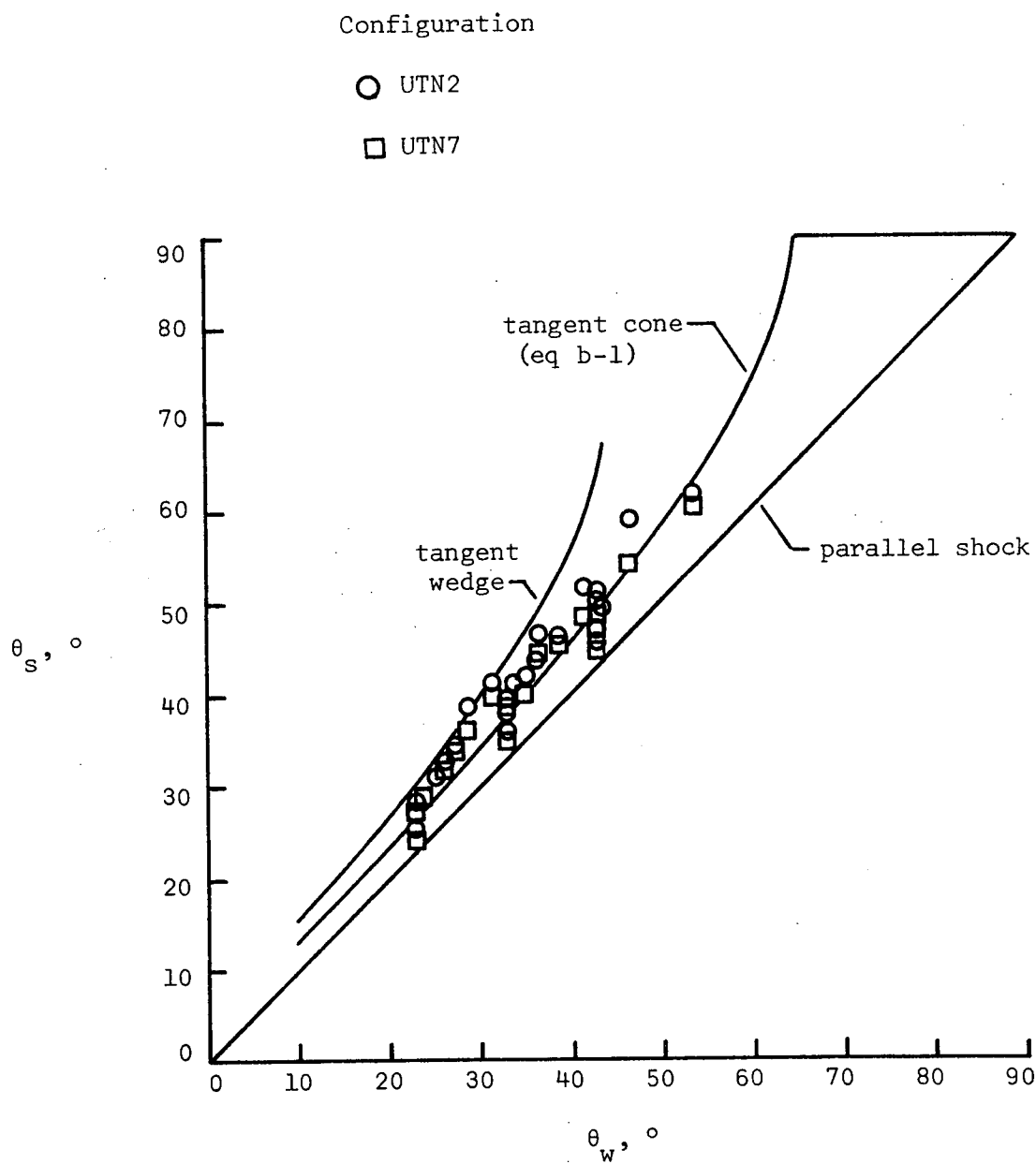
Figure B1. - Comparison of the shock-angle measurements
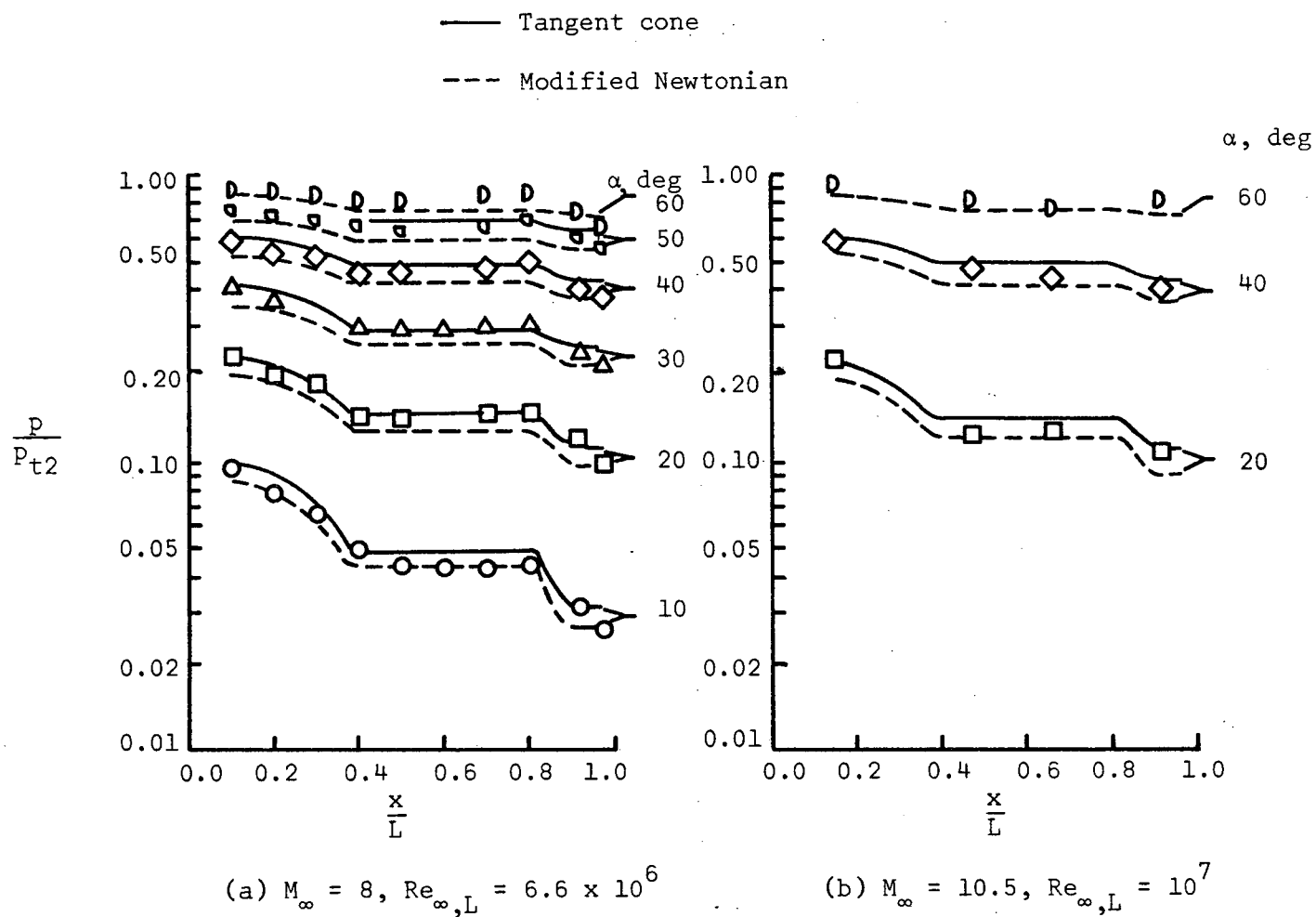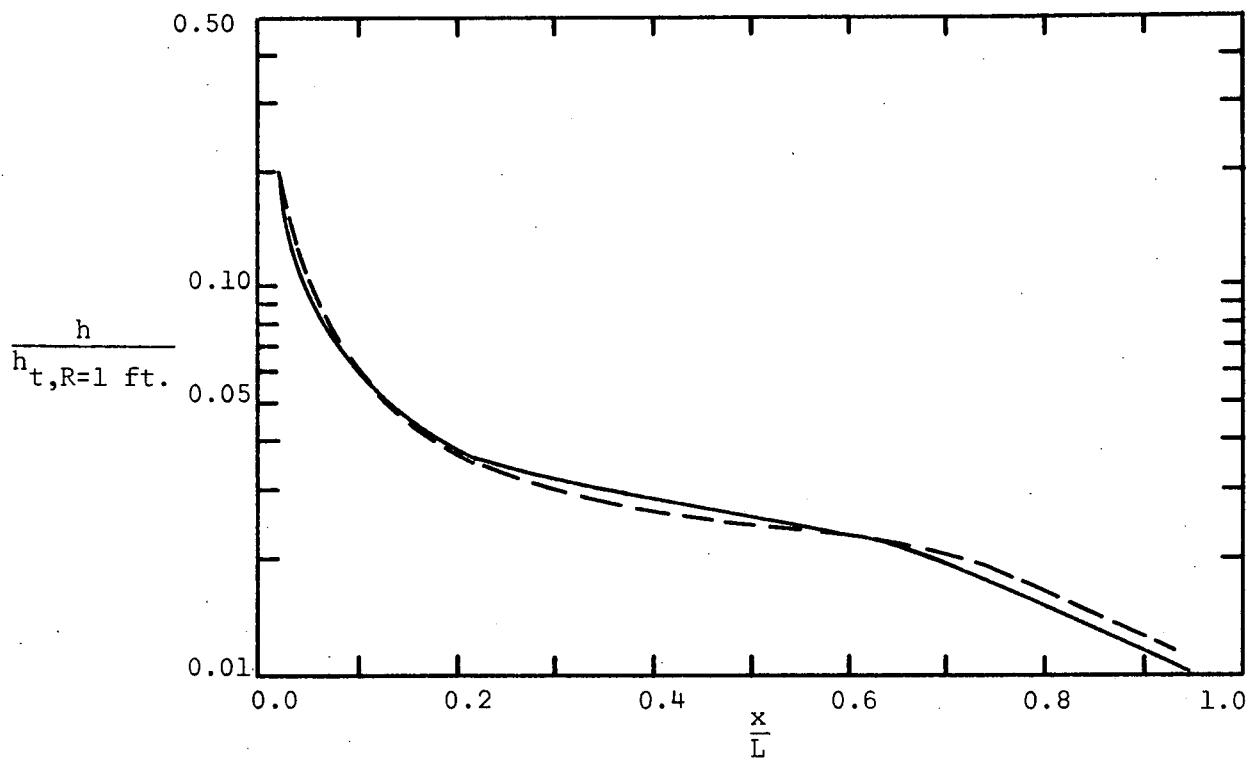   with analytical calculations.

157

Figure B2. - Pressure distributions for the windward pitch-plane
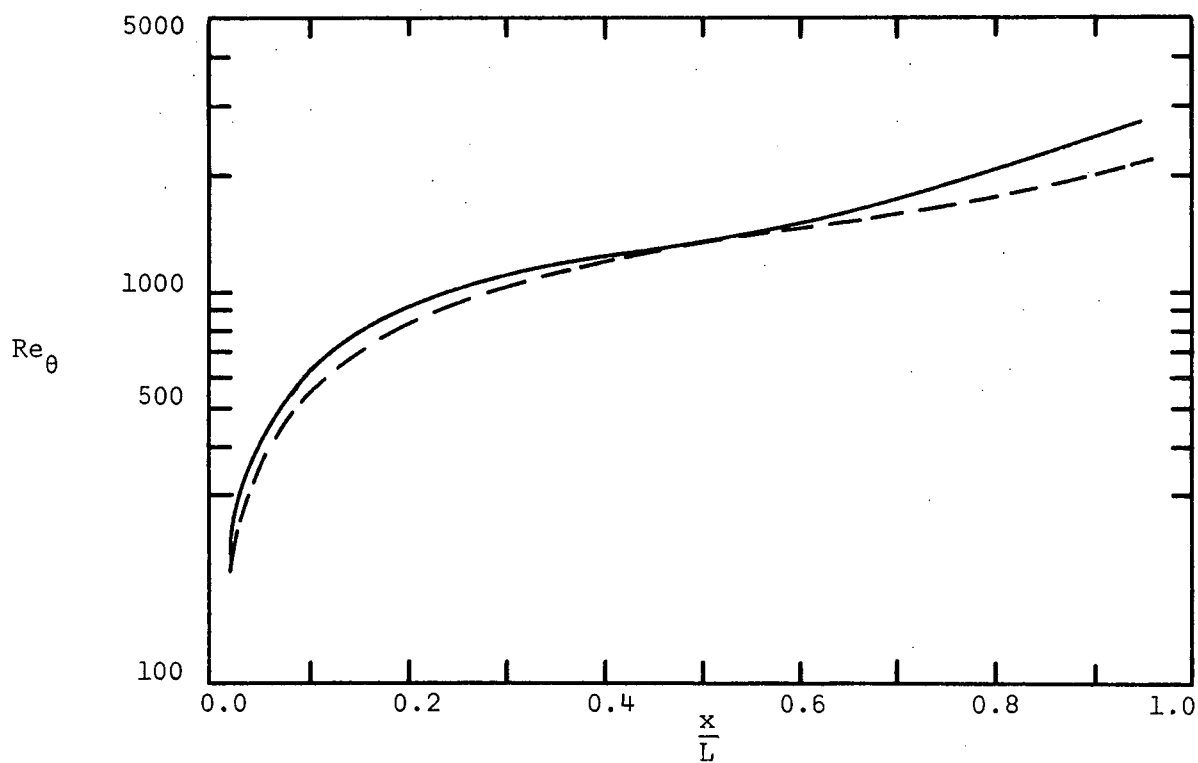of a MDAC orbiter-configuration.

158

Figure B-3. – Comparison of the present solution with a numerical solution for a nonsimilar boundary-layer. $Re_{\infty, L} = 7.5 \times 10^6$, $\alpha = 20°$

159